

**MEASUREMENTS IN THE BIMODAL REGION OF A WING-BODY
JUNCTION FLOW WITH A RAPIDLY-SCANNING TWO-VELOCITY-
COMPONENT LASER-DOPPLER VELOCIMETER**

by

Kevin A. Shinpaugh

Dissertation submitted to the Faculty of the

Virginia Polytechnic Institute and State University

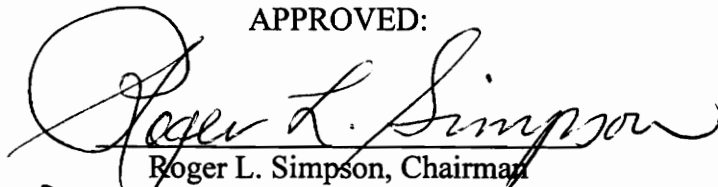
in partial fulfillment of the requirements for the degree of

Doctor of Philosophy

in

Aerospace Engineering


APPROVED:


Roger L. Simpson, Chairman


William J. Devenport


Bernard Grossman


Dana A. Walker


Alfred L. Wicks

August, 1994

Blacksburg, Virginia

C.2

LD

5655

V856

1994

S483

C.2

**MEASUREMENTS IN THE BIMODAL REGION OF A WING-BODY
JUNCTION FLOW WITH A RAPIDLY-SCANNING TWO-VELOCITY-
COMPONENT LASER-DOPPLER VELOCIMETER**

by

Kevin A. Shinpaugh

Roger L. Simpson, Chairman

Aerospace Engineering

(ABSTRACT)

The structure and behavior of the bimodal flow of the horseshoe vortex at the nose of a wing-body junction flow was studied. The wing consists of a 3:2 elliptic nose and a NACA 0020 tail joined at the maximum thickness (t). Measurements were performed with an approach flow conditions of $U_{ref} = 27.5$ m/s, $Re_{\theta} = 6700$ at $x/t = -2.15$, and $\delta/t = 0.5$.

A rapidly-scanning two-velocity-component laser-Doppler anemometer system was developed for use in investigating this flow. U and V velocity components were measured simultaneously with surface pressure measurements at the location of the most bimodal pressure histogram ($x/t = -0.26$).

Mean (U , V) and rms (u' , v') velocity components were obtained at four x locations, $x/t = -0.15$, -0.20 , -0.25 , -0.30 , and show the same flow features measured in previous studies at this facility.

Cross-correlations between the velocity and the surface pressure fluctuations were obtained. Large correlations were found between the u fluctuations ($x/t = -0.15, -0.25,$ and -0.30) near the wall, $y/t < 0.05$, and the surface pressure fluctuations. The u fluctuations for $y/t > 0.1$ at all four x -locations lead the surface pressure fluctuations.

Space-time correlations between the velocity fluctuations near the wall with the velocity fluctuations along the scan were also obtained. The correlations at $x/t = -0.25$ and $x/t = -0.30$ show that the fluctuations in the outer region, $y/t > 0.1$, are significantly correlated with and lead the velocity fluctuations near the wall.

These measurements support a model of a single primary junction vortex that changes size and location in front of the wing. The strength or circulation of this vortex varies by only 20%. Event-threshold conditional-averages of velocity were obtained based on the surface pressure signal, which is sensitive to the movement of the junction vortex. These show that the junction vortex is concentrated near the nose, with large backflow, when the surface pressure signal is above the mean. The junction vortex is larger, with smaller backflow near the nose, when the surface pressure signal is below the mean.

The velocity-pressure cross-correlations and space-time correlations indicate that the behavior of the junction vortex is influenced by fluctuations originating upstream and propagating inward and downward toward the wing.

Acknowledgments

The author would like to express his deep appreciation to his advisor, Dr. Roger L. Simpson who gave invaluable guidance and assistance throughout this project. Without his encouragement, support and guidance, it would have been difficult to accomplish this work.

He also would like to thank Dr. William Devenport, Dr., Bernard Grossman, Dr. Dana A. Walker and Dr. Alfred L. Wicks for serving on the Advisory Committee and for their helpful comments and suggestions on this project.

He also wishes to thank his friends, in and outside of Blacksburg, for their time and support. Especially Paul and Kari Duncan for allowing the author to live in their home during the final preparation of this manuscript.

This project was supported by grants from the Air Force Office of Scientific Research, the Office of Naval Research, and the Advanced Research Projects Agency.

Table of Contents

List of Symbols	ix
<i>Greek Symbols</i>.....	xi
<i>Subscripts</i>	xii
List of Tables.....	xiii
List of Figures	xiv
1. Introduction.....	1
1.1 Review of Previous Work.....	2
1.1.1 Studies using a 3:2 elliptic nose/NACA 0020 tail wing.....	2
1.1.2 Studies of other appendage geometries.....	5
1.1.3 Suggested Models of the junction vortex.....	8
1.2 Objectives and outline of this Work	9

2. Experimental Apparatus and Techniques	11
2.1 Facilities and Equipment.....	11
2.1.1 Wind Tunnel	11
2.1.2 Wing-body Junction Model	12
2.2 Instrumentation	13
2.2.1 Scanning laser-Doppler anemometer	13
2.2.2 Calibration of Scanner Position	15
2.2.3 Pressure Measurements.....	16
2.2.4 Data Acquisition	17
2.3 Data Reduction.....	18
2.4 Uncertainty Analysis.....	25
3. Results	30
3.1 Experimental Flow and Measurement Locations.....	30
3.1.1 Coordinate System	31
3.2 Comparison with Previous Studies	31
3.3 Cross-correlations of Pressure-Velocity	33
3.4 Joint histograms	36
3.4.1 Joint velocity probability density functions.....	37
3.4.2 Joint velocity and pressure probability functions	38
3.5 Space-time correlations.....	41

3.6 Quadrant analysis.....	44
3.7 Mode averages	46
4. Discussion.....	48
4.1 Relationship between velocity correlations and velocity-pressure cross-correlations.....	48
4.2 Possible simple flow models of the vortical structure	53
4.2.1 Sequence of flow events	54
4.2.2 Other models.....	56
4.3 Source of bimodal velocity and surface pressure histograms.....	57
5. Conclusions	59
References	62
Tables	65
Figures.....	71
Appendix A. A Rapidly Scanning Two-Velocity-Component Laser Doppler Velocimeter	142
References	159
Figures.....	160

Vita 177

List of Symbols

B	Frequency bandwidth
c	Chord of wing
f_D	Doppler frequency
f_B	Bragg cell frequency shift
N	Sample size
p	Fluctuating surface pressure
pdf	Probability density function
PMT	Photomultiplier tube
R_{xx}	Autocorrelation function
R_{xy}	Cross-correlation function
Re	Reynolds number based on wing thickness ($=\rho U t / \mu$)
Re_θ	Reynolds number based on momentum thickness ($=\rho U \theta / \mu$)
rms.....	Root mean square

- St Strouhal number based on maximum wing thickness ($= \frac{\bar{f}t}{U_{ref}}$)
- T Time
- t Maximum thickness of wing
- U Mean velocity in the streamwise direction
- U Instantaneous velocity component in the streamwise direction ($=U+ u$)
- u Fluctuating velocity component in the x direction
- U_{ref} Reference mean free-stream velocity measured at $x/t=-19.39$
- V Mean velocity component normal to floor
- V $V+v$, Instantaneous velocity component in the y direction
- v Fluctuating velocity component in the y direction
- V_s Scan velocity of measurement volume
- W Mean velocity component in the z direction
- $\mathbf{x}, \mathbf{x}_s, \mathbf{x}_1$ Position vector, position vector of a surface location, position vector of a fixed point
- x, y, z Right-handed coordinates in the streamwise, normal to floor, spanwise direction, respectively

Greek Symbols

- α Velocity gradient in scan direction
- β Mean velocity (used in bias estimate)
- Γ Circulation around a closed contour
- λ Laser wavelength
- λ_{FS} Fringe spacing
- ε Normalized rms error
- ρ Density
- ρ_{xx} Normalized autocorrelation coefficient function
- ρ_{xy} Normalized cross-correlation coefficient function
- τ Time delay
- ϕ Half-angle beam intersection

Subscripts

- up.....Cross-correlation between u and p
- vp.....Cross-correlation between u and p
- uu.....Cross-correlation between u (at fixed point) and u (along scan)
- uv.....Cross-correlation between u (at fixed point) and v (along scan)
- vu.....Cross-correlation between v (at fixed point) and u (along scan)
- vv.....Cross-correlation between v (at fixed point) and v (along scan)

List of Tables

Table 1: Uncertainties on the cross-correlation coefficient function for the velocity measurement location for the u component.66

Table 2: Uncertainties on the cross-correlation coefficient function for the velocity measurement location for the v component.67

Table 3: Uncertainties on the space-time correlation coefficient function for ρ_{uu} as a function of measurement location.....68

Table 4: Uncertainties on the space-time correlation coefficient function for ρ_{vv} as a function of measurement location.....69

Table 5: Uncertainties on the space-time correlation coefficient function for ρ_{uv} as a function of measurement location.....70

List of Figures

Figure 1. Schematic of a wing-body junction flow.....	72
Figure 2. Oil flow in the nose region of the wing-body junction from Devenport and Simpson (1990a).	73
Figure 3 Mean velocity vectors showing the mean junction vortex (Devenport and Simpson, 1990a).	74
Figure 4. Side view schematic of the boundary layer wind tunnel used for the wing-body junction experiments.....	75
Figure 5. Top view of Rapidly Scanning Laser Doppler Velocimeter (RSLDV).....	76
Figure 6. View of wing-body showing the coordinate system, pressure transducer, laser beams and receiving optics.	77
Figure 7. Schematic of data acquisition system.....	78
Figure 8. Measurement volume scan velocity at the four measurement locations.	79
Figure 9. U component mean velocity comparisons with Devenport and Simpson (1990b).	80
Figure 10. V component mean velocity comparisons with Devenport an Simpson (1990b).	81
Figure 11. U component mean square velocity comparisons with Devenport an Simpson (1990b).	82
Figure 12. V component mean square velocity comparisons with Devenport an Simpson (1990b).	83

Figure 13. Histograms of U velocity at $x/t=-0.15$	84
Figure 14. Histograms of U velocity at $x/t=-0.20$	85
Figure 15. Histogram of U velocity at $x/t=-0.25$	86
Figure 16. Histograms of V velocity at $x/t=-0.25$	87
Figure 17. Histograms of U velocity at $x/t=-0.30$	88
Figure 18. Histograms of V velocity at $x/t=-0.30$	89
Figure 19. Probability density function of pressure fluctuations measured at $x/t=-0.26$ for each velocity measurement positions.....	90
Figure 20. Cross-correlation coefficient function ρ_{up} between u fluctuation at $x/t=-0.15$ and the pressure fluctuations at $x/t=-0.26$	91
Figure 21. Cross-correlation coefficient function ρ_{up} between u fluctuation at $x/t=-0.20$ and the pressure fluctuations at $x/t=-0.26$	92
Figure 22. Cross-correlation coefficient function ρ_{up} between u fluctuation at $x/t=-0.25$ and the pressure fluctuations at $x/t=-0.26$	93
Figure 23. Cross-correlation coefficient function ρ_{vp} between v fluctuation at $x/t=-0.25$ and the pressure fluctuations at $x/t=-0.26$	94
Figure 24. Cross-correlation coefficient function ρ_{up} between u fluctuation at $x/t=-0.30$ and the pressure fluctuations at $x/t=-0.26$	95
Figure 25. Cross-correlation coefficient function ρ_{vp} between v fluctuation at $x/t=-0.30$ and the pressure fluctuations at $x/t=-0.26$	96
Figure 26. Contours of joint U and V velocity probability density functions for $x/t=-0.25$ at four y locations (note: pdf X 1000).....	97
Figure 27. Contours of joint U and V velocity probability density functions for $x/t=-0.30$ at four y/t locations (note: pdf X 1000).	98
Figure 28. Contours of joint U velocity and surface pressure probability density functions for $x/t=-0.15$ at six y locations (note: pdf X 1000).	99

Figure 29. Contours of joint U velocity and surface pressure probability density functions for $x/t=-0.20$ at six y/t locations (note: pdf X 1000).	100
Figure 30. Contours of joint U velocity and surface pressure probability density functions for $x/t=-0.25$ at six y/t locations (note: pdf X 1000).	101
Figure 31. Contours of joint V velocity and surface pressure probability density functions for $x/t=-0.25$ at six y/t locations (note: pdf X 1000).	102
Figure 32. Contours of joint U velocity and surface pressure probability density functions for $x/t=-0.30$ at six y/t locations (note: pdf X 1000).	103
Figure 33. Contours of joint V velocity and surface pressure probability density functions for $x/t=-0.30$ at six y/t locations (note: pdf X 1000).	104
Figure 34. Space-time correlations coefficient ρ_{uu} for u fluctuations between a fixed y location and points along the scan for $x/t=-0.15$.	105
Figure 35. Space-time correlations coefficient ρ_{uu} for u fluctuations between a fixed y location and points along the scan for $x/t=-0.15$.	106
Figure 36. Space-time correlations coefficient ρ_{uu} for u fluctuations between a fixed y location and points along the scan for $x/t=-0.20$.	107
Figure 37. Space-time correlations coefficient ρ_{uu} for u fluctuations between a fixed y location and points along the scan for $x/t=-0.20$.	108
Figure 38. Space-time correlations coefficient ρ_{uu} for u fluctuations between a fixed y location and points along the scan for $x/t=-0.25$.	109
Figure 39. Space-time correlations coefficient ρ_{uu} for u fluctuations between a fixed y location and points along the scan for $x/t=-0.25$.	110
Figure 40. Space-time correlations coefficient ρ_{vv} for v fluctuations between a fixed y location and points along the scan for $x/t=-0.25$.	111
Figure 41. Space-time correlations coefficient ρ_{vv} for v fluctuations between a fixed y location and points along the scan for $x/t=-0.25$.	112
Figure 42. Space-time correlations coefficient ρ_{uv} for u fluctuations between a fixed y location and v fluctuations along the scan for $x/t=-0.25$.	113

Figure 43. Space-time correlations coefficient ρ_{uv} for u fluctuations between a fixed y location and v fluctuations along the scan for $x/t=-0.25$	114
Figure 44. Space-time correlations coefficient ρ_{vu} for v fluctuations between a fixed y location and u fluctuations along the scan for $x/t=-0.25$	115
Figure 45. Space-time correlations coefficient ρ_{vu} for v fluctuations between a fixed y location and u fluctuations along the scan for $x/t=-0.25$	116
Figure 46. Space-time correlations coefficient ρ_{uu} for u fluctuations between a fixed y location and points along the scan for $x/t=-0.30$	117
Figure 47. Space-time correlations coefficient ρ_{uu} for u fluctuations between a fixed y location and points along the scan for $x/t=-0.30$	118
Figure 48. Space-time correlations coefficient ρ_{vv} for v fluctuations between a fixed y location and points along the scan for $x/t=-0.30$	119
Figure 49. Space-time correlations coefficient ρ_{vv} for v fluctuations between a fixed y location and points along the scan for $x/t=-0.25$	120
Figure 50. Space-time correlations coefficient ρ_{uv} for u fluctuations between a fixed y location and v fluctuations along the scan for $x/t=-0.30$	121
Figure 51. Space-time correlations coefficient ρ_{uv} for u fluctuations between a fixed y location and v fluctuations along the scan for $x/t=-0.30$	122
Figure 52. Space-time correlations coefficient ρ_{vu} for v fluctuations between a fixed y location and u fluctuations along the scan for $x/t=-0.30$	123
Figure 53. Space-time correlations coefficient ρ_{vu} for v fluctuations between a fixed y location and u fluctuations along the scan for $x/t=-0.30$	124
Figure 54. Quadrant analysis of u fluctuations at $y/t=0.032$ versus four other y locations for $x/t=-0.15$	125
Figure 55. Quadrant analysis of u fluctuations at $y/t=0.032$ versus four other y locations for $x/t=-0.20$	126
Figure 56. Quadrant analysis of u fluctuations at $y/t=0.032$ versus four other y locations for $x/t=-0.25$	127

Figure 57. Quadrant analysis of v fluctuations at $y/t=0.032$ versus four other y locations for $x/t=-0.25$	128
Figure 58. Quadrant analysis of u fluctuations at $y/t=0.032$ versus four other y locations for $x/t=-0.30$	129
Figure 59. Quadrant analysis of v fluctuations at $y/t=0.032$ versus four other y locations for $x/t=-0.30$	130
Figure 60. Mode averaged velocity vectors based on the bimodal pressure probability density functions.	131
Figure 61. Probability density functions of the time between successive positive crossings of the threshold level of the surface pressure signal.	132
Figure 62. Velocity vectors averaged at the instant the surface pressure signal makes a negative transition across the threshold at the peak in the bimodal pressure pdf below the mean.	133
Figure 63. Velocity vectors averaged at the instant the surface pressure signal makes a positive transition across the threshold at the peak in the bimodal pressure pdf below the mean.	134
Figure 64. Velocity vectors averaged at the instant the surface pressure signal makes a positive transition across the threshold at the mean.	135
Figure 65. Velocity vectors averaged at the instant the surface pressure signal makes a positive transition across the threshold at the peak in the bimodal pressure pdf above the mean.	136
Figure 66. Velocity vectors averaged at the instant the surface pressure signal makes a negative transition across the threshold at the peak in the bimodal pressure pdf above the mean.	137
Figure 67. Velocity vectors averaged at the instant the surface pressure signal makes a negative transition across the threshold at the mean.	138
Figure 68. Plots of $\partial U / \partial y$ at $x/t=-0.25$ versus y/t and $\overline{u(y_1)v}$ and $\overline{v(y_1)v}$ at $y/t=0.039$ for $x/t=-0.25$	139
Figure 69. The kernel of equations 4.5 (for both $\overline{pu(y_1)}$ and $\overline{pv(y_1)}$) as a function of distance from the wall, y	140

Figure 70. Model for the sequence of flow events in the nose region of a wing-body
junction flow.141

1. Introduction

The turbulent flow around a wing-body junction is a complex, highly turbulent three-dimensional flow. This is a fairly common flow, resulting when a turbulent boundary layer encounters an obstruction protruding from a surface, as shown in Figure 1. The approach boundary layer has a distribution of spanwise vorticity. The adverse pressure gradient near the wing causes the boundary layer to separate from the wall. The distribution of spanwise vorticity in the boundary layer then rolls up into a vortical structure and wraps around the wing to form a horseshoe or necklace vortex.

The understanding of this type of flow phenomenon is important since it is encountered in many flows and typically has adverse effects. Junction flows occur at aircraft wing roots, in turbo-machinery, ship and submarine appendage-hull junctions, and at the base of support structures. The vortical nature of junction flows can lead to erosion around support pillars, high heat transfer at the root of turbine blades, excessive noise and vibration in aircraft, ships and submarines due to the high turbulence. Greater understanding of this phenomenon may lead to means for controlling the adverse effects.

1.1 Review of Previous Work

The flow past an appendage has been of considerable research interest. Many different shapes have been studied including blunt obstructions, circular cylinders and streamlined bodies, including the present wing (3:2 elliptic nose/NACA 0020 tail). Most of this research has quantified the mean flowfield. Devenport and Simpson (1990a) provide a discussion of the earlier work. The review of earlier work given here is of studies reporting results on the time-dependent structure of junction flows in the nose region. The review is considered in two sections: studies of the flowfield around a wing with a 3:2 elliptic nose/NACA 0020 tail and studies of the flowfield in the nose region of other appendage geometries.

1.1.1 Studies using a 3:2 elliptic nose/NACA 0020 tail wing

Devenport and Simpson (1987, 1990a, and 1990b) conducted an extensive survey of the flowfield around the wing-body. Surface oil flows on the wall and on the wing were made. Mean pressure measurements were also made on the test wall and the surface of the wing. Figure 2 is an oil flow that shows the symmetric separation line with a three-dimensional stagnation point located approximately at $x/t=-0.47$ and the line of low shear (open separation) near the nose of the wing. The flow around the wing was investigated

with a single component hot wire anemometer and three-velocity-component LDV measurements in the plane of symmetry in front of the wing. Figure 3 shows the mean velocity vectors obtained in the plane of symmetry in front of the wing. This figure shows that the mean junction vortex lies in the region from $x/t=-0.1$ to $x/t=-0.3$.

Devenport and Simpson (1987, 1989) reported the first bimodal (double-peaked) velocity histograms, which correspond to high levels of turbulence intensities. One peak occurred near the zero u velocity (zero mode) and the other occurred for a moderately large backflow velocity (backflow mode). Short term cross-correlations were made between the LDV measurements and a hot-wire probe at 93% of the boundary layer thickness when the velocity signal changes between the two modes. Significant negative correlations were obtained and indicate that the change from backflow to near zero velocity is preceded by a drop in the velocity at the boundary layer edge.

The flow structure based on decomposing the bimodal histogram was made with velocity vectors for the zero-flow mode and backflow mode (Devenport and Simpson, 1990a). This decomposition was constructed without considering any phase shift of mode transition between neighboring measurement positions. Found that the frequencies of the large-scale fluctuations in the backflow to be $0.05U_{ref} / \delta$, based on the mean period of the transition between the two modes.

In a water tunnel, Kim, Walker, and Simpson (1991) studied the wing-body junction flow at two approach boundary layer Reynolds numbers based on maximum

wing thickness, $Re_\theta = 330$ and $Re_\theta = 1100$. Hydrogen-bubble flow visualization and single-velocity-component LDV measurements were made in the plane of symmetry at the lower Reynolds number; only LDV measurements were made at the higher Reynolds number. The LDV measurements show the same features as found by Devenport and Simpson (1990a,b): bimodal histograms and a large backflow near the wall. The hydrogen-bubble visualizations showed a complicated time-dependent flow structure in the vicinity of the nose. A primary junction vortex was observed to interact with a series of secondary vortices that were shed near the three-dimensional stagnation point location. Found that the junction vortex exhibited an acyclic behavior which is related to the stretching of the horseshoe vortex system. The switching frequency between the two modes was determined from both the LDV data, $St = 0.34$ for $Re_\theta = 330$ and $St = 0.40$ for $Re_\theta = 1100$, and flow visualizations, $St = 0.28$.

Rife, Devenport and Simpson (1992) studied the relationship between surface pressure fluctuations and velocity fluctuations in the bimodal region of the same flowfield. A two-component LDV system was used to measure the U and V components of velocity. Surface pressure fluctuations, using microphones insensitive to the mean pressure signal, were measured at two locations simultaneously with each component of velocity. From velocity/pressure correlations and cross-spectra, the bimodal zone was found to be dominated by low frequency turbulent structures. These low frequency structures have non-dimensional frequencies of $ft/U_{ref} = 6 \times 10^{-3}$ to $ft/U_{ref} = 0.5$.

Khan (1994) used flow visualization and a three-velocity-component LDV (with simultaneous U , V , W) to study the nose region of this wing-body junction flow in a water tunnel. Regions of tri-modal velocity histograms were observed, attributed to the dynamic movement of the junction vortex system. Hydrogen bubble flow visualizations show that there are three flow modes dependent on the Reynolds number based on the maximum thickness of the wing. The approach Reynolds number based on the momentum thickness was not mentioned for the flow visualizations. A steady vortex system was observed for Reynolds numbers below 2500, Mode I. This system consisted of three main vortices with two counter-rotating foci-structures. For Reynolds numbers of 2500 to 3500 an oscillatory vortex system was observed, Mode II. Shedding-splitting of the vortex system was observed for Reynolds numbers of 3500 to 6000, Mode III. Prior to splitting of the shed vortex, a new one is formed. They found that the oscillating/shedding frequency, non-dimensionalized by the free-stream velocity and the maximum wing thickness, varied almost linearly with Reynolds number. The characteristic frequency of these motions ranged from $St=0.17$ at $Re=2500$ to $St=0.26$ at $Re=3500$ for Mode II and $St=0.27$ at $Re=3800$ to $St=0.285$ at $Re=5800$ for Mode III.

1.1.2 Studies of other appendage geometries

Thomas (1987) used smoke visualization in front of a circular cylinder to characterize the flowfield for a laminar junction flow. The flowfield in front of the

cylinder was found to be periodic and cyclic. A vortex is periodically created just downstream of the separation point and is convected toward the face of the cylinder. The vortex then becomes highly stretched around the cylinder and then is pinched-off. The process then repeats. The frequencies of these motions were found to scale on the cylinder diameter and the free-stream velocity, fd / U_{ref} . This ranged from 0.1 at $Re_D = 5000$ to 0.32 at $Re_D = 13000$

Dargahi (1989) used hydrogen bubble visualization and hot film measurements to study the flow around a circular cylinder normal to a flat plate. The results indicated that the number of vortices increases with Reynolds number and that the vortices are shed “quasi-periodically”, $St_D=0.32$.

Agui and Andreopoulos (1990) also investigated flow around a circular cylinder using flow visualization and surface pressure fluctuation measurements. A primary vortex was observed in the flow visualizations, which induces an eruption of wall fluid. These eruptions can result in the formation of counter-rotating vortices, which evolve quickly in time and space so are not apparent in the mean flow. Space-time pressure correlations decreased downstream of the separation area and longer time scales were also observed.

Fleming, Simpson, and Devenport (1991) from the study of inviscid flow around various wing shapes determined a relationship (correlation) between nose bluntness and the average vortex stretching rate around the nose.

Larousse, Martinuzzi, and Tropea (1992) studied the flow around obstacles with square cross-section and cross-channel widths varying from a cube to that of a two-dimensional rib. Oil flow visualization and a two-component LDV were used in this study. Bimodal velocity histograms were observed except for higher width to height aspect ratio obstacles, above 10. A mode analysis similar to what was done by Devenport and Simpson (1990a) was used to decompose the bimodal velocity histograms into two flow modes. These two flow modes are similar to those obtained by Devenport and Simpson (1990a). They did not discuss the switching frequency between modes in this study.

Martinuzzi and Tropea (1993) studied the flowfield around surface mounted prismatic obstacles with different spanwise aspect ratios using crystal violet oil-film and laser sheet visualizations. Static surface pressure measurements were also made. The purpose of their study was to investigate the differences between two-dimensional and three-dimensional obstacle-junction flows. The flow in front of these obstacles was found to be inherently three-dimensional. For obstacles with aspect width/height ratios greater than 10, the flow in front of the obstacle develops cellular structures and passes over the obstacle in preferred paths. Small aspect ratio obstacles showed the presence of two alternating states. In one mode, high inertia fluid moves down the face of the obstacle and is deflected to form a backflow jet adjacent to the wall. This jet loses energy and rolls up to form a system of up to four vortices, which characterizes the second mode.

Ölçmen and Simpson (1994) conducted a study of various streamlined body shapes to determine the influence on the pressure fluctuations. They determined an empirical relationship between the rms pressure fluctuations and the wing geometry. This relationship showed that the rms pressure fluctuations are logarithmically related to the V momentum rate and to the 0.4 power of the U momentum rate of the flow at the nose region.

1.1.3 Suggested Models of the junction vortex

Many models have been suggested for the flow structure in front of wing-junction flows. Most of these have been based on the results from oil flow visualizations and on mean velocity measurements. These models usually consist of a two or more vortex system in the plane of symmetry of the appendage (Baker, 1980; Dargahi, 1989; and Thomas, 1987). These models usually apply to low Reynolds number flows. However, such models would not apply to junction flows that exhibit bimodal velocity or surface pressure histograms.

Devenport and Simpson (1990a), Agui and Andreopoulos (1990), and Larousse, Martinuzzi and Tropea (1992), have reported the observation of a high speed backflow jet near the wall. The jet was observed from the results of mode averages of the bimodal velocity histograms. The proposed jet is seen to originate from irrotational free-stream

fluid moving down the front of the nose. This fluid, in order to preserve its irrotationality would form the jet.

From the observations of Kim, Walker, and Simpson (1991); Rife, Devenport, and Simpson (1992); and Khan (1994) they suggest that the observed bimodal behavior is due to the primary junction vortex moving in space with varying size and strength. Kim, Walker, and Simpson (1991) also report the intermittent collapses of the recirculation region in front of the nose that may lead to the bimodal unsteadiness.

1.2 Objectives and outline of this Work

Although many measurements have been performed on the wing-body junction flow, many questions still remain. Mean velocity and turbulence profiles have already been measured, as well as pressure fluctuations, but no satisfactory model of the structure in the bimodal zone has emerged. Simultaneous space and time-dependent velocity and pressure measurements in the plane of symmetry in the near nose region can provide some information to improve our understanding of this type of flow. The works of Rife, Devenport, and Simpson (1992) and Ölçmen and Simpson (1994) show the importance of surface pressure to the behavior of the junction flow. The objectives of this work are:

1. Obtain space and time dependent U and V components of velocity using a rapidly-scanning directionally-sensitive LDV and obtain simultaneous pressure fluctuations.
2. Analyze the space-time structure of the near nose region through space-time correlations and mode-averaged velocity profiles.
3. Confirm or develop a model of the structure of the flow in this region.

Chapter 2 describes the facilities and apparatus used in this work. This includes description of the wind tunnel, the wing-body model, a brief description of the scanning LDV system and the experimental techniques used in this work. The data reduction procedure is also discussed as well as the uncertainties in the measured and calculated quantities. Chapter 3 makes comparisons of the results of this study to previous studies. The results of this work are presented here. Chapter 4 provides discussion of the results found in this work, including the relationship between the velocity-pressure cross-correlations and the velocity cross-correlations. Conclusion made from this study are given in chapter 5.

2. Experimental Apparatus and Techniques

2.1 Facilities and Equipment

2.1.1 Wind Tunnel

The measurements were performed in the AOE Department low-speed boundary-layer tunnel at Virginia Tech. This tunnel has been used in much of the previous work concerning the wing-body junction flow studies done at Virginia Tech: Devenport and Simpson (1990a,b); Fleming, Simpson, and Devenport (1991); Rife, Devenport and Simpson (1992); and Ölçmen and Simpson (1994). The tunnel is an open circuit design. A 25 horsepower centrifugal blower sucks air through an air filter and blows the air through a fixed-setting flow damper (used to control flow speed), a section of honeycomb

to reduce flow swirl, a series of 7 turbulence-reducing screens, and a two-dimensional 4:1 contraction ratio nozzle into the test section.

The test section, shown in Figure 4, is 6 m long and 0.91 m wide with a rectangular cross-section. The upper wall is made of Plexiglas reinforced with aluminum channel. The side walls are float plate glass to avoid optical aberrations in the use of laser anemometry. The floor of the tunnel is made of high quality plywood, except in the vicinity of the model where Plexiglas inserts are used. A slot just upstream of the test section entrance is used to introduce seeding for laser anemometry measurements. The boundary layer along the lower wall is tripped at the test section entrance by a 0.63 cm high upstream facing step.

2.1.2 Wing-body Junction Model

The wing used in this study has a chord, c , of 30.5 cm, a height of 22.9 cm and a maximum thickness, t , of 7.17 cm. The cross-section consists of a 3:2 elliptical nose, with the major axis aligned with chord and a NACA 0020 as the tail joined at the maximum thickness. The wing is mounted at zero angle of attack with the leading edge 2.92 m downstream of the test section entrance. A gap of 3.7 cm was left between the ceiling and the top of the model to prevent the formation of a second junction vortex. Blockage effects are minimized by using side wall liners to simulate the streamlines

(Devenport and Simpson, 1990a). The boundary layer on the wing is tripped by 0.635 cm wide 120 grit sandpaper strips mounted 2.29 cm upstream of the maximum thickness location.

2.2 Instrumentation

2.2.1 Scanning laser-Doppler anemometer

Velocity Measurements were performed with a two-color two-velocity-component rapidly scanning laser-Doppler velocimeter (RSLDV) designed by the author and is shown as a schematic in Figure 5. See Appendix A for more information. The system uses a Coherent Innova 90 argon-ion laser operating in the all-wavelengths mode with an etalon. The laser was operated with a total output power of approximately 2 watts; at higher power levels the 488 nm (blue) beam did not stay in the TEM_{00} mode. Optics from a TSI two-color two-velocity-component system are used to generate the necessary beams. The blue (488 nm) and green (514.5 nm) beams are separated and used. The beam for each color is split into two equal intensity beams. One beam from each color is frequency-shifted by a Bragg cell, 40 MHz for the green and 30 MHz for the blue. All four laser beams pass through a series of lenses to expand and focus the beams.

A series of mirrors are used to aim the laser beams at a oscillating galvanometer mirror scanner (model 325 DT from General Scanning Inc.). The laser beams are then directed to another set of mirrors used to direct the beams to form the measurement volume.

The two green laser beams cross to form a measurement volume with fringes moving in the horizontal plane that measure the U component of velocity. The fringe spacing is $3.33\ \mu\text{m}$ and remains perpendicular to the free-stream direction throughout the scan. To measure the V component of velocity, the blue laser beams form a measurement volume with fringes moving in the near vertical direction, at half the scan angle off the vertical in the positive Z direction for a downward scan angle. The fringe spacing for the blue fringes is $20.66\ \mu\text{m}$. The maximum scan angle is approximately 1.25 degrees downward.

Diocetyl phthalate (DOP) smoke with a mean particle diameter of $2\ \mu\text{m}$ was used as seeding material and was introduced into the boundary layer at the leading edge of the test section floor, see Figure 4.

Forward scattered light from the measurement volume is collected at about 15 degrees off-axis in the upstream direction through a 50 mm diameter 100 mm focal length achromat. An achromat is used so that the scattered light from the two-color measurement volume is focused at the same location. The light is focused onto a vertical slit attached to the housing of a Thorn-EMI model 9813B photo-multiplier tube. The magnification ratio for the collecting optics is 0.2, which means that a 50 mm scan is imaged as a 10

mm scan on the slit. The floor was covered with a flat black adhesive covering to reduce reflections.

2.2.2 Calibration of Scanner Position

The x-measurement locations were determined by placing a metal scale at the tip of the wing-body model along the center line. The laser beam power at the probe volume was adjusted so that the beams were barely visible on the surface of the scale. The beams were scanned so as to hit the scale and the laser table was translated until the desired position was reached. The measurement location could be adjusted to be within ± 0.2 mm of the desired location.

In order to determine the y location of the measurement volume the position output from the scanner was sampled. To calibrate the output voltage from the scanner versus probe volume distance from the wall, y , the following procedure was used. Fine stainless steel wire (0.0254 mm diameter) was stretched across a slot cut in an aluminum channel, machined to stand vertically. The wires were spaced vertically every 2.54 mm, and were measured by a height gage. The block is placed in the tunnel with the wires located at the measurement location. The probe volume is then manually scanned to hit each wire while noting the voltage output from the scanner position signal. A linear

regression was then performed on the voltage-position data and the following calibrations were obtained:

$$y(x / t = -0.15, -0.20) = -7.263 \times \text{volts} + 5.120 \quad (2.1)$$

$$y(x / t = -0.25) = -7.240 \times \text{volts} + 4.956 \quad (2.2)$$

$$y(x / t = -0.30) = -7.208 \times \text{volts} + 4.942 \quad (2.3)$$

2.2.3 Pressure Measurements

Pressure measurements were performed so that the bimodal state could be assessed. The pressure transducer was located at $x/t=-0.26$ during all the velocity measurements, since this location appeared to have the most bimodal histogram for the pressure fluctuations. The measurements were performed by using an Endevco model 8510B-2 pressure transducer. The transducer has a 14 KPa range and a sensitivity of 14.8 mv/KPa. The transducer was connected to a Measurement Group strain gauge amplifier model 2210 with the gain set at 2400 and with a low pass filter of 1 KHz.

2.2.4 Data Acquisition

The Data acquisition system used with a scanning LDV system requires that the exact location of the measurement volume be known when a signal is detected. This is done by sampling the position output of the scanner and knowing the corresponding arrival time of the velocity signal. The data acquisition system used in these experiments is shown in Figure 7.

The signal from the PM tube is amplified and split. Each signal is then frequency down-mixed, by 30 MHz for the U signal and by 27.5 MHz for the V . The down-mixed signals are then connected to a Macrodyne FDP 3100 signal processor. The bandwidth setting on the Macrodyne FDP 3100 for the U signal was 20 MHz and the V was 5 MHz. The best data rate was found to be with a setting of 128 sample points for both of the LDV processors. The data rate was on the order of 500/sec.

The digital output from the Macrodyne FDP 3100s are connected to a computer through a Analogic PDIO-96 digital I/O PC board. The data are passed as a 16 bit number representing the measured frequency given by:

$$freq = mantisa(bit10 \Leftrightarrow bit0) \times \exp(bit15 \Leftrightarrow bit12) \quad (2.4)$$

The arrival time is handle by an Analogic CTRTM-05 counter/timer board configures as a “32-bit counter with hardware save”. The scanner position and pressure signal are sampled by an Analogic HSDAS-16 data acquisition card. The sampling rate

per channel was 2500 Hz with 16 bit resolution. A digital interface was designed to handle the handshaking between the FDP 3100s and the data acquisition boards. The digital output from the HSDAS-16 was used as a master trigger for all the boards.

Data were sampled for approximately 400 seconds. The acquired data were saved in binary form in five files: one for each velocity component, Doppler burst arrival time data, and one containing both the pressure and scanner position signals. Twenty sets of data were taken at each of the four x measurement locations. This resulted in approximately 4 million U and V velocity samples per location. Since the arrival time was obtained for each velocity channel, coincidence could be performed in post-processing.

2.3 Data Reduction

The Macrodyne FDP 3100 processors acquire the velocity signals in terms of frequency. The conversion to velocity is given by:

$$U = (f_D - f_B)\lambda_{FS} \quad (2.5)$$

$$V = (f_D - f_B)\lambda_{FS} - V_S \quad (2.6)$$

where f_D is the Doppler frequency, f_B is the Bragg cell or shift frequency, λ_{FS} is the fringe spacing given by:

$$\lambda_{FS} = \frac{\lambda}{2 \sin \phi} \quad (2.7)$$

and V_s is the instantaneous scan velocity. The arrival time measured by the CTRTM-05 counter/timer board is determined from the “data valid” signal from each Macrodyne FDP 3100. The processing time for the Macrodyne FDP 3100 is 610 μ s for 128 sample points, this means the particle passed through the probe volume 610 μ s in the past from the measured arrival time.

The measurement volume position is determined by fitting a fourth order polynomial through the five sampled points of the scanner position signal that occurred closest in time to the Doppler burst time (arrival time). The measurement volume scan velocity, V_s , is the time derivative of this fourth order polynomial. The scan velocities versus distance from the wall obtained by this method are shown in Figure 8 for each of the velocity measurement locations. As can be seen from this figure, the up and down scans are mirror images of each other. The entire scan is not shown in the figure, but only where the scan location fell onto the active area of the PM-tube.

It was found that the signal arrival time accumulated error as the count proceeded. To correct this problem, the mean velocities were calculated for the first-half and last-half

of the data file for both the up-scans and down-scans. The error in time was found by including an additive time constant for each counter cycle and the differences in the four mean profiles were then minimized by changing this time constant. The final time error in the data is believed to be less than 5 μ s.

Velocity histograms were formed with a bin size of 0.51 mm in y and with velocity bin widths of 0.23 m/s. In order to calculate the higher statistical moments for these data, data in the outlying skirts of the histograms needed to be removed. This was done by using a Savitzky-Golay smoothing filter (Press, Flannery, Teukolsky, and Vetterling, 1992) near the base of the skirts in the histograms. Where the filtered data crossed one occurrence per bin, the data beyond this point were removed from the data files. This resulted in smoother higher order moments and only resulted in the removal of less than 1% of the total data.

Coincidence between the U and V velocity signals are also needed in this study. Since the data are used to look at the structural information and fine turbulence information is not needed, the coincidence criteria can be relaxed. The U and V velocity signals were considered coincident if they occurred in the same y bin (bin size = 0.762 mm) during the same scan. The coincident U and V data are used in the calculations of the joint-velocity histograms.

Since the surface pressure fluctuations and the velocity signals were obtained simultaneously, velocity-pressure cross-correlations can be computed. The cross-

correlation function of two quantities $x(t)$ and $y(t)$ is the average over time T of the product of $x(t)$ at time t with $y(t)$ at time $(t + \tau)$ (Bendat and Piersol, 1986):

$$R_{xy}(\tau) = \frac{1}{T} \int_0^T x(t)y(t + \tau)dt \quad (2.8)$$

The cross-correlation coefficient function is the cross-correlation function normalized by the square root of the product of the two autocorrelation functions of the two quantities at $\tau = 0$. The cross-correlation coefficient function between the u fluctuations at a position y_i and the surface pressure fluctuations is estimated by:

$$\rho_{up}(y_i, \tau) = \frac{\sum u(y_i, t) \times p(t + \tau) / N}{\sqrt{u^2(y_i) \times p^2}} \quad (2.9)$$

where N is the number of samples in the summation. The cross-correlations coefficient function between the v fluctuations at a position y_i and the surface pressure fluctuations is estimated by:

$$\rho_{vp}(y_i, \tau) = \frac{\sum v(y_i, t) \times p(t + \tau) / N}{\sqrt{v^2(y_i) \times p^2}} \quad (2.10)$$

These correlations were computed for time delays up to ± 30 ms.

The space-time correlation function of two quantities $f_1(\mathbf{x}, t)$ and $f_2(\mathbf{x}, t)$ is the average over time T of the product of $f_1(\mathbf{x}_i, t)$ at time t and fixed position \mathbf{x}_i with $f_2(\mathbf{x}_j, t)$ at time $(t + \tau)$ and position \mathbf{x}_j , which is a function of time τ , is given by:

$$R_{f_1 f_2}(\mathbf{x}_j - \mathbf{x}_i, \tau) = \frac{1}{T} \int_0^T f_1(\mathbf{x}_i, t) f_2(\mathbf{x}_j, t + \tau) dt \quad (2.11)$$

Space-time correlation coefficient function $\rho_{uu}(y_j - y_i, \tau)$ of the u fluctuations at a fixed point y_i and the u fluctuations at a y_j position during the scan is estimated by:

$$\rho_{uu}(y_j - y_i, \tau) = \frac{\sum u(y_i, t) \times u(y_j, t + \tau) / N}{\sqrt{\overline{u^2}(y_i) \times \overline{u^2}(y_j)}} \quad (2.12)$$

The following space time correlations coefficient functions can also be calculated:

$$\rho_{vv}(y_j - y_i, \tau) = \frac{\sum v(y_i, t) \times v(y_j, t + \tau) / N}{\sqrt{\overline{v^2}(y_i) \times \overline{v^2}(y_j)}} \quad (2.13)$$

$$\rho_{uv}(y_j - y_i, \tau) = \frac{\sum u(y_i, t) \times v(y_j, t + \tau) / N}{\sqrt{\overline{u^2}(y_i) \times \overline{v^2}(y_j)}} \quad (2.14)$$

$$\rho_{vu}(y_j - y_i, \tau) = \frac{\sum v(y_i, t) \times u(y_j, t + \tau) / N}{\sqrt{\overline{v^2}(y_i) \times \overline{u^2}(y_j)}} \quad (2.15)$$

where y_i is the fixed position and y_j is the position of the velocity fluctuation that is time delayed. The space-time correlations were obtained for locations in the bimodal region and for time delays of less than 30 ms. For the space-time correlation the time delay was chosen so as to include three forward (positive time) and backward (negative time) scans. Only the first forward and backward scans are presented since the correlation coefficients for the other cycles are insignificantly small.

Due to the speed at which the Macrodynes process the data and the low data rate near the wall, space-time correlations could not be computed between neighboring y locations less than 0.015 y/t apart.

The existence of low correlation coefficients between two regions of the flow does not necessarily mean that there is no relationship between those regions. Quadrant analysis or correlation-diagrams can reveal possible dependencies between flow in the two regions. The instantaneous fluctuating velocity at one point versus the instantaneous fluctuating velocity at another point during the same upward scan of the measurement volume are viewed in the quadrant plane.

Mode averages of velocity were made based on the bimodal histograms of the surface pressure fluctuations at $x/t=-0.26$ taken with each of the velocity measurement locations. The velocity can be conditionally averaged based on whether the pressure signal is in the upper or lower part of the bimodal pressure pdf. Mode 0 is the average of the velocity vectors when the pressure is in the lower part of the bimodal pressure pdf and

Mode 1 is the average of the velocity vectors for the higher part of the bimodal pressure pdf.

The frequency between the switching between the two modes was investigated by considering the length of time for the surface pressure signal to make a complete cycle for a given threshold level. The effects of threshold level were also considered by employing three threshold levels. The levels chosen were the peak in the bimodal surface pressure pdf closest to zero (peak 0), the mean pressure value, and the peak in the bimodal pressure pdf farthest from zero (peak 1).

A second type of mode average, an “event threshold” (ET) average, can be made by averaging the velocity over a short period of time after the pressure signal crosses a threshold. The average is done for a period of up to 1.5 ms after the threshold has been crossed. This value was chosen based on the average period of the pressure signal and on the time scales from the velocity-pressure cross-correlations. Three thresholds are used: the values of p for the most positive peak, the mean pressure, and the peak close to zero in the surface pressure probability density functions (Figure 19). Averages are made for both the rising and falling surface pressure signal crossing the thresholds.

2.4 Uncertainty Analysis

The uncertainty of the measured velocity is influenced by many factors. Most important of these factors is the estimation of the fringe spacing and Doppler frequency estimate. The velocity is then found from equations 2.5 and 2.6. From the analysis method of Kline and McClintock (1953) for the 95% confidence limits the uncertainties in the instantaneous values of velocity are due primarily to the uncertainties in the measurement of the fringe spacing, which is determined by the geometry. The uncertainties in the instantaneous velocities are $\pm 0.4\%$ of U_{ref} for U and $\pm 1.6\%$ of U_{ref} for V .

The uncertainty in the x position of the scanning measurement volume is less than ± 0.2 mm. Slight differences in the x measurement position from those of Devenport and Simpson (1990a,b) and Rife, Devenport, and Simpson (1992) can be expected.

The uncertainty in the vertical position, y , of a velocity sample is a function the accuracy of determining the arrival time, the accuracy in sampling of the scanner output voltage, and the measurement volume diameter. The error in the arrival time was found to be less than $5 \mu\text{s}$ and has a negligible contribution to the position uncertainty. The use of a 16-bit data acquisition board to sample the position voltage signal from the scanner also has a negligible contribution to the measurement volume position uncertainty.

Therefore, the uncertainty in the relative position of the measurement volume is determined by the measurement volume diameter, which in this case is 0.3 mm.

The calibration for scan position was done with the tunnel off. However, when the tunnel was operated the plexiglas plate on which the model set bowed inwards. This led to a substantial error in the absolute y position. This error in y position was corrected by comparing the mean and mean square velocities to the previous work of Devenport and Simpson (1990a) and shifting the profiles in y to get the best match between the two data sets. These shifts were less than 1.0 mm and corresponded to approximate visual determination of the flex of the Plexiglas floor.

Since the measurement volume is moving, the scan velocity V_s needs to be subtracted from the apparent velocity determined by the processors as indicated by equation (2.5 and 2.6). The variance in the vertical scan velocity V_s is 0.08 m/s. However, the instantaneous scan velocity is used. The uncertainty in the instantaneous scan velocity is ± 0.01 m/s. This was determined from an analysis using a model sinusoid sampled at 50 points per cycle. A fourth order polynomial was fit, as was done to the data, to five points. The position and velocity were computed from the curve fit and was compared to the exact quantities.

Chehroudi and Simpson (1984) discuss velocity bias considerations for scanning LDV systems. The velocity bias is proportional to σ/\bar{U} which is the ratio of the RMS of the velocity fluctuations to the mean velocity. In a scanning LDV system the mean

velocity should be taken relative to the scanning measurement volume. Thus a scanning LDV has the effect of decreasing the bias error as compared to point-wise systems. For the present measurements the statistics of the flow were calculated with and without velocity bias corrections. Velocity bias corrections usually are performed by calculating the statistics with a weighting function taken as the reciprocal of the instantaneous velocity. The weighting function used here is given by:

$$w = \frac{1}{\sqrt{V_s^2 + U^2}} \quad (2.16)$$

where V_s is the scan velocity and U is the instantaneous velocity of the measured velocity component. This method was used because not all the U and V velocity data were “coincident” in time and the instantaneous $\sqrt{V^2 + U^2}$ could not be calculated.

Durst, Lehmann, and Tropea (1981) looked at the effects of averaged statistics of the velocity taken over a finite bin width for scanning LDV systems. They found that the normalized error in the mean velocity can be given as

$$\epsilon_{\bar{u}} = \frac{1}{12} \left(\frac{1}{0.5 + \xi} \right)^2 \quad (2.17)$$

and the normalized error in the RMS

$$\epsilon_{\sigma} = \frac{1}{1 + 2\xi} \quad (2.18)$$

where ξ , the bias parameter, is given by

$$\xi = \frac{\beta}{\Delta y \alpha} \quad (2.19)$$

where β is the mean velocity and α is the velocity gradient for the interval or bin width Δy for which the statistics are calculated. The errors in the mean and rms velocities correspond to steep flow gradients, low mean velocities, and large averaging intervals.

The uncertainties in the statistical estimates of the correlation function are given by Bendat and Piersol (1986). The normalized rms error for the autocorrelation function is given as

$$\varepsilon[R_{xx}(0)] = \frac{1}{\sqrt{BT}} \quad (2.20)$$

$$\varepsilon[R_{xx}(\tau)] = \frac{1}{\sqrt{2BT}} [1 + \rho_{xx}^{-2}(\tau)]^{\frac{1}{2}} \quad (2.21)$$

and cross-correlation function as:

$$\varepsilon[R_{xy}(\tau)] = \frac{1}{\sqrt{2BT}} [1 + \rho_{xy}^{-2}(\tau)]^{\frac{1}{2}} \quad (2.22)$$

where B is the sampling bandwidth, T is the record length, ρ_{xx} and ρ_{xy} are the correlation coefficients. The factor BT can be taken as the number of sample points, N , used in the

calculation of the correlations. The rms error in the correlation coefficient function $\rho_{xx}(\tau)$ is given by:

$$\varepsilon[\rho_{xx}(\tau)] = \sqrt{\left[\frac{\delta\rho_{xx}}{\delta R_{xx}(\tau)} \varepsilon[R_{xx}(\tau)] \right]^2 + \left[\frac{\delta\rho_{xx}}{\delta R_{xx}(0)} \varepsilon[R_{xx}(0)] \right]^2} \quad (2.23)$$

and $\rho_{xy}(\tau)$ by:

$$\varepsilon[\rho_{xy}(\tau)] = \sqrt{\left[\frac{\delta\rho_{xy}}{\delta R_{xy}(\tau)} \varepsilon[R_{xy}(\tau)] \right]^2 + \left[\frac{\delta\rho_{xy}}{\delta R_{xx}(0)} \varepsilon[R_{xx}(0)] \right]^2 + \left[\frac{\delta\rho_{xy}}{\delta R_{yy}(0)} \varepsilon[R_{yy}(0)] \right]^2} \quad (2.24)$$

Typical values of the uncertainty, as rms errors, for all the correlations calculated in this work are shown in Tables 1-5.

3. Results

3.1 Experimental Flow and Measurement

Locations

The measurements were conducted with a free stream velocity, U_{ref} , of 27.5 m/s $\pm 1\%$ as determined by a pitot-static probe located at the throat of the test section $x=-1.39$ m, see Figure 4. This corresponds to a Reynolds number, Re_θ , based on the momentum thickness of the approach boundary layer is 6700 at $x=2.15t$ (Devenport and Simpson, 1990a).

3.1.1 Coordinate System

The coordinate system used for these experiments is a right-handed system with its origin at the junction of the wing leading edge and the floor of the test section, as shown in Figure 6. The X and U are positive in the downstream direction with Y and V positive vertically upwards.

Velocity measurements were performed at four locations on the centerline of the wing/body junction in the same bimodal zone reported by Devenport and Simpson (1990a); these locations are $x/t = -0.15, -0.20, -0.25,$ and -0.30 . Both U and V components of velocity were measured simultaneously but coincidence of these two signals at the same time window Δt was not required. Due to a partial failure in a component of the data acquisition system, the V velocity data were not correct at the locations of $x/t=-0.15$ and $x/t=-0.20$ and were discarded.

3.2 Comparison with Previous Studies

Mean flow measurements are shown in Figures 9-12. As can be seen from these figures the flow measured shows some of the same trends as the measurements performed by Devenport and Simpson (1990a). For the measurements at $x/t=-0.15$ and $x/t=-0.20$, it

was found that statistical estimates from unweighted LDV data agreed best with the earlier work; this was also found to be true for the V velocity measurements. The measurements at $x/t=-0.25$ and $x/t=-0.30$ the weighted estimates (eq. 2.16) were found to agree best with the measurements of Devenport and Simpson. The mean square velocity estimates also show agreement with those of Devenport and Simpson. The differences observed between the present data and the results from Devenport and Simpson (1990a) are probably due to the averaging of these quantities over a finite bin width as discussed by Durst, Lehmann, and Tropea (1981) instead of a velocity bias. The maximum differences are found where the flow gradient in the vertical, y , direction is the greatest and also where the mean velocity is near zero. These differences are smaller than equations 2.17 and 2.18 would indicate, this is due to the high level of turbulence at these locations which is not considered in the derivation of those equations.

The velocity histograms obtained in this study are shown in Figures 13-18. The U histograms for $x/t=-0.25$ and $x/t=-0.30$ are computed with the velocity weighting, equation 2.16. The U velocity histograms at $x/t=-0.15$ (Figure 13) do not show any distinct bimodal histograms, although skewed velocity histograms are observed below $y/t=0.6$. Bimodal U velocity histograms are observed for $x/t=-0.20$ (Figure 14) below $y/t=0.046$ and skewed histograms below $y/t=0.07$. For the location at $x/t=-0.25$ bimodal velocity histograms are observed below $y/t=0.046$ for the U velocity (Figure 15) and below $y/t=0.053$ for the V velocity (Figure 16). Bimodal velocity histograms are also

observed for the location of $x/t=-0.30$ for the U velocity below $y/t=0.046$ (Figure 17) and for the V velocity below $y/t=0.053$ (Figure 18). The shape of the histograms are similar to those observed by Devenport and Simpson (1990a).

The pressure measurements were made with the pressure transducer located at $x/t=-0.26$ and the histograms are shown in Figure 19. The pressure histograms obtained show definite bimodality. While the histograms differ quantitatively, they extend over the same range of pressure and have qualitative similar shapes, this maybe due to slight differences in temperature and/or seeding conditions. These histograms qualitatively agree with those of Ölçmen and Simpson (1994).

3.3 Cross-correlations of Pressure-Velocity

The cross-correlation coefficient functions of velocity and pressure fluctuations at $x/t=-0.26$ are shown in Figures 20-25. The cross-correlation coefficient function between the velocity fluctuations and surface pressure fluctuations are defined by equations 2.9 and 2.10. A positive non-dimensional time delay indicates that the disturbance is seen in the velocity signal before the pressure signal. These Figures illustrate the relationship between velocity and pressure and the sequence of events through the flow field at the measurement locations.

Figure 20 shows the cross-correlation ρ_{up} of the u velocity fluctuations at $x/t=-0.15$ with the surface pressure fluctuations at $x/t=-0.26$. Velocity and pressure fluctuations are of opposite sign for $y/t<0.05$. The maximum negative correlation, $\rho_{up} = -0.4$, occurs at $y/t=0.025$, the closest point to the wall in these measurements. The pressure and velocity fluctuations occur nearly simultaneously for $y/t<0.05$. Farther from the wall, the velocity and surface pressure fluctuation have the same sign and the velocity fluctuations lead the pressure fluctuations. The maximum positive correlation, $\rho_{up} = 0.4$, occurs near $y/t=0.12$ and then decreases farther from the wall. The correlation coefficient is nearly zero for all time lags at $y/t=0.05$, which is the location of the time mean vortex center (Figure 3). The peaks at $y/t=0.025$ and $y/t=0.12$ appear to be the areas where the effects of the vortex are the strongest. The two peaks in the correlation coefficients for $y/t>0.05$ could be due to the time scales associated with the different flow modes. The smaller of these two peaks occurs at a time lag of zero. The u velocity fluctuations for $y/t > 0.12$ lead the surface pressure fluctuations.

The cross-correlation coefficient function ρ_{up} between the u velocity fluctuations at $x/t=-0.20$ and the surface pressure fluctuations at $x/t=-0.26$ is shown in Figure 21. The correlation coefficients are not as significant as those observed at $x/t=-0.15$. Correlations of opposite sign are observed for $y/t<0.05$, with a maximum negative correlation of $\rho_{up} = -0.15$. The u fluctuations and surface pressure fluctuations are of the same sign for

$y/t > 0.05$, with a maximum correlation of $\rho_{up} = 0.28$ at $y/t = 0.10$ and $TU_{ref}/t = 2$. The velocity fluctuations for $y/t > 0.05$ lead the surface pressure fluctuations.

Figure 22 shows the cross-correlations ρ_{up} of the u fluctuations at $x/t = -0.25$ with the surface pressure fluctuations at $x/t = -0.26$. Large positive correlations are near the wall, $y/t < 0.05$, with a slight positive time lag. The maximum correlation, $\rho_{up} = 0.55$, occurs at $y/t = 0.032$ and $TU_{ref}/t = 0.2$. The largest negative peak occurs near $y/t = 0.10$ and $TU_{ref}/t = 0.2$. The velocity fluctuations for $y/t > 0.1$ slightly lead the surface pressure fluctuations and have opposite sign. The correlations at this location show an opposite trend to those observed at $x/t = -0.15$ and $x/t = -0.20$ in the sign of the correlations as a function of y/t .

Figure 23 shows the correlation coefficient function ρ_{vp} between the v velocity at $x/t = -0.25$ and surface pressure fluctuations at $x/t = -0.26$. The correlation coefficients are small and are only significant between $y/t = 0.025$ and $y/t = 0.09$. The maximum negative peak occurs at $y/t = 0.025$ and at a slight negative time lag. The highest positive correlation occurs at $y/t = 0.05$ with a positive time lag.

Figure 24 shows the result for the cross-correlations of the u velocity fluctuations at $x/t = -0.30$ with surface pressure fluctuations at $x/t = -0.26$. The same trends are seen as those for $x/t = -0.25$ for the u velocity. The maximum correlation coefficient, $\rho_{up} = 0.65$, occurs at $y/t = 0.025$ and $y/t = 0.039$, the two y locations nearest the wall, and at a time lag

of zero. Farther from the wall the positive peak is larger than the negative peak and occurs at $TU_{ref} / t = 2$. The u fluctuations lead the surface pressure fluctuations with the lead time increasing farther from the wall. The highest correlations between the velocity fluctuations and surface pressure fluctuations are observed at this x -location.

The correlations of v velocity at $x/t=-0.30$ with the surface pressure fluctuations at $x/t=-0.26$ are shown in Figure 25. Only negative correlations are observed with the peak at zero time lag. The peak correlation, $\rho_{vp} = 0.49$, occurs at $y/t=0.046$ and there are no significant correlations above $y/t=0.15$.

The cross-correlations between the velocity fluctuations and surface pressure fluctuations are qualitatively similar to those obtained by Rife, Devenport and Simpson (1992). In that study the microphones were located at $x/t=0.00$ and $x/t=-0.20$.

3.4 Joint histograms

Joint probability density functions (pdfs) were computed between the U and V velocity, U velocity and surface pressure P and V velocity and surface pressure P as outlined in chapter 2. These joint probability density functions show the relationship between U and V velocity and the surface pressure and velocity at a given y location. These are shown in Figures 26-33.

3.4.1 Joint velocity probability density functions

Figure 26 shows the results at $x/t=-0.25$. Near the wall at $y/t=0.037$ there is a well-defined peak in the pdf for near zero U velocity and negative V velocity. This primary peak is associated with the largest peaks in the U and V histograms at the same y location from Figures 15 and 16. There appears to be a much smaller secondary peak associated with negative U and positive V velocities. However besides the primary peak (zero flow mode) the flow does not seem to be attracted to any other definite flow mode.

For $y/t=0.048$ the primary peak still shows a negative V velocity associated with near zero and positive U velocity. For negative U velocity at this y location there appears to be little preference for either a positive or negative V velocity. Farther from the wall, $y/t=0.059$, the primary peak in the pdf shifts to a more positive U velocity but still is associated with a negative V . The secondary peak in the pdf is associated with negative U and positive V velocities, and becomes more distinct at this position. At $y/t=0.069$, the primary peak is very dominate; below zero U velocity there appears to be more preferences for positive V velocities. Beyond this y location, the pdfs take on a more Gaussian distribution.

The results at $x/t=-0.30$ are shown in Figure 27. Near the wall, $y/t=0.037$, a primary peak shows negative V velocities primarily associated with positive U velocities. Besides this peak no other preferences are shown, except that the pdf distribution has

more area associated with negative U and positive V . The primary peak in the pdf at $y/t=0.048$ is again associated with negative V and positive U velocities. The extent of the pdf in the second quadrant appears to have increased. For $y/t=0.059$ the primary peak has moved closer to zero V velocity and is centered around $U=7$ m/s. For small positive U and negative U velocities the pdf shows a preference for positive V velocity. Again, beyond this y location the pdfs take on a Gaussian shape.

The joint probability density functions all show primary peaks associated with negative V velocity and near zero and positive U velocity. When the flow is in this state there appears to be little variation in both the U and V velocities. When the flow is not in this mode, large variations in the U and V velocities are seen.

3.4.2 Joint velocity and pressure probability functions

Figures 28-33 show the joint probability functions between velocity and the surface pressure at $x/t=-0.26$. These figures illustrate the relationship between velocity and surface pressure fluctuations. The joint pdf between the U velocity at $x/t=-0.15$ and surface pressure at $x/t=-0.26$ are shown in Figure 28. Near the wall, the two modes in the bimodal histogram show associations with the two peaks in the velocity histograms, Figure 13, with the positive pressure fluctuations (Figure 19) corresponding to the most negative peak in the velocity histogram. The pressure fluctuations near zero correspond

to velocities nearer to zero. Farther from the wall, the pressure fluctuations near zero are associated with the velocity fluctuations near zero velocity. The pressure fluctuations for the most positive peak in the bimodal pressure histogram occur with a wide velocity range. The peaks in the pdfs occur near zero velocity. There are no readily apparent secondary peaks, since the near zero pressure peak in the surface pressure pdf is not well defined in the pressure pdf.

The same pattern is seen for the joint pdfs between the U velocity at $x/t=-0.20$ and surface pressure at $x/t=-0.26$ as shown in Figure 29. The pressure fluctuations in the positive part of the bimodal pdf show no preference for any U velocity range. The peak in these joint pdfs corresponds to the peaks in the U velocity histograms (Figure 14). Again, the pressure fluctuations near zero show a narrower range of associated U velocities.

The joint probability density functions between U at $x/t=-0.25$ and the surface pressure at $x/t=-0.26$ are shown in Figure 30. Near the wall, $y/t=0.025$ to $y/t=0.039$, the peaks in the bimodal pressure pdf (Figure 19) corresponds to a peak in the U velocity pdf (Figure 15) at that y location. The positive pressure fluctuations are associated with velocity fluctuations near zero velocity, whereas, the pressure fluctuations near zero correspond to velocity fluctuations with the more negative peak in the velocity pdfs. Farther from the wall, the distinct bimodal joint pdfs disappear. The velocity fluctuations near zero velocity correspond to the positive pressure fluctuations for $y/t=0.06$ and

$y/t=0.053$. For $y/t=0.06$, the velocity fluctuations near zero velocity are now associated with the pressure fluctuations near zero, this switch in preference corresponds to the switch in sign in the velocity and pressure cross-correlations shown in Figure 22.

Figure 31 shows the V velocity at $x/t=-0.25$ and surface pressure at $x/t=-0.26$ joint probability density functions. Trimodal pdfs are seen for the two locations $y/t=0.025$ and $y/t=0.03$ and disappear above $y/t=0.04$. The surface pressure pdf (Figure 19) and V velocity pdfs (Figure 16) at these locations only show bimodal distributions. The primary peaks in the joint pdfs are all associated with a negative V velocity, which does not correspond to the peak in the V velocity pdfs. The secondary peaks in the trimodal pdfs are associated with the primary peak in the V velocity pdfs and the near zero peak in the pressure pdf. The third peak in the trimodal pdfs correspond to the secondary peak in the velocity pdfs and the positive half of the near zero peak in the pressure pdf. Above $y/t=0.04$, there is no preference in velocity for the near zero pressure fluctuations.

The joint probability density functions for U velocity at $x/t=-0.30$ and surface pressure at $x/t=-0.26$ are shown in Figure 32. The pressure fluctuations in the positive half of the bimodal pressure pdf (Figure 19) is associated with the velocity fluctuations on the positive side of the peak in the U velocity pdfs (Figure 17). The near zero peak in the pressure pdf corresponds of velocity fluctuations near zero velocity.

The joint V velocity and pressure probability density functions at $x/t=-0.30$ are shown in Figure 33. The positive peak in the pressure pdf is associated with a negative V velocity. There is no velocity preference for the near zero peak in the pressure pdf.

3.5 Space-time correlations

The results of the space-time correlations are shown in Figures 34-53. The heavy solid line in these figures is the correlations for the upward scan and the dashed line is for the downward scan. The scan position is shown as lines on the lag- y/t plane and the correlation coefficient is projected as a function of time on the lag-correlation plane. The unity autocorrelation point at time delay of zero has been removed in all plots. A positive non-dimensional time delay in these figures indicate that the velocity fluctuations at the fixed y point lag behind the velocity fluctuations at the position in the scan.

The space-time correlation coefficient function ρ_{uu} for the u velocity fluctuations at $x/t=-0.15$ is shown in Figures 34-35. The correlations are insignificant except for positions close in space and time to the fixed y position at which the correlations are computed. The regions of significant correlation occur within $TU_{ref} / t = 0.7$ in time and $\Delta(y / t)$ of 0.05 in space to the fixed point. The correlations with the fixed point at $y/t < 0.046$ are negative except for the y position closest to the fixed point. The

correlations with the fixed point at $y/t=0.053$ are positive, this location is located in the forward flow. The correlations change sign between regions spanning the time mean vortex center located at $y/t=0.05$ (Figure 3).

The results for the space-time correlations ρ_{uu} for the u fluctuations at $x/t=-0.20$, shown in Figures 36-37. The correlations show wider area of significant correlation compared to those at $x/t=-0.15$. Significant correlations span $TU_{ref} / t = 1.0$ and $\Delta(y / t)$ of 0.1 around the y fixed position.

Figures 38-45 show the space-time correlations results for the location at $x/t=-0.25$. The correlations ρ_{uu} between the u velocity fluctuations are shown in Figures 38-39. The maximum correlations occur for points along the upward scan lying close to the fixed correlation point. Negative correlations are observed between the backflow region, $y/t < 0.06$, and the region of forward flow, $y/t > 0.08$, for the forward cycle time delay. The correlations for the forward cycle time delays are significant up to $TU_{ref} / t = 2$. The correlations for the negative cycle time delay are significant and positive for non-dimensional time delay up to $TU_{ref} / t = 4$.

The v velocity fluctuation correlations ρ_{vv} , Figures 40-41, also show very high correlations between near by fluid to the fixed point, the correlations remain significant for non-dimensional time delays of up to 1.5. The correlations are positive, even between points in the flow where the mean V flow is of opposite sign. Correlations between the u

fluctuations at a point in the backflow region with the v fluctuations through the scan, Figures 42-43, show significant correlation for up to ± 1.5 non-dimensional time delay and extending up to $y/t=0.18$. The maximum correlation is around -0.25 at zero time delay. For the correlations between the v fluctuating velocity at a point in the backflow region and the u fluctuating velocity through the scan, Figures 44-45, significant correlations are only seen for near zero non-dimensional time lag or for position very close to the correlation point. This may indicate that the u fluctuations change more rapidly than the v fluctuations.

The space-time correlations for $x/t=-0.30$ are shown in Figures 46-53. The correlations for the u fluctuations in the back flow region, Figures 51-53, show high positive correlations with regions in the backflow and negative correlations with regions in the forward flow for forward cycle time delays. The backward cycle time delays show high levels of significant positive correlations. These two observations indicate that the events in the backflow region are greatly influenced by events preceding them and have little influence on events following them. The v fluctuations correlations, Figures 54-56, appear symmetric about zero time delay and have positive correlation coefficients. The space-time cross-correlations ρ_{uv} , correlations between u at a point and v through the scan (Figures 57-58), and ρ_{vu} , correlations between v at a point and u through the scan (Figures 59-60), show high negative correlations near zero time lag and appear

symmetric. Both sets of cross-correlations indicate that the u fluctuations lead the v fluctuations.

3.6 Quadrant analysis

Quadrant analysis is performed in this study by plotting the velocity fluctuations at one y/t location versus velocity fluctuations at another y/t location during the same scan. This method was used by Chehroudi and Simpson (1985). This technique can show the relationship between two flow regions during a short period of time that long time record correlation may miss. Figures 54-59 show the results of the quadrant analysis for $y/t=0.032$ versus several locations along the vertical scan. The number of occurrences in each quadrant is written in the corresponding corner.

The results for the location at $x/t=-0.15$ are shown in Figure 54. The data rate near the wall at this location was low, so the data is sparse. There appears to be no correlation at this location between the various locations; except for fluctuations of $y/t=0.32$ versus $y/t=0.046$. At this location moderate linear positive correlation between the velocity fluctuations is seen, with the fluctuations occurring in the third quadrant 50% of the time. A random distribution is seen at the other y locations, with the quadrant 2 and 4 being preferred.

The quadrant analysis results for $x/t=-0.20$ are shown in Figure 55. The velocity fluctuations occur in the third quadrant 35 to 40 percent of the time. Quadrant analysis for locations above $y/t=0.06$ show no correlation. The u fluctuations at $y/t=0.032$ have a higher variance for positive fluctuations.

Figure 56 shows the quadrant analysis results for the u velocity fluctuations at $x/t=-0.25$. For $y/t \leq 0.06$ the fluctuations fall into two regions, one along a 45 deg. line offset from the origin and the other in a vertical band in the negative half plane. Also at these y locations from 35% to 50% of the time the fluctuations occur in quadrant 3. The results at $y/t=0.1098$ indicate no correlation. The negative u fluctuations for all y positions show smaller variance than the positive u fluctuations.

The v velocity fluctuation quadrant analysis at $x/t=-0.25$ is shown in Figure 57. Moderate correlations are seen between velocity fluctuations for locations less than $y/t=0.1$, indicated by the higher occurrences in quadrant 1 and 3. Here again, 35 to 50 percent of the fluctuations occur in quadrant 3. Also, the fluctuations in quadrant 3 show less variance than in the other quadrants.

Quadrant analysis of the u fluctuations at $x/t=-0.30$ are shown in Figure 58. The results show a high degree of correlation as observed in the space-time correlations at this x location. Two bands of correlation are observed for $y/t \leq 0.1098$, a band at 45 deg and a vertical band in the negative half plane. These results show that positive u fluctuations

are tightly grouped together and therefore have little variation. No correlation is seen at $y/t=0.1098$ for this analysis.

Figure 59 shows the results of quadrant analysis for the v fluctuations at $x/t=-0.30$. Fluctuations in quadrant 3 are dominant and account for 50% of the observations. These negative v fluctuations also show very little variance.

These results for both u and v fluctuations at $x/t=-0.30$ show a stable flow mode with fluid from the boundary layer moving inward and downward toward the wing.

3.7 Mode averages

Mode averages for the U and V mean velocities were performed based on the bimodal pressure histogram as outlined in chapter 2. Figure 60 shows the velocity vectors associated with the two mode averages based on the bimodal pressure probability density function (Figure 19). Mode 0 is the average of the velocity vectors when the surface pressure is below the mean pressure. Mode 1 is the average of the velocity when the surface pressure is above the mean value.. For Mode 0 the back flow near the wing is smaller than that for the Mode 1. Also for Mode 0 the backflow at $x/t=-0.25$ and $x/t=-0.30$ is large and almost nonexistent for the other mode. The mean flow at $x/t=-0.30$ for Mode 1 is toward the wing and the tunnel floor. This flow mode can also be observed in

the flow visualizations of Kim, Walker, And Simpson (1991) approximately 50% of the time.

Figure 61 shows the probability density function of the time between switches for surface pressure fluctuations. The figure is plotted with the log of the pdf versus time. For all three threshold levels chosen the mean value for the time between switches is 7 ms and the most probable value is 2 ms. A straight line in this figure would imply a Markov type process (Martinuzzi, 1992).

The event-threshold (ET) conditionally averaged results are shown in Figures 62-67. The figures show the time-mean velocity vectors averaged for up to 1.5 ms after the surface pressure signal crosses a threshold level. These averages are performed for both a positive and negative transition across a threshold level. From these figures the time-mean position of the junction vortex can be seen in relation to the surface pressure signal.

4. Discussion

4.1 Relationship between velocity correlations and velocity-pressure cross-correlations

The Poisson equation relates the pressure fluctuations to the velocity field. This can be used to illustrate the relationship between the velocity and surface pressure fluctuations for the pressure-velocity cross-correlation coefficient functions. The Poisson equation from the Reynolds-averaged Navier-Stokes Equation for the pressure fluctuations is:

$$\frac{1}{\rho} \nabla^2 p = -2 \frac{\partial U_m}{\partial x_n} \frac{\partial u_n}{\partial x_m} + \frac{\partial^2}{\partial x_m \partial x_n} (\overline{u_m u_n} - u_m u_n) \quad (4.1)$$

The pressure fluctuation, p , at a point on the surface, \mathbf{x}_s , is given as (Townsend, 1976):

$$\frac{1}{\rho} p(\mathbf{x}_s) = \frac{1}{4\pi} \iiint \left[2 \frac{\partial U_m}{\partial x_n} \frac{\partial u_n}{\partial x_m} + \frac{\partial^2}{\partial x_m \partial x_n} (u_m u_n - \overline{u_m u_n}) \right] \frac{dV(\mathbf{x})}{|\mathbf{x}_s - \mathbf{x}|} \quad (4.2)$$

where the volume integration is over the entire velocity field. The term $(\partial U_m / \partial x_n)(\partial u_n / \partial x_m)$ represents an interaction between the mean velocity gradients and the turbulent velocity gradients. The term $(\partial^2 / \partial x_m \partial x_n)(u_m u_n - \overline{u_m u_n})$ is the effect of fluctuations of the Reynolds stress about the mean value; this term in shear flows is usually much smaller than the first term (Townsend, 1976) and will be neglected here. The terms $\partial U / \partial x$, $\partial V / \partial x$, $\partial V / \partial y$, and $\partial W / \partial z$ are much smaller than $\partial U / \partial y$ for the present data locations. The terms $\partial U / \partial z$, $\partial V / \partial z$, $\partial W / \partial x$, and $\partial W / \partial y$ are zero since the measurements are in the plane of symmetry. The time-averaged cross-correlation between velocity and pressure can then be given as:

$$\frac{1}{\rho} \overline{p(\mathbf{x}_s)u(\mathbf{x}_1)} = \frac{1}{2\pi} \int \frac{\partial U}{\partial y} \frac{\partial \overline{u(\mathbf{x}_1)v(\mathbf{x})}}{\partial x} \frac{dV(\mathbf{x})}{|\mathbf{x}_s - \mathbf{x}|} \quad (4.3)$$

$$\frac{1}{\rho} \overline{p(\mathbf{x}_s)v(\mathbf{x}_1)} = \frac{1}{2\pi} \int \frac{\partial U}{\partial y} \frac{\partial \overline{v(\mathbf{x}_1)v(\mathbf{x})}}{\partial x} \frac{dV(\mathbf{x})}{|\mathbf{x}_s - \mathbf{x}|} \quad (4.4)$$

where \mathbf{x}_s and \mathbf{x}_1 are fixed points and \mathbf{x} is throughout volume. This indicates that the cross-correlations of surface pressure fluctuations with the velocity fluctuations at \mathbf{x}_1 are

mainly due to interactions between the mean flow gradient in the y direction with the Reynolds turbulence stress terms. Equations 4.3 and 4.4 show that the cross-correlations should be large where the mean flow gradients are large and also where the stress terms are large.

To see the effects of some of the terms in equations 4.3 and 4.4, we will assume the following form for the integration for the location $x/t=-0.25$ next to the pressure transducer at $x/t=-0.26$:

$$\overline{pu(y_1)} = \frac{1}{2\pi} \iiint \frac{\partial U}{\partial y} \frac{\partial \overline{u(y_1)v}}{\partial x} \frac{dxdydz}{|y|} \quad (4.5)$$

$$\overline{pv(y_1)} = \frac{1}{2\pi} \iiint \frac{\partial U}{\partial y} \frac{\partial \overline{v(y_1)v}}{\partial x} \frac{dxdydz}{|y|} \quad (4.6)$$

Here it is assumed that the term $\partial \overline{u(y_1)v} / \partial x$ is a function of the Δx spacing, r_x , from the pressure transducer. This term then would be proportional to $\overline{u(y_1)v}$.

To see the contributions of the terms in equations 4.5 and 4.6, the values of components of the kernel will be estimated from the data at $x/t=-0.25$ and $y_1/t=0.039$. The terms $\partial U / \partial y$, $\overline{u(y_1)v}$, and $\overline{v(y_1)v}$ are shown as a function of distance from the wall in Figure 68. The maximum flow gradient occurs at $y/t=0.046$ and decays exponentially away from this point. The two velocity cross-correlation terms, $\overline{u(y_1)v}$ and $\overline{v(y_1)v}$, for

$y_1 / t = 0.039$ are large at $y/t=0.039$. These functions also decay exponentially away from this point.

The kernel in equations 4.5 and 4.6 can be given as $\frac{\partial U}{\partial y} \overline{u(y_1)v} \frac{1}{y}$ and

$\frac{\partial U}{\partial y} \overline{v(y_1)v} \frac{1}{y}$. These are shown as a function of the distance from the wall in Figure 69.

The contribution of each kernel to the integral is maximum at the fixed y_1 locations at which the velocity-pressure cross-correlation is being computed. The contribution decays exponentially and there is no contribution for $y/t > 0.1$.

These results indicate that the substantial contribution to the velocity-pressure cross-correlations is in the vicinity of the fixed y_1 location at which the correlations are computed or measured. The results also indicate that higher correlations would occur for regions near the wall where the mean velocity gradient is largest and would decay exponentially farther away from the wall.

Figure 60 shows the conditionally-averaged velocity vectors based on whether the surface pressure signal was above or below the mean pressure. This figure can also be used to show the relationship between the velocity and pressure as observed in the velocity-pressure cross-correlations. In this figure Mode 0 is the conditional-averaged velocity vectors when the surface pressure signal is below the mean and Mode 1 is for above the mean. The time-mean vortex in Mode 0 is large and located far from the nose

of the wing. In Mode 1 the junction vortex is smaller and located near the nose of the wing.

At $x/t=-0.15$, Figure 60 shows that the velocities fluctuations near the wall increase and away from the wall decrease when the pressure fluctuations are below the mean pressure. The opposite is observed for the pressure fluctuations above the mean. These give the negative correlations seen in the backflow region and the positive correlations in the outer region as seen in Figure 20.

At $x/t=-0.20$, Figure 60 shows little variation in the velocity with the change in the surface pressure signal. This would explain the lower correlations observed at this location as shown in Figure 21.

For the locations at $x/t=-0.25$ and $x/t=-0.30$, the u fluctuations near the wall are negative and positive for $y/t>0.05$ when the surface pressure is below the mean. The opposite occurs for the surface pressure above the mean. This gives a positive correlation near the wall and negative in the outer region, $y/t>0.05$. The change in magnitude of the u fluctuations near the wall is large, on the order of $0.5U_{ref}$. This would explain the large values for the near wall correlations for the u fluctuations found at these two locations.

4.2 Possible simple flow models of the vortical structure

Figures 62-67 of the “event-threshold” (ET)-averaged velocity vectors support the simplest model of the junction vortex. The model is of a single primary vortex that changes size, strength and position in front of the wing-body junction. These figures were derived by taking three thresholds, one at each peak in the bimodal surface pressure probability distribution function and one at the mean. Figure 70 shows a composite of these ET-averaged velocity vectors and pressure threshold levels. Averages of the velocity at a given y were made over time (up to 1.5 ms) after a threshold was crossed. Averages were made for both positive and negative transitions of the surface pressure signal across the threshold levels.

These figures indicate that the primary junction vortex is tracked by the surface pressure signal at $x/t=-0.26$. When the surface pressure is below the mean value (Figures 62, 63, 67, and 70) the time-averaged vortex is located farther from the wing. The recirculation region is larger, however the backflow near the nose is lower. When the surface pressure is above the mean value the junction vortex lies closer to the nose (Figures 64, 65, 66 and 70). The backflow near the nose is also more intense. At $x/t=-0.30$ the flow is directed inward and downward toward the wing. This would bring

in more energetic fluid into the recirculation region. From the quadrant analysis, Figures 58 and 59, at this location this flow situation occurs 50% of the time.

The “event-threshold” (ET) averaged velocity vectors are similar to the pattern of the flow structure observed in the flow visualizations of Kim, Walker and Simpson (1991). There are smaller (weaker) secondary vortices present slightly farther from the wall ($0.15 < y/t < 0.25$) that do not show up in the ET averaged results.

4.2.1 Sequence of flow events

The sequence of events is shown in Figure 70. From the cross-correlations of velocity and pressure and the space-time correlations it is possible to deduce the sequence of events. From Figures 20-25 the cross-correlations (ρ_{up} and ρ_{vp}) indicate that the u velocity fluctuations for $y/t > 0.1$ at all four x locations lead the surface pressure fluctuations at $x/t = -0.26$. This lead time is $TU_{ref} / t \approx 2.0$ for this region. Near the wall, $y/t < 0.05$, at $x/t = -0.15$ the surface pressure fluctuations lead the u velocity fluctuations by $TU_{ref} / t \approx -0.3$. For the near wall at the other three x locations ($x/t = -0.20, -0.25, -0.30$), the velocity and surface pressure fluctuations occur nearly simultaneously. These results indicate that the fluctuations in the outer region determine the flow structure. The highest cross-correlation coefficients between the velocity and surface pressure fluctuations are observed at $x/t = -0.30$.

The space-time correlations indicate that the time scales at $x/t=-0.15$ and $x/t=-0.20$ are small, on the order of $TU_{ref} / t = 1.5$. At $x/t=-0.25$ and $x/t=-0.30$, the space-time correlations between the u fluctuations for the forward cycle time delay show time scales on the order of $TU_{ref} / t = 5$. These results also indicate that the fluctuations in the outer part, $y/t > 0.1$, determine the fluctuations near the wall and thus the flow structure. The largest space-time correlations are at $x/t=-0.30$.

From the above observations, it is proposed that the u fluctuations in the outer region, $y/t > 0.1$, for $x/t \geq -0.25$ determine the flow structure. When these fluctuations are less than the mean, the junction vortex tends to be large (Figures 62, 63, 67, and 70). The vortex tends to be smaller when the u fluctuations in the outer region are larger than the mean (Figures 64-66, 70). Therefore the size (and/or location) and strength of the junction vortex is determined by the velocity fluctuations in the outer region. The circulation of the vortex in each of the Figure 62-67 was estimated by considering a closed counter clockwise contour from $x/t=-0.30$ along the surface to the nose, along the nose from the surface to $y/t=0.23$, back to $x/t=-0.30$ along $y/t=0.23$, and finally down to the surface at $x/t=-0.30$. The following results were obtained: $\Gamma / U_{ref}t = 0.4882$ for Figure 62, $\Gamma / U_{ref}t = 0.4672$ for Figure 63, $\Gamma / U_{ref}t = 0.5563$ for Figure 64, $\Gamma / U_{ref}t = 0.5787$ for Figure 65, $\Gamma / U_{ref}t = 0.5436$ for Figure 66, and $\Gamma / U_{ref}t = 0.5095$ for Figure 67. The circulation is higher when the vortex lies closer to the nose.

Devenport and Simpson (1987, 1989, and 1990a) found from correlations with a hot wire at 93% of the boundary layer thickness ($y/t=0.4$, $x/t=-0.20$) and the velocity fluctuations in the backflow region to be significant. This indicated that the change from backflow to near zero velocity in the near wall region was preceded by a drop in velocity at the boundary layer edge. From these results it is conjectured that the fluctuations at the boundary layer edge propagate downward and inward toward the junction vortex, instead of traveling down the nose of the wing. Another possibility is that changes at the separation location are responsible for the observed changes in the vortex location. These data do not prove or disprove either one of these conjectures.

4.2.2 Other models

Devenport and Simpson (1990a) and Larousse, Martinuzzi and Tropea (1992), have reported the presence of a near-wall backflow jet. This jet is believed to be free-stream fluid moving down the front of the nose and back along the floor. The data in this study do not support this idea.

For such events we would expect that the backflow velocity fluctuations near the nose would lead the surface pressure fluctuations at some distance from the nose. The correlation should also be negative. From Figures 20 and 21, the pressure fluctuations at $x/t=-0.26$ are seen to lead the u velocity fluctuations at $x/t=-0.15$ and $x/t=-0.20$. This

strong negative ρ_{up} at a slightly negative τ , indicates that the positive pressure fluctuations at $x/t=-0.26$ occurs before an increasingly negative u occurs downstream at $x/t=-0.20$ and $x/t=-0.15$. This would imply that the fluctuations in velocity are related to events occurring upstream of this position.

Also, the jet should give high correlations between velocity fluctuations in the outer part of the layer with the velocity fluctuations in the backflow region. From the results for the space-time correlations, Figures 34-37, the correlations between the backflow region and the outer region are insignificant. This would indicate that possible free-stream fluid moving down the nose is not forming an increased backflow in the form of a jet.

4.3 Source of bimodal velocity and surface pressure histograms

The unsteadiness in the junction vortex is attributed to the observations of bimodal probability distribution functions of velocity and surface pressure (Devenport and Simpson, 1990a; Kim, Walker and Simpson, 1991; Larousse, Martinuzzi and Tropea, 1991; and Khan, 1994). The movement of the primary junction vortex (Figures 62-67) would expose a fixed probe to rapid changes in velocity or pressure. One idea maybe that

there are two flow states since the pdfs are bimodal. From Figures 62-67 we see this is not the case. The flow visualizations of Kim, Walker and Simpson (1991) indicate that the junction vortex moves in an aperiodic fashion. Also, the joint histograms of the U and V velocities (Figures 26-27) show only one primary peak in the pdf. Two flow states should be indicated by the presence of two distinct peaks in these figures, which is not the case. However, the flow structure at $x/t=-0.25$ and $x/t=-0.30$ for when the flow is inward and downward toward the wing shows small variations in velocity which are shown in the quadrant analysis in Figures 64-66.

5. Conclusions

Velocity measurements with a rapidly-scanning laser-Doppler velocimeter were performed in the plane of symmetry of a wing-body junction. The flow was scanned at a rate of 50 Hz from near the wall to $y/t = 0.25$ at four x/t locations, -0.15, -0.20, -0.25, and -0.30. Surface pressure measurements were made at $x/t = -0.26$, which was found to be the location of the most bimodal pressure probability density functions.

The velocity measurements show a similar flow structure to that measured by Devenport and Simpson (1990a,b): mean flow quantities, normal stress and the location of bimodal probability density functions for velocity.

Large cross-correlation were found between the velocity fluctuations near the wall and surface pressure fluctuations at $x/t = -0.26$. The velocity fluctuations for $y/t > 0.1$ at all four x -locations lead the surface pressure fluctuations by $TU_{ref} / t \approx 2.0$. The velocity fluctuations near the wall, $y/t < 0.05$, lead the surface pressure fluctuations for locations

upstream of the pressure transducer ($x/t = -0.26$). The velocity fluctuations near the wall slightly lag the pressure fluctuations at $x/t = -0.20$ and $x/t = -0.15$.

Space-time correlations show that for $x/t = -0.25$ and $x/t = -0.30$ the velocity fluctuations in the outer region, $y/t > 0.1$, are significantly correlated with and lead the velocity fluctuations near the wall. The highest correlations were observed at $x/t = -0.30$.

These measurements support a model of a single primary the junction vortex that changes size and location in front of the wing. The strength or circulation of this vortex is about constant within about 20%. The surface pressure signal at $x/t = -0.26$ is sensitive to movement of the vortex in front of the nose. Event-threshold conditional-averages of the velocity were obtained based on the surface pressure signal. These show that when the surface pressure signal is above the mean value, the junction vortex is concentrated near the nose. When the surface pressure signal is below the mean value, the vortex lies farther from the nose and the backflow near the nose is lower. The velocity-pressure cross-correlations and the space-time correlations indicate that the vortex changes location and size in response to fluctuations propagating inward and downward toward the wing. These fluctuations may be due to disturbances in the free-stream propagating downward or to fluctuations at the separation location.

This model is consistent with the observations of Kim, Walker, and Simpson. Further study may be needed to resolve the issue of whether the fluctuations at the

boundary layer edge or at the separation location are responsible for the unsteady motion of the junction vortex.

References

- Abid R. and Schmitt R., "Experimental Study of a Turbulent Horseshoe Vortex Using a Three-Component Laser Velocimeter", AIAA/ASME 4th Fluid Mechanics, Plasma Dynamics and Laser Conference, Georgia, AIAA-86-1069, 1986.
- Agui, J., and Andreopoulos, J., "Experimental Investigation of a Three-Dimensional Boundary Layer Flow in the Vicinity of an Upright Wall Mounted Cylinder" AIAA 21st Fluid Dynamics, Plasma Dynamics, and Lasers Conference, AIAA 90-1545, June 18-20, 1990.
- Baker, C. J., "The Turbulent Horseshoe Vortex", *Journal of Wind Engineering and Industrial Aerodynamics*, Vol. 6, Nos. 1-2, pp. 9-23, 1980.
- Baker, C. J., "The Position of Points of Maximum and Minimum Shear Stress Upstream of Cylinders Mounted Normal to Flat Plates", *Journal of Wind Engineering and Industrial Aerodynamics*, Vol. 18, pp. 263-274, 1985.
- Belik, L., "The Secondary Flow About Circular Cylinders Mounted Normal to a Flat Plate", *Aeronautical Quarterly*, Vol. 24, pp. 47-54, February 1973.
- Bendat, J. S., and Piersol, A. G., *Random Data Analysis and Measurement Procedures*, John Wiley and Sons, New York, 1986.
- Bradshaw, P., "'Inactive' Motion and Pressure Fluctuations in Turbulent Boundary Layers", *Journal of Fluid Mech.*, Vol. 30, pp. 241-258, 1967.

- Chehroudi, B. and Simpson, R. L., "Space-time results for a separating turbulent boundary layer using a rapidly scanning laser anemometer", *Journal of Fluid Mechanics*, vol. 160, pp. 77-92, 1985.
- Dargahi, B., "The Turbulent Flow Field Around a Circular Cylinder", *Experiments in Fluids*, Vol. 8, N0. 1-12, 1989.
- Devenport, W. J. and Simpson, R. L., "Time-Dependent and Time-Averaged Turbulence Structure near the Nose of a Wing-Body Junction", *Journal of Fluid Mechanics*, Vol. 210, pp. 23-55, 1990a.
- Devenport, W. J. and Simpson, R. L., "An Experimental Investigation of the Flow Past an Idealized Wing-Body Junction: Preliminary Data Report v. 5", *AOE Dept., VPI&SU*, 1990b.
- Dickinson, S. C., "An Experimental Investigation of Appendage-Flat Plate Junction Flow Volume 1: Description", *DTNSRDC-86/051*, December 1986.
- Eckerle, W. A., and Langston, L. S., "Horseshoe Vortex Formation Around a Cylinder", *Journal of Turbomachinery*, Vol. 109, pp. 278-285, April 1987.
- Fleming, J. L., Simpson, R. L., and Devenport, W. J., "An Experimental Study of a Turbulent Wing-Body Junction and Wake Flow", *VPI Technical Report No. VPI-AOE-172*, VPI & SU (available from DTIC), 1991.
- Hasan, M. A. Z., Casarella, M. J., and Rood, E. P., "An Experimental Study of the Flow and Wall-Pressure Field Around a Wing-Body Junction", *Shear Flow-Structure Interaction Phenomena*, (ed. A. Akay & M. Reischman), ASME NCA-1, pp. 89-95, 1985.
- Khan, M. J., "Experimental Investigation of Wing Sweep on Juncture Flow", *Ph.D. Dissertation*, Dept. Aerospace Engr., Texas A&M Univ., College Station, Texas, May 1994.
- Kim, S., Walker, D. A., and Simpson, R. L., "Observation and Measurement of Flow Structures in the Stagnation Region of a Wing-Body Junction", *VPI Technical Report No. VPI-E-91-20*, VPI & SU (available from DTIC), 1991.
- Kline, S. J. and McClintock, F. A., "Describing Uncertainty in Single-Sample Experiments", *Mechanical Engineering*, January, pp. 3-8, 1953.

- Kubendran, L. R., McMahon, H. M., and Hubbartt, J. E., "Turbulent Flow Around a Wing/Fuselage-Type Junction", *AIAA Journal*, Vol. 24, No. 9, pp. 1447-1452, September 1986.
- Larousse, A., Martinuzzi, R., and Tropea, C., "Flow Around Surface-Mounted, Three-Dimensional Obstacles", *Selected Papers of the 8th Symp. on Turb. Shear Flows*, München, Springer-Verlag Germany, 1992.
- Martinuzzi, R., and Tropea, C., "The Flow Around Surface-Mounted, Prismatic Obstacles Placed in a Fully Developed Channel Flow", *Journal Fluids Engineering*, Vol. 115, pp. 85-92, 1993.
- Mehta, R. D., "Effects of Wing Nose Shape on the Flow in a Wing-Body Junction", *The Aero Journal of the Royal Aero. Soc.*, pp. 456-460, December 1984.
- Ölçmen, S. M. and Simpson, R. L., "Influence of Wing Shapes on Surface Pressure Fluctuations at Wing-Body Junctions", *AIAA Journal*, Vol. 32, No. 1, January 1994.
- Press, W. H., Saul, A. T., Vetterling, W. T., and Flannery, B. P., *Numerical Recipes in C, The Art of Scientific Computing*, 2nd. Ed., Cambridge University Press, 1992.
- Rife, M. C., Devenport, W. J., and Simpson, R. L., "An Experimental Study of the Relationship Between Velocity and Pressure Fluctuations in a Wing-Body Junction", *VPI Technical Report No. VPI-AOE-188*, VPI & SU (available from DTIC), 1991.
- Thomas, A. S. W., "The Unsteady Characteristics of Laminar Juncture Flow", *Phys. Fluids*, Vol. 30, pp. 283-285, 1987.
- Townsend, A. A., *The Structure of Turbulent Shear Flow*, Cambridge University Press, New York, 1976.

Tables

Table 1: Uncertainties on the cross-correlation coefficient function for the velocity measurement location for the u component.

$x/t=-0.15$			
$ \rho_{up} $	$y/t<0.04$	$0.04<y/t<0.08$	$y/t>0.08$
0.1	3.75×10^{-3}	1.68×10^{-3}	1.94×10^{-3}
0.2	2.93×10^{-3}	1.20×10^{-3}	1.15×10^{-3}
0.3	3.65×10^{-3}	1.41×10^{-3}	1.14×10^{-3}
0.4	4.68×10^{-3}	1.81×10^{-3}	1.34×10^{-3}
$x/t=-0.20$			
$ \rho_{up} $	$y/t<0.04$	$0.04<y/t<0.08$	$y/t>0.08$
0.1	2.13×10^{-3}	1.14×10^{-3}	1.74×10^{-3}
0.2	2.22×10^{-3}	8.89×10^{-4}	1.03×10^{-3}
0.3	3.08×10^{-3}	1.11×10^{-3}	1.02×10^{-3}
0.4	4.05×10^{-3}	1.42×10^{-3}	1.20×10^{-3}
$x/t=-0.25$			
$ \rho_{up} $	$y/t<0.04$	$0.04<y/t<0.08$	$y/t>0.08$
0.1	1.28×10^{-3}	1.33×10^{-3}	1.96×10^{-3}
0.2	1.25×10^{-3}	8.64×10^{-4}	1.11×10^{-3}
0.3	1.71×10^{-3}	9.50×10^{-4}	1.01×10^{-3}
0.4	2.24×10^{-3}	1.17×10^{-3}	1.14×10^{-3}
0.5	2.78×10^{-3}	1.42×10^{-3}	1.33×10^{-3}
0.6	3.34×10^{-3}	1.69×10^{-3}	1.68×10^{-3}
0.7	3.89×10^{-3}	1.97×10^{-3}	1.80×10^{-3}
$x/t=-0.30$			
$ \rho_{up} $	$y/t<0.04$	$0.04<y/t<0.08$	$y/t>0.08$
0.1	1.09×10^{-3}	1.97×10^{-3}	2.40×10^{-3}
0.2	9.24×10^{-4}	1.17×10^{-3}	1.32×10^{-3}
0.3	1.20×10^{-3}	1.16×10^{-3}	1.14×10^{-3}
0.4	1.55×10^{-3}	1.37×10^{-3}	1.23×10^{-3}
0.5	1.92×10^{-3}	1.64×10^{-3}	1.41×10^{-3}
0.6	2.30×10^{-3}	1.93×10^{-3}	1.64×10^{-3}
0.7	2.68×10^{-3}	2.23×10^{-3}	1.88×10^{-3}

Table 2: Uncertainties on the cross-correlation coefficient function for the velocity measurement location for the v component.

x/t=-0.25			
$ \rho_{vp} $	y/t<0.04	0.04<y/t<0.08	y/t>0.08
0.05	2.58×10^{-3}	4.99×10^{-3}	1.33×10^{-2}
0.1	1.37×10^{-3}	2.54×10^{-3}	6.70×10^{-3}
0.2	1.12×10^{-3}	1.56×10^{-3}	3.45×10^{-3}
x/t=-0.30			
$ \rho_{vp} $	y/t<0.04	0.04<y/t<0.08	y/t>0.08
0.1	1.36×10^{-3}	3.35×10^{-3}	7.96×10^{-3}
0.2	8.87×10^{-4}	1.79×10^{-3}	4.09×10^{-3}
0.3	9.75×10^{-4}	1.46×10^{-3}	2.93×10^{-3}
0.4	1.20×10^{-3}	1.49×10^{-3}	2.50×10^{-3}
0.5	1.44×10^{-3}	1.66×10^{-3}	2.41×10^{-3}

Table 3: Uncertainties on the space-time correlation coefficient function for ρ_{uu} as a function of measurement location.

x/t=-0.15		
$ \rho_{uu} $	y/t<0.08	y/t>0.08
0.1	1.79×10^{-3}	1.95×10^{-3}
0.2	1.61×10^{-3}	1.56×10^{-3}
0.3	2.14×10^{-3}	1.98×10^{-3}
0.4	2.79×10^{-3}	2.54×10^{-3}
0.5	3.46×10^{-3}	3.14×10^{-3}
x/t=-0.20		
$ \rho_{uu} $	y/t<0.08	y/t>0.08
0.1	1.06×10^{-3}	1.10×10^{-3}
0.2	1.16×10^{-3}	9.27×10^{-4}
0.3	1.62×10^{-3}	1.20×10^{-3}
0.4	2.13×10^{-3}	1.56×10^{-3}
x/t=-0.25		
$ \rho_{uu} $	y/t<0.06	y/t>0.06
0.1	2.22×10^{-3}	2.39×10^{-3}
0.2	1.91×10^{-3}	1.64×10^{-3}
0.3	2.49×10^{-3}	1.90×10^{-3}
0.4	3.23×10^{-3}	2.38×10^{-3}
0.5	4.00×10^{-3}	2.92×10^{-3}
x/t=-0.30		
$ \rho_{uu} $	y/t<0.06	y/t>0.06
0.1	2.63×10^{-3}	2.31×10^{-3}
0.2	2.11×10^{-4}	1.70×10^{-3}
0.3	2.68×10^{-3}	2.06×10^{-3}
0.4	3.45×10^{-3}	2.62×10^{-3}
0.5	4.27×10^{-3}	3.22×10^{-3}
0.6	5.10×10^{-3}	3.85×10^{-3}

Table 4: Uncertainties on the space-time correlation coefficient function for ρ_{vv} as a function of measurement location.

x/t=-0.25		
$ \rho_{vv} $	y/t<0.08	y/t>0.08
0.1	1.86×10^{-3}	3.25×10^{-3}
0.2	1.69×10^{-3}	2.68×10^{-3}
0.3	2.25×10^{-3}	3.44×10^{-3}
0.4	2.93×10^{-3}	4.44×10^{-3}
0.5	3.63×10^{-3}	5.49×10^{-3}
x/t=-0.30		
$ \rho_{vv} $	y/t<0.08	y/t>0.08
0.1	5.33×10^{-3}	1.17×10^{-2}
0.2	3.68×10^{-3}	6.65×10^{-3}
0.3	4.25×10^{-3}	6.16×10^{-3}
0.4	5.32×10^{-3}	6.96×10^{-3}
0.5	6.53×10^{-3}	8.21×10^{-3}

Table 5: Uncertainties on the space-time correlation coefficient function for ρ_{uv} as a function of measurement location.

x/t=-0.25		
$ \rho_{uv} $	y/t<0.08	y/t>0.08
0.1	1.86×10^{-3}	3.25×10^{-3}
0.2	1.69×10^{-3}	2.68×10^{-3}
0.3	2.25×10^{-3}	3.44×10^{-3}
0.4	2.93×10^{-3}	4.44×10^{-3}
0.5	3.63×10^{-3}	5.49×10^{-3}
x/t=-0.30		
$ \rho_{uv} $	y/t<0.08	y/t>0.08
0.1	5.33×10^{-3}	1.17×10^{-2}
0.2	3.68×10^{-3}	6.65×10^{-3}
0.3	4.25×10^{-3}	6.16×10^{-3}
0.4	5.32×10^{-3}	6.96×10^{-3}
0.5	6.53×10^{-3}	8.21×10^{-3}

Figures

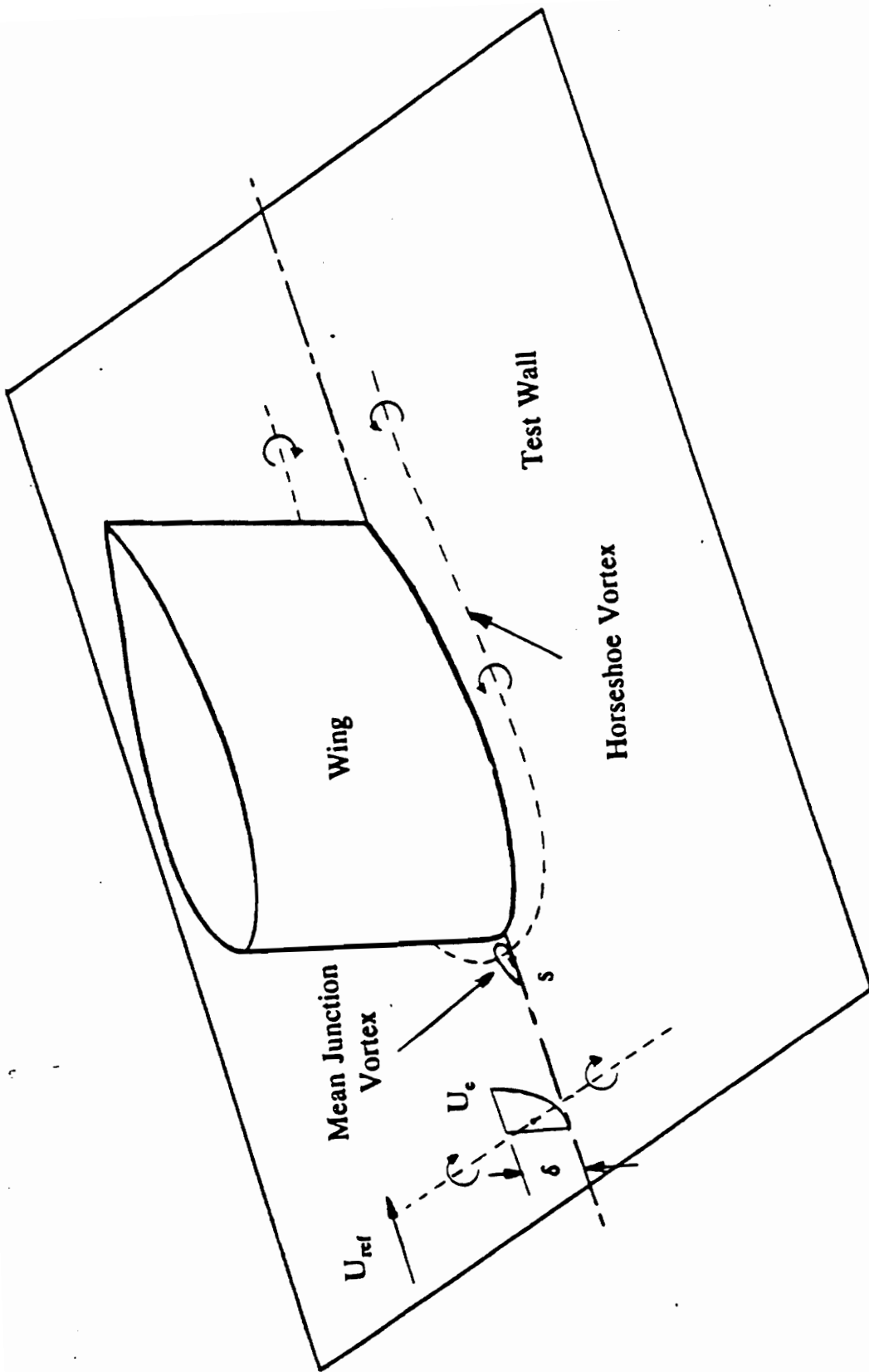


Figure 1. Schematic of a wing-body junction flow.

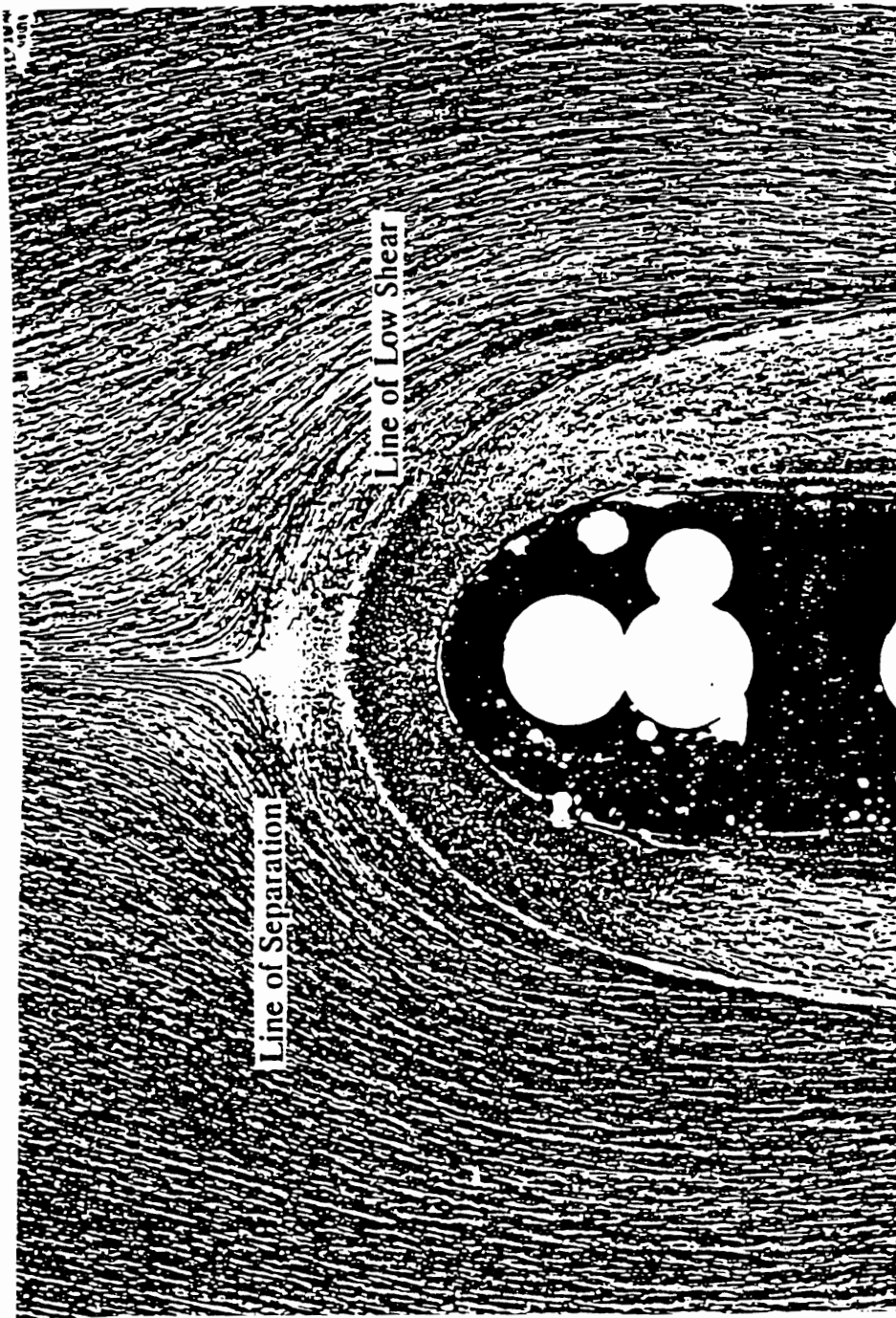


Figure 2. Oil flow in the nose region of the wing-body junction from Devenport and Simpson (1990a). Note: A closed separation line passes through the 3-D stagnation point. The line of low shear is an open separation line.

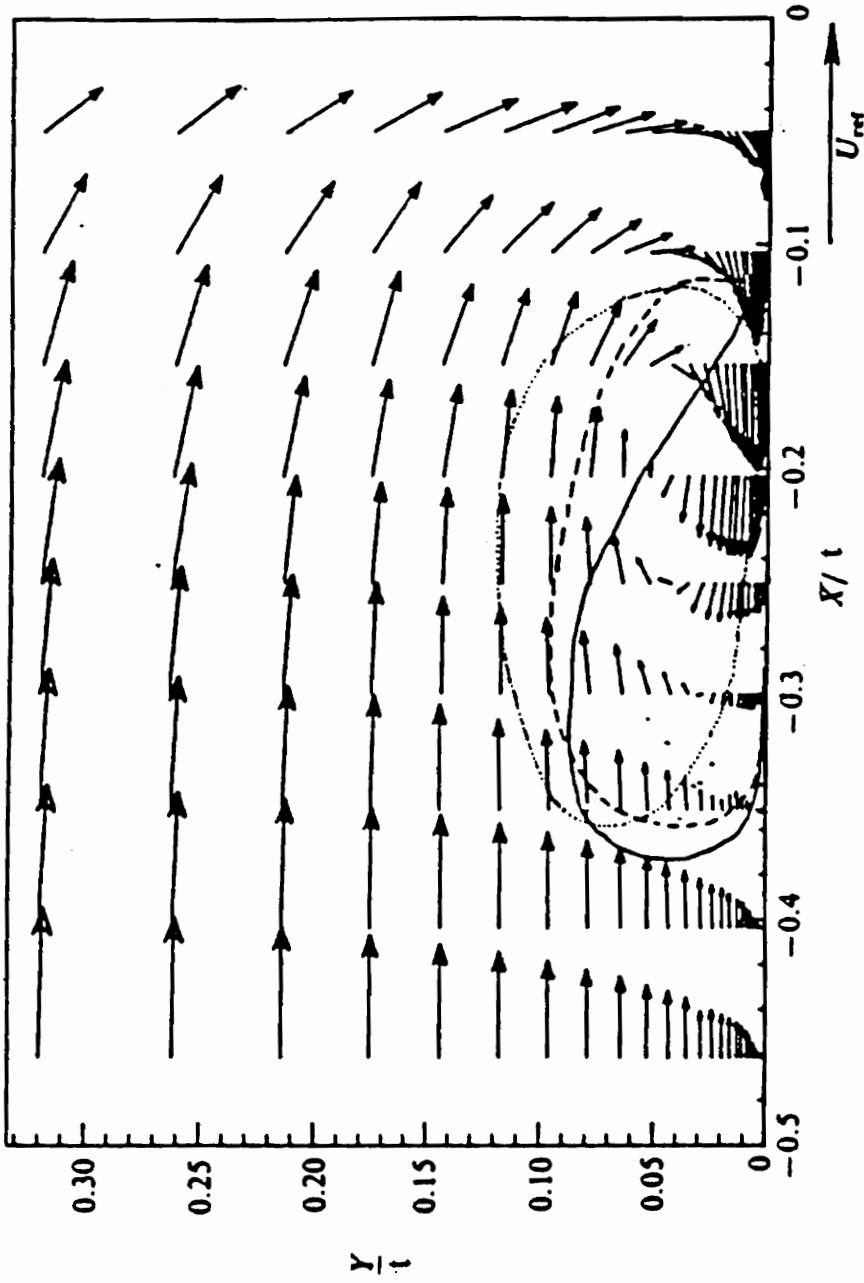


Figure 3. Mean velocity vectors showing the mean junction vortex (Devenport and Simpson, 1990a). Note: Solid line shows the extent of U bimodal flow, dashed line shows extent of V bimodal flow, and dotted line shows extent of UV bimodal flow.

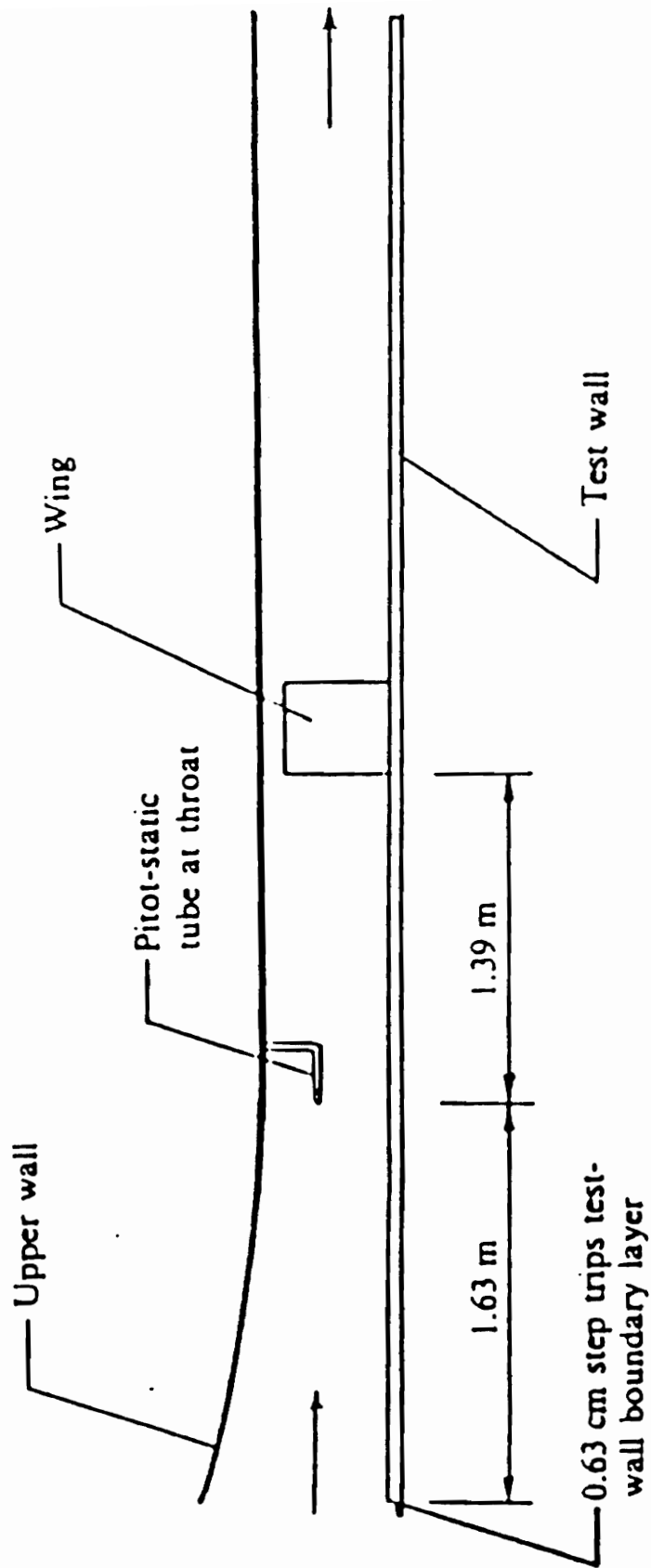


Figure 4. Side view schematic of the boundary layer wind tunnel used for the wing-body junction experiments.

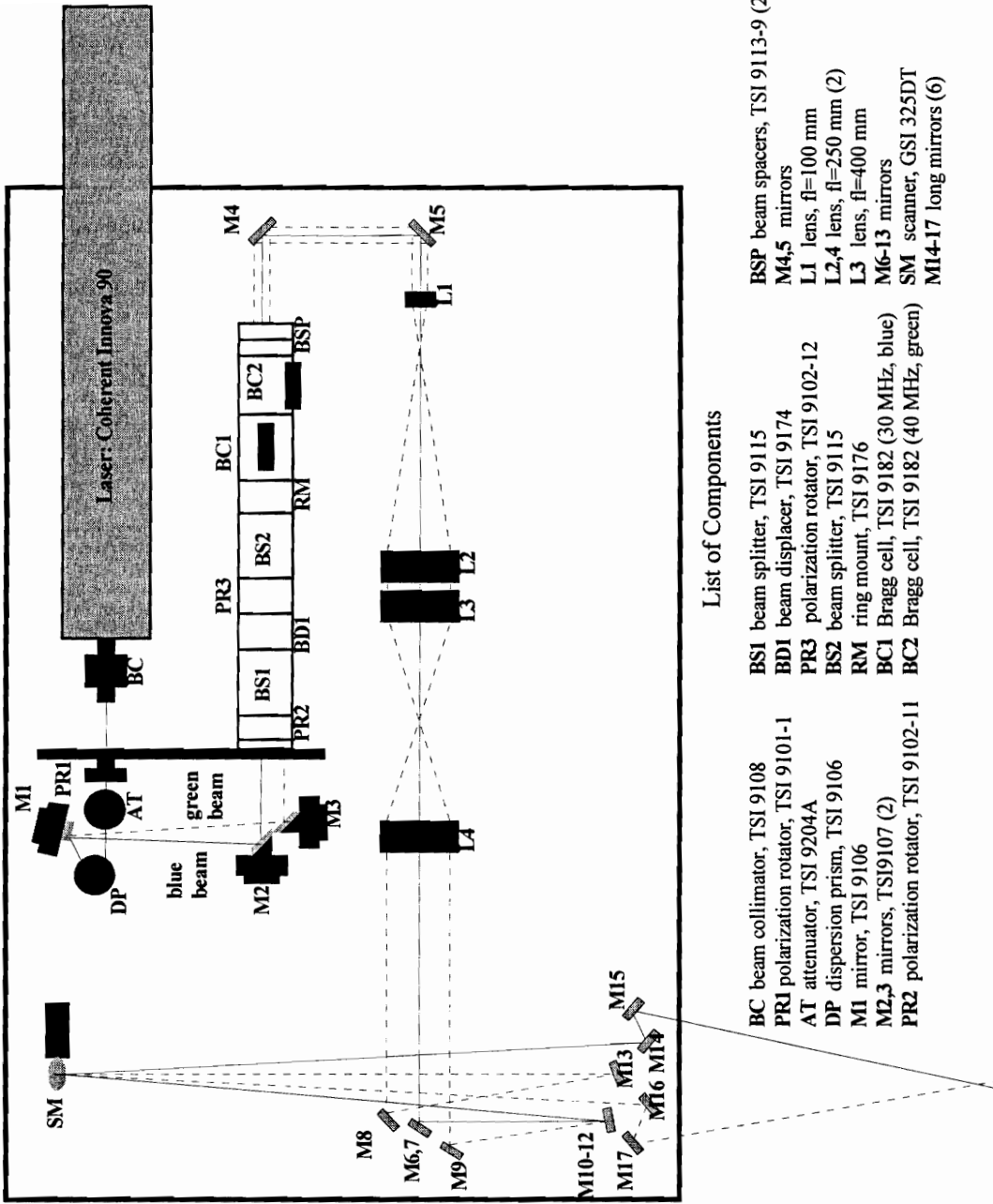


Figure 5. Top view of Rapidly Scanning Laser Doppler Velocimeter (RSLDV).

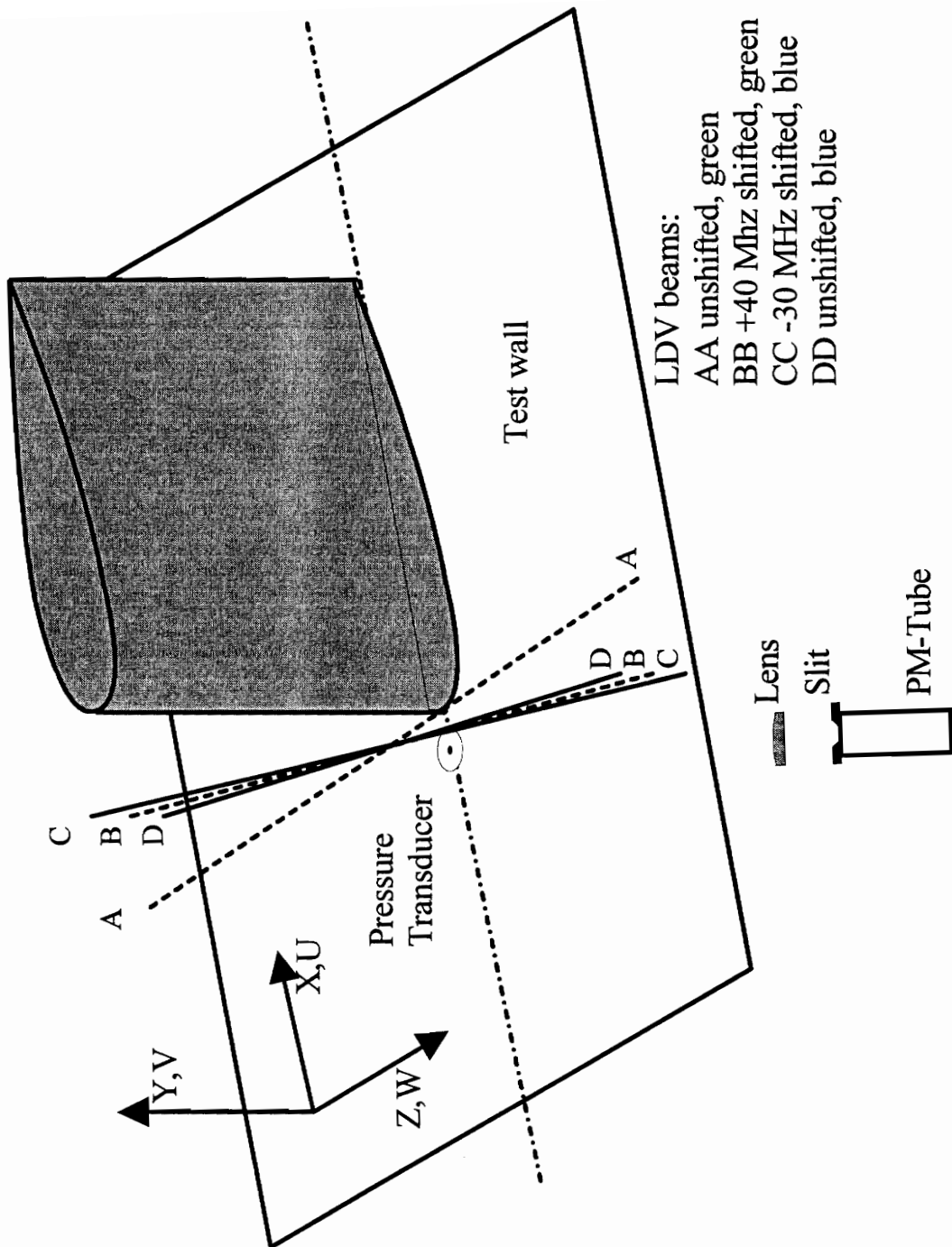


Figure 6. View of wing-body showing the coordinate system, pressure transducer, laser beams and receiving optics.

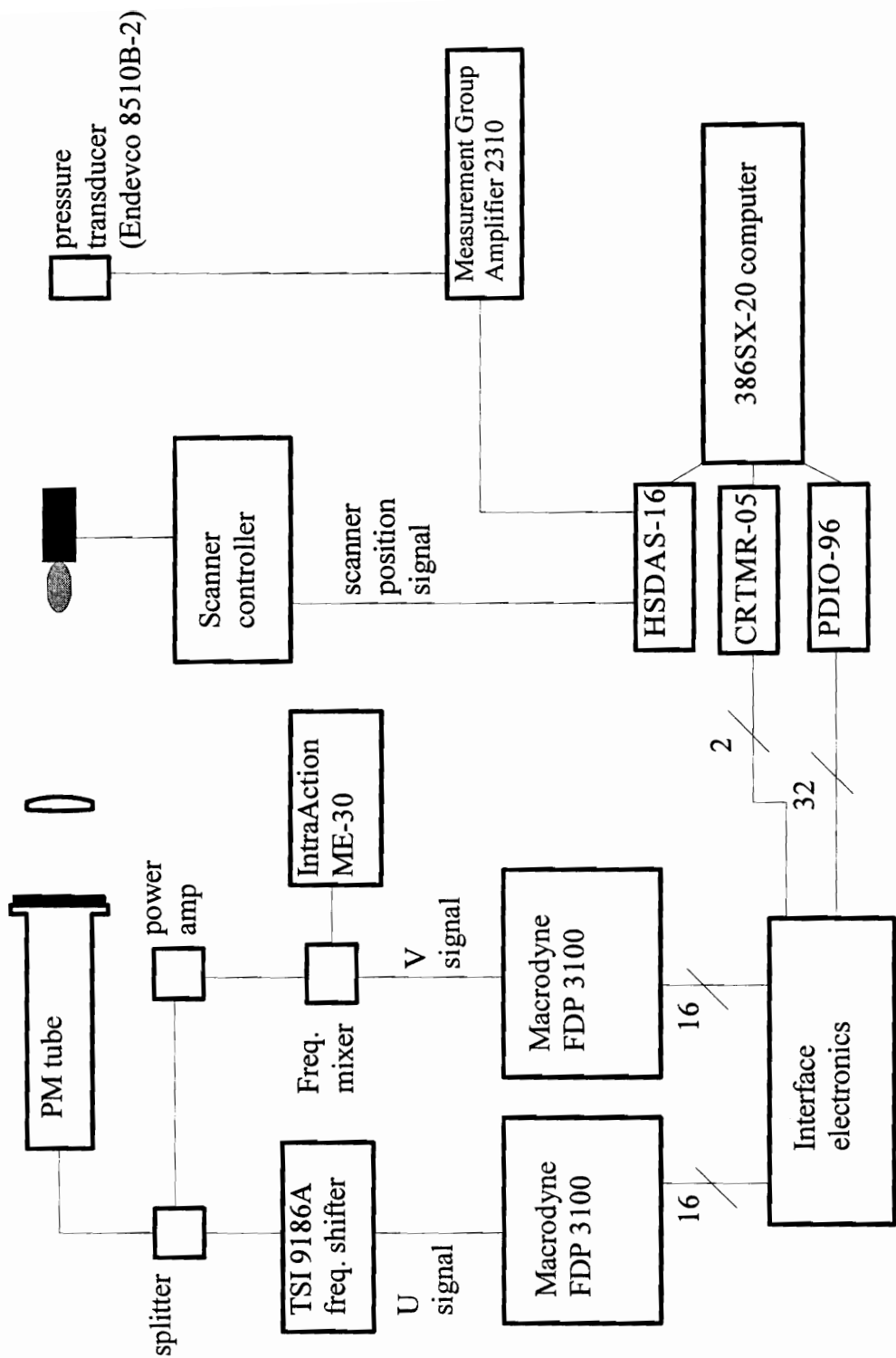


Figure 7. Schematic of data acquisition system.

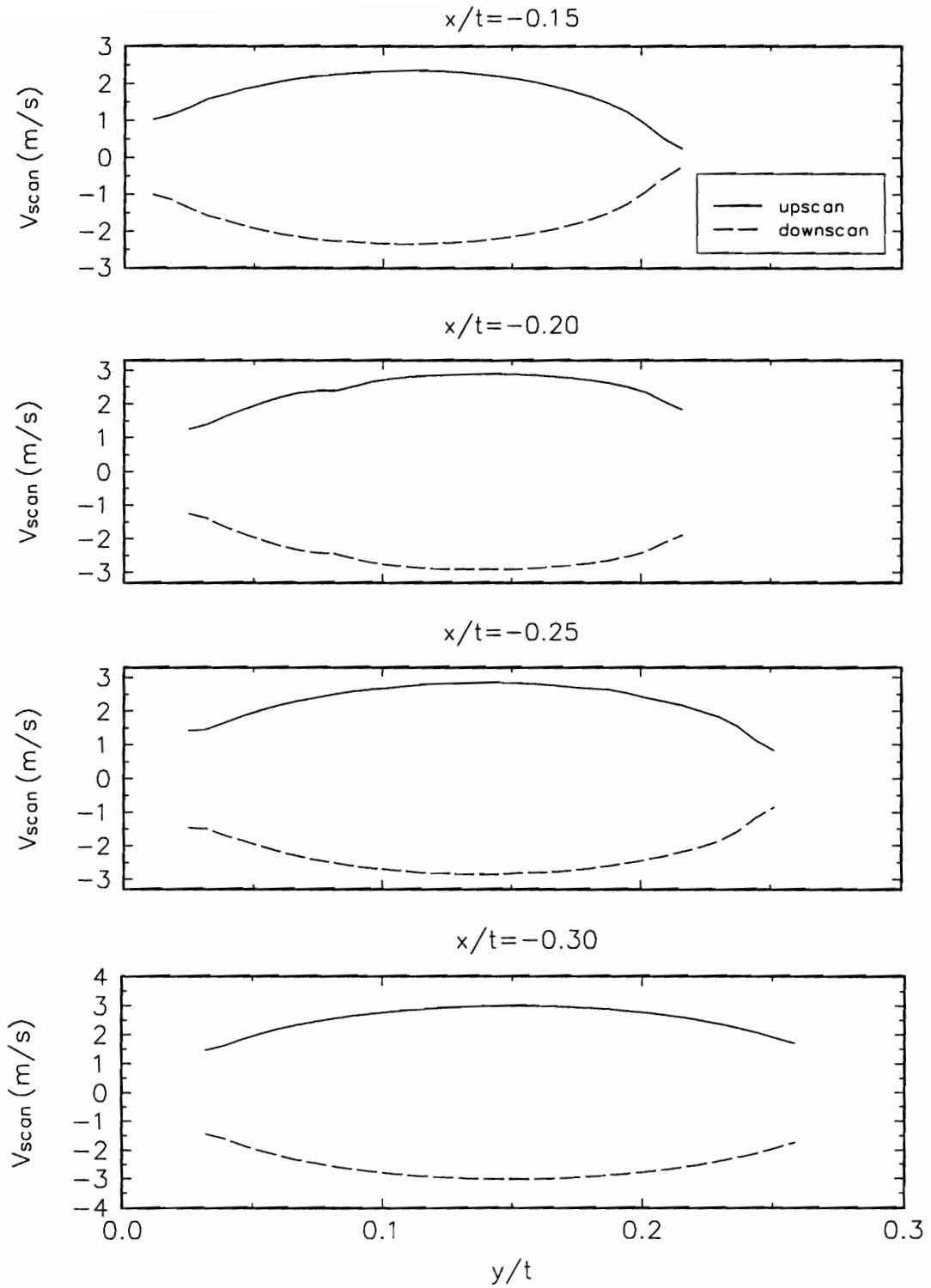


Figure 8. Measurement volume scan velocity at the four measurement locations.

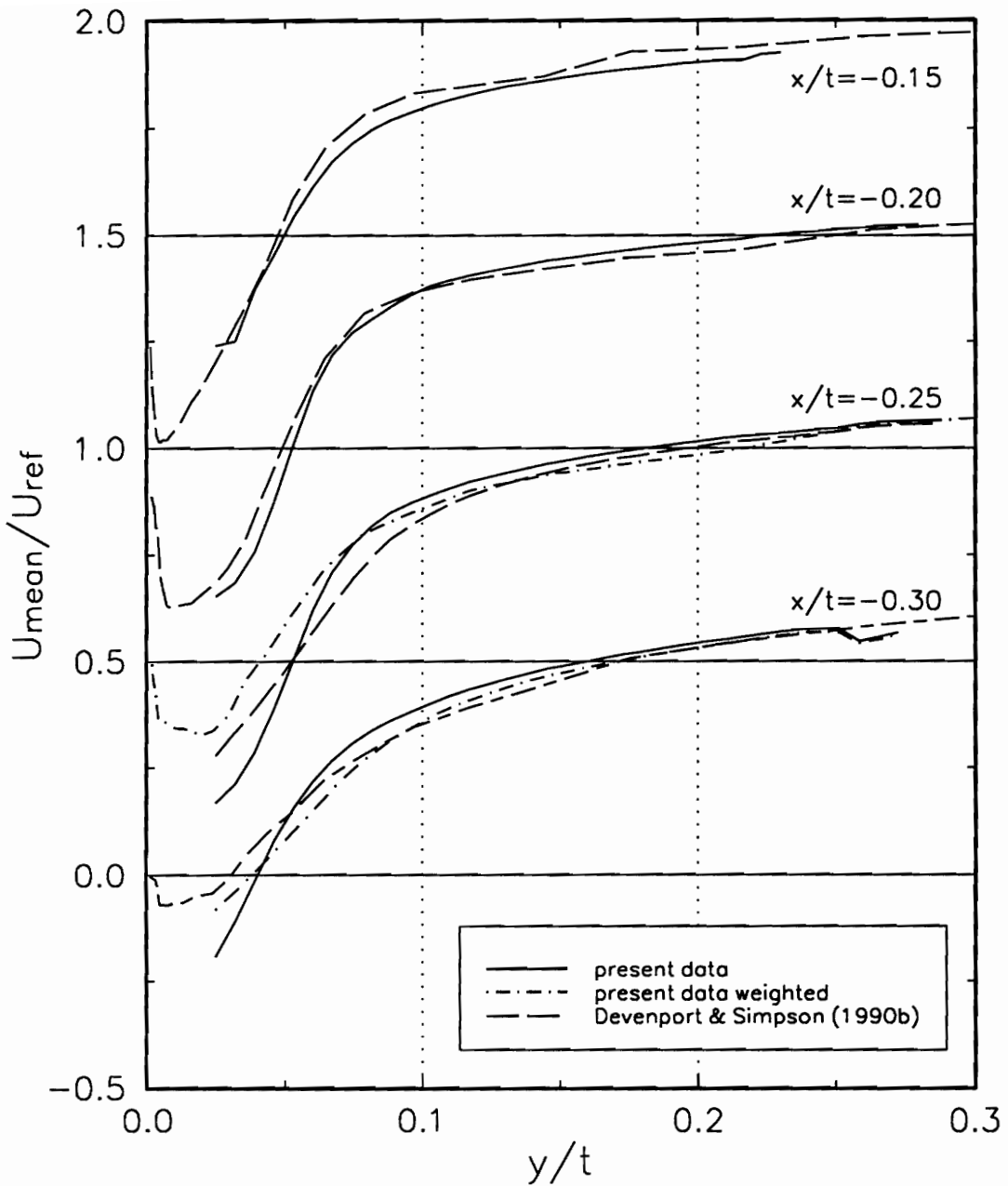


Figure 9. U component mean velocity comparisons with Devenport and Simpson (1990b). Weighted mean velocities were calculated using equation 2.16. Note: $x/t=-0.15$, $x/t=-0.20$, and $x/t=-0.25$ are offset in U_{mean}/U_{ref} by 1.5, 1.0, and 0.5 respectively.

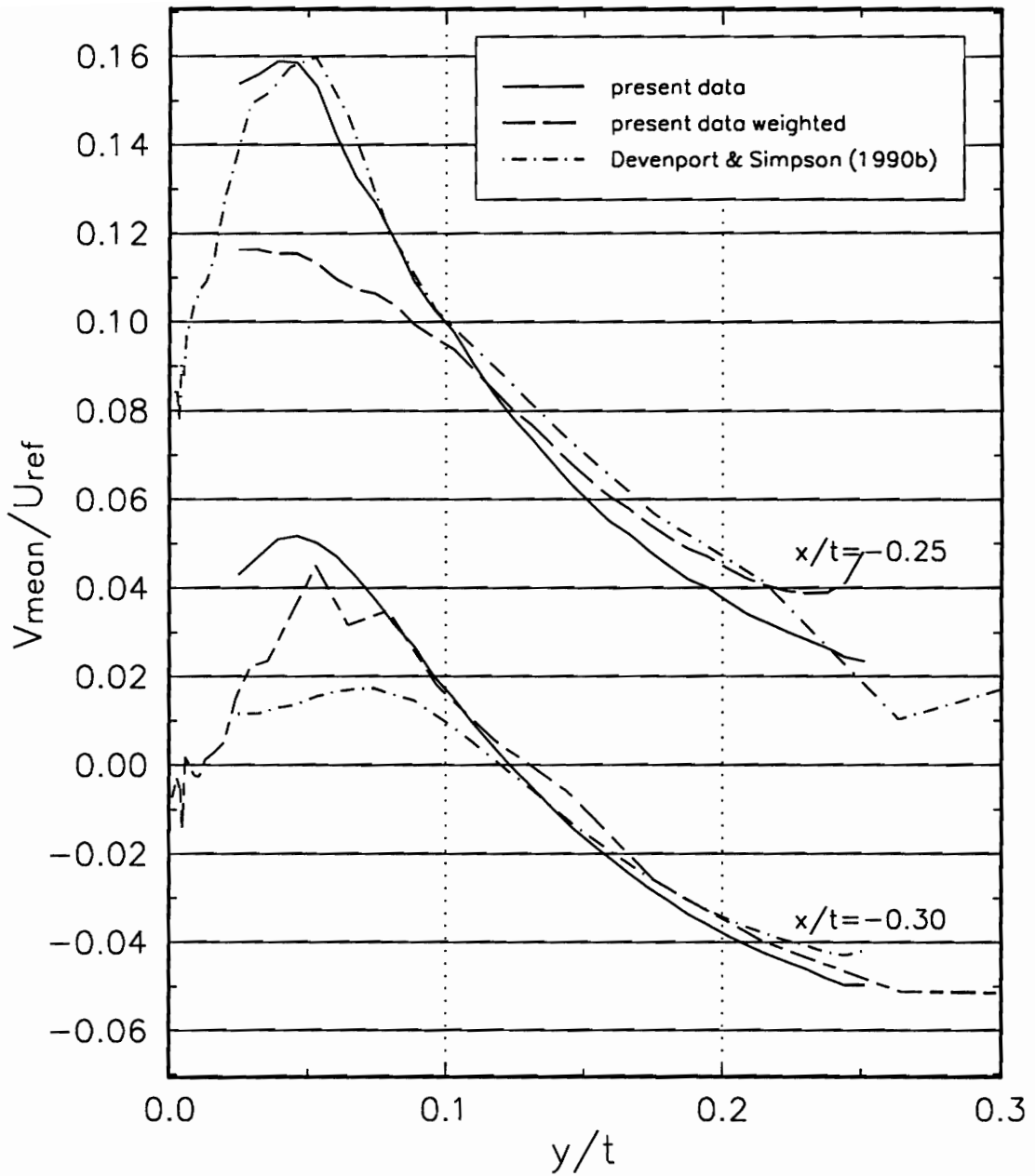


Figure 10. V component mean velocity comparisons with Devenport an Simpson (1990b). Weighted mean velocities were calculated using equation 2.16. Note: $x/t=-0.25$ is offset in V_{mean}/U_{ref} by 0.1.

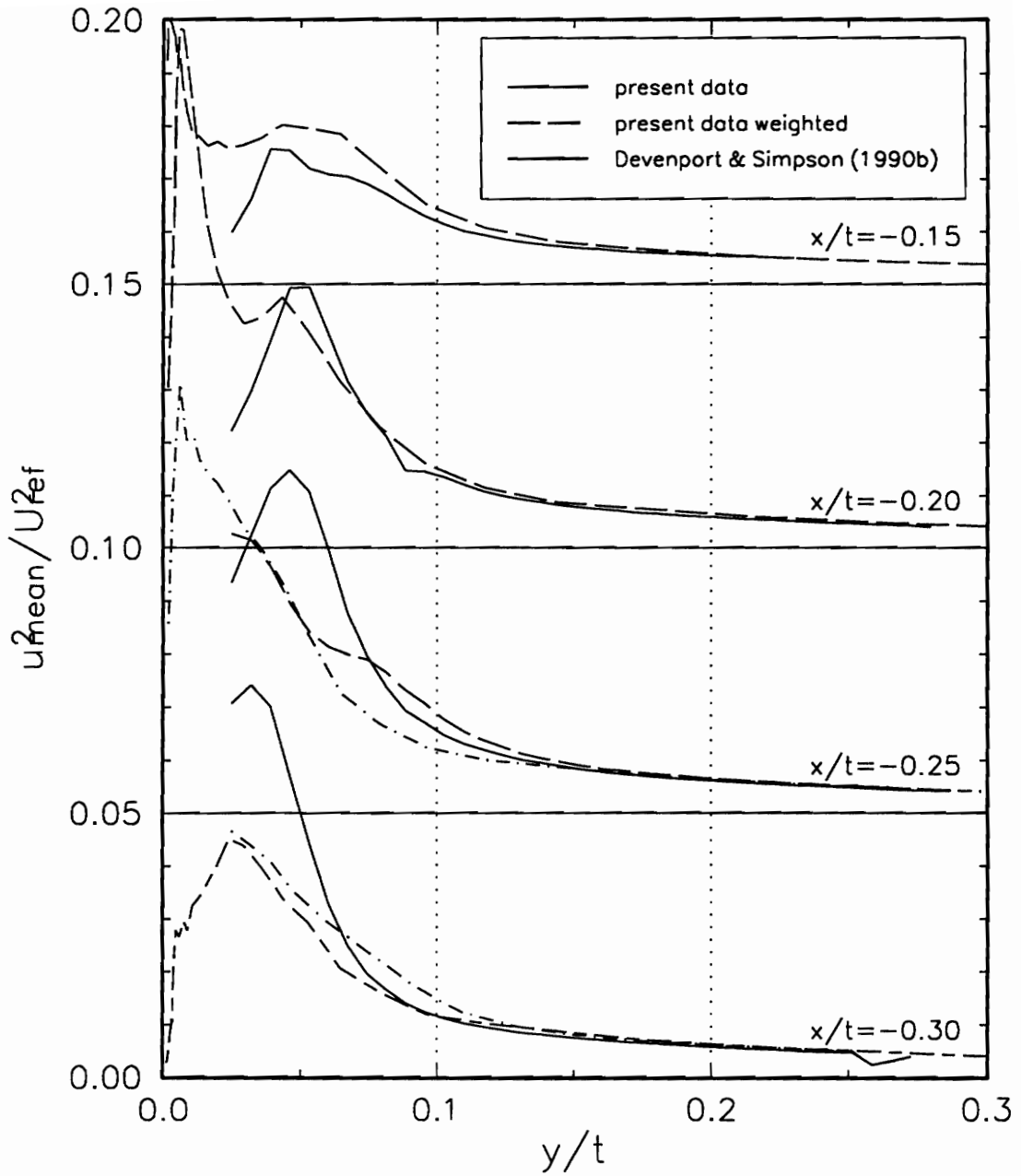


Figure 11. U component mean square velocity comparisons with Devenport and Simpson (1990b). Weighted mean velocities were calculated using equation 2.16. Note: $x/t=-0.15$, $x/t=-0.20$, and $x/t=-0.25$ are offset in U_{mean}^2/U_{ref}^2 by 0.15, 0.1, and 0.05 respectively.

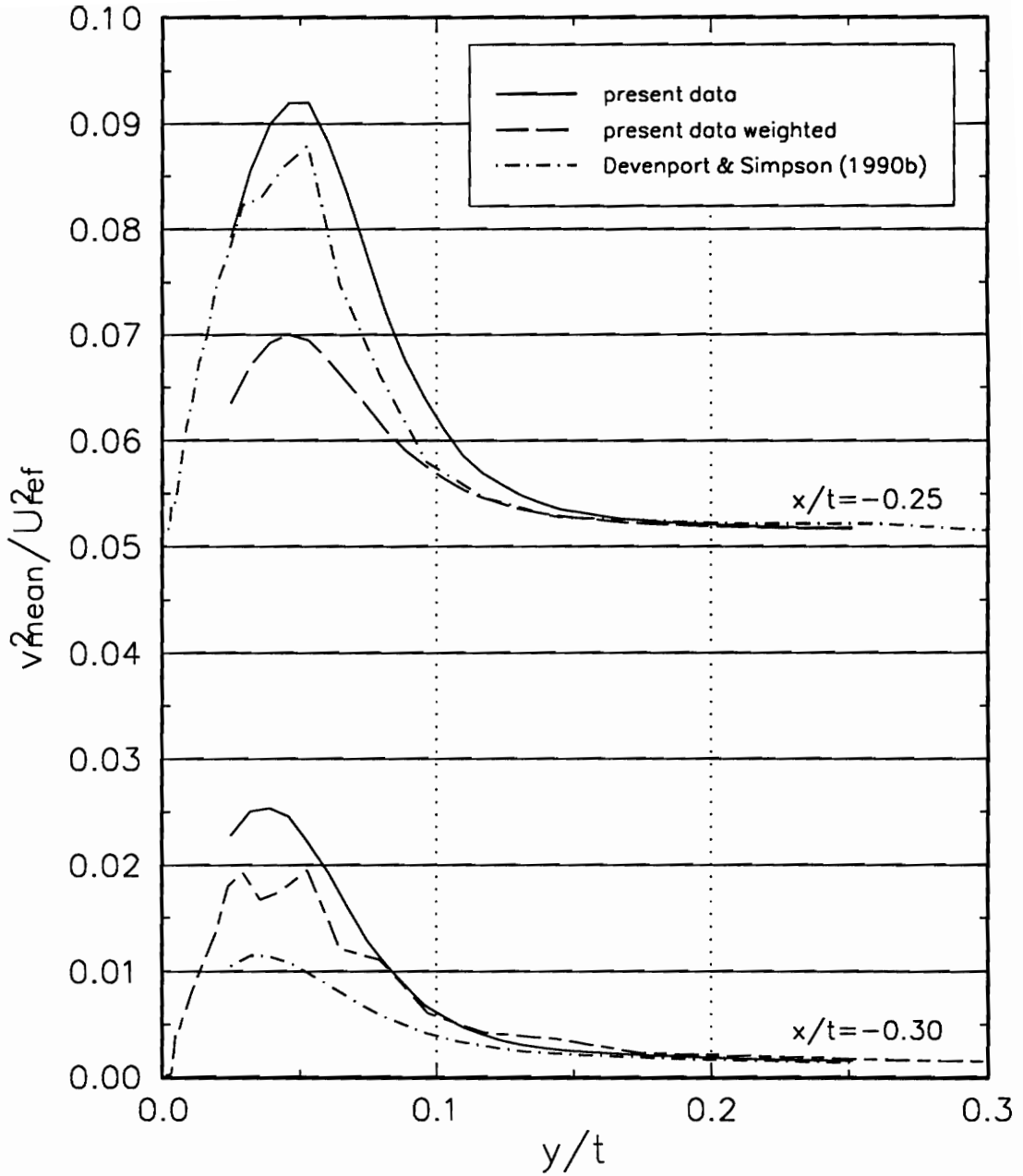


Figure 12. V component mean square velocity comparisons with Devenport and Simpson (1990b). Weighted mean velocities were calculated using equation 2.16. Note: $x/t=-0.25$ is offset in V_{mean}^2/U_{ref}^2 by 0.05.

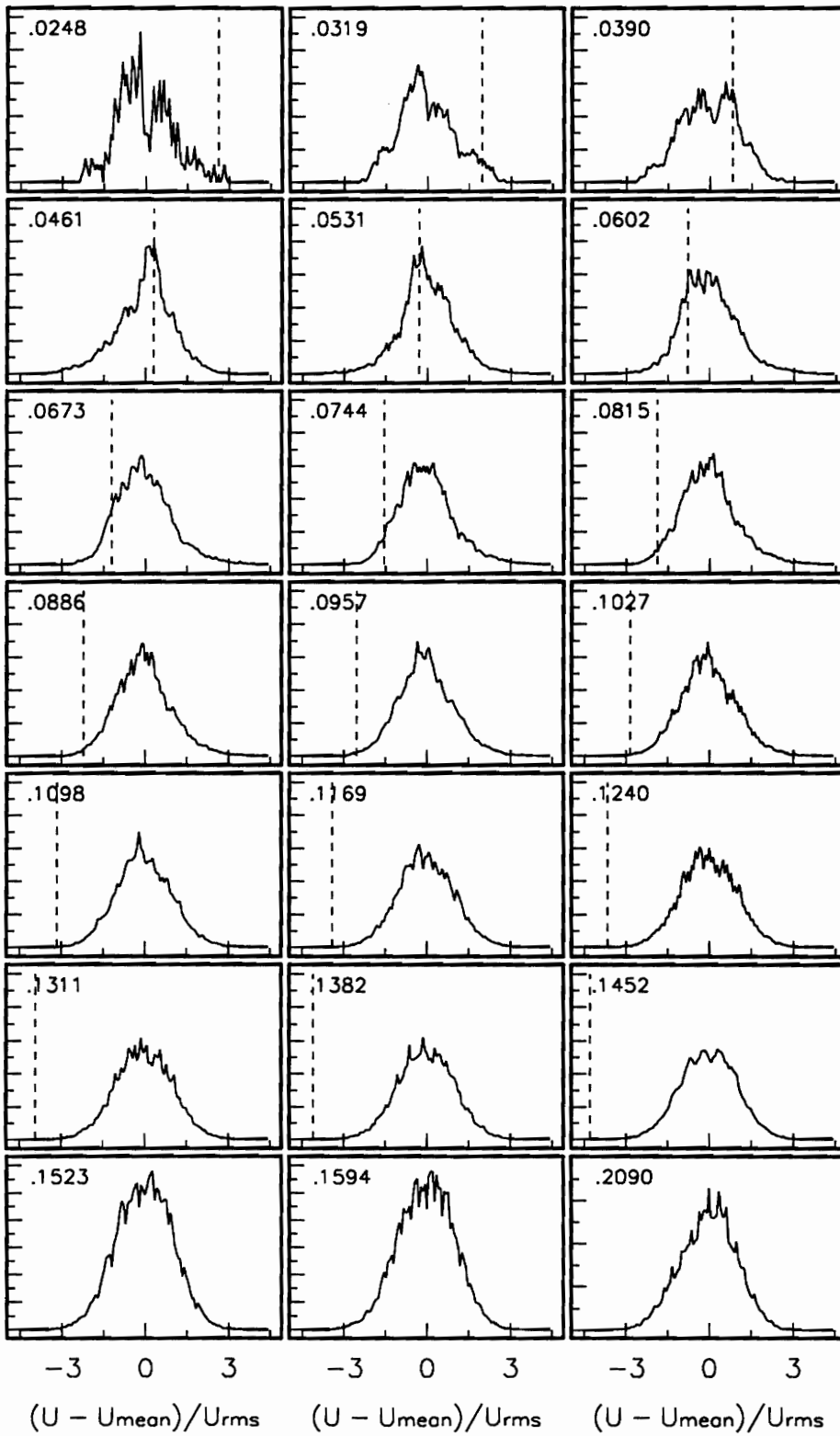


Figure 13. Histograms of U velocity at $x/t=-0.15$. Note: Dashed line is zero velocity.

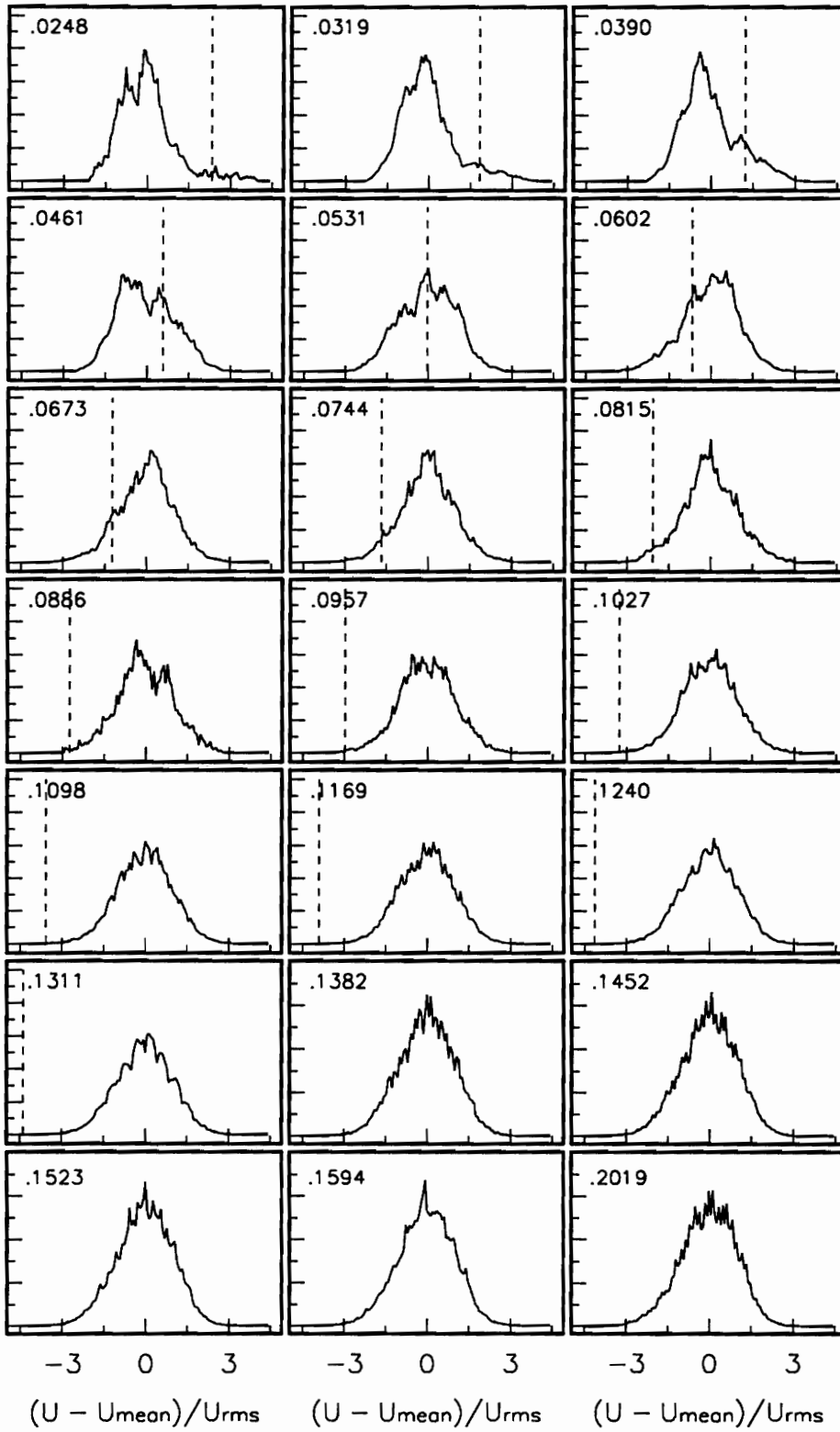


Figure 14. Histograms of U velocity at $x/t=-0.20$. Note: Dashed line is zero velocity.

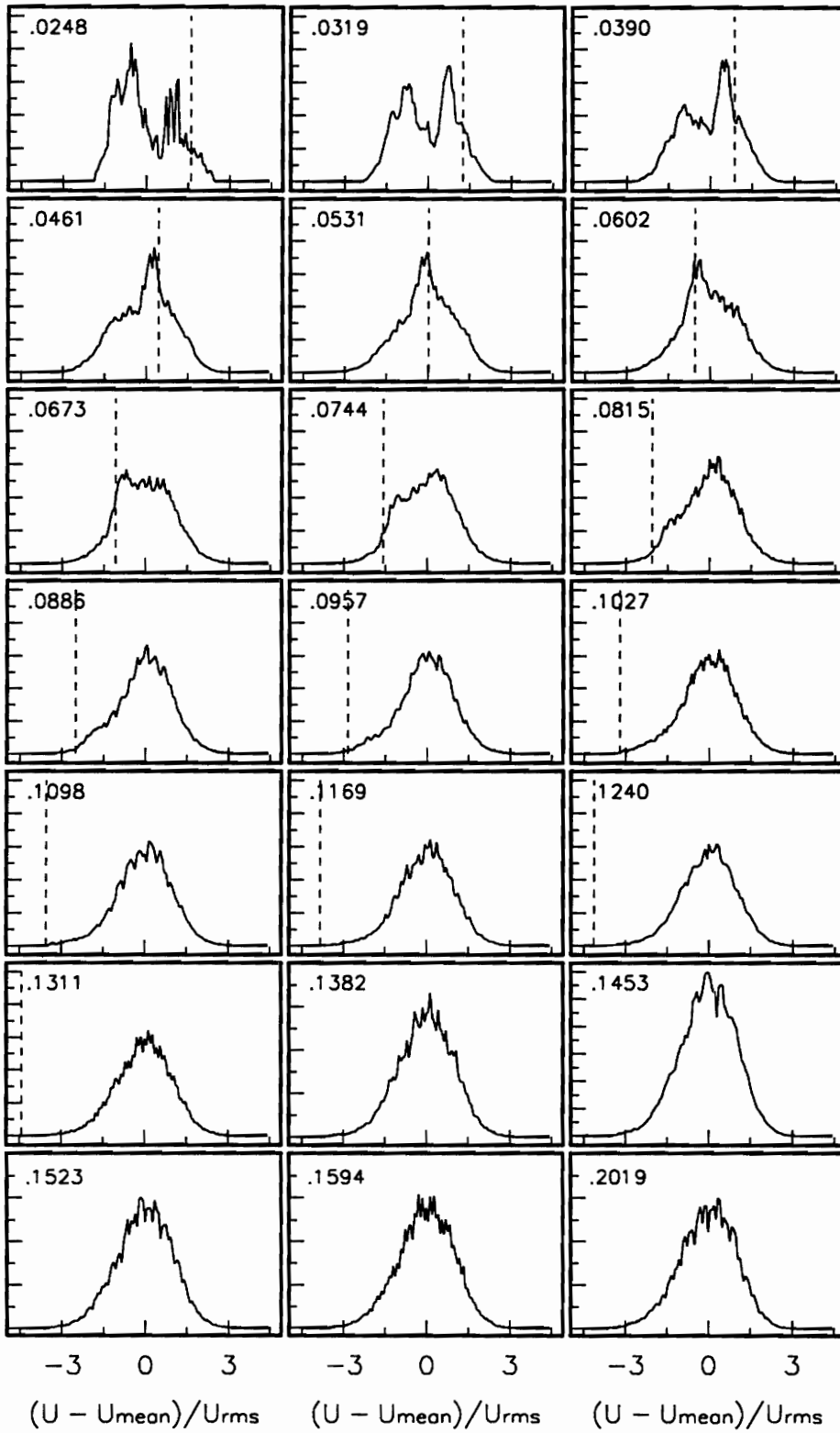


Figure 15. Histogram of U velocity at $x/t=-0.25$. Note: Dashed line is zero velocity.

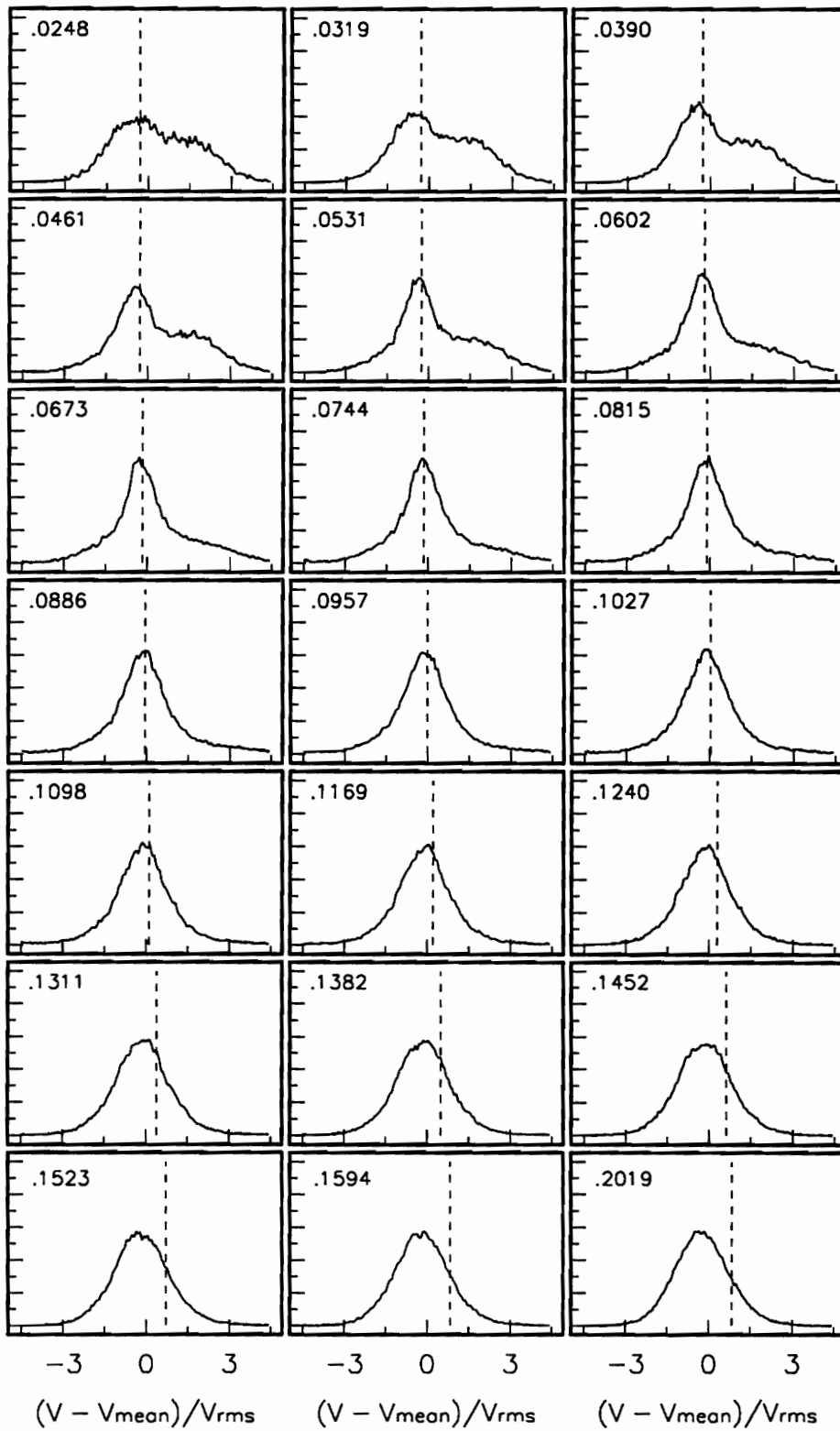


Figure 16. Histograms of V velocity at $x/t=-0.25$. Note: Dashed line is zero velocity.

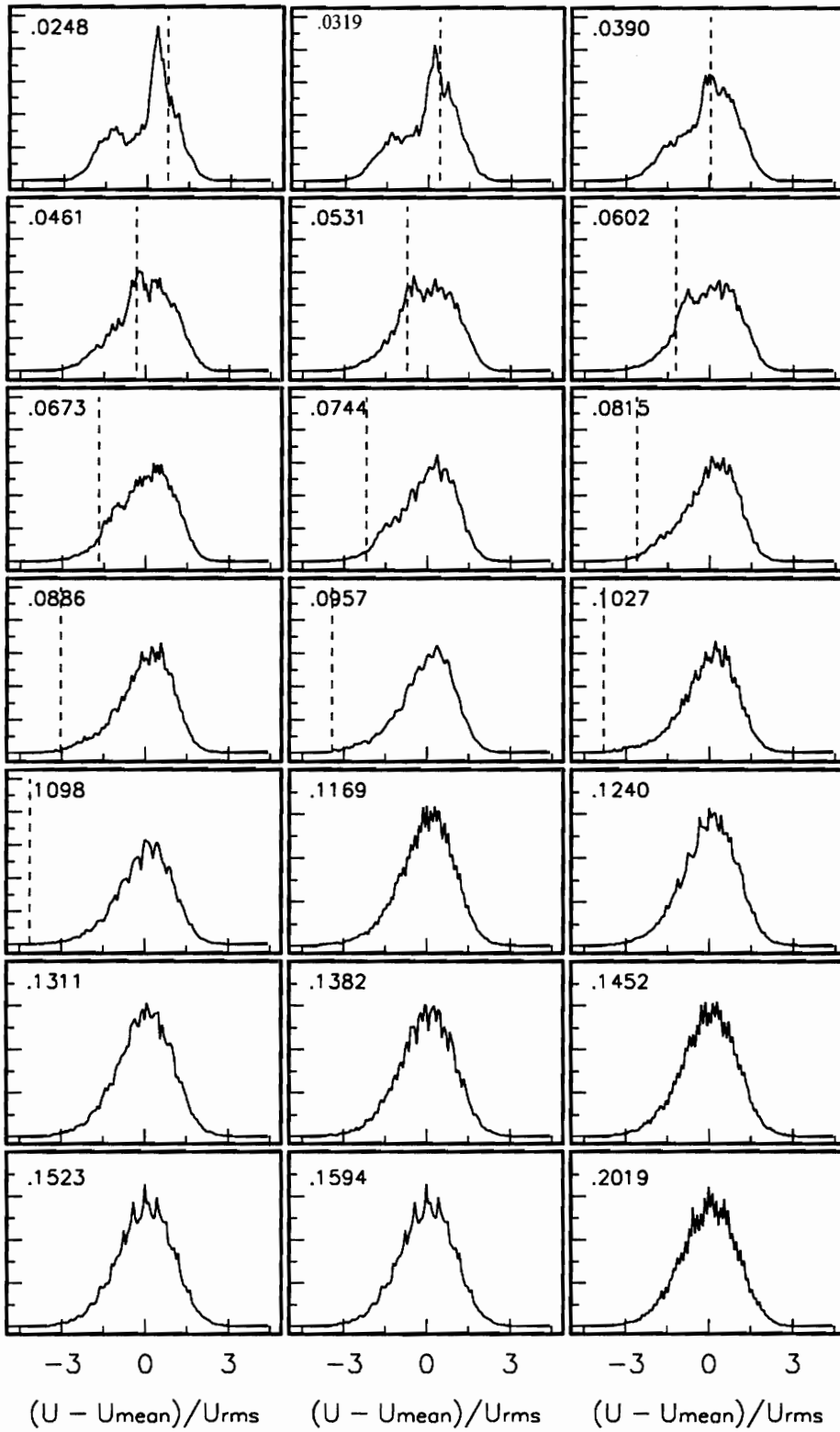


Figure 17. Histograms of U velocity at $x/t=-0.30$. Note: Dashed line is zero velocity.

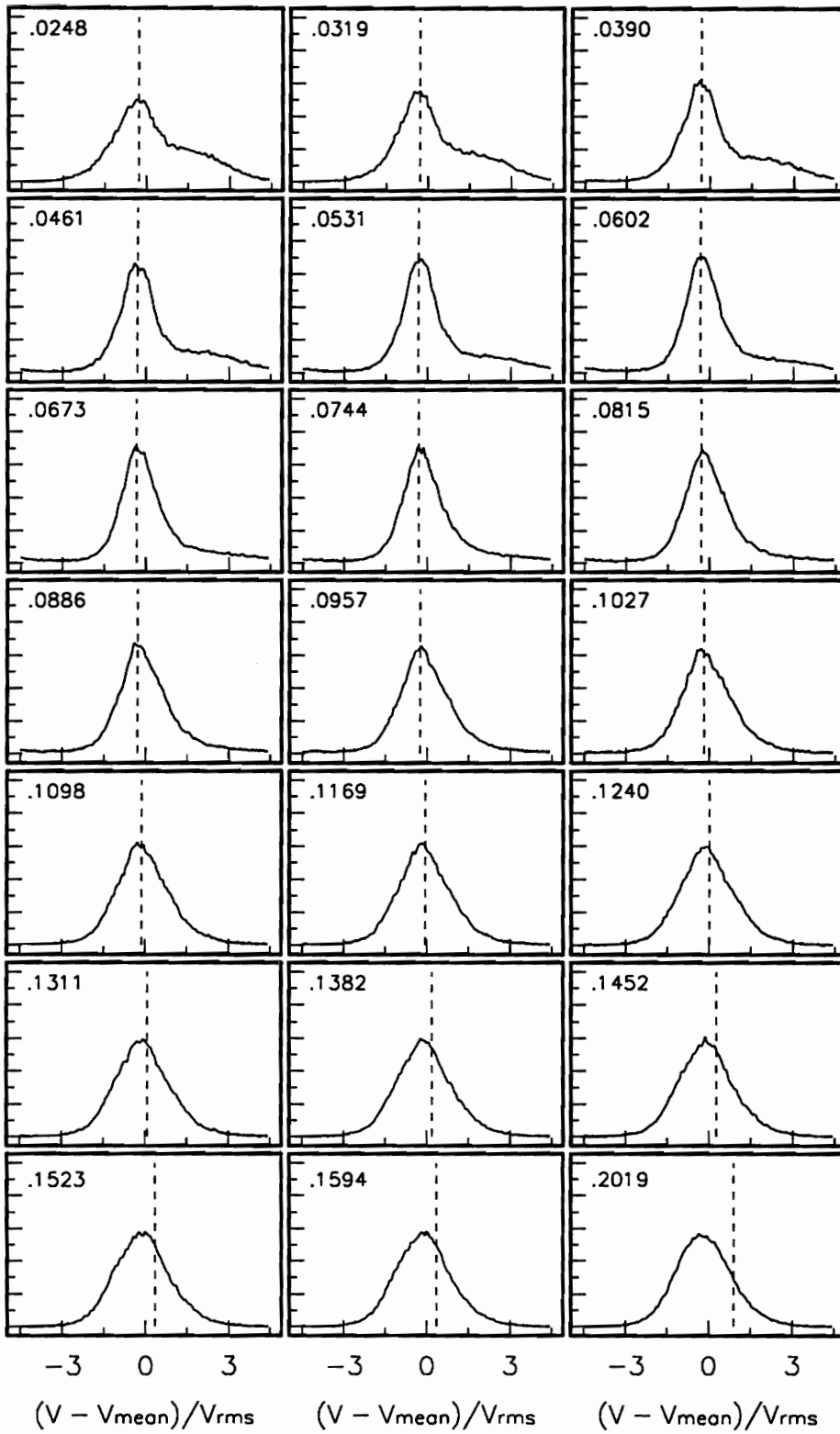


Figure 18. Histograms of V velocity at $x/t=-0.30$. Note: Dashed line is zero velocity.

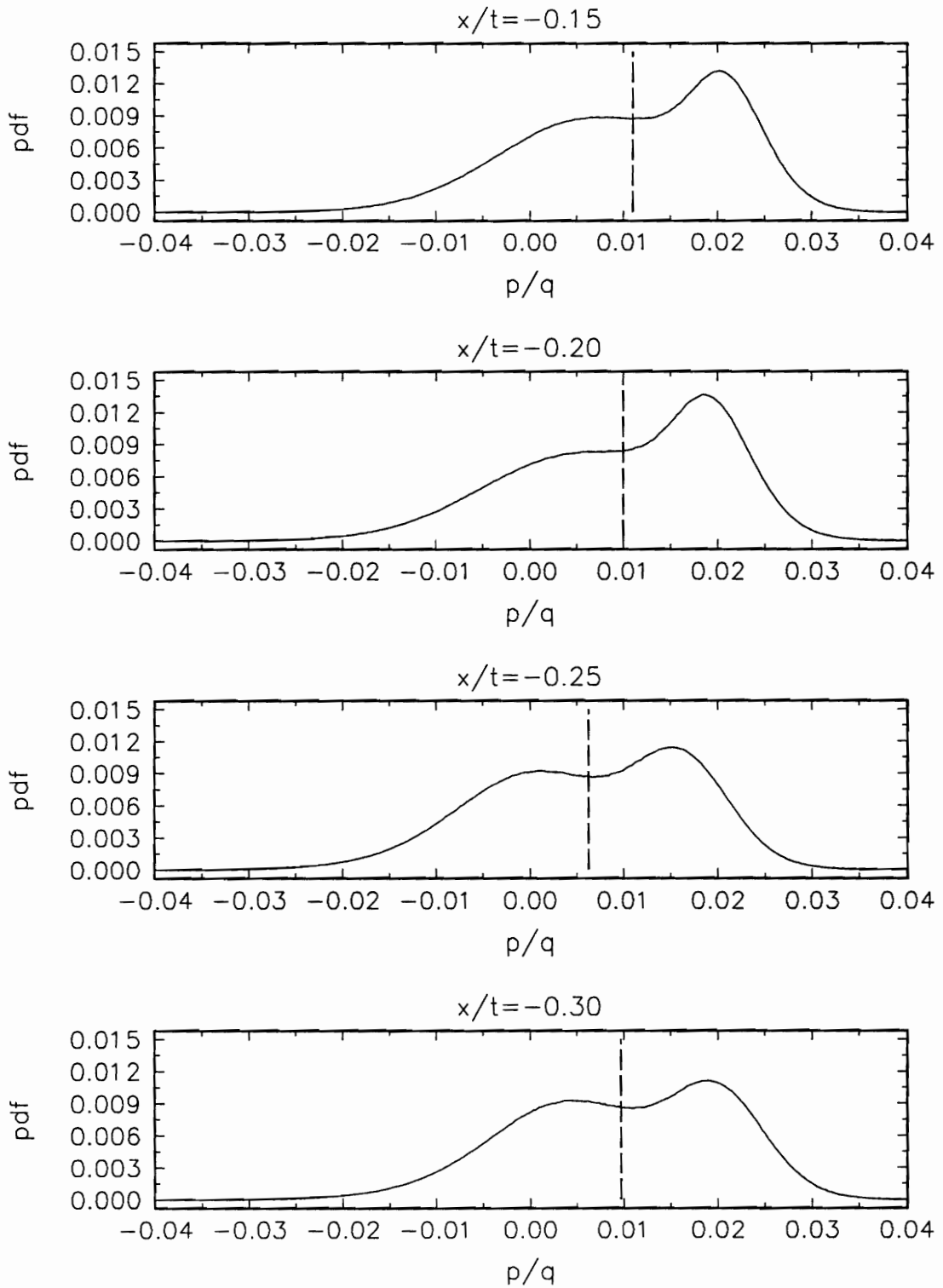


Figure 19. Probability density function of pressure fluctuations measured at $x/t = -0.26$ for each velocity measurement positions. Note: Dashed line is the mean.

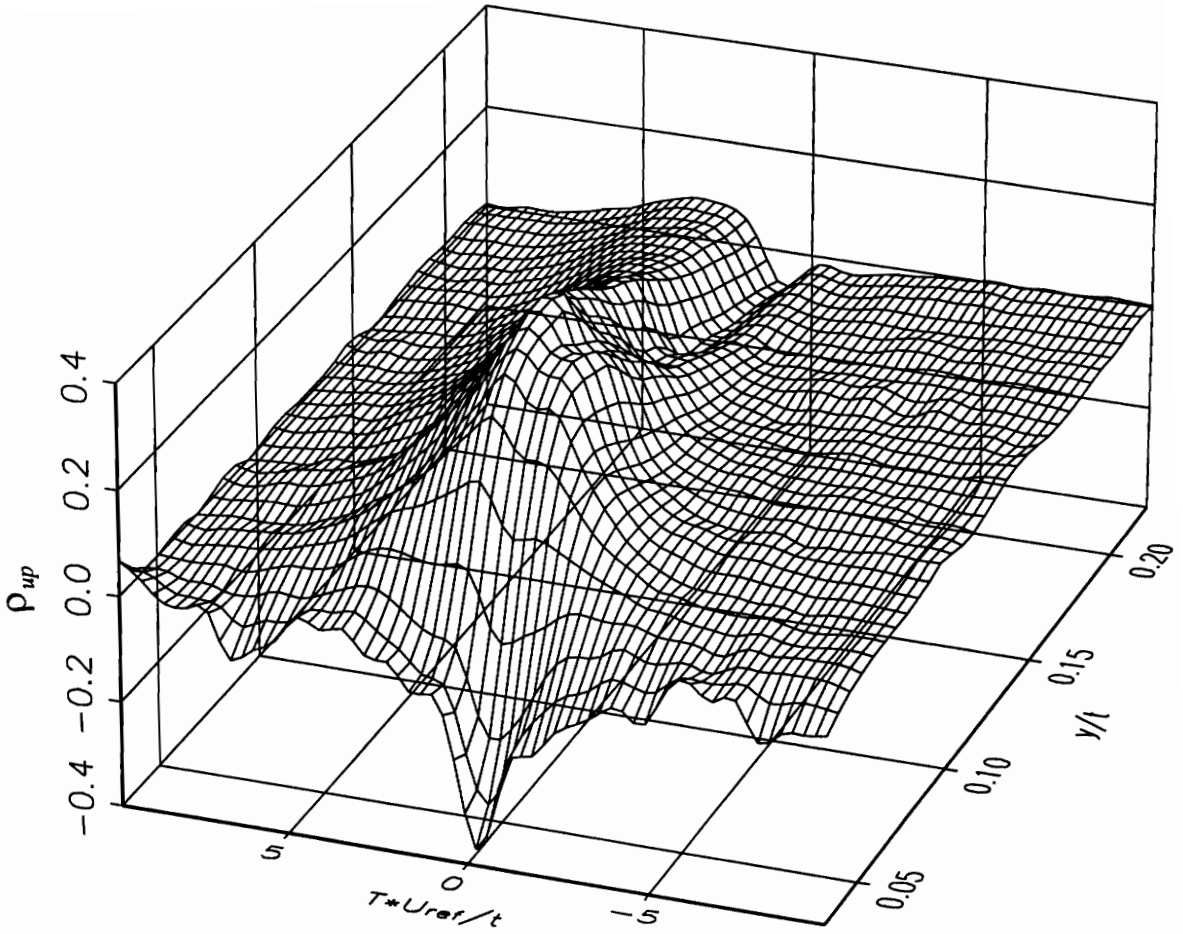


Figure 20. Cross-correlation coefficient function ρ_{up} between u fluctuation at $x/t=-0.15$ and the pressure fluctuations at $x/t=-0.26$.

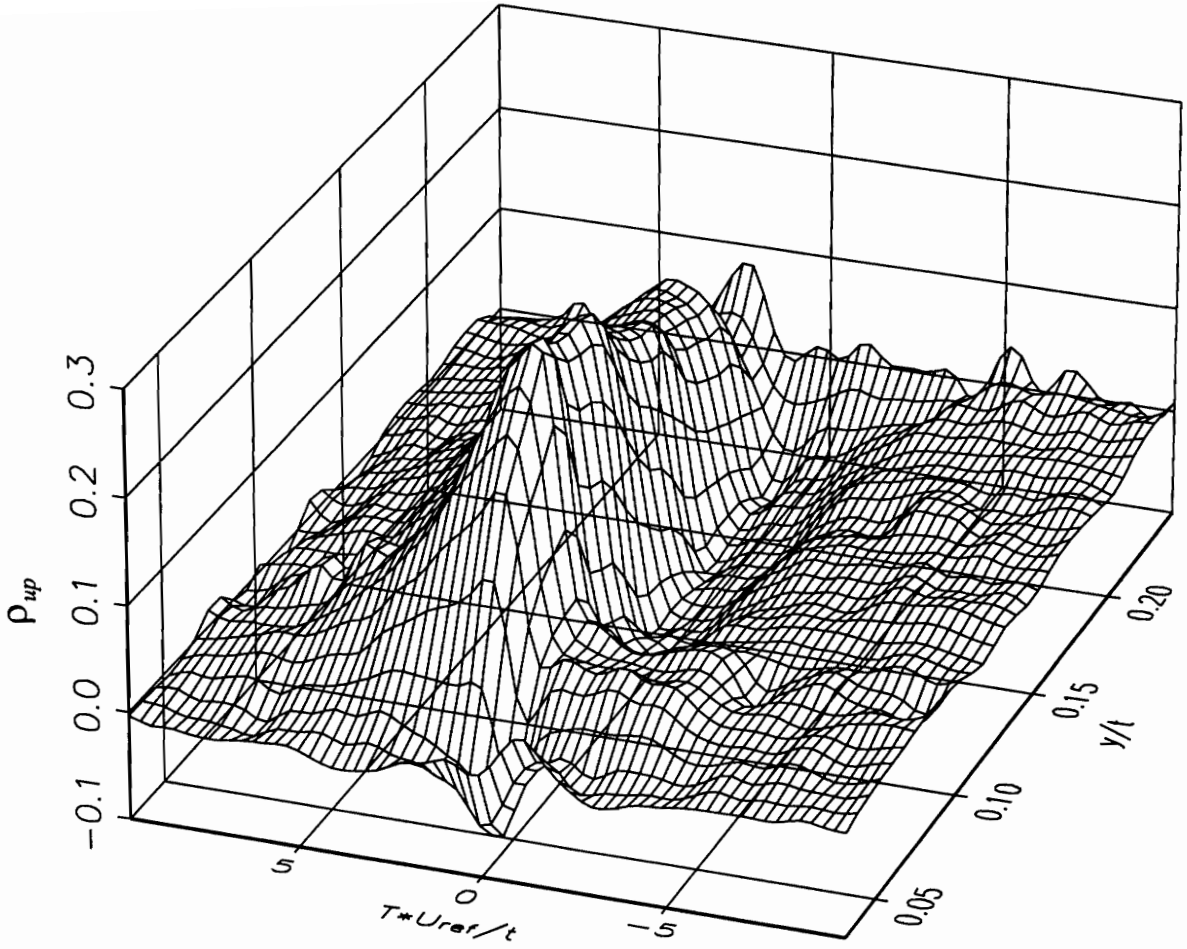


Figure 21. Cross-correlation coefficient function ρ_{up} between u fluctuation at $x/t=-0.20$ and the pressure fluctuations at $x/t=-0.26$.

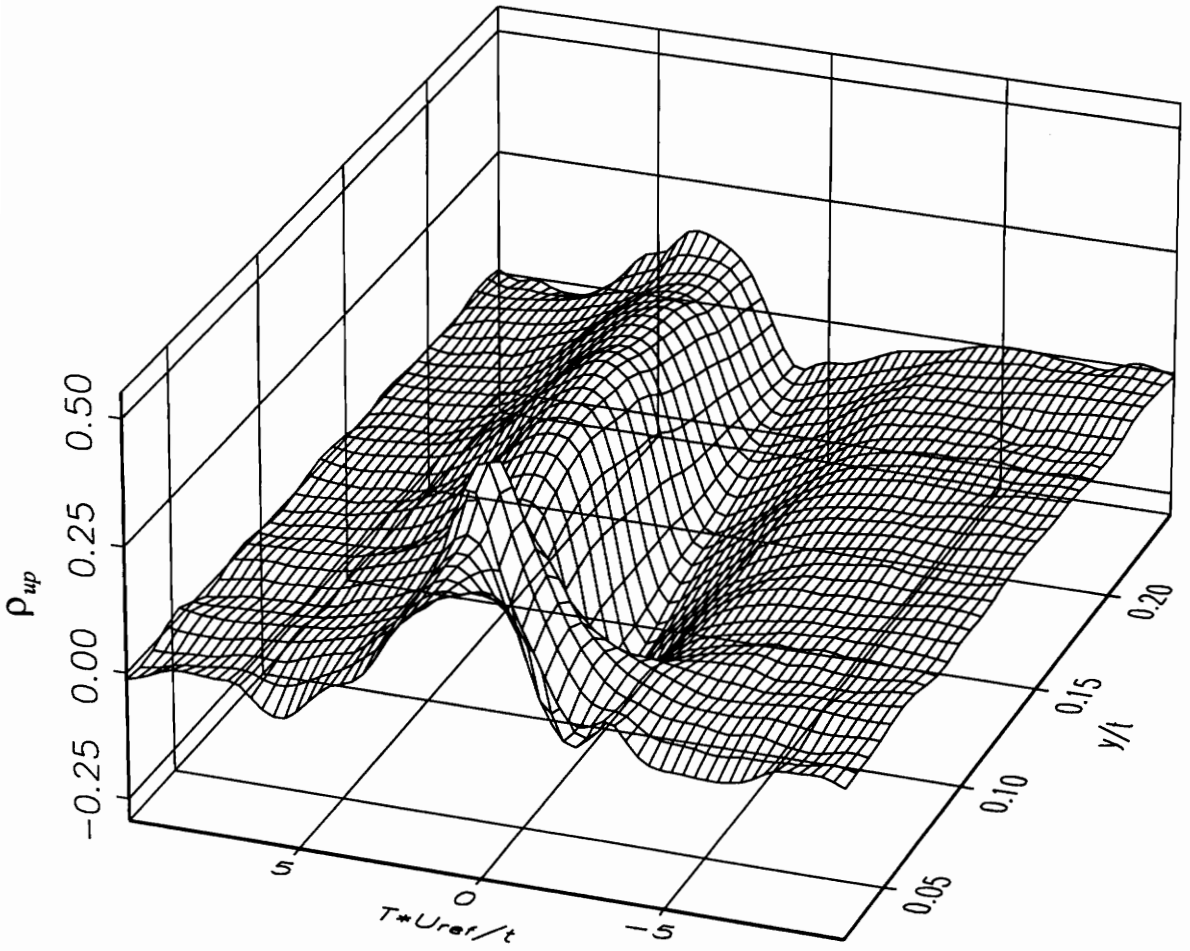


Figure 22. Cross-correlation coefficient function ρ_{up} between u fluctuation at $x/t=-0.25$ and the pressure fluctuations at $x/t=-0.26$.

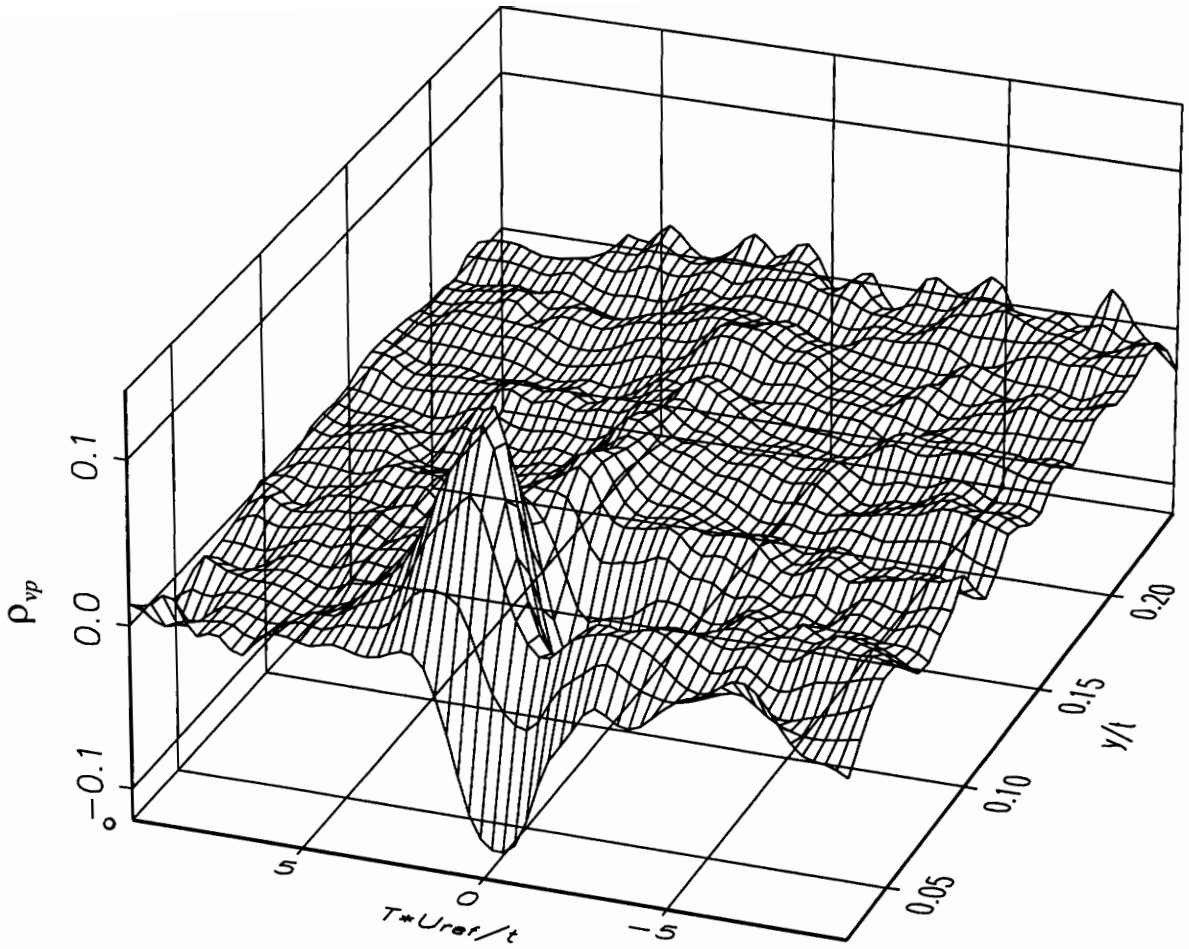


Figure 23. Cross-correlation coefficient function ρ_{vp} between v fluctuation at $x/t=-0.25$ and the pressure fluctuations at $x/t=-0.26$.

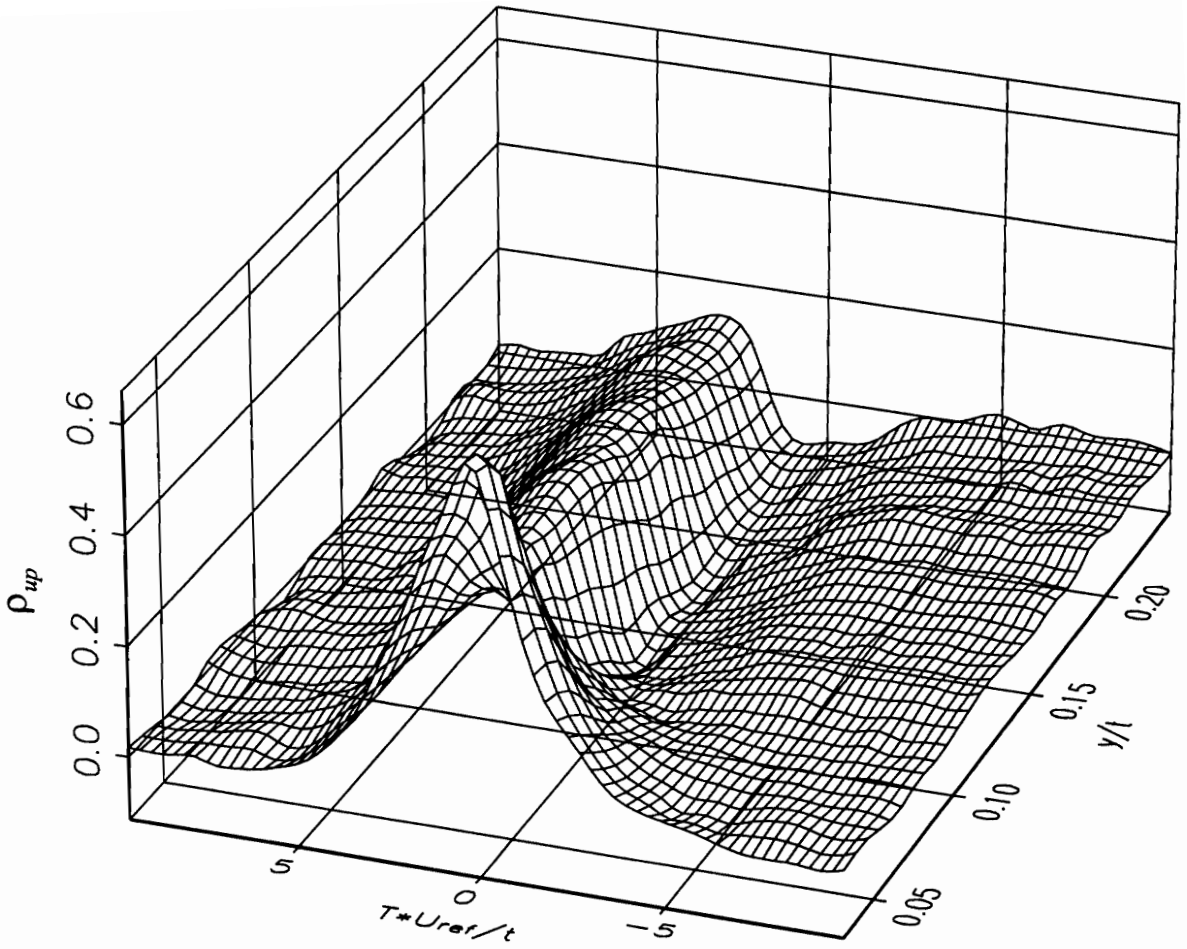


Figure 24. Cross-correlation coefficient function ρ_{up} between u fluctuation at $x/t=-0.30$ and the pressure fluctuations at $x/t=-0.26$.

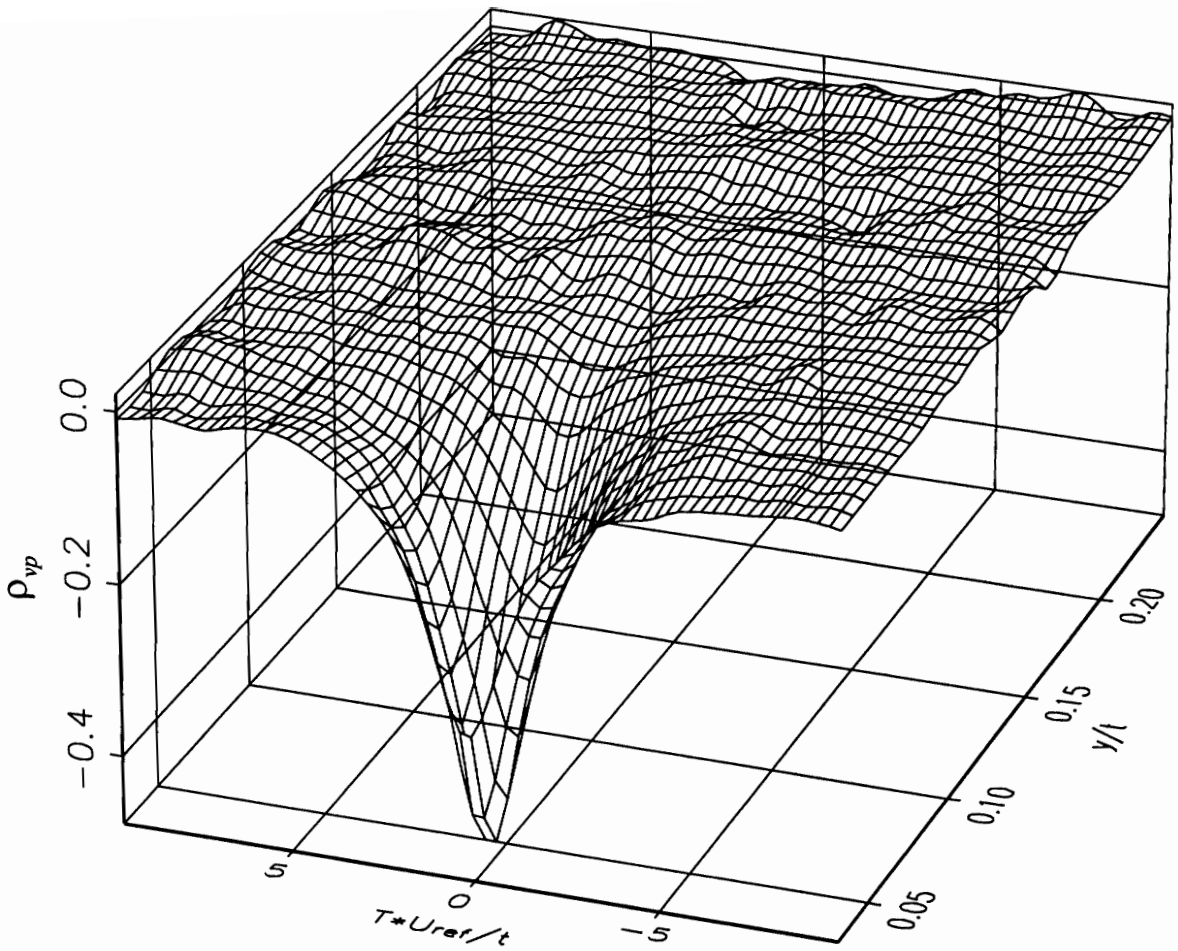


Figure 25. Cross-correlation coefficient function ρ_{vp} between v fluctuation at $x/t=-0.30$ and the pressure fluctuations at $x/t=-0.26$.

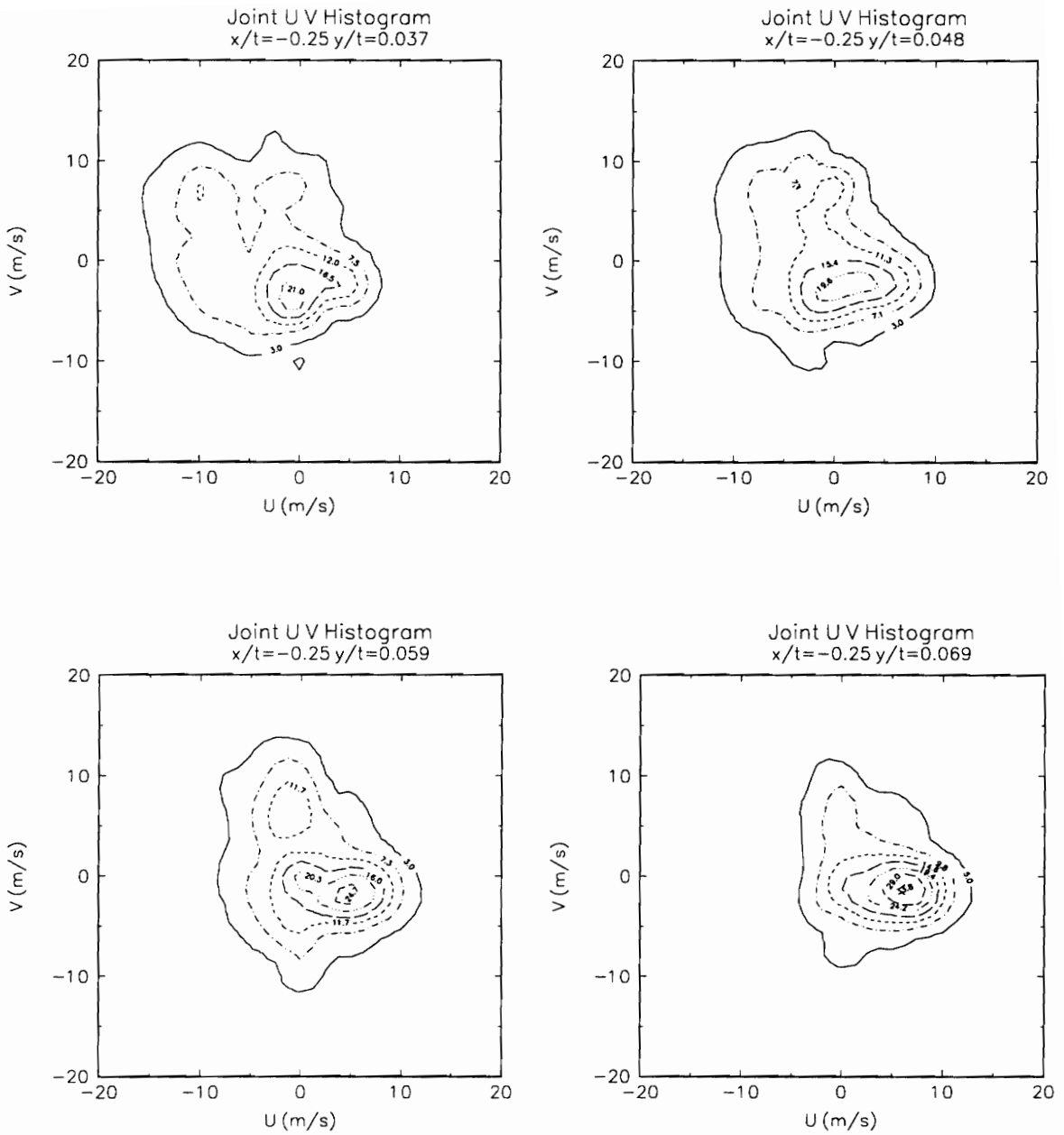


Figure 26. Contours of joint U and V velocity probability density functions for $x/t = -0.25$ at four y locations (note: pdf X 1000).

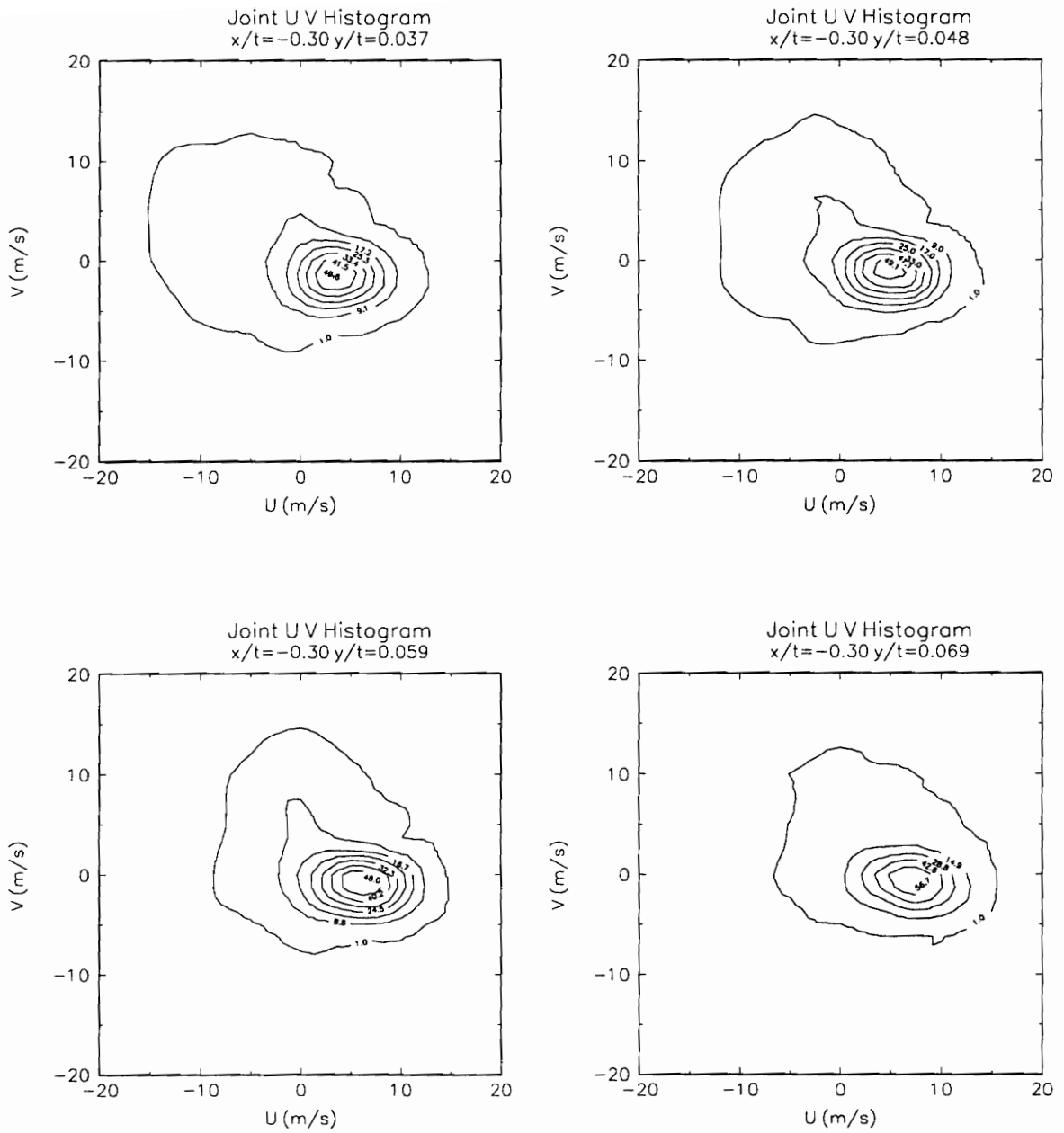


Figure 27. Contours of joint U and V velocity probability density functions for $x/t = -0.30$ at four y/t locations (note: pdf X 1000).

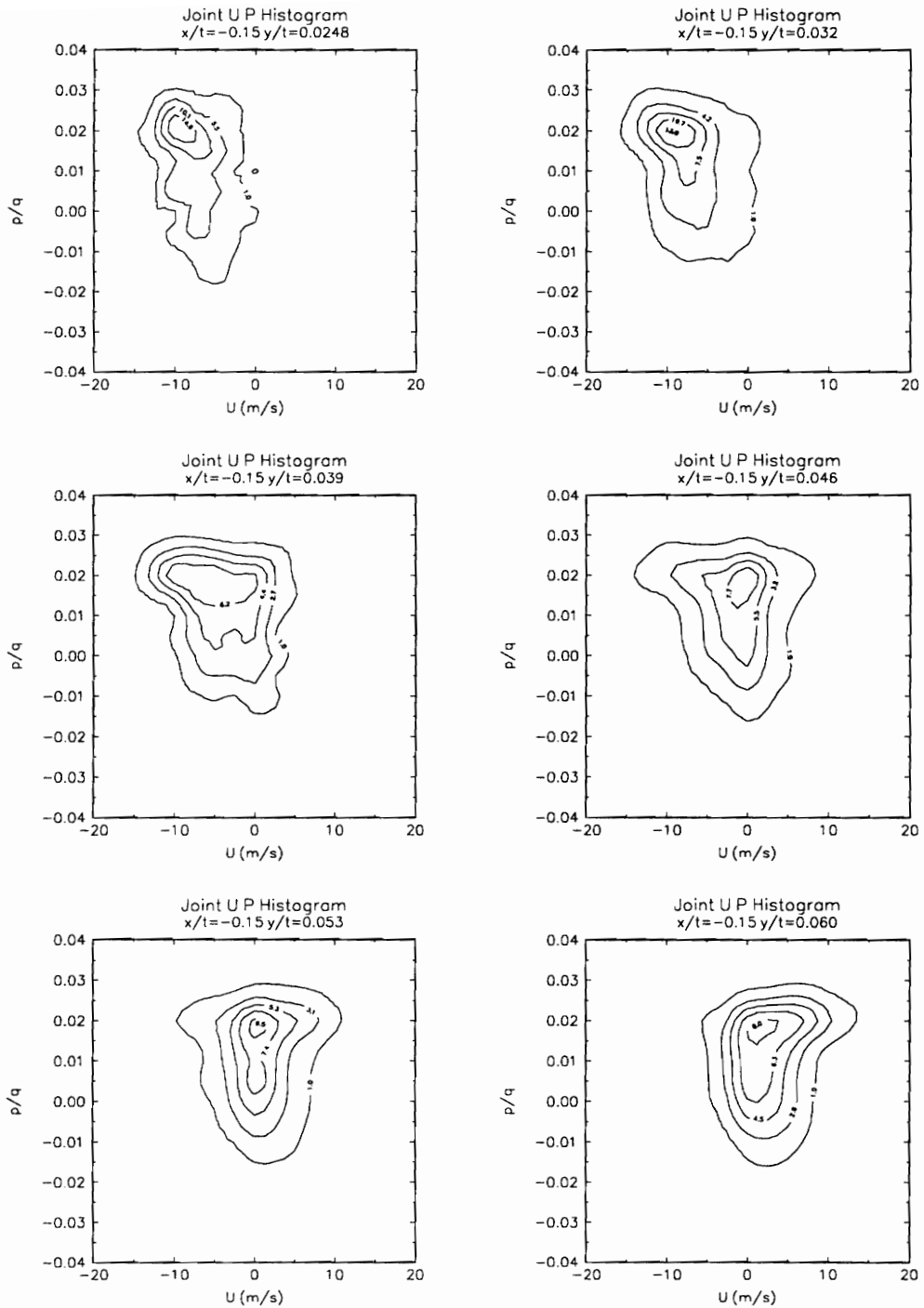


Figure 28. Contours of joint U velocity and surface pressure probability density functions for $x/t = -0.15$ at six y locations (note: pdf X 1000).

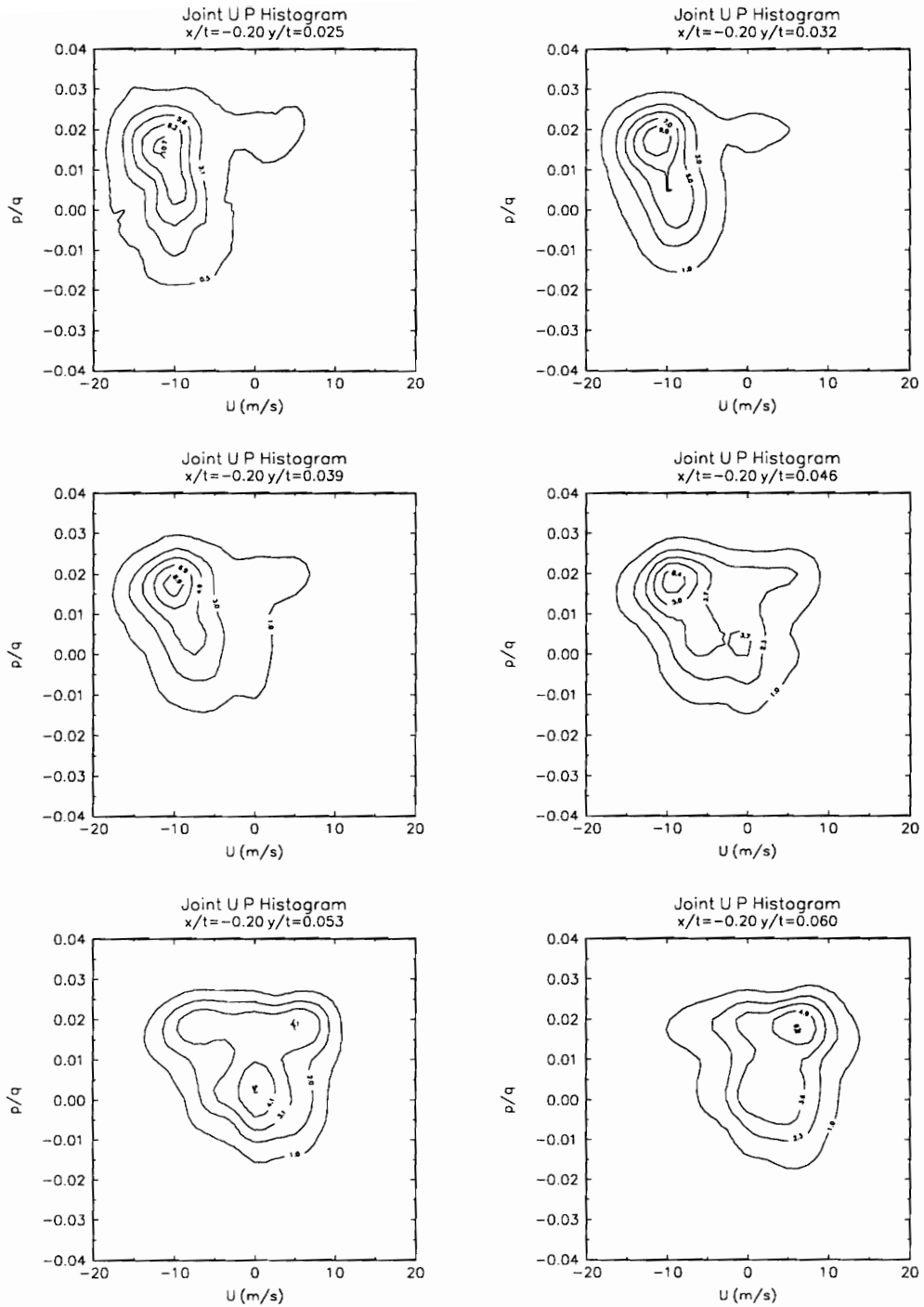


Figure 29. Contours of joint U velocity and surface pressure probability density functions for $x/t = -0.20$ at six y/t locations (note: pdf X 1000).

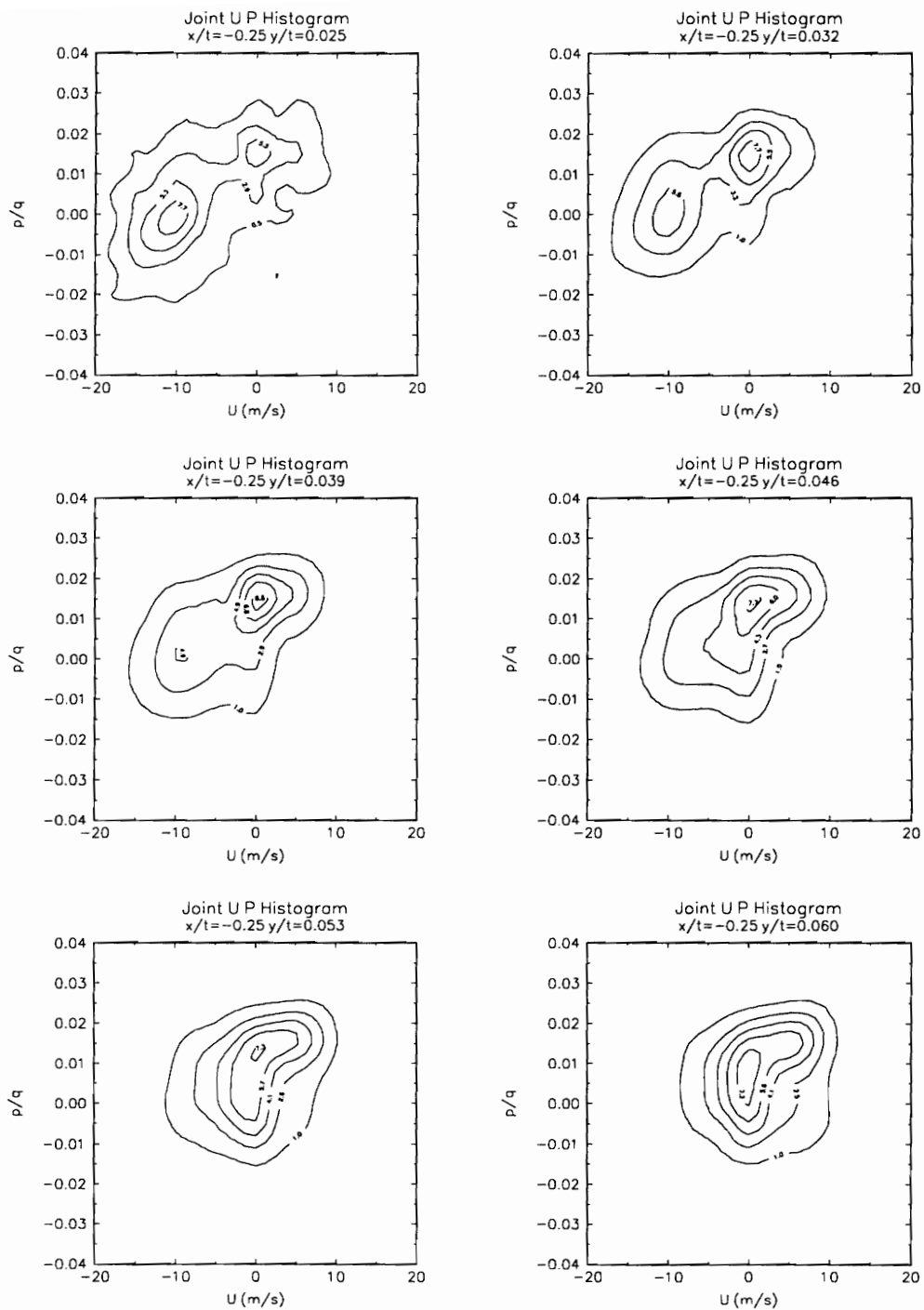


Figure 30. Contours of joint U velocity and surface pressure probability density functions for $x/t = -0.25$ at six y/t locations (note: pdf X 1000).

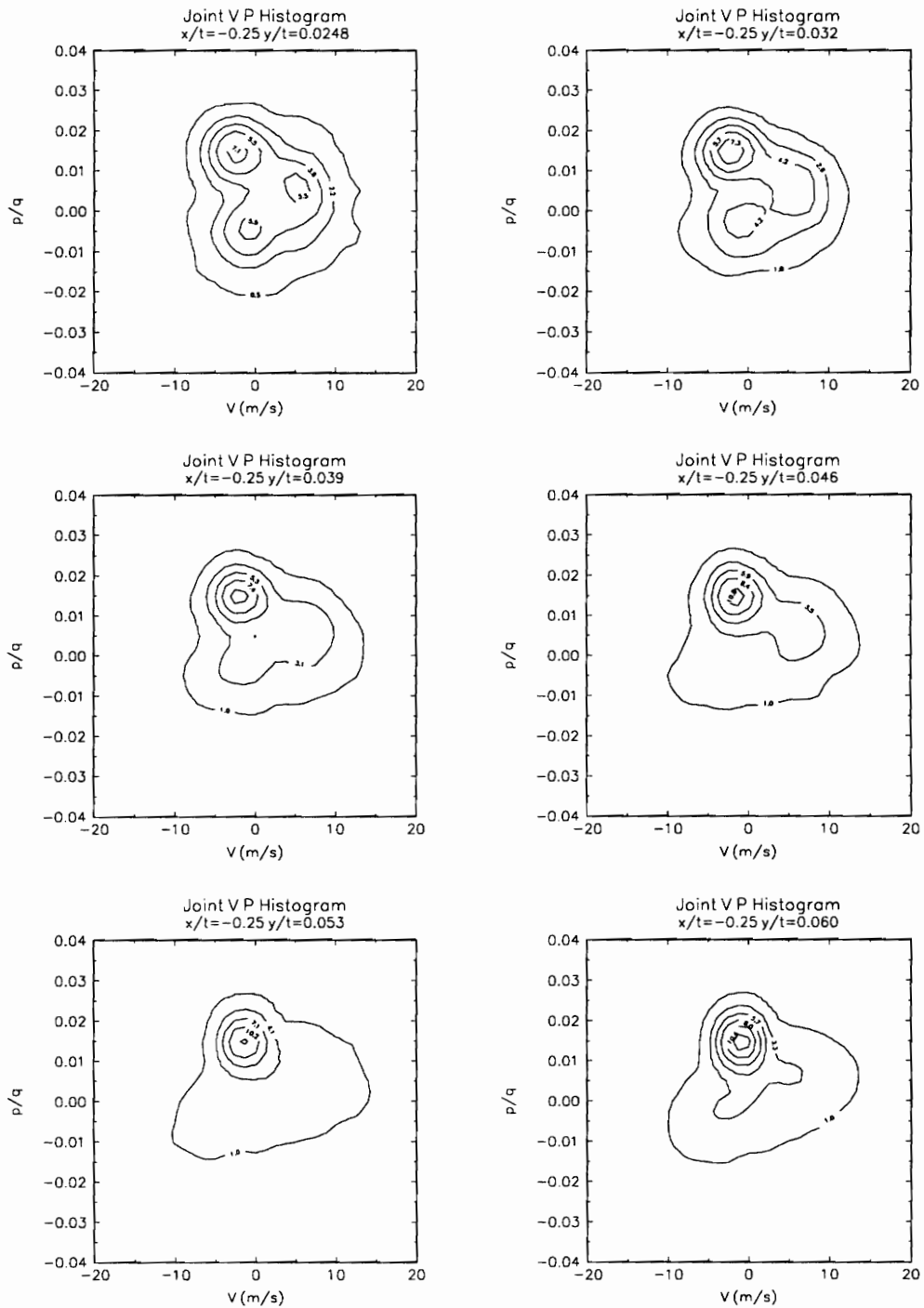


Figure 31. Contours of joint V velocity and surface pressure probability density functions for $x/t = -0.25$ at six y/t locations (note: pdf X 1000).

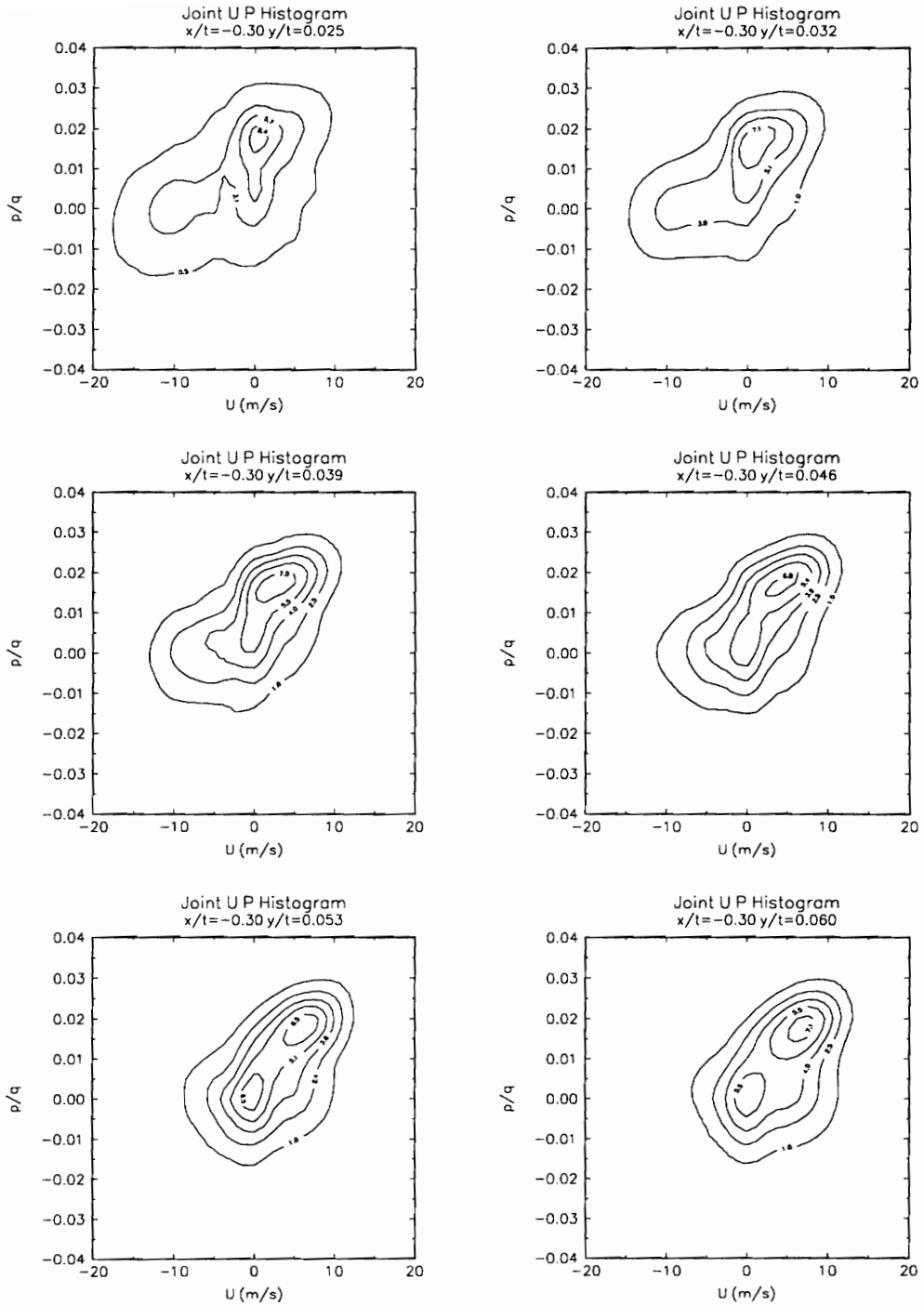


Figure 32. Contours of joint U velocity and surface pressure probability density functions for $x/t = -0.30$ at six y/t locations (note: pdf X 1000).

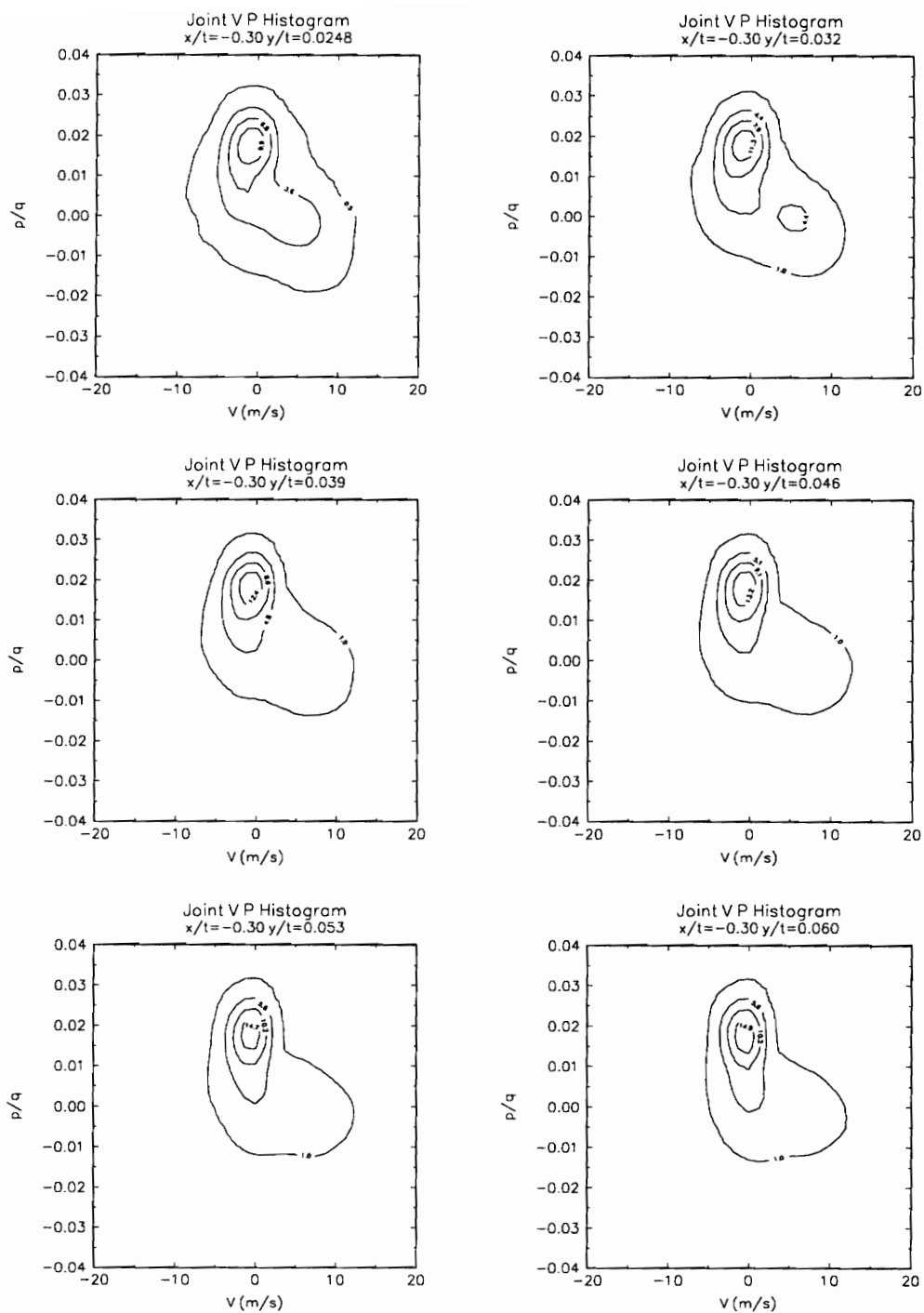


Figure 33. Contours of joint V velocity and surface pressure probability density functions for $x/t=-0.30$ at six y/t locations (note: pdf X 1000).

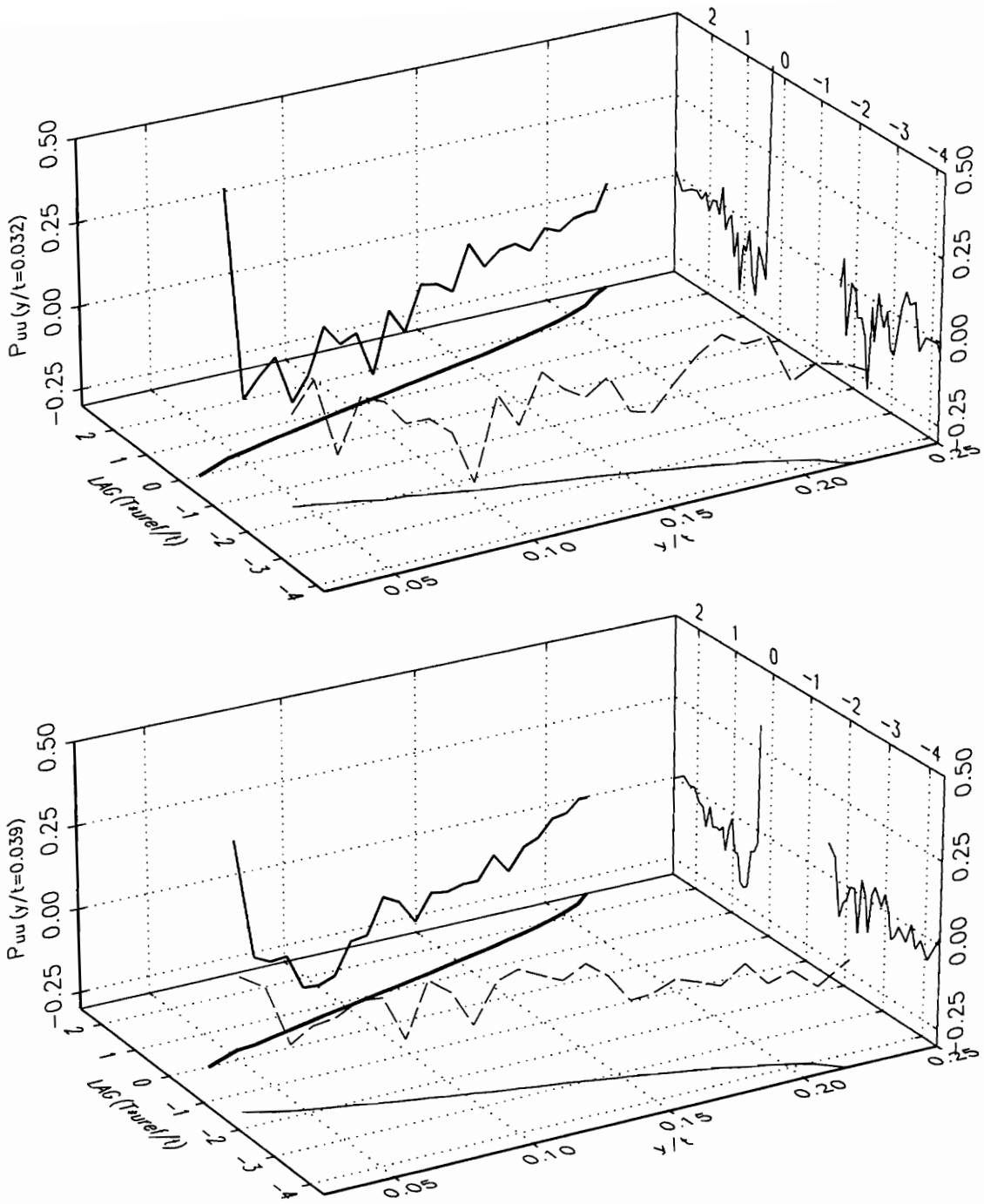


Figure 34. Space-time correlations coefficient ρ_{uu} for u fluctuations between a fixed y location and points along the scan for $x/t = -0.15$. Note: Heavy line is upscan and light line is downscan. Lines on lag- y/t plane are the scan position. Correlation function is projected on lag- ρ_{uu} plane.

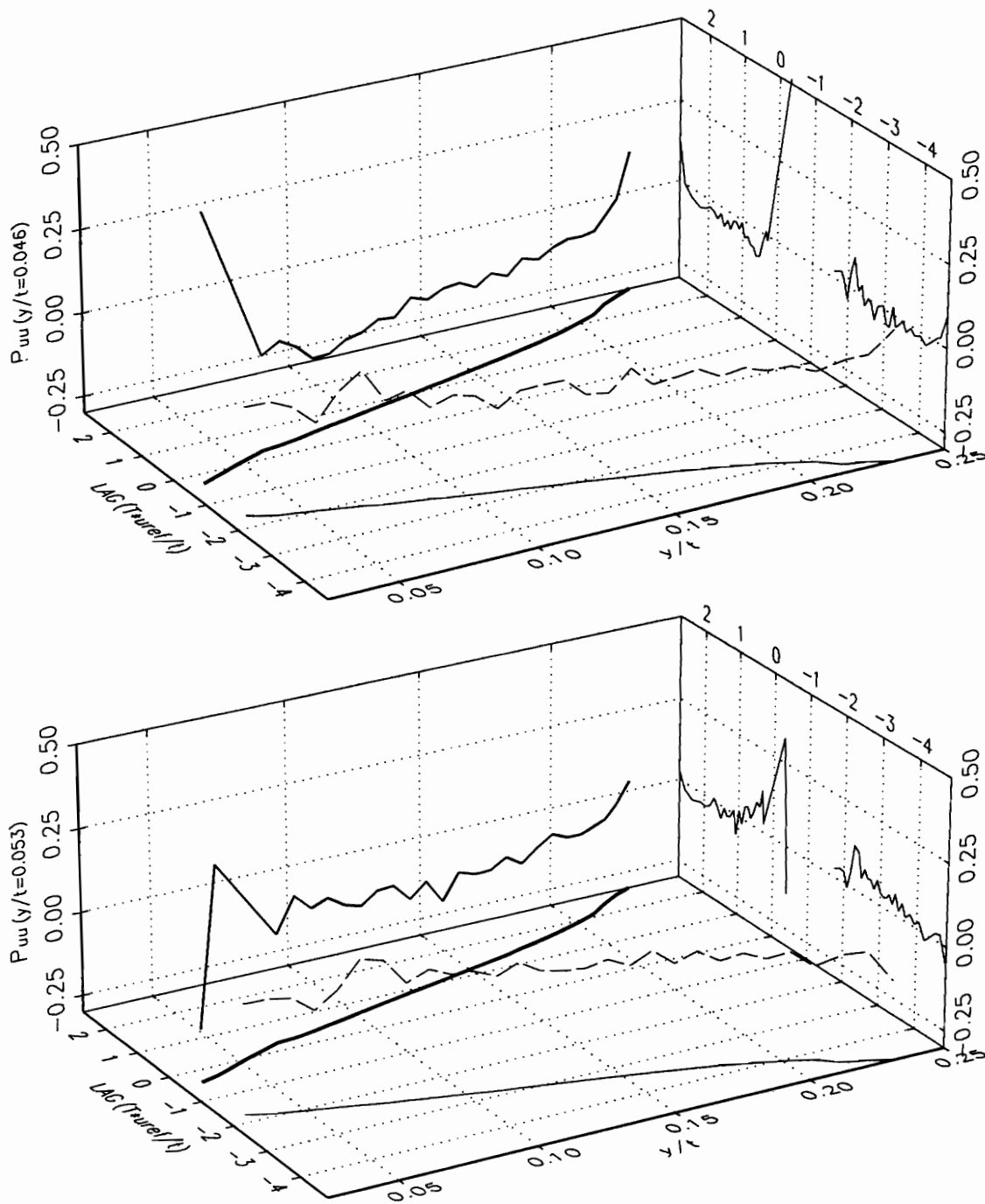


Figure 35. Space-time correlations coefficient ρ_{uu} for u fluctuations between a fixed y location and points along the scan for $x/t=-0.15$. Note: Heavy line is upscan and light line is downscan. Lines on lag- y/t plane are the scan position. Correlation function is projected on lag- ρ_{uu} plane.

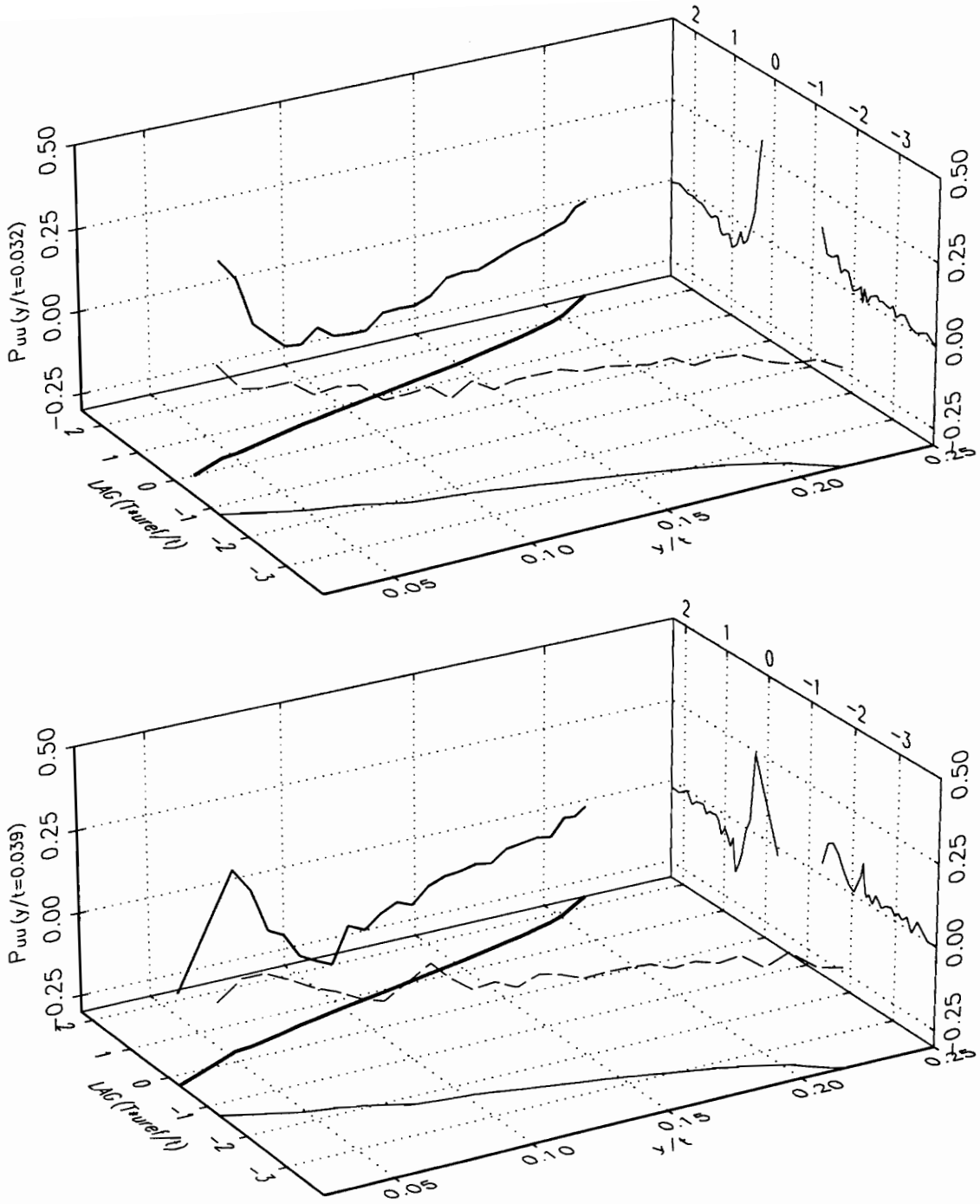


Figure 36. Space-time correlations coefficient ρ_{uu} for u fluctuations between a fixed y location and points along the scan for $x/t = -0.20$. Note: Heavy line is upscan and light line is downscan. Lines on lag- y/t plane are the scan position. Correlation function is projected on lag- ρ_{uu} plane.

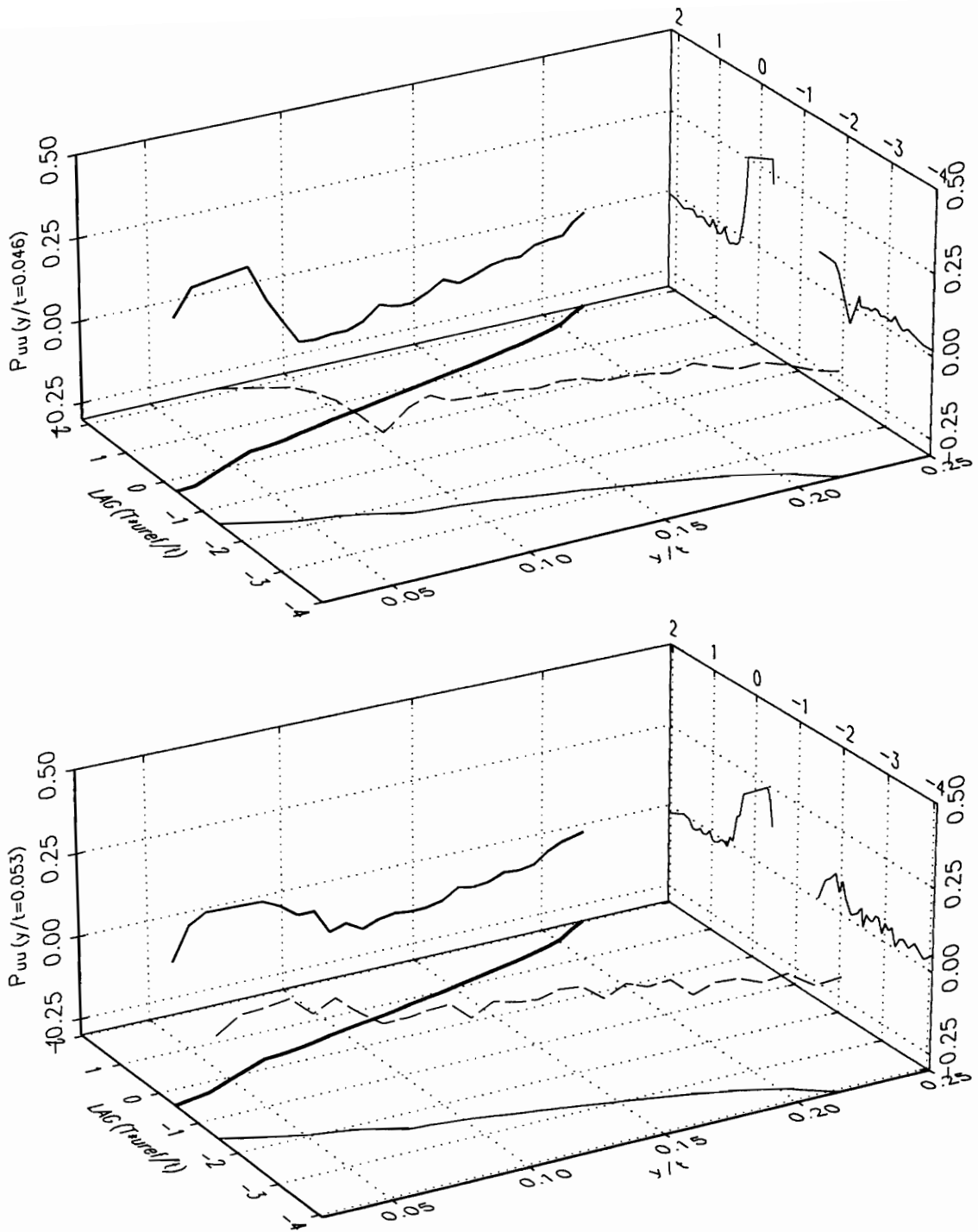


Figure 37. Space-time correlations coefficient ρ_{uu} for u fluctuations between a fixed y location and points along the scan for $x/t = -0.20$. Note: Heavy line is upscan and light line is downscan. Lines on lag- y/t plane are the scan position. Correlation function is projected on lag- ρ_{uu} plane.

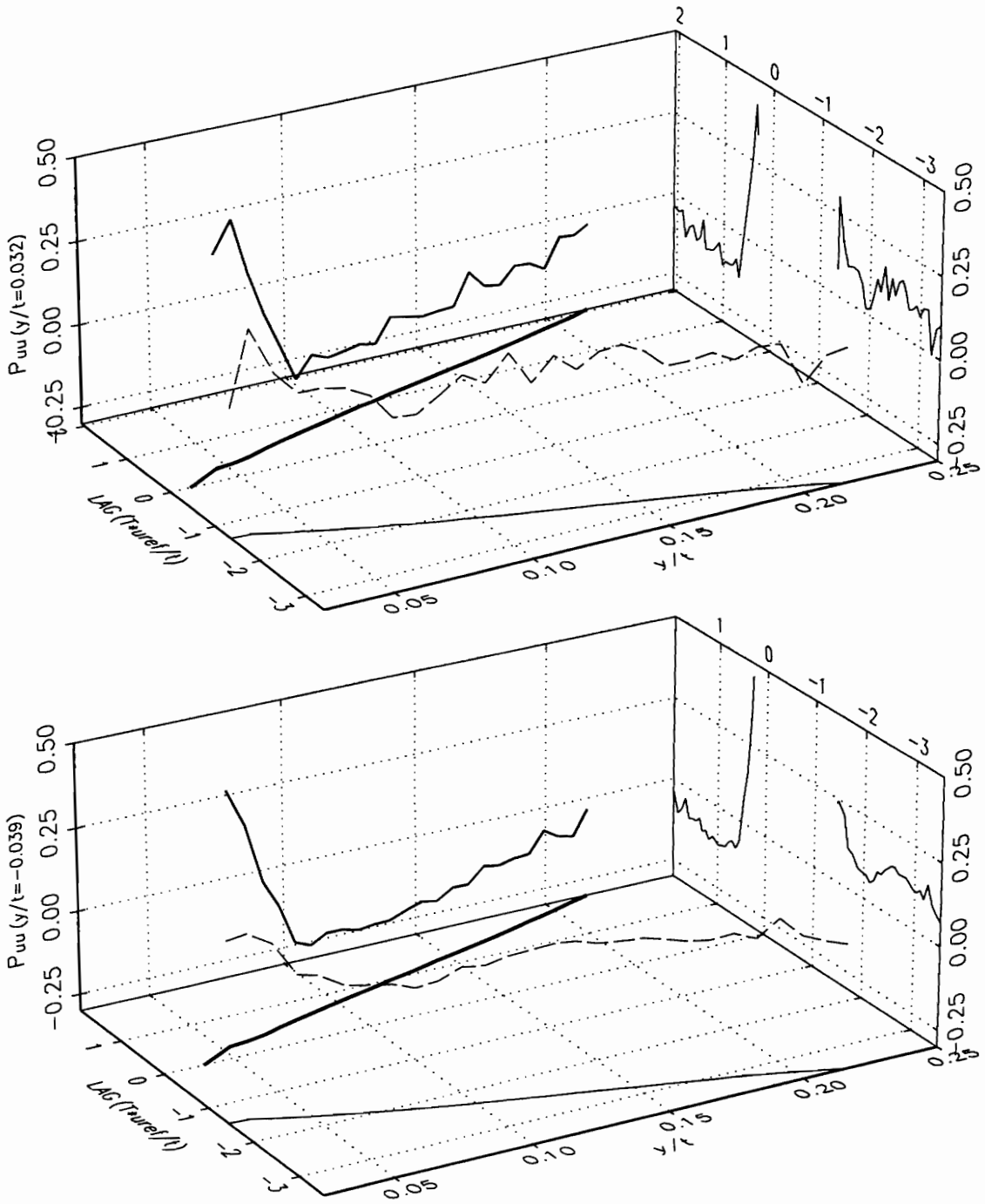


Figure 38. Space-time correlations coefficient ρ_{uu} for u fluctuations between a fixed y location and points along the scan for $x/t = -0.25$. Note: Heavy line is upscan and light line is downscan. Lines on lag- y/t plane are the scan position. Correlation function is projected on lag- ρ_{uu} plane.

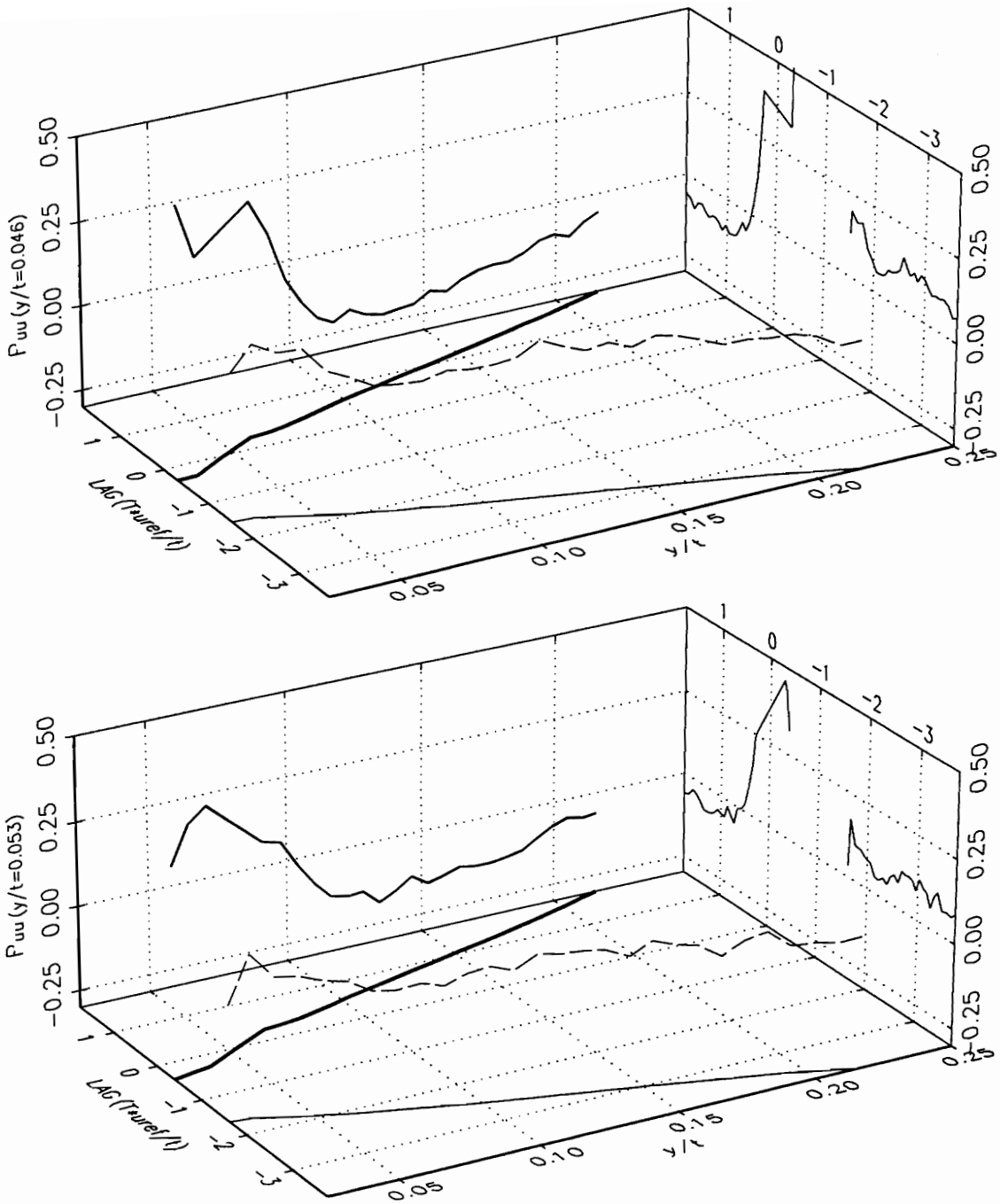


Figure 39. Space-time correlations coefficient ρ_{uu} for u fluctuations between a fixed y location and points along the scan for $x/t=-0.25$. Note: Heavy line is upscan and light line is downscan. Lines on lag- y/t plane are the scan position. Correlation function is projected on lag- ρ_{uu} plane.

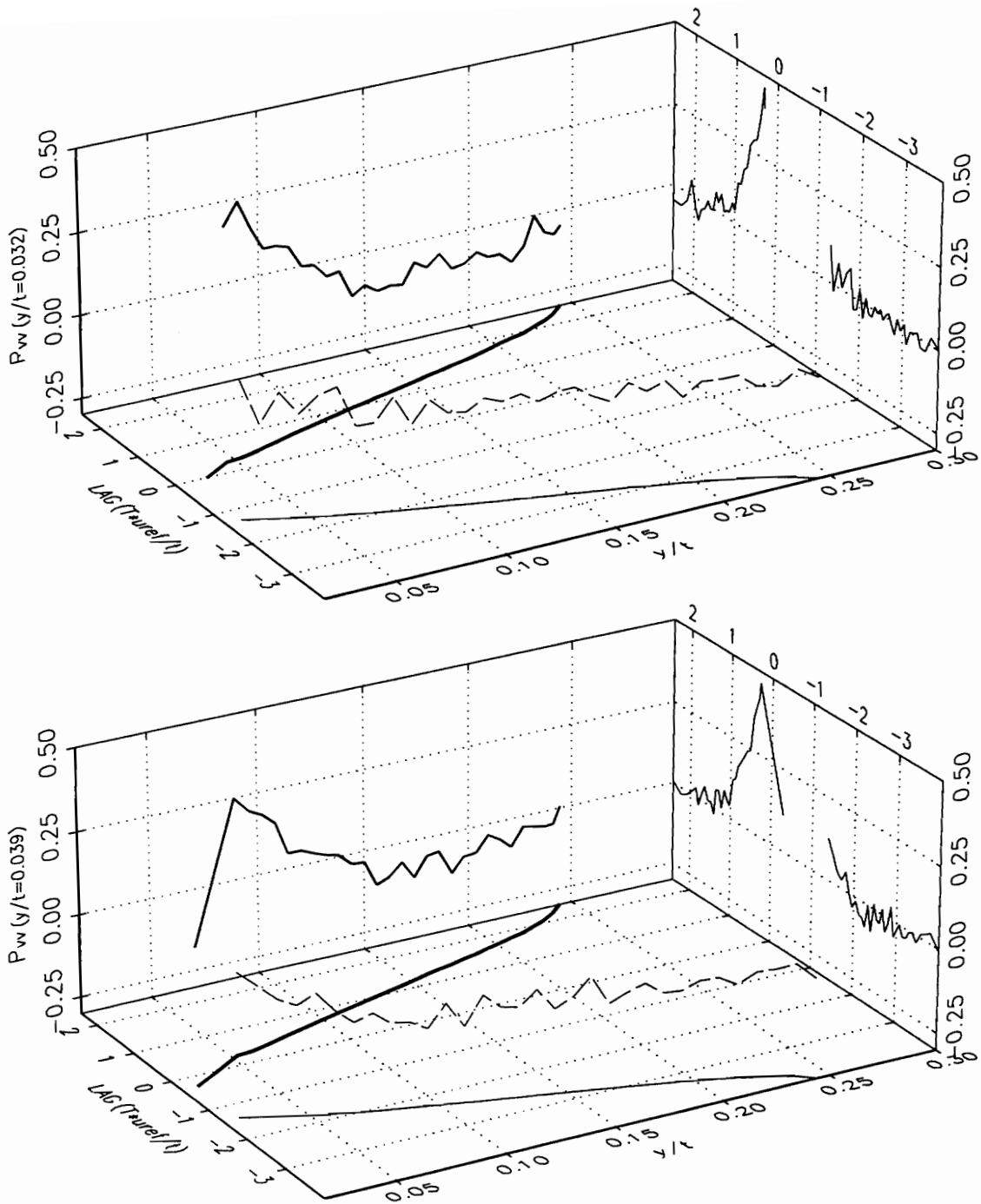


Figure 40. Space-time correlations coefficient ρ_{vv} for v fluctuations between a fixed y location and points along the scan for $x/t = -0.25$. Note: Heavy line is upscan and light line is downscan. Lines on lag- y/t plane are the scan position. Correlation function is projected on lag- ρ_{vv} plane.

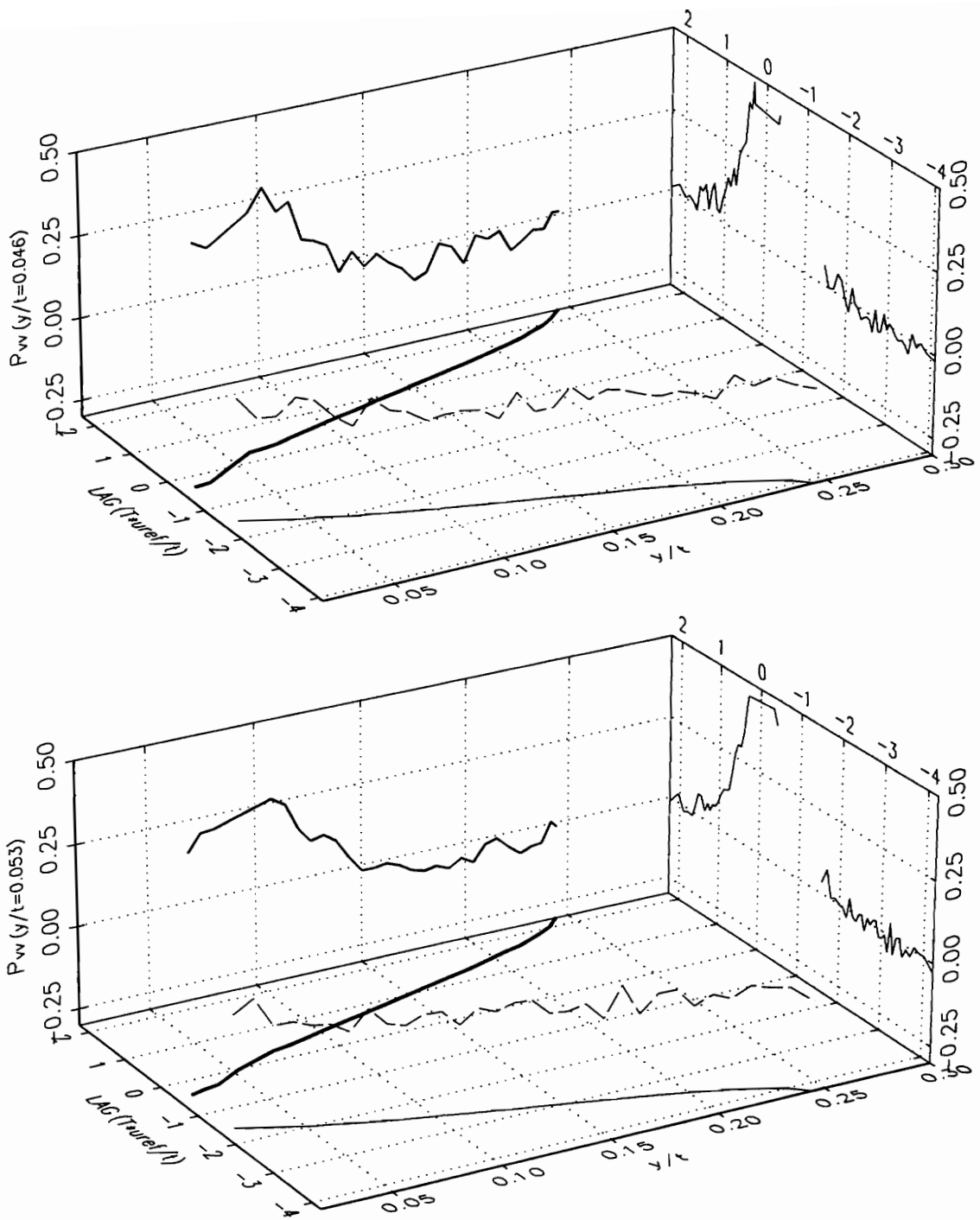


Figure 41. Space-time correlations coefficient ρ_{vv} for v fluctuations between a fixed y location and points along the scan for $x/t=-0.25$. Note: Heavy line is upscan and light line is downscan. Lines on lag- y/t plane are the scan position. Correlation function is projected on lag- ρ_{vv} plane.

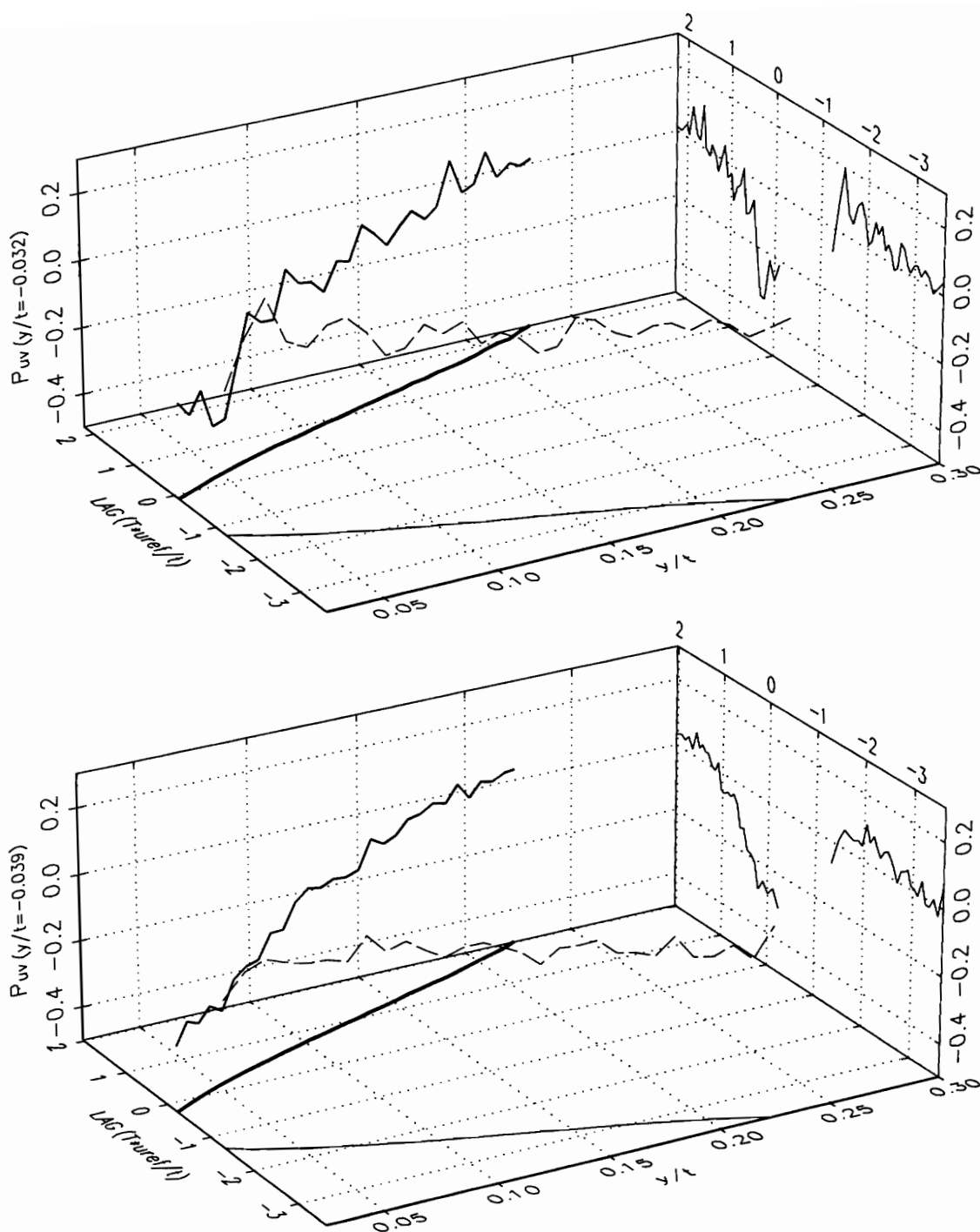


Figure 42. Space-time correlations coefficient ρ_{uv} for u fluctuations between a fixed y location and v fluctuations along the scan for $x/t = -0.25$. Note: Heavy line is upscan and light line is downscan. Lines on lag- y/t plane are the scan position. Correlation function is projected on lag- ρ_{uv} plane.

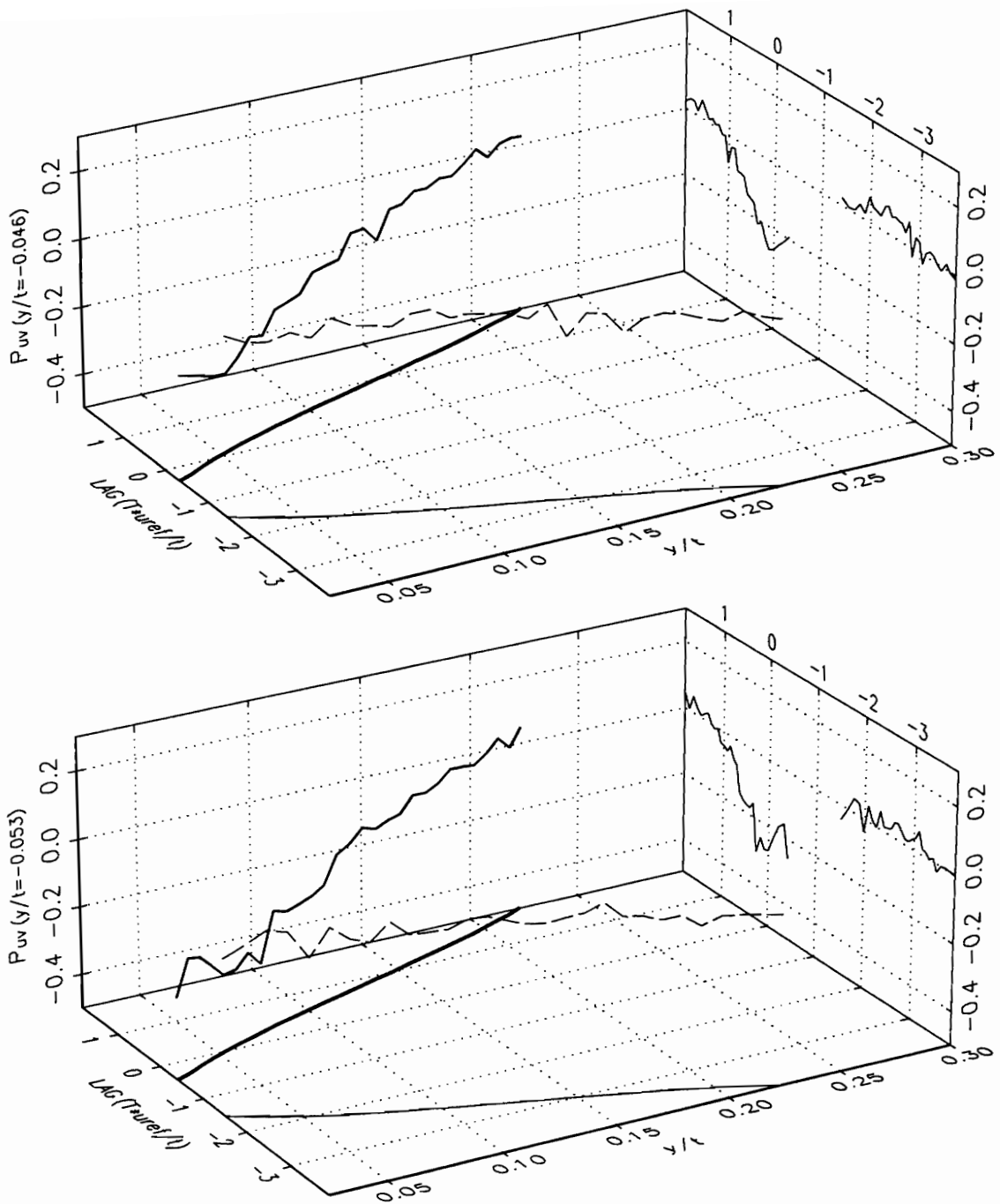


Figure 43. Space-time correlations coefficient ρ_{uv} for u fluctuations between a fixed y location and v fluctuations along the scan for $x/t = -0.25$. Note: Heavy line is upscan and light line is downscan. Lines on lag- y/t plane are the scan position. Correlation function is projected on lag- ρ_{uv} plane.

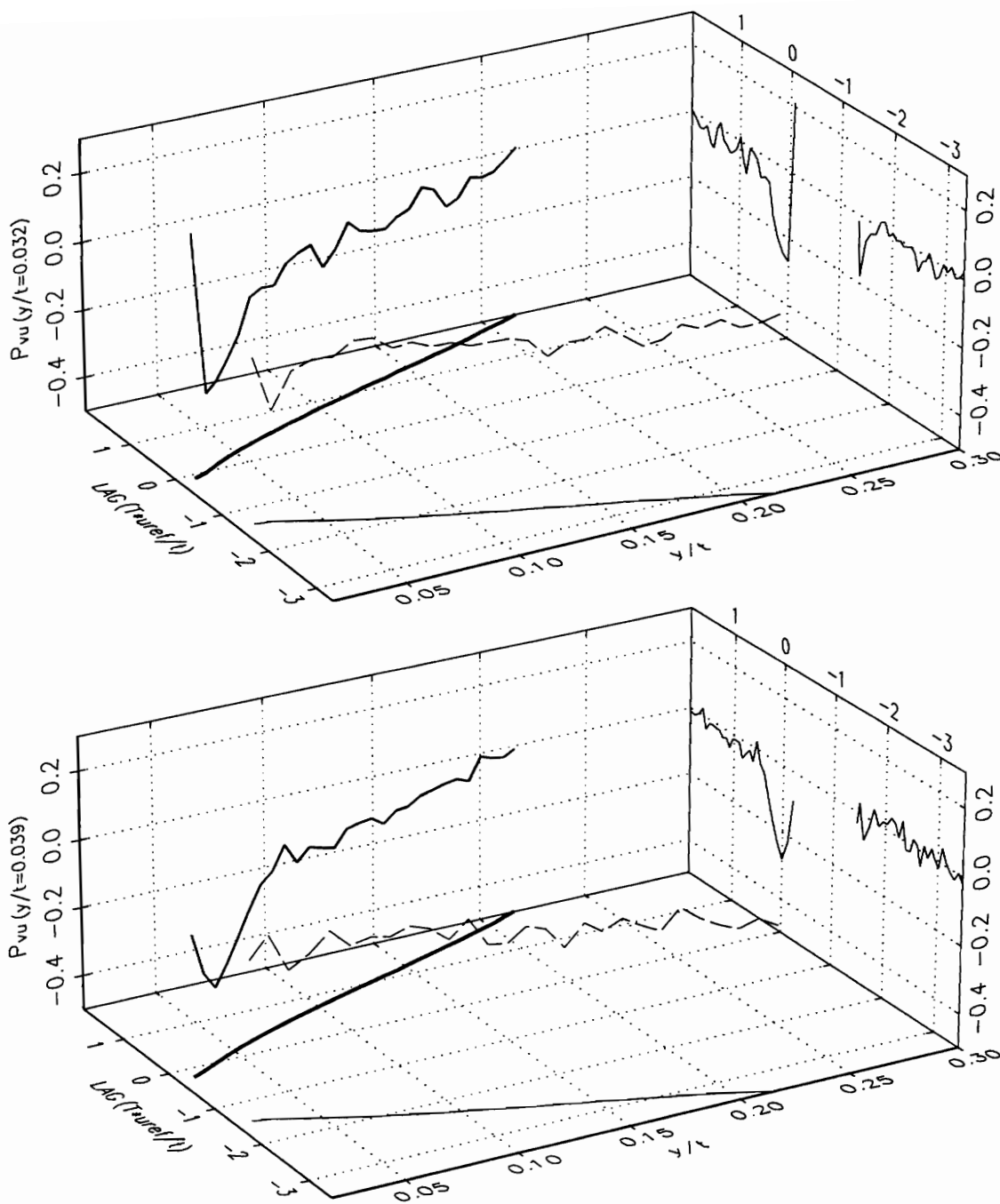


Figure 44. Space-time correlations coefficient ρ_{vu} for v fluctuations between a fixed y location and u fluctuations along the scan for $x/t=-0.25$. Note: Heavy line is upscan and light line is downscan. Lines on lag- y/t plane are the scan position. Correlation function is projected on lag- ρ_{vu} plane.

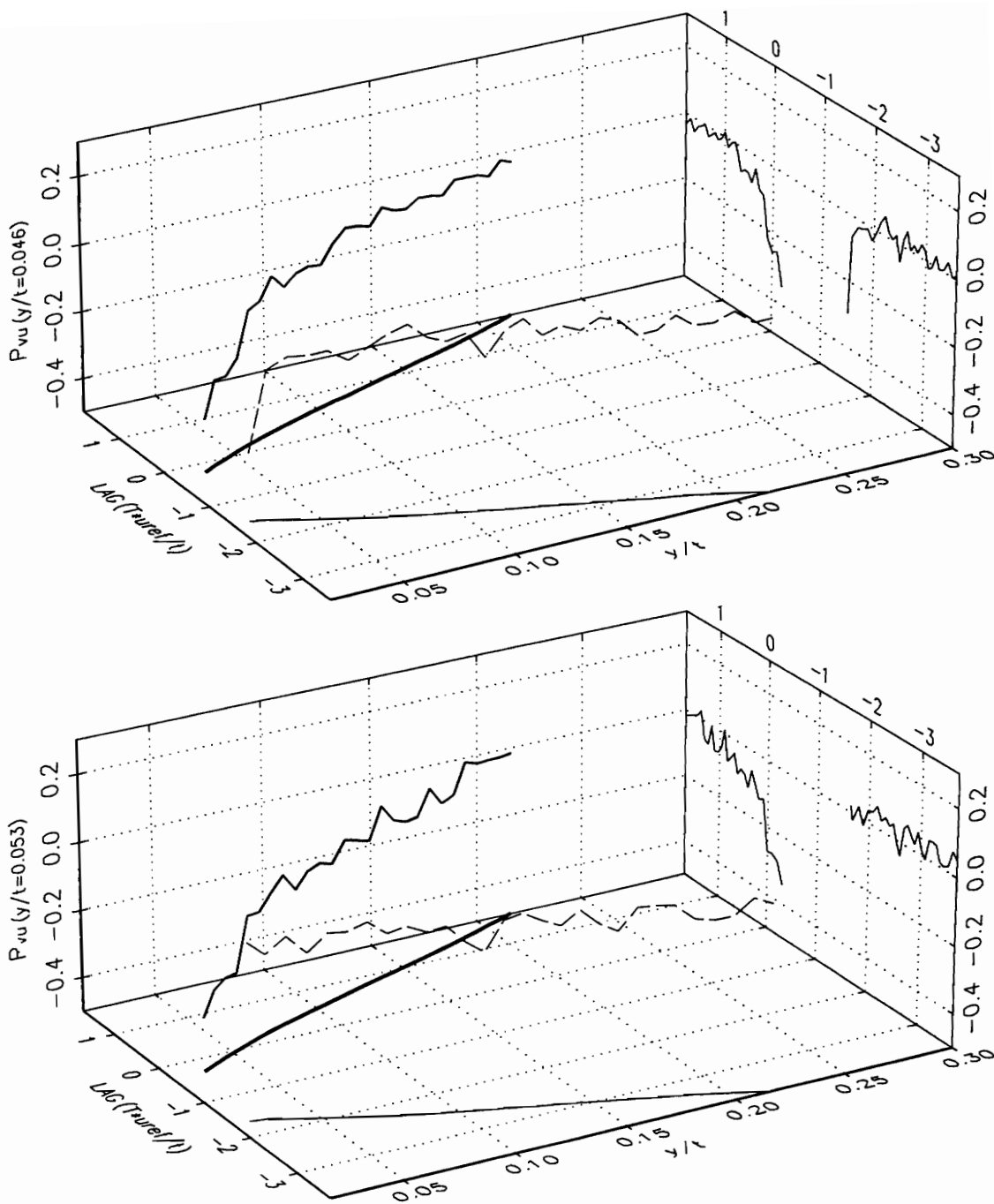


Figure 45. Space-time correlations coefficient ρ_{vu} for v fluctuations between a fixed y location and u fluctuations along the scan for $x/t = -0.25$. Note: Heavy line is upscan and light line is downscan. Lines on lag- y/t plane are the scan position. Correlation function is projected on lag- ρ_{vu} plane.

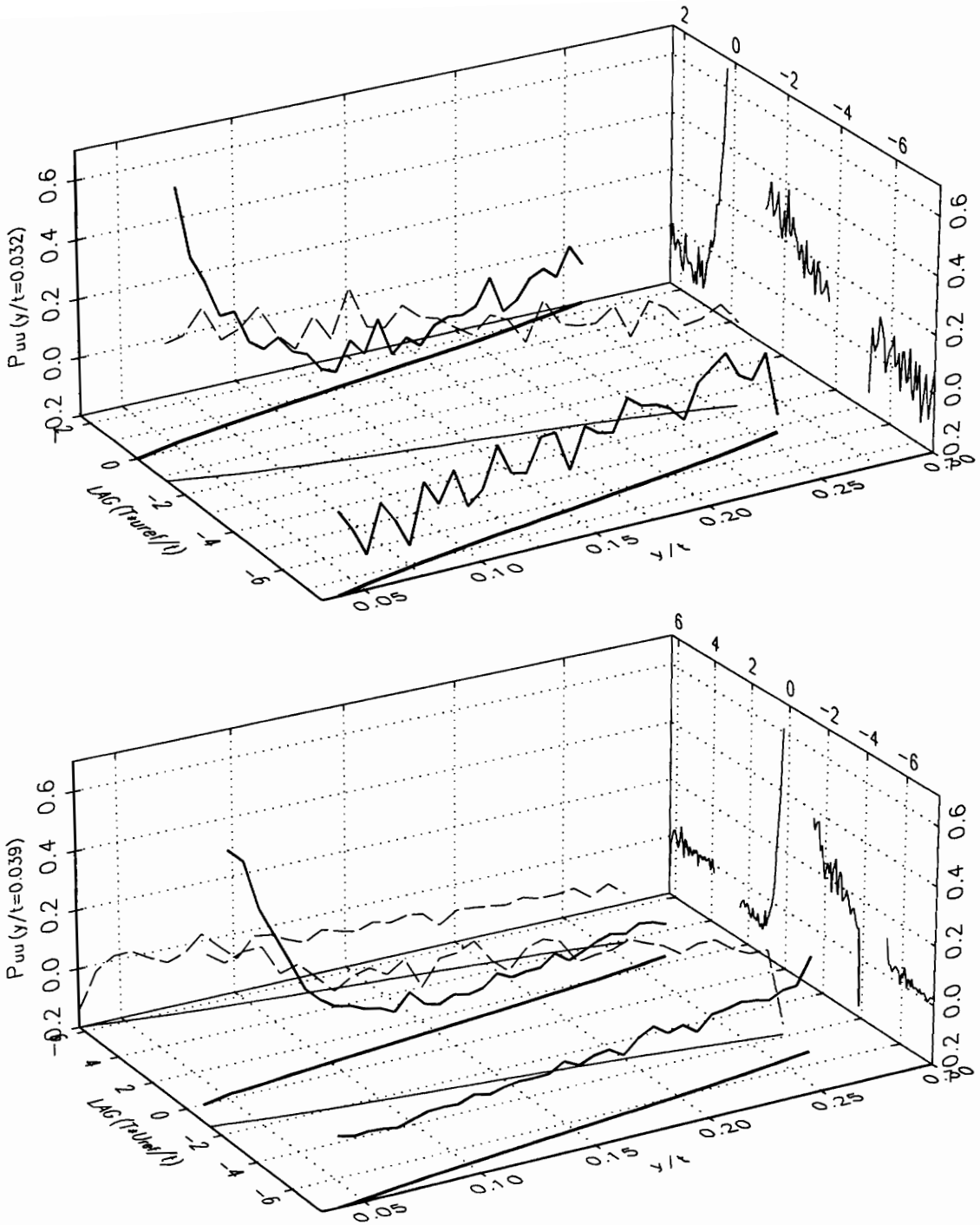


Figure 46. Space-time correlations coefficient ρ_{uu} for u fluctuations between a fixed y location and points along the scan for $x/t=-0.30$. Note: Heavy line is upscan and light line is downscan. Lines on lag- y/t plane are the scan position. Correlation function is projected on lag- ρ_{uu} plane.

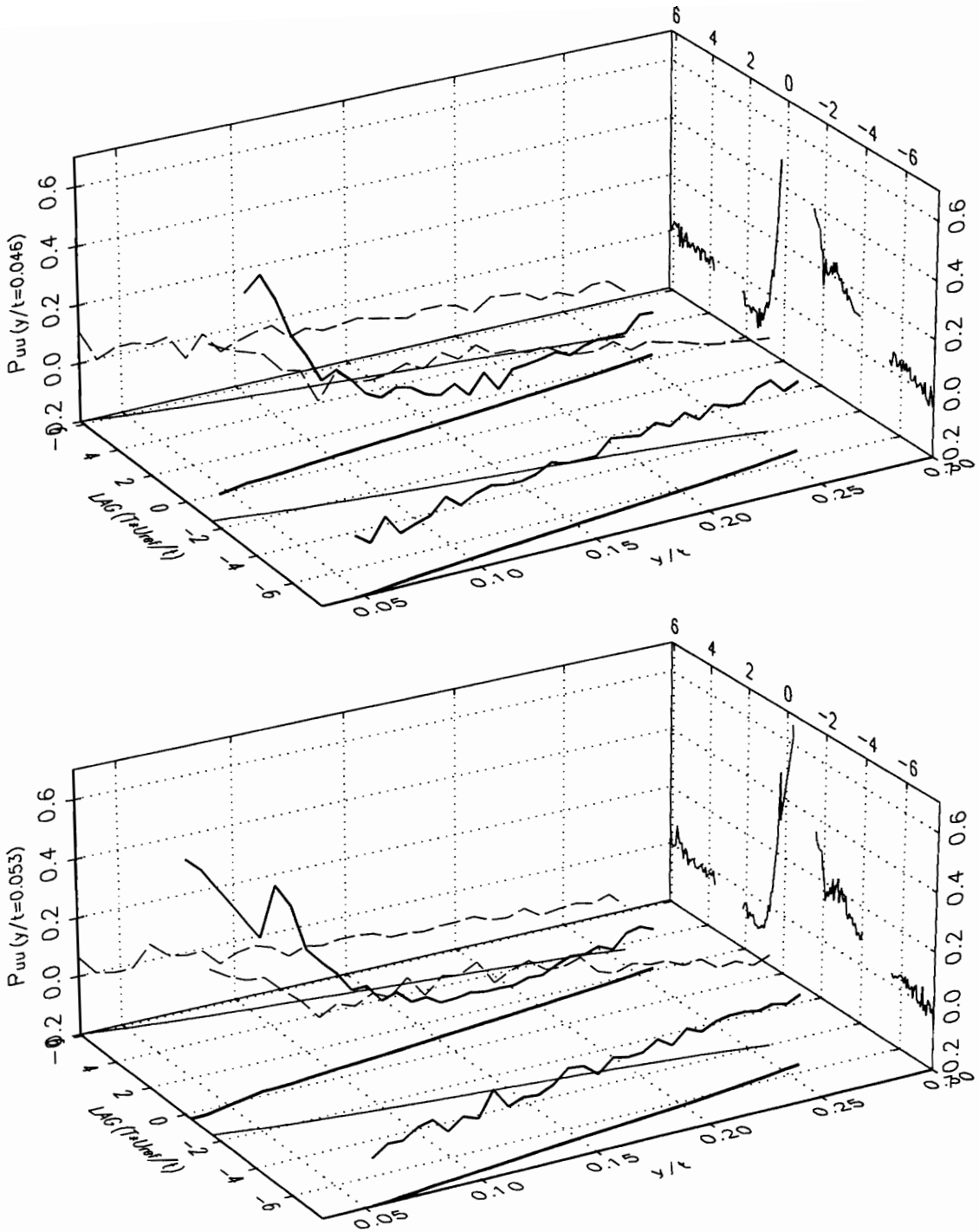


Figure 47. Space-time correlations coefficient ρ_{uu} for u fluctuations between a fixed y location and points along the scan for $x/t=-0.30$. Note: Heavy line is upscan and light line is downscan. Lines on lag- y/t plane are the scan position. Correlation function is projected on lag- ρ_{uu} plane.

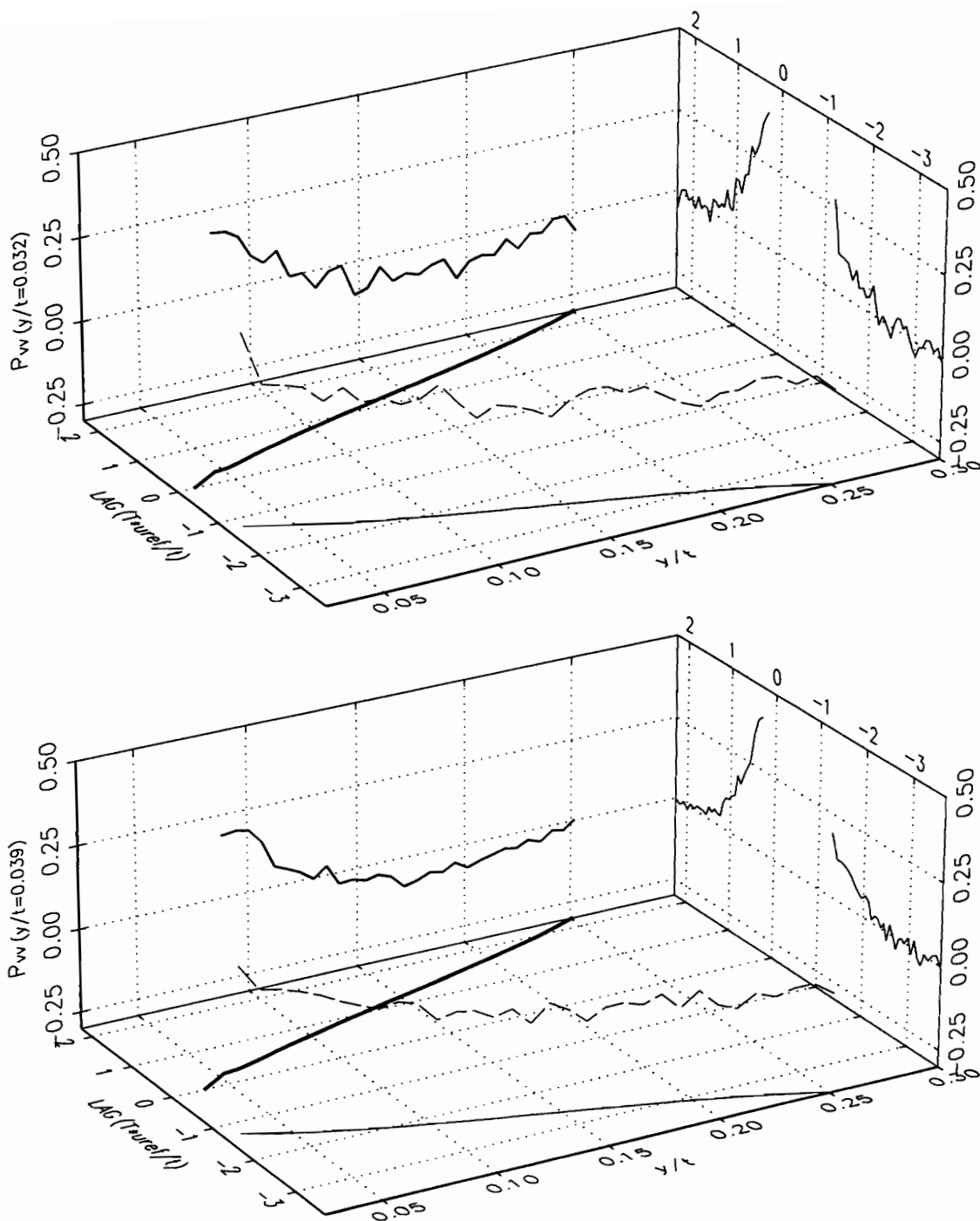


Figure 48. Space-time correlations coefficient ρ_{vv} for v fluctuations between a fixed y location and points along the scan for $x/t = -0.30$. Note: Heavy line is upscan and light line is downscan. Lines on lag- y/t plane are the scan position. Correlation function is projected on lag- ρ_{vv} plane.

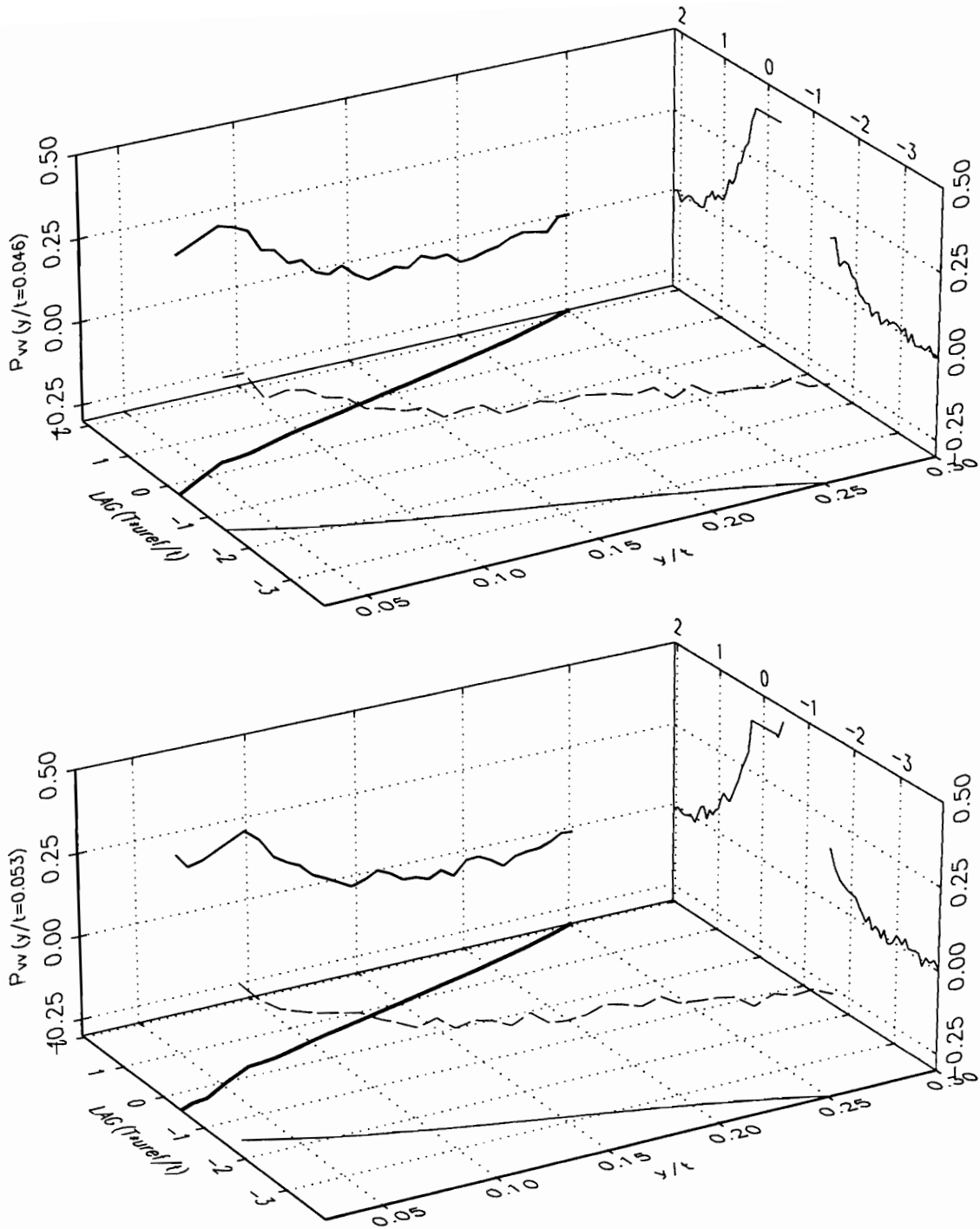


Figure 49. Space-time correlations coefficient ρ_{vv} for v fluctuations between a fixed y location and points along the scan for $x/t=-0.25$. Note: Heavy line is upscan and light line is downscan. Lines on lag- y/t plane are the scan position. Correlation function is projected on lag- ρ_{vv} plane.

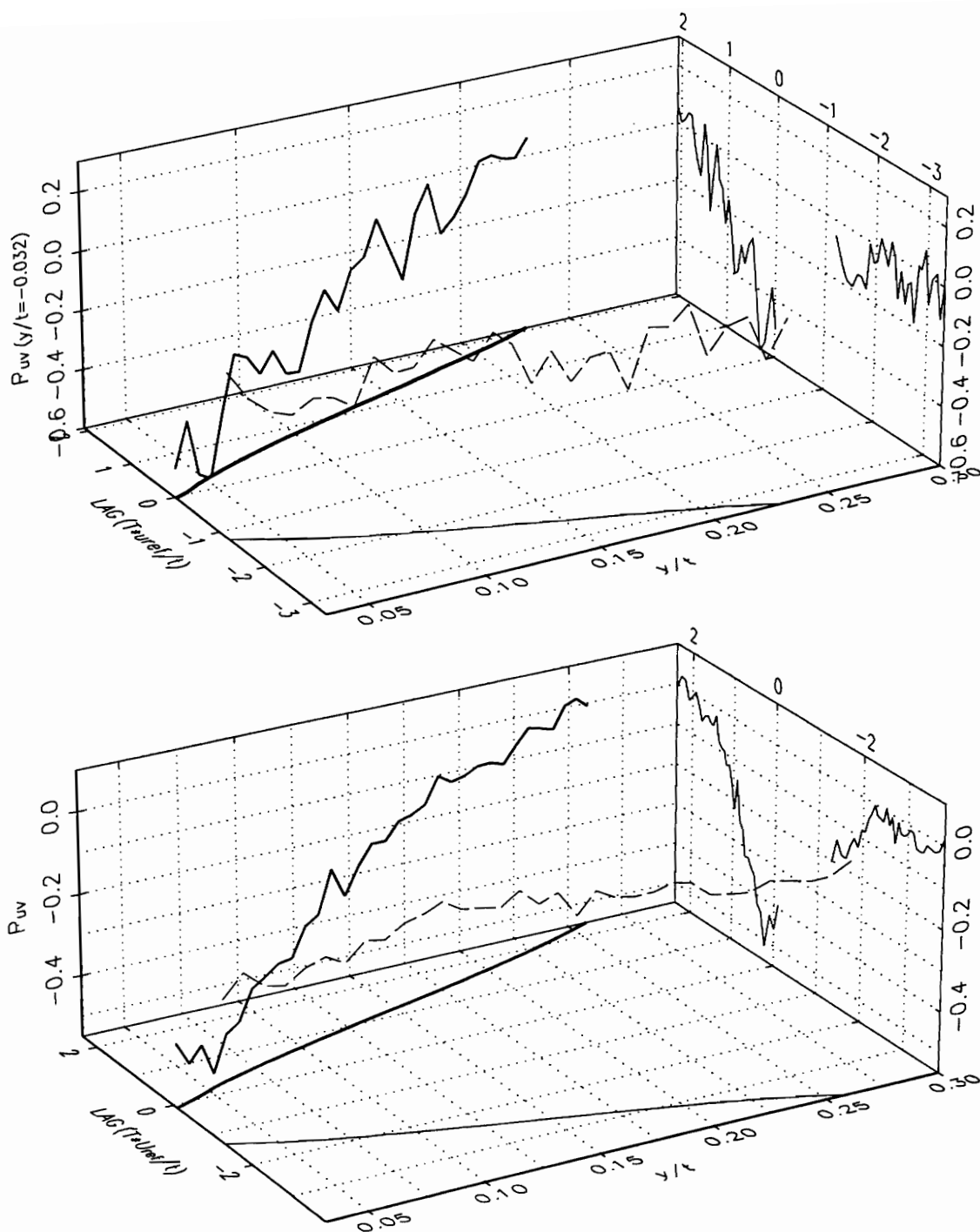


Figure 50. Space-time correlations coefficient ρ_{uv} for u fluctuations between a fixed y location and v fluctuations along the scan for $x/t = -0.30$. Note: Heavy line is upscan and light line is downscan. Lines on lag- y/t plane are the scan position. Correlation function is projected on lag- ρ_{uv} plane.

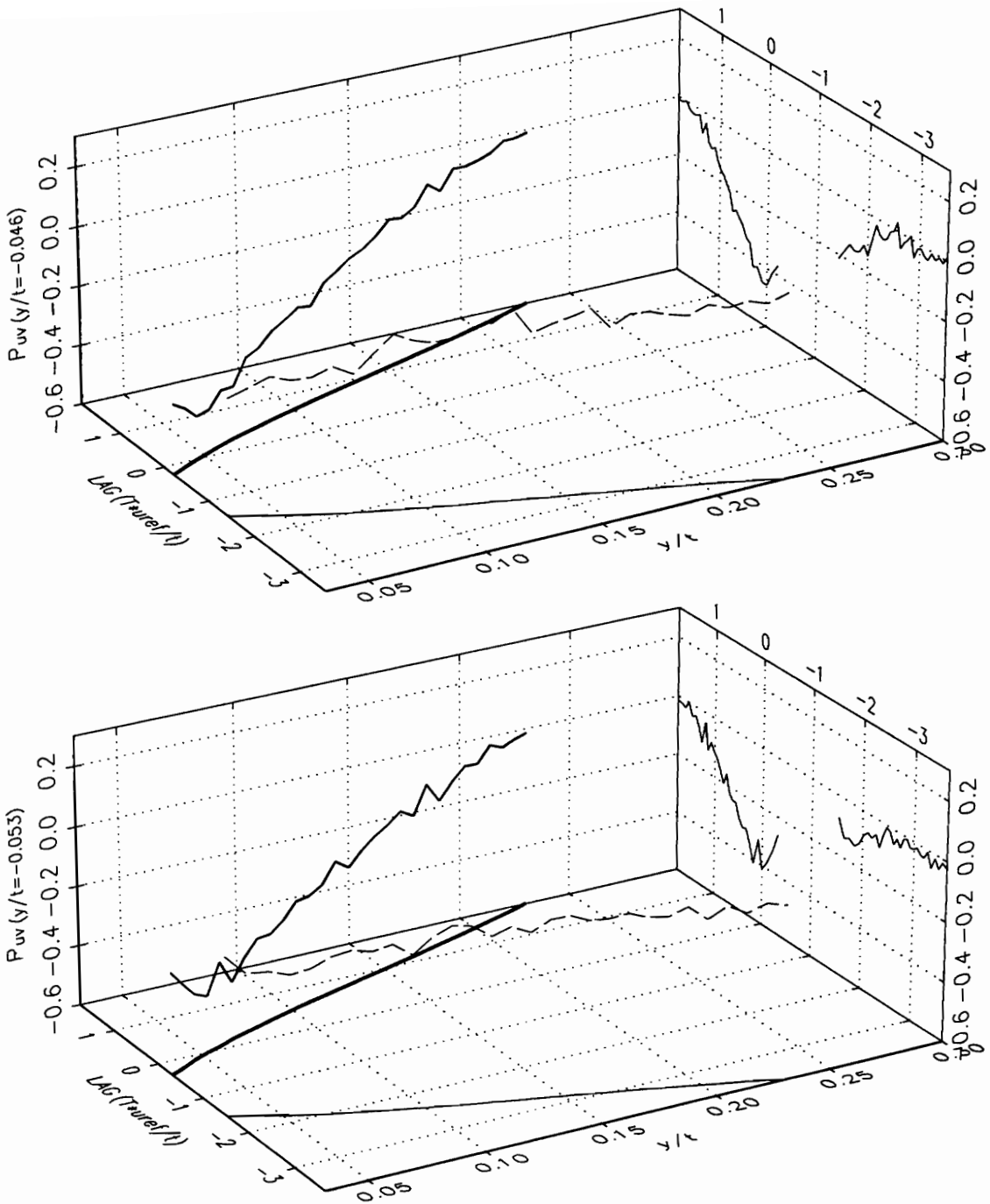


Figure 51. Space-time correlations coefficient ρ_{uv} for u fluctuations between a fixed y location and v fluctuations along the scan for $x/t=-0.30$. Note: Heavy line is upscan and light line is downscan. Lines on lag- ρ_{uv} plane are the scan position. Correlation function is projected on lag- ρ_{uv} plane.

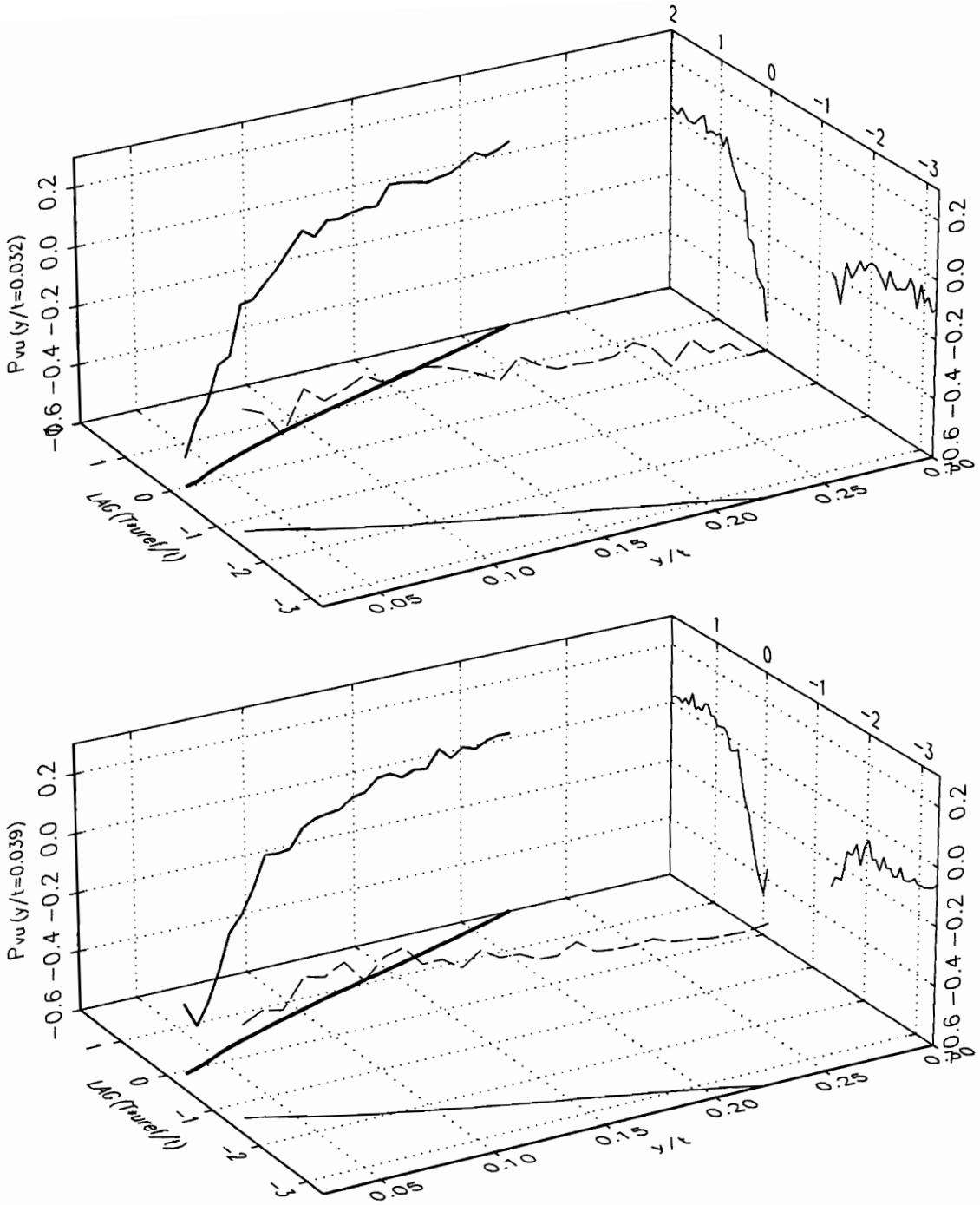


Figure 52. Space-time correlations coefficient ρ_{vu} for v fluctuations between a fixed y location and u fluctuations along the scan for $x/t=-0.30$. Note: Heavy line is upscan and light line is downscan. Lines on lag- y/t plane are the scan position. Correlation function is projected on lag- ρ_{vu} plane.

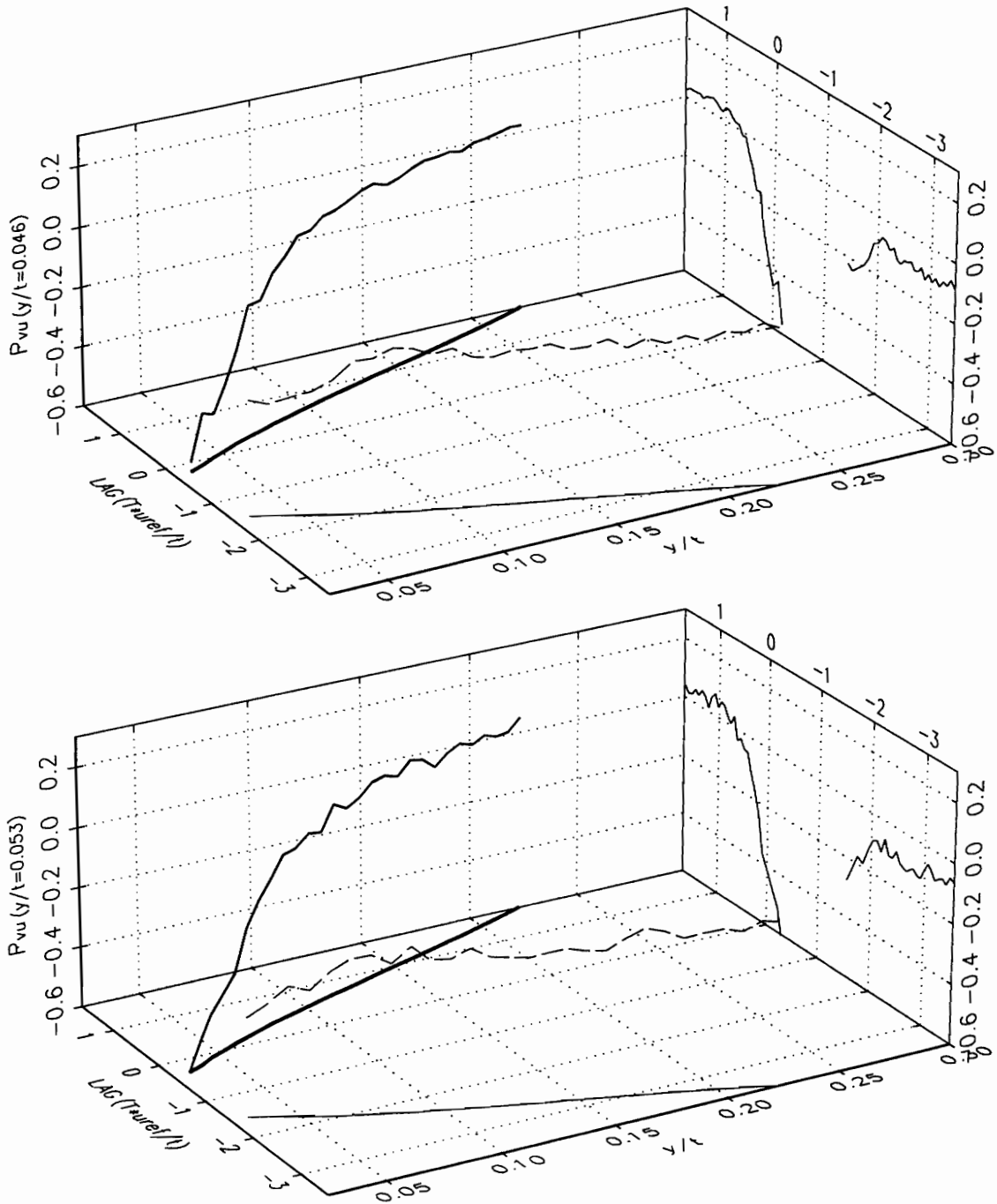


Figure 53. Space-time correlations coefficient ρ_{vu} for v fluctuations between a fixed y location and u fluctuations along the scan for $x/t=-0.30$. Note: Heavy line is upscan and light line is downscan. Lines on lag- y/t plane are the scan position. Correlation function is projected on lag- ρ_{vu} plane.

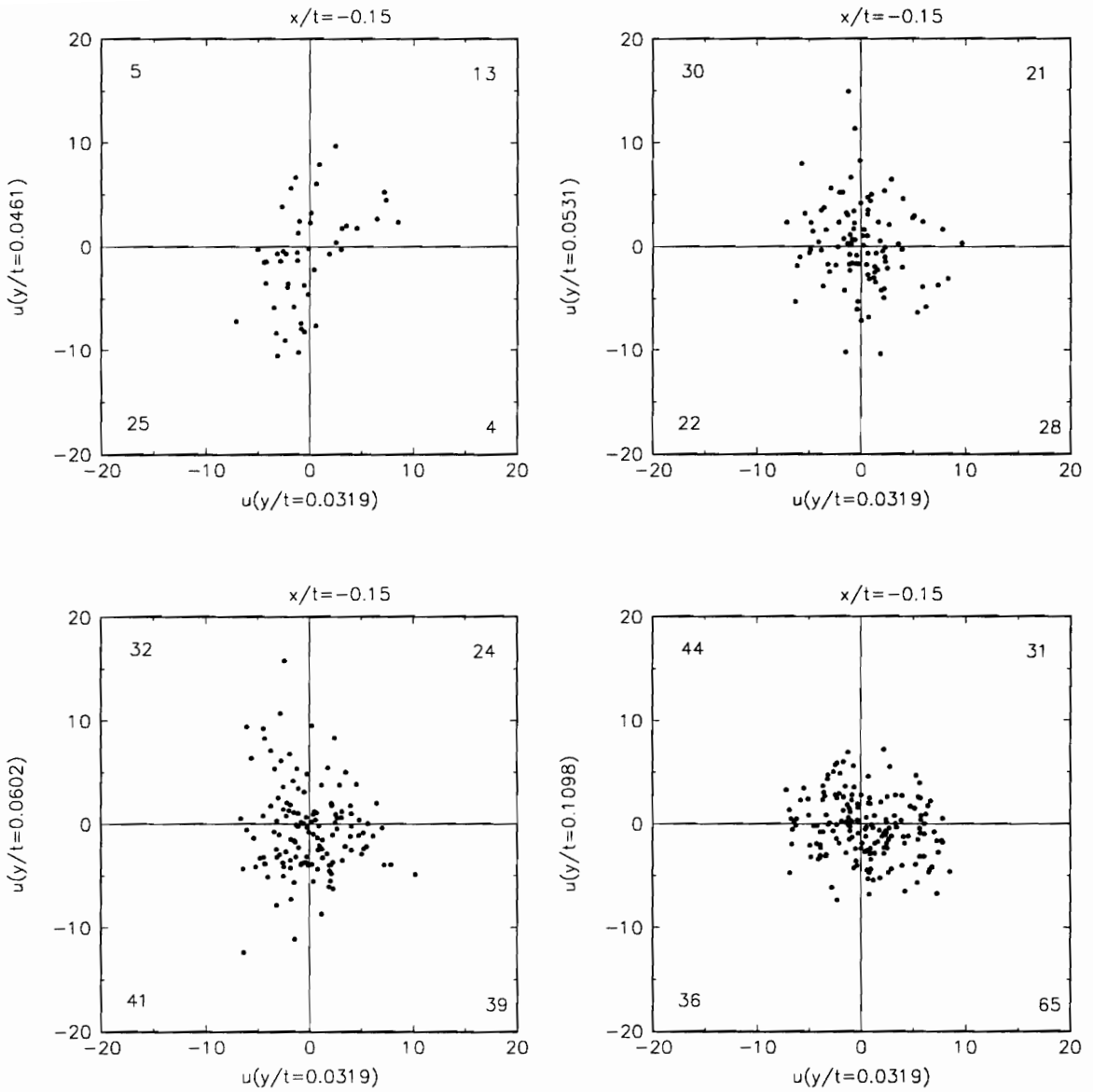


Figure 54. Quadrant analysis of u fluctuations at $y/t=0.032$ versus four other y locations for $x/t=-0.15$. Note: The number of occurrences in each quadrant is noted in each corner.

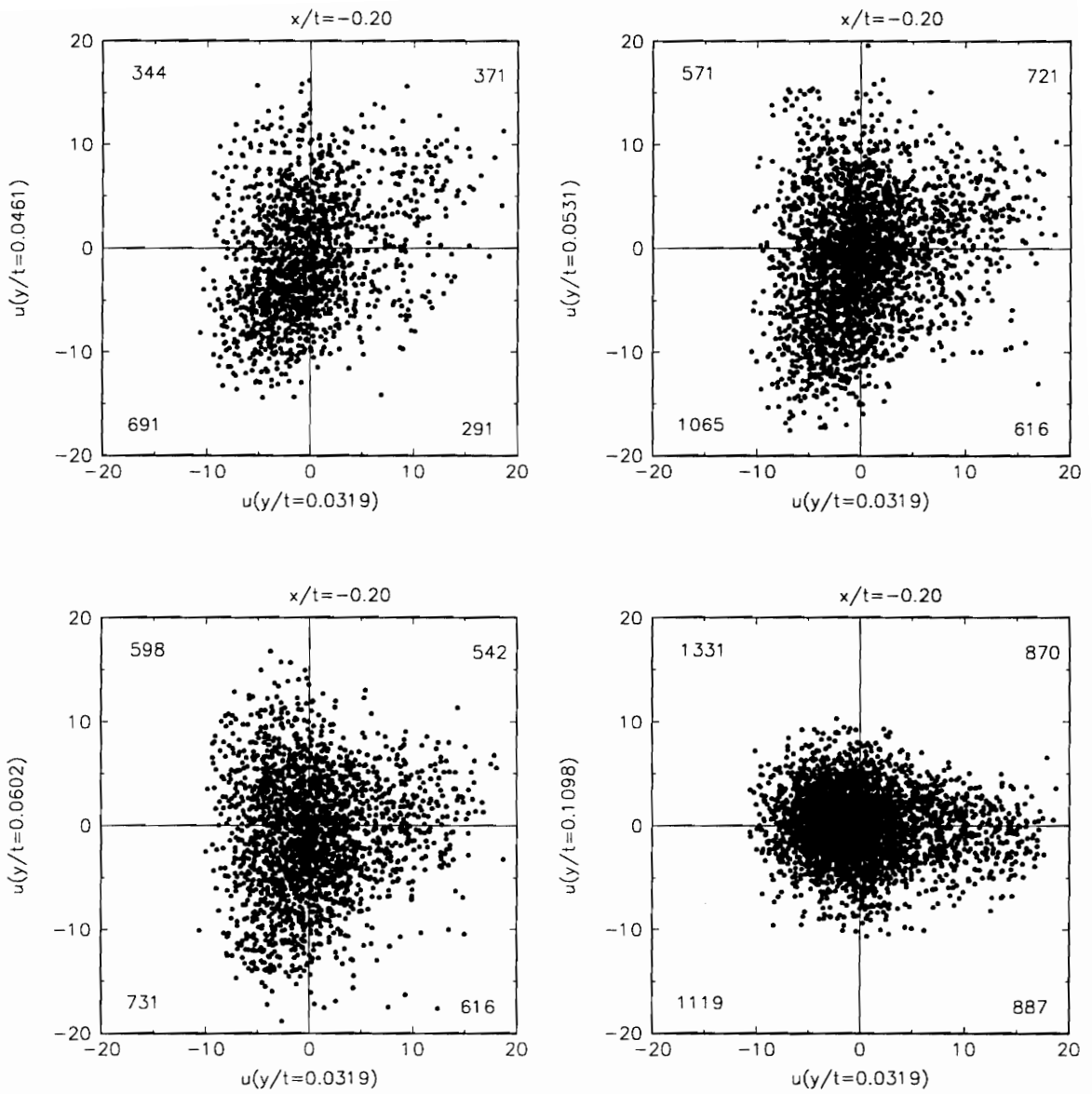


Figure 55. Quadrant analysis of u fluctuations at $y/t=0.032$ versus four other y locations for $x/t=-0.20$. Note: The number of occurrences in each quadrant is noted in each corner.

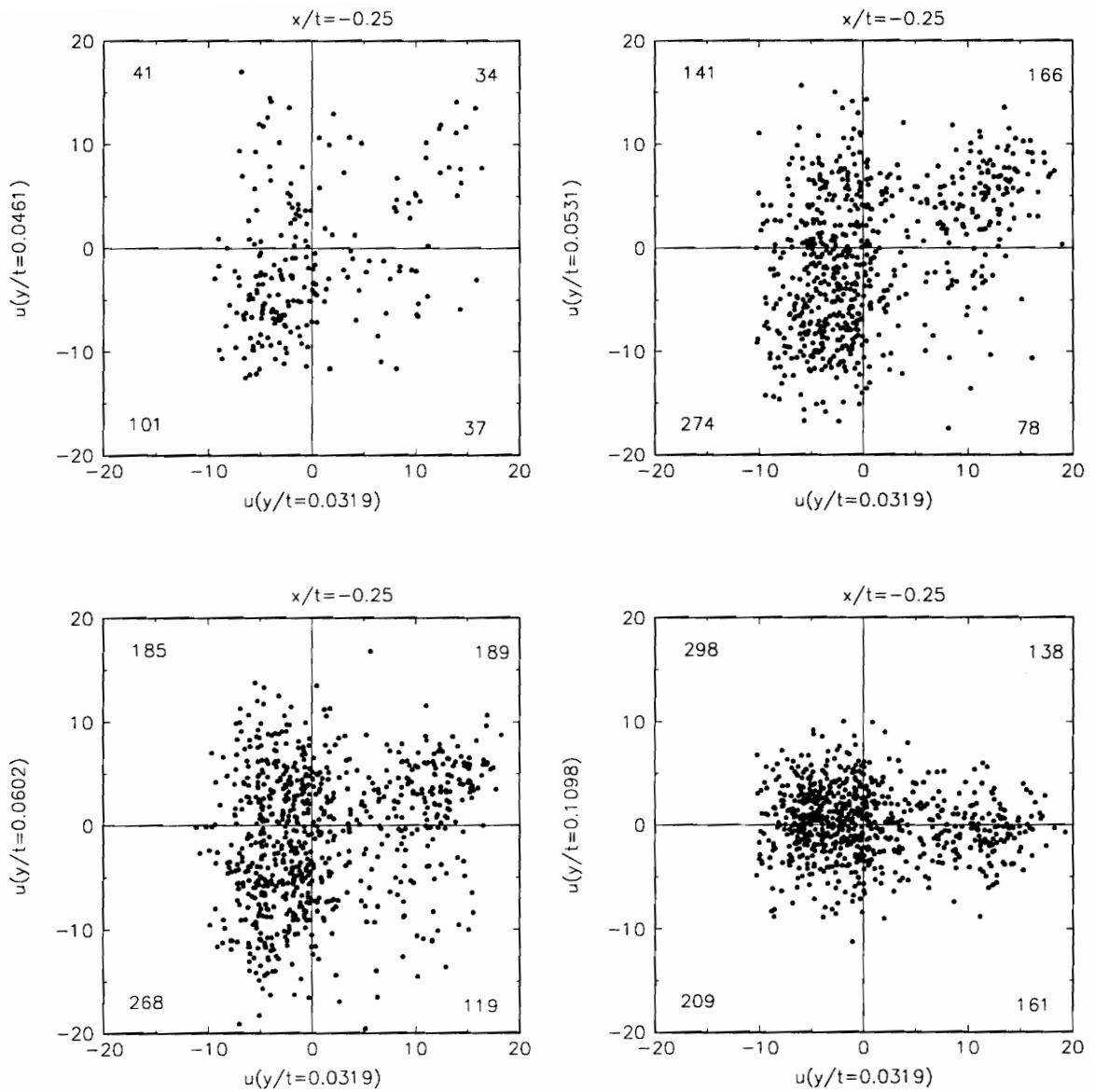


Figure 56. Quadrant analysis of u fluctuations at $y/t=0.032$ versus four other y locations for $x/t=-0.25$. Note: The number of occurrences in each quadrant is noted in each corner.

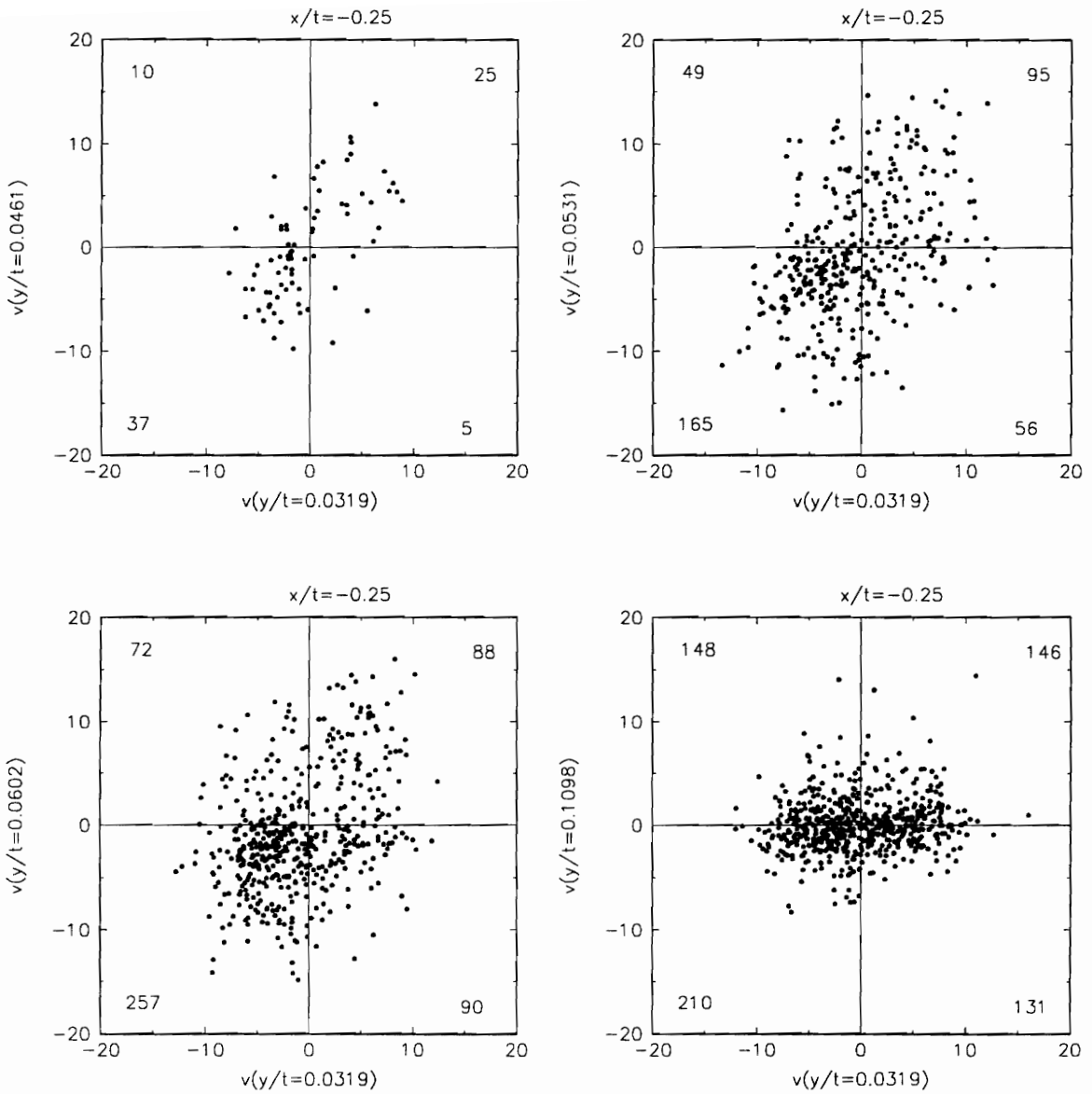


Figure 57. Quadrant analysis of v fluctuations at $y/t=0.032$ versus four other y locations for $x/t=-0.25$. Note: The number of occurrences in each quadrant is noted in each corner.

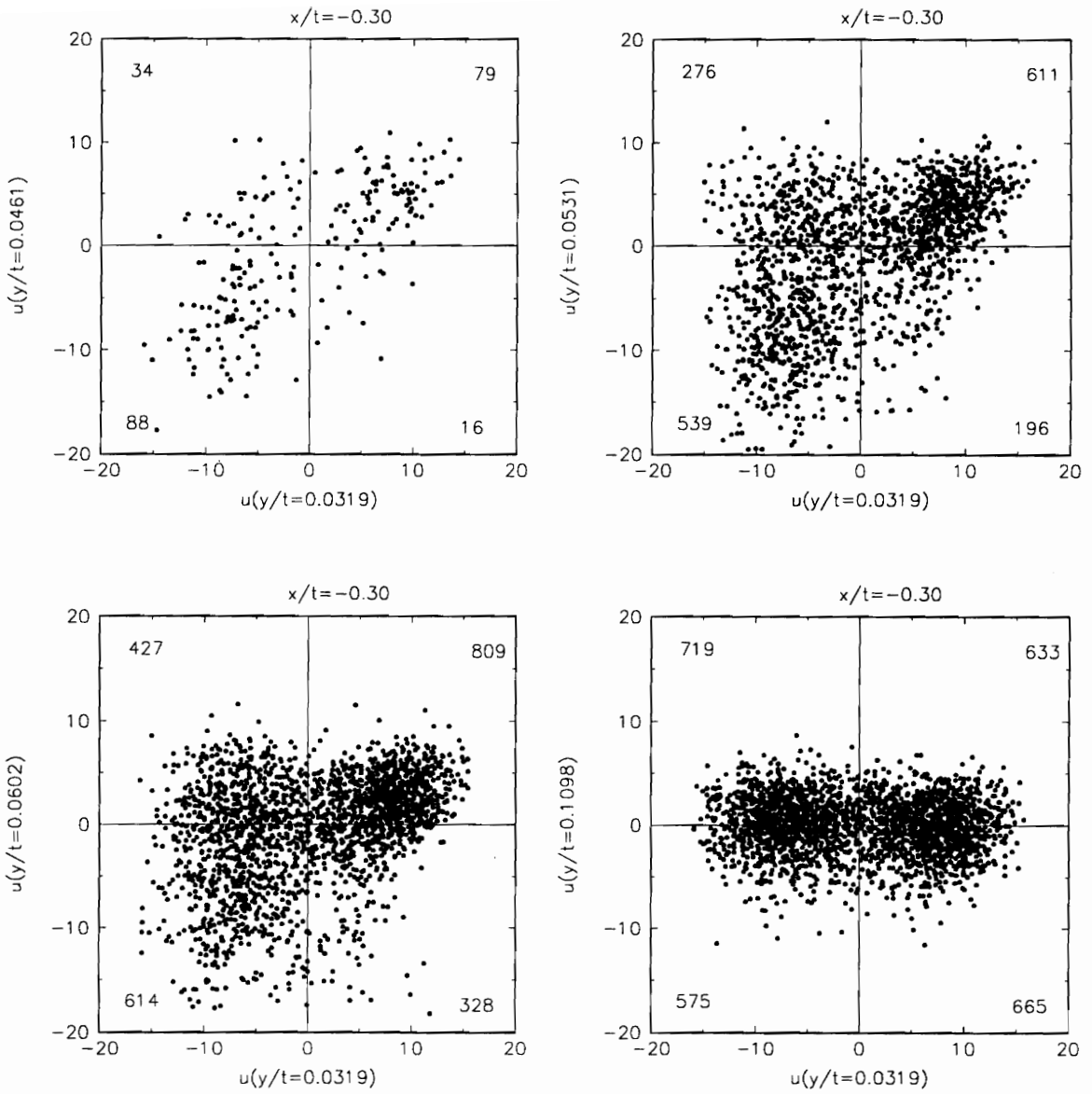


Figure 58. Quadrant analysis of u fluctuations at $y/t=0.032$ versus four other y locations for $x/t=-0.30$. Note: The number of occurrences in each quadrant is noted in each corner.

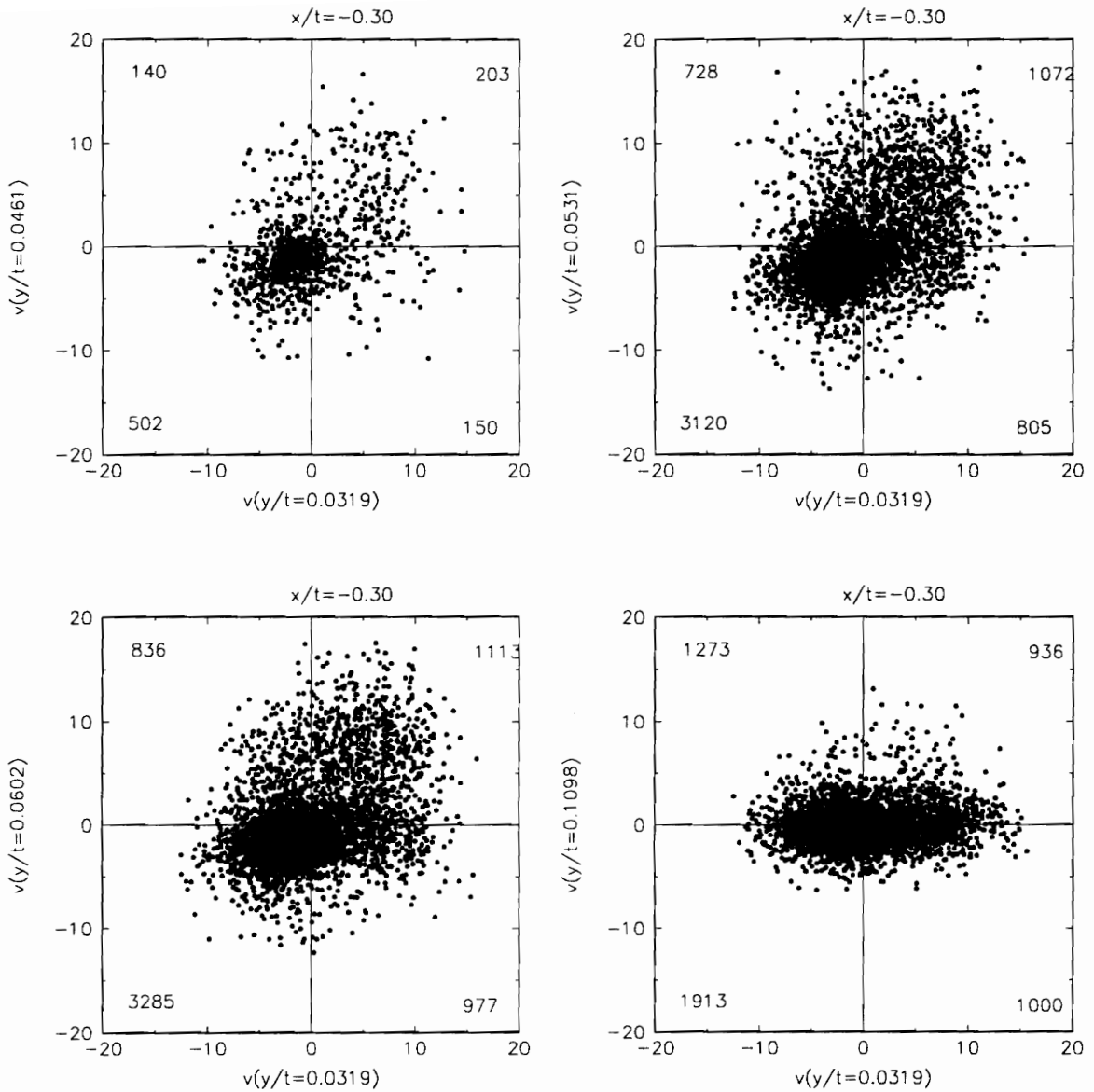


Figure 59. Quadrant analysis of v fluctuations at $y/t=0.032$ versus four other y locations for $x/t=-0.30$. Note: The number of occurrences in each quadrant is noted in each corner.

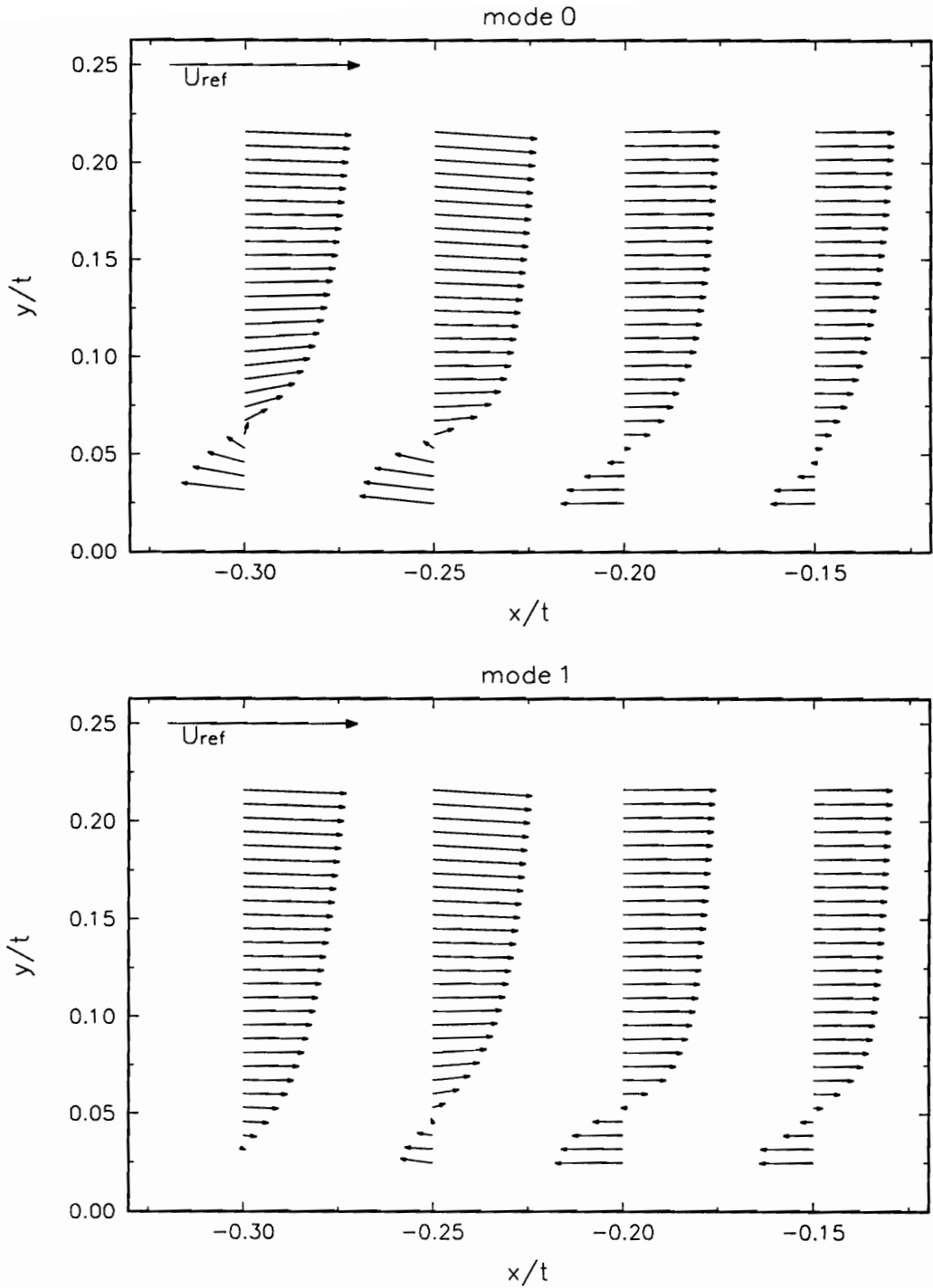


Figure 60. Mode averaged velocity vectors based on the bimodal pressure probability density functions. Mode 0 is the average of the velocity when the surface pressure signal is below the mean and Mode 1 is the average for above the mean. Note: V were not obtained at $x/t=-0.15$ and -0.20 .

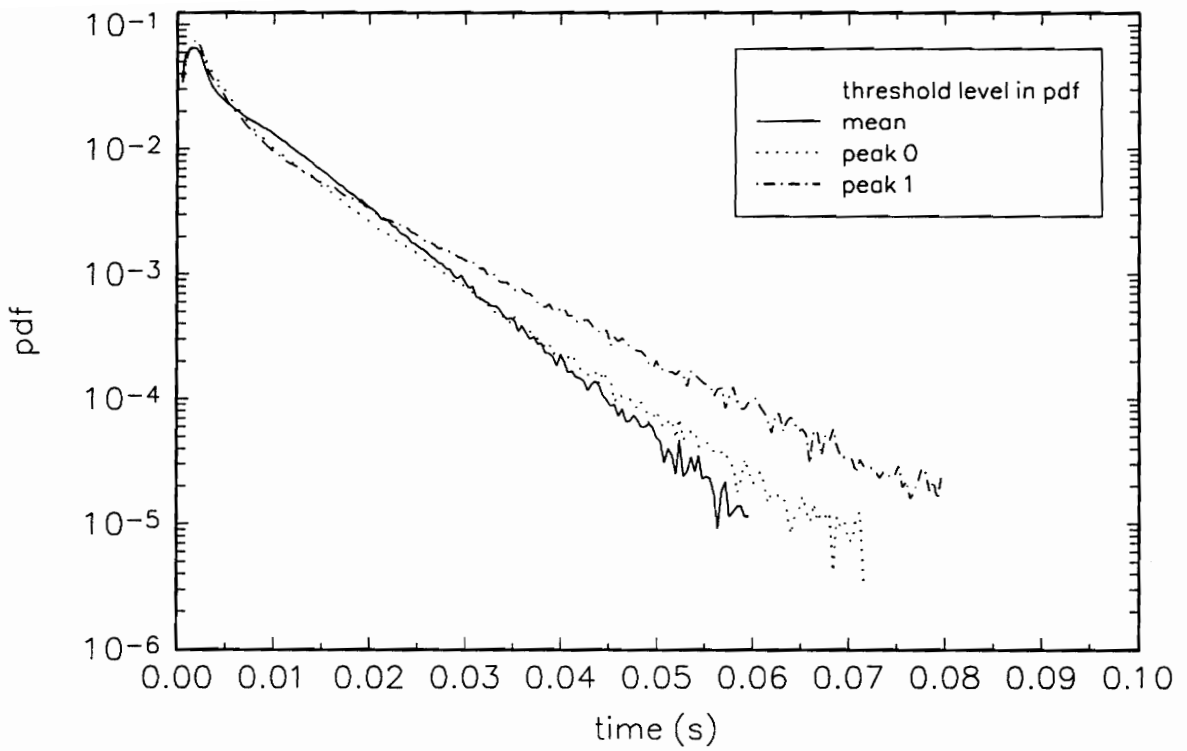


Figure 61. Probability density functions of the time between successive positive crossings of the threshold level of the surface pressure signal.

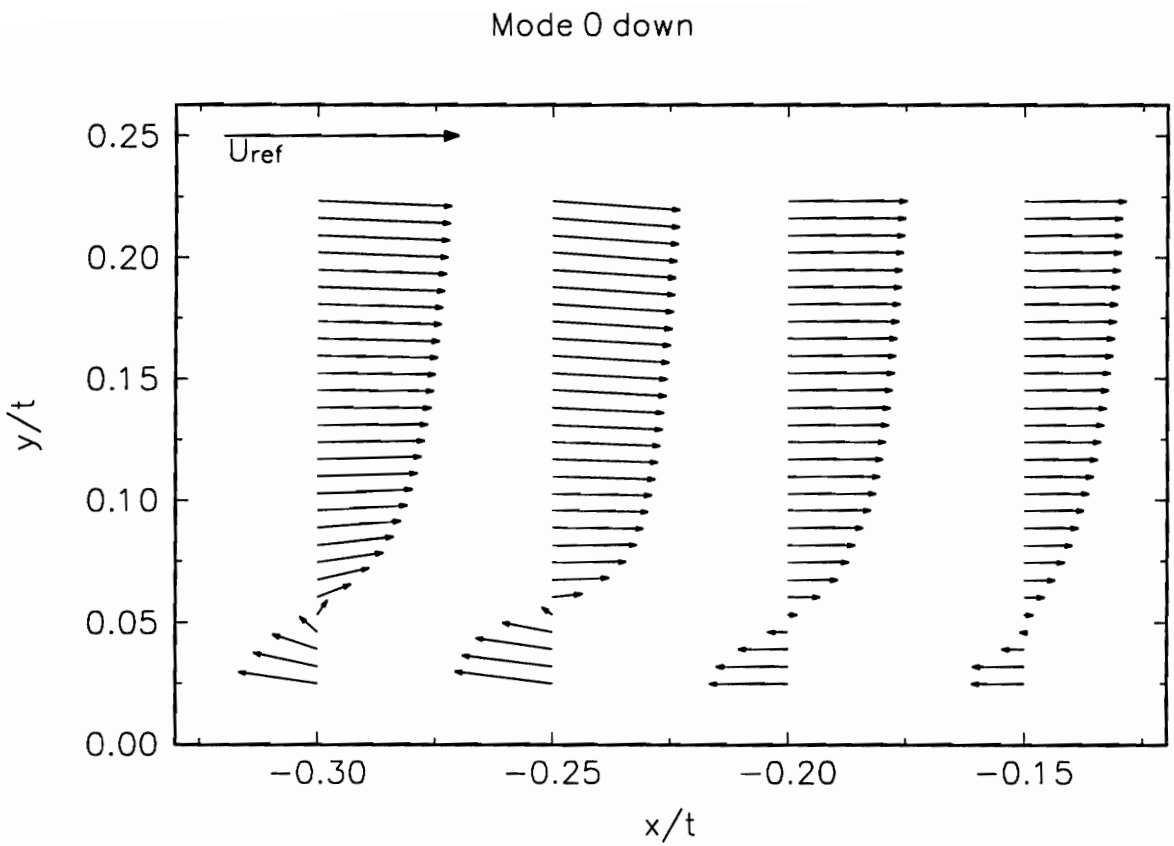


Figure 62. Velocity vectors averaged at the instant the surface pressure signal makes a negative transition across the threshold at the peak in the bimodal pressure pdf below the mean. Note: V were not obtained at $x/t=-0.15$ and -0.20 .

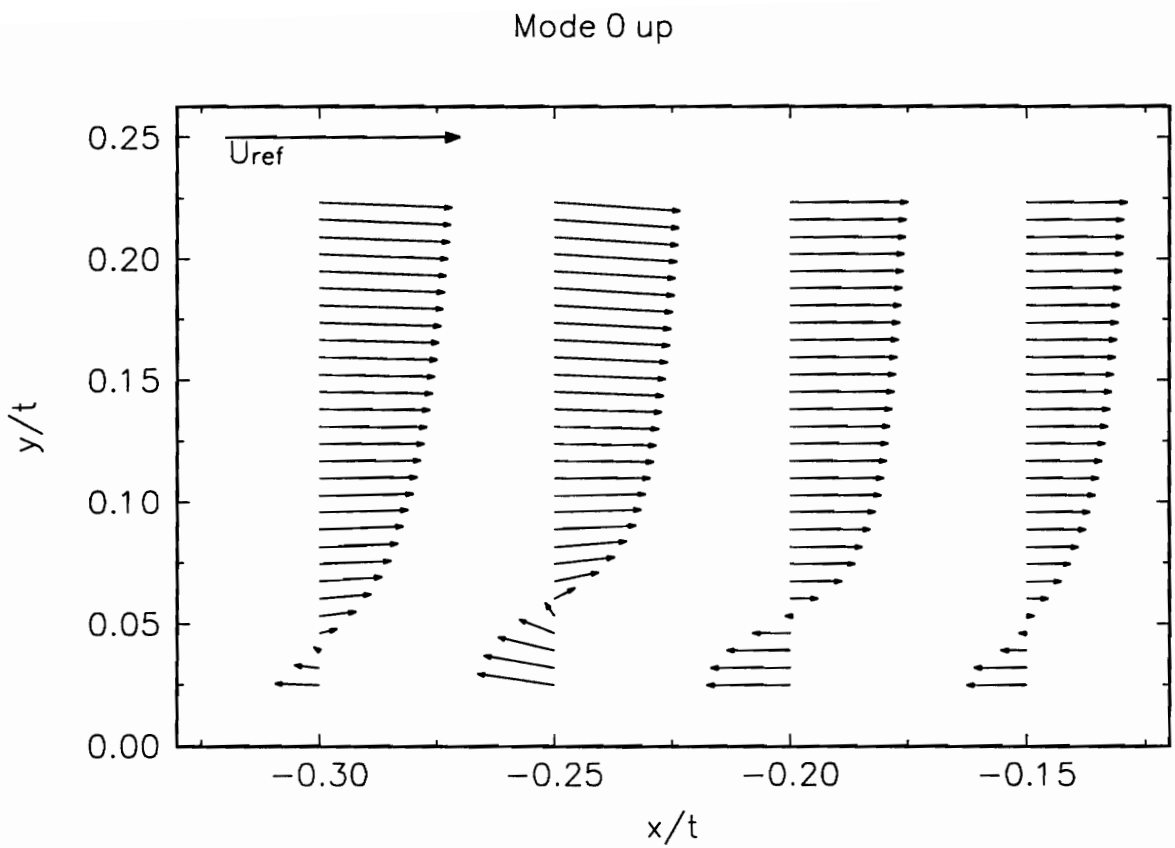


Figure 63. Velocity vectors averaged at the instant the surface pressure signal makes a positive transition across the threshold at the peak in the bimodal pressure pdf below the mean. Note: V were not obtained at $x/t = -0.15$ and -0.20 .

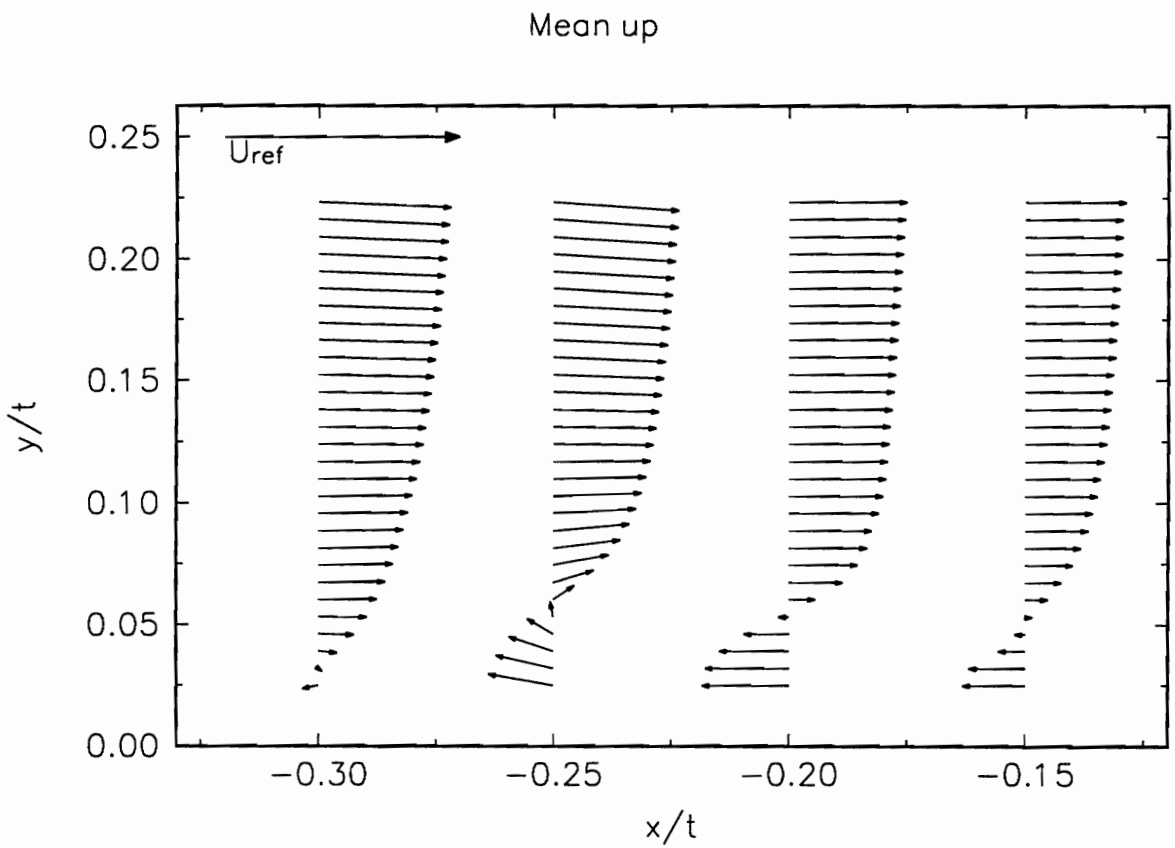


Figure 64. Velocity vectors averaged at the instant the surface pressure signal makes a positive transition across the threshold at the mean. Note: V were not obtained at $x/t=-0.15$ and -0.20 .

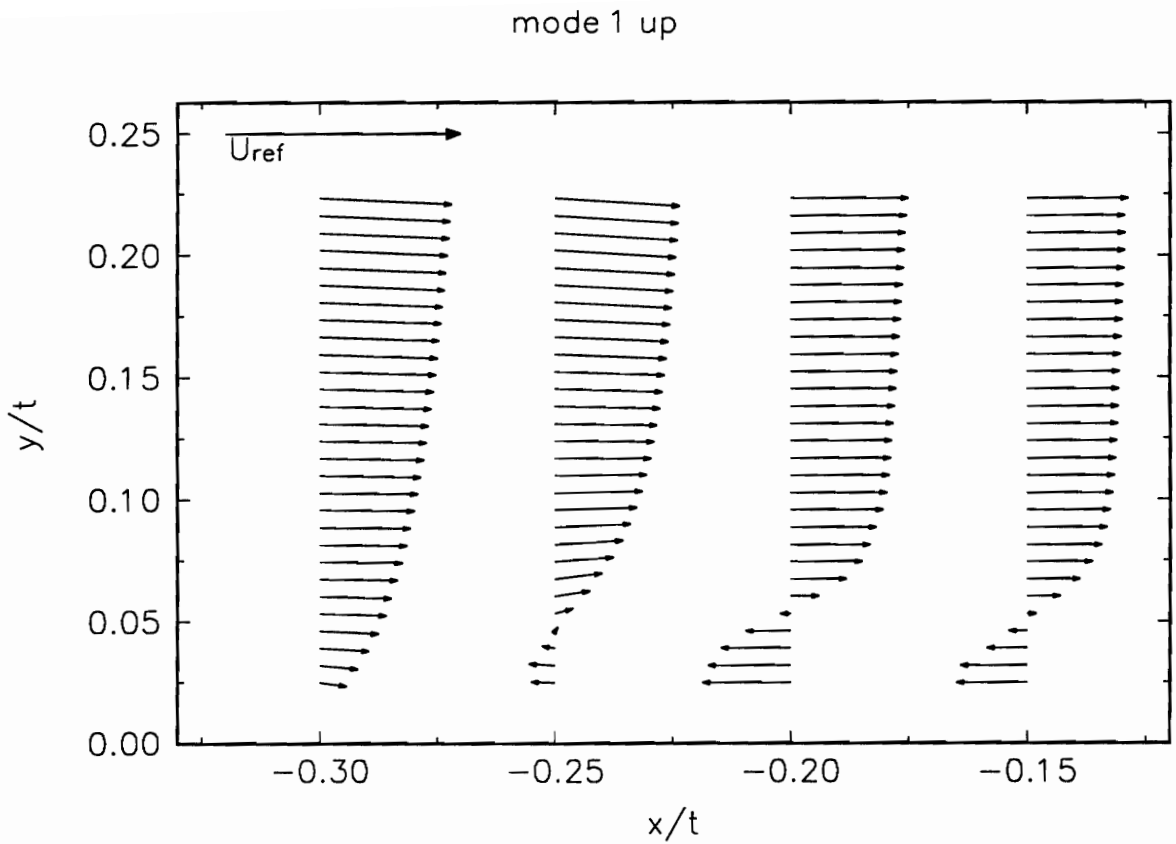


Figure 65. Velocity vectors averaged at the instant the surface pressure signal makes a positive transition across the threshold at the peak in the bimodal pressure pdf above the mean. Note: V were not obtained at $x/t=-0.15$ and -0.20 .

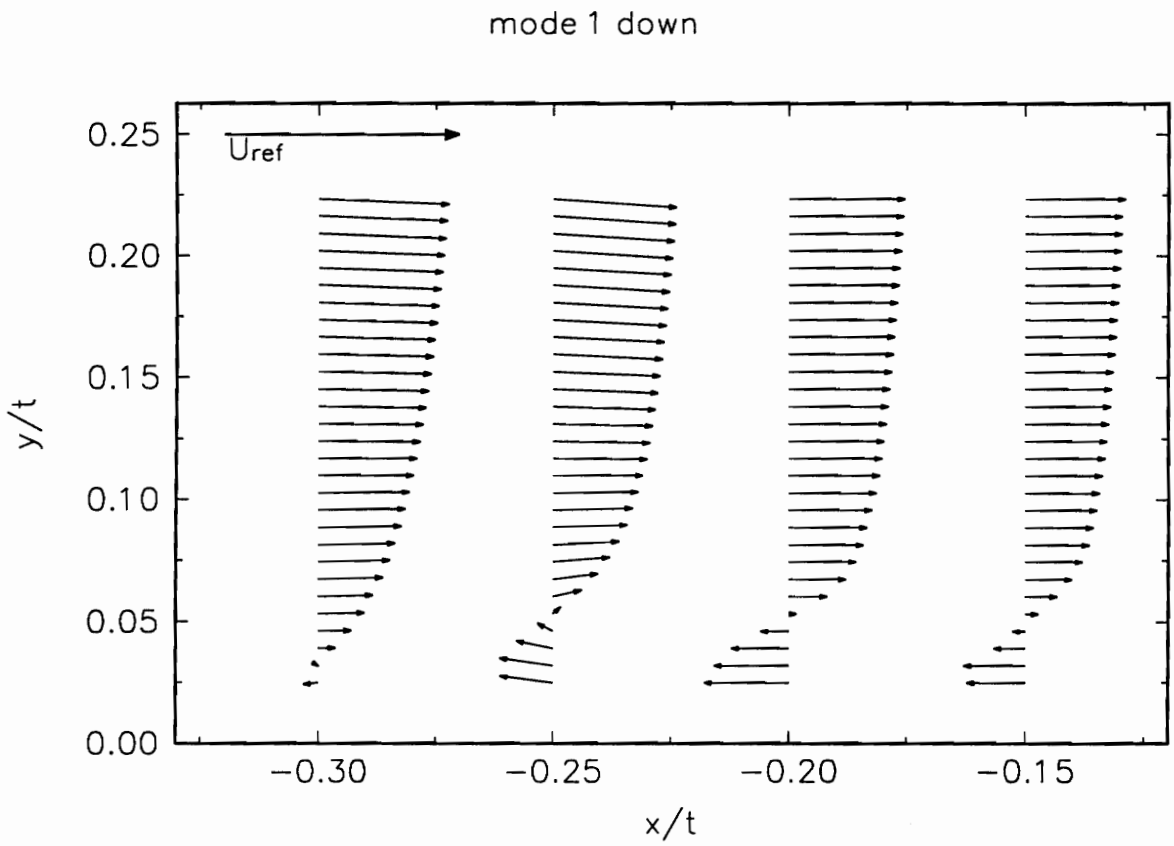


Figure 66. Velocity vectors averaged at the instant the surface pressure signal makes a negative transition across the threshold at the peak in the bimodal pressure pdf above the mean. Note: V were not obtained at $x/t=-0.15$ and -0.20 .

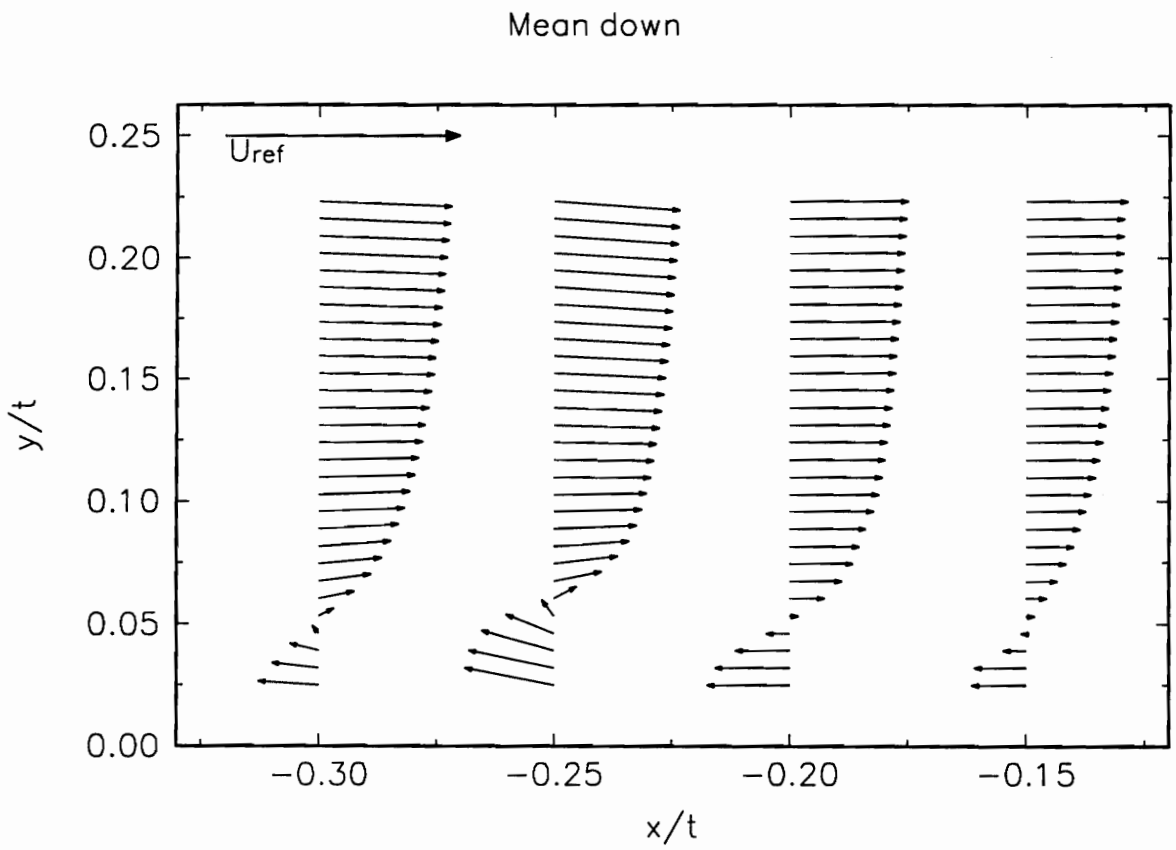


Figure 67. Velocity vectors averaged at the instant the surface pressure signal makes a negative transition across the threshold at the mean. Note: V were not obtained at $x/t=-0.15$ and -0.20 .

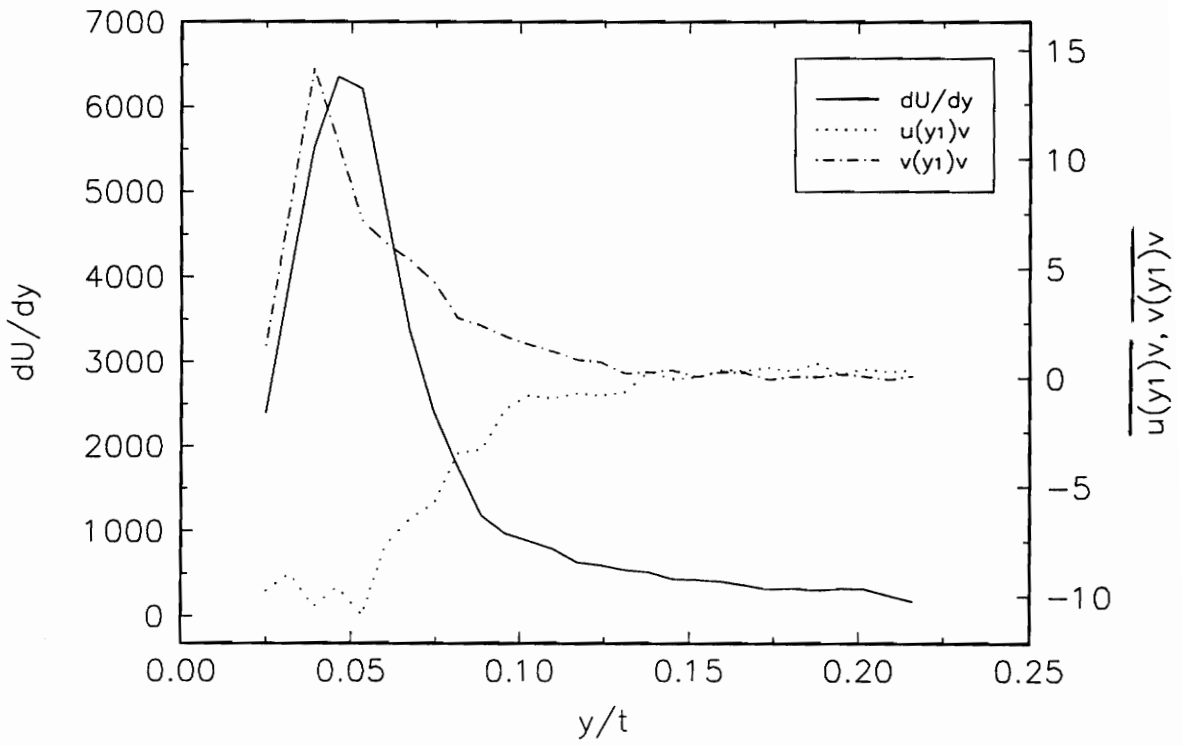


Figure 68. Plots of $\partial U / \partial y$ at $x/t=-0.25$ versus y/t and $\overline{u(y_1)v}$ and $\overline{v(y_1)v}$ at $y/t=0.039$ for $x/t=-0.25$. Note: Units for $\partial U / \partial y$ are $1/s$; $\overline{u(y_1)v}$ and $\overline{v(y_1)v}$ are m^2/s^2 .

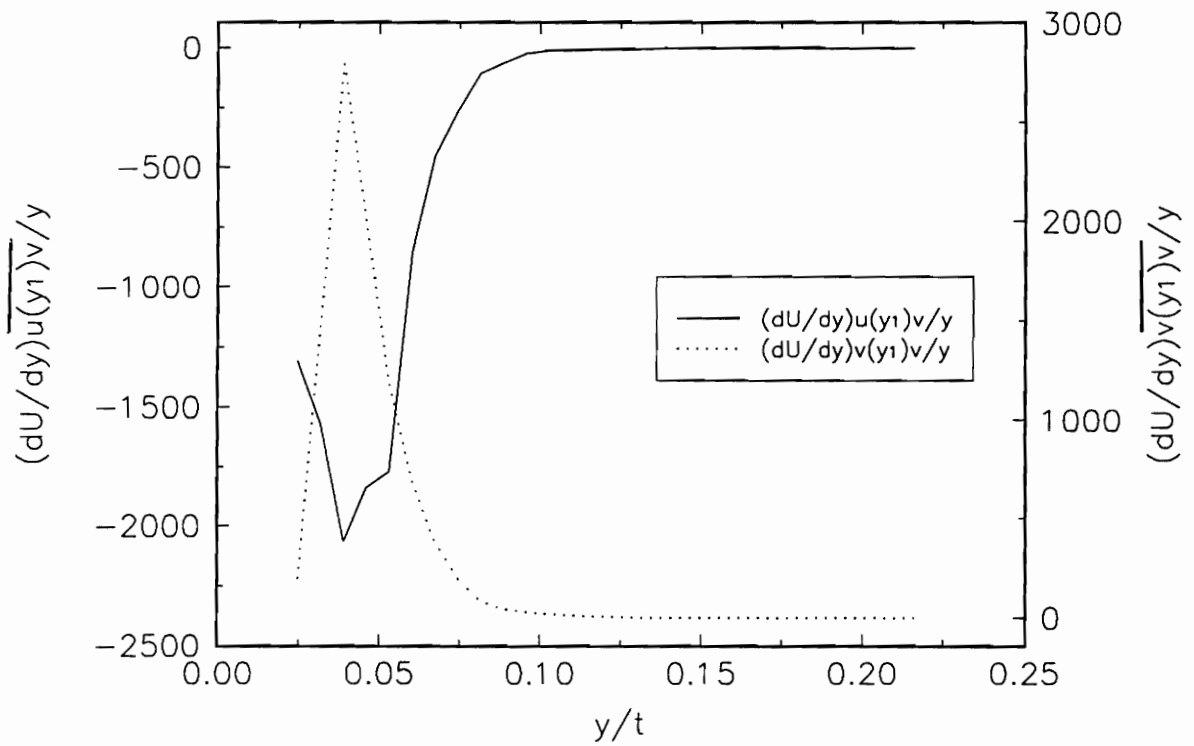


Figure 69. The kernel of equations 4.5 (for both $\overline{pu(y_1)}$ and $\overline{pv(y_1)}$) as a function of distance from the wall, y . Note: The left and right axis have been scaled by $1/10000$.

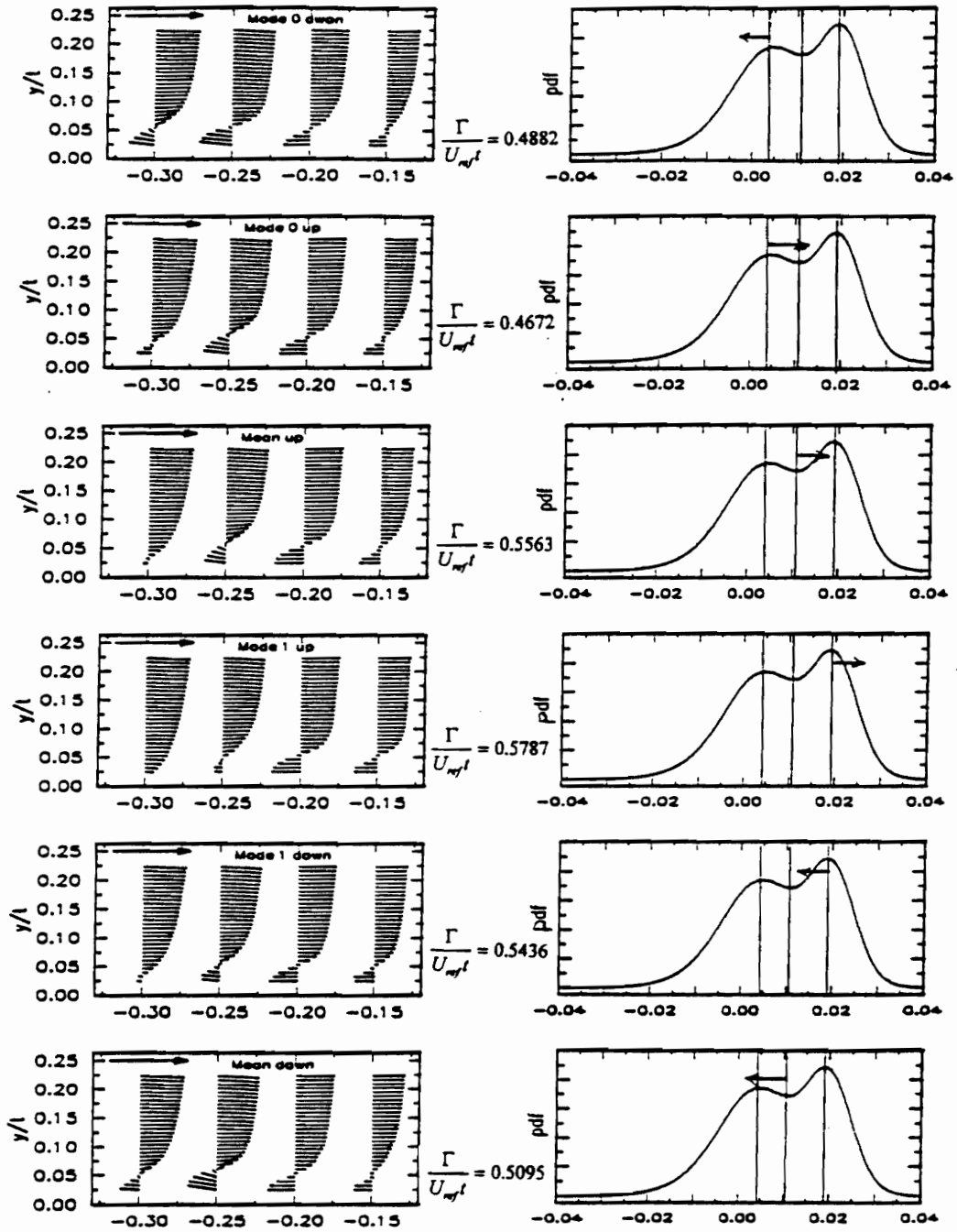


Figure 70. Model for the sequence of flow events in the nose region of a wing-body junction flow. The ET-averaged velocity vectors, the circulation, and the threshold level in the surface pressure pdf are shown.

Appendix A. A Rapidly Scanning Two-Velocity-Component Laser Doppler Velocimeter

Abstract

A rapidly-scanning two-velocity-component directionally-sensitive fringe-type laser-Doppler velocimeter (RSLDV) which scans the measurement volume perpendicular to the optical axis of the transmitting optics and normal to the test floor is described. Scan rates of up to 300 Hz are possible over 75 mm using sinusoidal scanning of position versus time. Measurements were performed in the highly turbulent complex three dimensional flow in front of a wing-body junction. Space-time correlations were obtained and show that the velocity fluctuations in the outer region of this flow are correlated and lead the velocity fluctuations for the near-wall or bimodal flow region.

Introduction

The laser Doppler velocimeter (LDV) has become a valuable tool in the field of experimental fluid mechanics because of its ability to measure the local instantaneous flow velocity accurately and non-intrusively. The increased understanding of complex three-dimensional turbulent and separated flows require that near instantaneous velocity profiles be obtained. Point-wise measurements can lead to a biased view of the behavior of some of flow structure that can be clarified by space-time measurements. In addition to global techniques such as particle image velocimetry and Doppler global velocimetry, the scanning LDV is a choice in these situations, since it has good spatial resolution, good velocity resolution and high data rates. The two-velocity-component rapidly scanning LDV (RSLDV) described here was developed to measure the highly turbulent unsteady flow structure in front of a wing-body junction.

Simpson (1989) reviewed the work done in scanning systems up to that time. Lehmann and Mante (1993) describe a scanning system capable of acquiring two-velocity components with scan rates of 2000 Hz. This system uses a single laser beam and two sets of lenses and fiber optic bundles to collect the scattered light. The fiber optic bundles are scanned by two optical fibers in a rotating disk. The light in these two fibers is passed on to an interferometer to determine the Doppler frequency. This system requires highly seeded flows otherwise signal dropout can occur.

Objectives

The motivation for developing this rapidly-scanning laser Doppler velocimeter was to understand better the structure of the flow in the nose-region of the wing-body junction flow that has been previously examined by point-wise LDV measurements (Devenport and Simpson, 1990). Insights on the structure of this flow can be obtained through the space-time information obtained by a scanning LDV system. The main area of interest is the bimodal flow structure in the nose region of this flow. The requirements for the scanning LDV system used to investigate this flow are as follows:

1. Obtain instantaneous U and V components of velocity, the mean on-axis velocity W velocity is zero.
2. Scan a vertical line of at least 20 mm high at 50 Hz in the plane of symmetry in front of the wing.
3. Obtain surface pressure mean and fluctuation measurements simultaneously with the velocity measurements.
4. Obtain space-time correlations for this flow.

Design Considerations

For the present measurements, the design requirements are a high scan rate through the bimodal flow region (approximately 2 cm in height) and small as possible

measurement volume to achieve a high data rate. However, the measurement volume needs to be large enough to ensure that the beams cross throughout the entire vertical scan.

To achieve a high scan rate, the distance from the scanner mirror to the measurement volume should be on the order of 1-2 meters to limit the scan angles to a few degrees of total range. This is necessary to minimize the acceleration of the scanner based on the inertia of the selected scanner mirror. The acceleration of the scanner can also be reduced by using a sinusoidal scan position versus time instead of the internally supplied ramp. The scanning rate may also be limited by the ability of the LDV signal processing hardware to process high velocities in the scan direction, due to signal bandwidth restrictions. In the present signal processing arrangement, the total bandwidth for the V velocity signal is 5 MHz. The higher scan rates also result in lower data rates. In the present study a scan rate of 50 Hz was used.

Another factor to consider is that a reflected beam from the oscillating scanner mirror will not scan in plane but in a conical arc. This can be shown in the following derivation for a beam in the horizontal plane incident onto the scanner mirror at some angle β . The reflected beam will have the following parametric form based on a scan angle of θ :

$$x = \rho \cos \beta \cos 2\theta \quad (1)$$

$$y = \rho \sin \beta \quad (2)$$

$$z = \rho \cos \beta \sin 2\theta \quad (3)$$

where x , is along the optical axis, y is in the vertical direction, z is along the scanner axis, and ρ is the distance along the beam from the scanner mirror. If the outgoing beam is incident on a vertical plane at a distance of x the following results:

$$y = \frac{x \tan \beta}{\cos 2\theta} \quad (4)$$

$$z = x \tan 2\theta \quad (5)$$

which are the parametric equations for a hyperbola. From these equations it can be seen that to ensure a nearly vertical scan that the angle β and the scan angle θ need to be minimized.

Description of the Optical System

The system, as used in this investigation, measures two components of velocity simultaneously. The green and blue lines of an argon-ion laser are used to form two coincident measurement volumes. The arrangement of the optical system is shown in Figure 1; a photograph is shown in Figure 2. The first part of the system uses optical components from a TSI two-component two-color LDV system.

The laser is a Coherent Innova-90 argon-ion laser with the all wavelengths mirror and etalon installed. The laser beam passes through a polarization rotator, **PR1** (TSI 9101-1), and attenuator, **AT** (TSI 9204A), permitting adjustment of the intensity of the out-going beam. The beam then passes through a set of dispersion prisms, **DP** (TSI 9106), that separate the laser beam into the used component colors, blue (488 nm) and green (514.5 nm). A set of mirrors, **M1** (TSI 9106), **M2** and **M3** (TSI 9107), are used to direct the beams toward the other optical component as two parallel beams. Other components from a TSI two-color two-component system, see Figure 1, are used to produce two beams for each color with frequency-shift for one each.

Mirrors **M4** and **M5**, dielectric coated for argon-ion wavelengths and 30 mm in diameter, direct the four beams into the beam expansion and focusing optics. Lenses **L1**, 100 mm focal length 25 mm dia. achromat, and **L2**, 250 mm focal length 75 mm dia. achromat, form the beam expansion optics for the transmitting optics. The lens pair **L3**, 400 mm focal length 75 mm dia. achromat, and **L4**, 250 mm focal length 75 mm dia. achromat, form the focusing optics. The beam expansion ratio was chosen as 4X, the maximum based on 13 mm input beam spacing and the 75 mm diameter of the transmitting lenses. The distance between lenses **L3** and **L4** then determines the location of the beam waist, approximately 2.25 m from lens **L4**. It was found that placing the 250 mm focal length lens before the 400 mm focal length lens resulted in better beam shapes at the measurement volume.

The four beams are then incident on mirrors **M6-M9**, which are 12 mm dia. dielectric coated for argon-ion wavelengths at 45 degree incidence. These mirrors direct the beams toward mirrors **M10-M13** that direct the beams toward the scanner mirror, **SM**, at the proper angle. These mirrors form beam steering pairs, which are used to position the beams properly on the scanning mirror and to insure that the beams cross at the measurement volume. The scanner is a galvanometer-type from General Scanning Inc., model 325 DT.

Mirrors **M15-M18** are long vertical mirrors, 200 mm long by 25 mm wide and 12 mm thick, used to redirect the scanning beams so that the beams will cross at the measurement location at the desired angle. The mirrors are flat to 1/2 wavelength over 25 mm, and do not contribute any error to maintaining beam crossings. The mirrors are attached to the positioners at their midpoint with silicon rubber, which allows for thermal expansion without mirror warping.

The beam crossing configuration is shown in Figure 3; a photograph is shown in Figure 4. The laser beams that form the U measurement volume, **AA-BB**, are in a plane that rotates with the scanner. The beams that form the V measurement volume, **CC-DD**, remain in the vertical plane as the measurement volume is scanned. Figure 3 also shows the wing-body junction, the coordinate system used in this study, and the approximate location of the receiving optics in forward scatter. The measurement volume size was 0.3 mm in diameter. The fringe spacing for the U system was 3.33 μm and 20.7 μm for the V system. Since this LDV system is used to obtain flow structural information, fine

turbulence information is not needed, and the measurement volume size should not be an important issue.

Receiving Optics

The receiving optics is operated in off-axis forward scatter. A 250 mm focal length achromat with 75 mm diameter is used to collect the scattered light. An achromat is used to ensure that the scattered light for the two colors will focus at the same spot and a better defined spot size can be realized compared to a non-achromat (Yariv, 1985). A slit 0.1 mm wide, made of 0.125 mm thick stainless steel shim stock, is attached onto the front of the PM-tube, model 9813B, to define the area of the measurement volume that light is collected. The active area of the Thorn-EMI PM-tube is approximately 46 mm in diameter but it was found that the best signals were obtained for the 15 mm diameter center. This requires that the image of the scanning measurement volume be contained in this area. The scan height was approximately of 22 mm, which requires at least a 0.25 magnification ratio for the receiving optics. The receiving optics are mounted on an optical rail. This rail is mounted on a tripod permitting changes in pitch, roll and yaw so that the slit can be aligned with the image of the scanning measurement volume.

Data Acquisition System

The Data acquisition system must sample two components of velocity and determine the position of the measurement volume for each velocity measurement. Also, it was desired that surface pressure measurements at a location in front of the wing-body junction be taken simultaneously with the LDV measurements. The pressure signal could then be used as a detector for determining the flow-mode. This section describes in detail the data acquisition system developed to meet the above requirements.

The schematic of the data acquisition system is shown in Figure 5. One photomultiplier-tube is used to receive the scattered light from both the U (green) and V (blue) measurement volumes. By using only one PMT to collect the scattered light, alignment of the receiving optics is simplified. The signal from the PMT is amplified and split. The signal used to determine the U velocity is down-mixed by 30 MHz by a TSI-9186A LV frequency shifter. The down-mixed output is fed into a Macrodyne FDP 3100 processor. The V signal is down-mixed by 27.5 MHz from an Interaction Bragg cell driver, model ME-30, and a Mini-Circuits mixer, model ZAD-6. The down-mixed signal is connected to another Macrodyne FDP 3100 processor.

The Macrodyne FDP 3100 frequency domain processors have a digital output interface. The processors were configured with the bandwidth set to 20 MHz for U and 5 MHz for V . The number of sample points was set to 128 for both processors, since this

was found to give a high data rate with a data-valid ratio of 90%. The digital output from the FDP-3100s were connected to a digital I/O board, Analogic PDIO-96, in a 386SX-20 MHz personal computer.

In order to determine the measurement volume location, the position output voltage of the scanner must be sampled. Since the pressure signal needs to be sampled at a continuous rate, this rules out using the trigger out of the FDP-3100s to trigger the A/D conversions. An Analogic HSDAS-16 data acquisition board was used for sampling the position and pressure signals. This board was selected, since it has 16-bit resolution and high speed DMA.

The arrival time information is obtained by a counter/timer board, Analogic CTRTM-05, configured as a "32-bit timer with hardware save" on an active going gate edge triggered by the falling edge of the data-valid signal from the Macrodyne FDP 3100.

The maximum scan rate achievable was 300 Hz over a 75 mm scan height using a sinusoidal scanning function. In order to get a high data rate for the measurements in the wing-body junction flow, the scan rate had to be limited to 50 Hz. The typical scan velocity versus distance from the surface during the course of the measurements in the wing-body junction flow is shown in Figure 6.

Uncertainties

The uncertainties in the measured instantaneous velocities are directly proportional to the accuracy that the beam angles can be determined from geometry. This results in uncertainties for U of $\pm 0.4\%$ and $\pm 1.6\%$ for V . The variance in the vertical scan velocity V_s is 0.08 m/s. However, the instantaneous scan velocity is used. The uncertainty in the instantaneous scan velocity is ± 0.01 m/s.

The uncertainty in the vertical position, y , of a velocity sample is a function the accuracy of determining the arrival time, the accuracy in sampling of the scanner output voltage, and the measurement volume diameter. The error in the arrival time was found to be less than 5 μs and has a negligible contribution to the position uncertainty. The use of a 16-bit data acquisition board to sample the position voltage signal from the scanner also has a negligible contribution to the measurement volume position uncertainty. Therefore, the uncertainty in measurement volume position is determined by the measurement volume diameter, which in this case is 0.3 mm.

Chehroudi and Simpson (1984) discuss velocity bias considerations for scanning LDV systems. The velocity bias is proportional to σ/\bar{U} which is the ratio of the RMS of the velocity fluctuations to the mean velocity. In a scanning LDV system the mean velocity should be taken relative to the scanning measurement volume. Thus a scanning LDV has the effect of decreasing the bias error as compared to point-wise systems. For the present measurements the statistics of the flow were calculated with and without

velocity bias corrections. Velocity bias corrections usually are performed by calculating the statistics with a weighting function taken as the reciprocal of the instantaneous velocity. The weighting function used here is given by:

$$w = \frac{1}{\sqrt{V_s^2 + U^2}} \quad (6)$$

where V_s is the scan velocity and U is the instantaneous velocity of the measured velocity component. This method was used because not all the U and V velocity data were “coincident”.

Durst, Lehmann, and Tropea (1981) look at the effects of averaged statistics of the velocity taken over a finite bin width for scanning LDV systems. They found that the normalized error in the mean velocity can be given as

$$\epsilon_{\bar{v}} = \frac{1}{12} \left(\frac{1}{0.5 + \xi} \right)^2 \quad (7)$$

and the normalized error in the RMS

$$\epsilon_{\sigma} = \frac{1}{1 + 2\xi} \quad (8)$$

where ξ , the bias parameter, is given by

$$\xi = \frac{\beta}{\Delta y \alpha} \quad (9)$$

where β is the mean velocity and α is the velocity gradient for the interval or bin width Δy for which the statistics are calculated. The errors in the mean and rms velocities correspond to steep flow gradients, low mean velocities, and large averaging intervals.

Measurements in Wing-body Junction Flow

The flow past a wing-body junction is a complex highly turbulent three-dimensional flow. This type of flow occurs when a turbulent boundary layer encounters an obstruction protruding from a surface. There has been considerable research into such flows, see Devenport and Simpson (1990). The mean velocity vectors for the wing-body junction flow study here are shown in Figure 7, from Devenport and Simpson (1990). The application of scanning LDV to the measurement of this flow may extend the understanding of the flow structures that lead to bimodal histograms, such as shown in Figure 8.

Figures 9 and 10 show the mean velocity profiles for U and V velocities at $x/t = -0.30$ in the plane of symmetry of the wing-body junction. The mean square fluctuations for u and v are shown in Figures 11 and 12 for the same measurement location, $x/t = -0.30$. The differences observed between the present data and the results from Devenport and Simpson (1990) are probably due to the averaging of these quantities over a finite bin width as discussed by Durst, Lehmann, and Tropea instead of a velocity bias. The

maximum differences are found where the flow gradient in the vertical, y , direction is greatest and also where the mean velocity is near zero. These differences are smaller than equations 7 and 8 would indicate, this is due to the high level of turbulence at these locations which is not considered in the derivation of those equations.

Space-time correlations were calculated in this study for regions in the bimodal and backflow zone. The space-time correlation function $R_{f_1 f_2}$ is the cross-correlation between function f_1 , fixed in space, and function f_2 for which the time lag is computed and the position in space is dependent on time is given by:

$$R_{f_1 f_2}(\mathbf{x}_2(\tau) - \mathbf{x}_1, \tau) = \int f_1(\mathbf{x}_1, t) \times f_2(\mathbf{x}_2(\tau), t + \tau) dt \quad (10)$$

The space-time correlation function can be calculated for correlations of the u fluctuations at a fixed distance from the wall with the u fluctuations throughout the rest of the scan and is estimated by:

$$\rho_{uu}(y_j - y_i, \tau) = \frac{\sum u(y_i, t) \times u(y_j, t + \tau) / N}{\sqrt{u^2(y_i) \times u^2(y_j)}} \quad (11)$$

where y_i is the fixed position, y_j is the position at some point during the scan and N is the total number in the summation. The following space-time correlation can also be computed:

$$\rho_{vv}(y_j - y_i, \tau) = \frac{\sum v(y_i, t) \times v(y_j, t + \tau) / N}{\sqrt{v^2(y_i) \times v^2(y_j)}} \quad (12)$$

$$\rho_{uv}(y_j - y_i, \tau) = \frac{\sum u(y_i, t) \times v(y_j, t + \tau) / N}{\sqrt{\overline{u^2}(y_i) \times \overline{v^2}(y_j)}} \quad (13)$$

$$\rho_{vu}(y_j - y_i, \tau) = \frac{\sum v(y_i, t) \times u(y_j, t + \tau) / N}{\sqrt{\overline{v^2}(y_i) \times \overline{u^2}(y_j)}} \quad (14)$$

The results for these measurements are shown in Figures 13-16. The gaps in the data are due to low data rates near the wall caused by flare. The gaps near the top are due to the image of the scanning measurement volume not falling on the active area of the PMT.

The space-time correlation coefficients for ρ_{uu} , Figure 13, show a region of high correlation for events preceding the fluctuations near the wall extending to a non-dimensional time lag of $-6.0 T \times U_{ref} / t$. For the events following the fluctuations at the wall, the correlations are positive for the backflow region, $y/t < 0.09$. The fluctuations are of opposite sign for $y/t > 0.09$.

The space-time correlation ρ_{vv} , Figure 14, shows that the v fluctuations near the wall are correlated with v fluctuations events close in time and space. The correlations are significant for time lags in the past up to $-2.25 T \times U_{ref} / t$ and $1.5 T \times U_{ref} / t$ into the future. The events near the wall appear to be correlated on average with events out to $y/t = 0.15$.

The space-time correlations for u fluctuations near the wall with the v fluctuations along the scan, ρ_{uv} , is shown in Figure 15. The fluctuations are of opposite sign and

show significant correlations for time lags of -2.25 to $1.5 T \times U_{ref}/t$. The correlations of the near wall fluctuations are significant out to $y/t=0.15$.

Figure 16 shows the space-time correlations of the v fluctuations near the wall with the u fluctuations along the scan ρ_{vu} . The fluctuations are of opposite sign. Significant correlations are seen for -4.0 to $1.0 T \times U_{ref}/t$ time lag. This shows that the u fluctuations preceding in time have the most influence on the v fluctuations near the wall. This influence is seen out to $y/t=0.25$ and beyond. For the positive time lags, the correlations are significant out to $y/t=0.12$.

See chapter 4 for a complete discussion of the results of the measurements performed in the wing-body junction flow with the RSLDV.

Conclusions

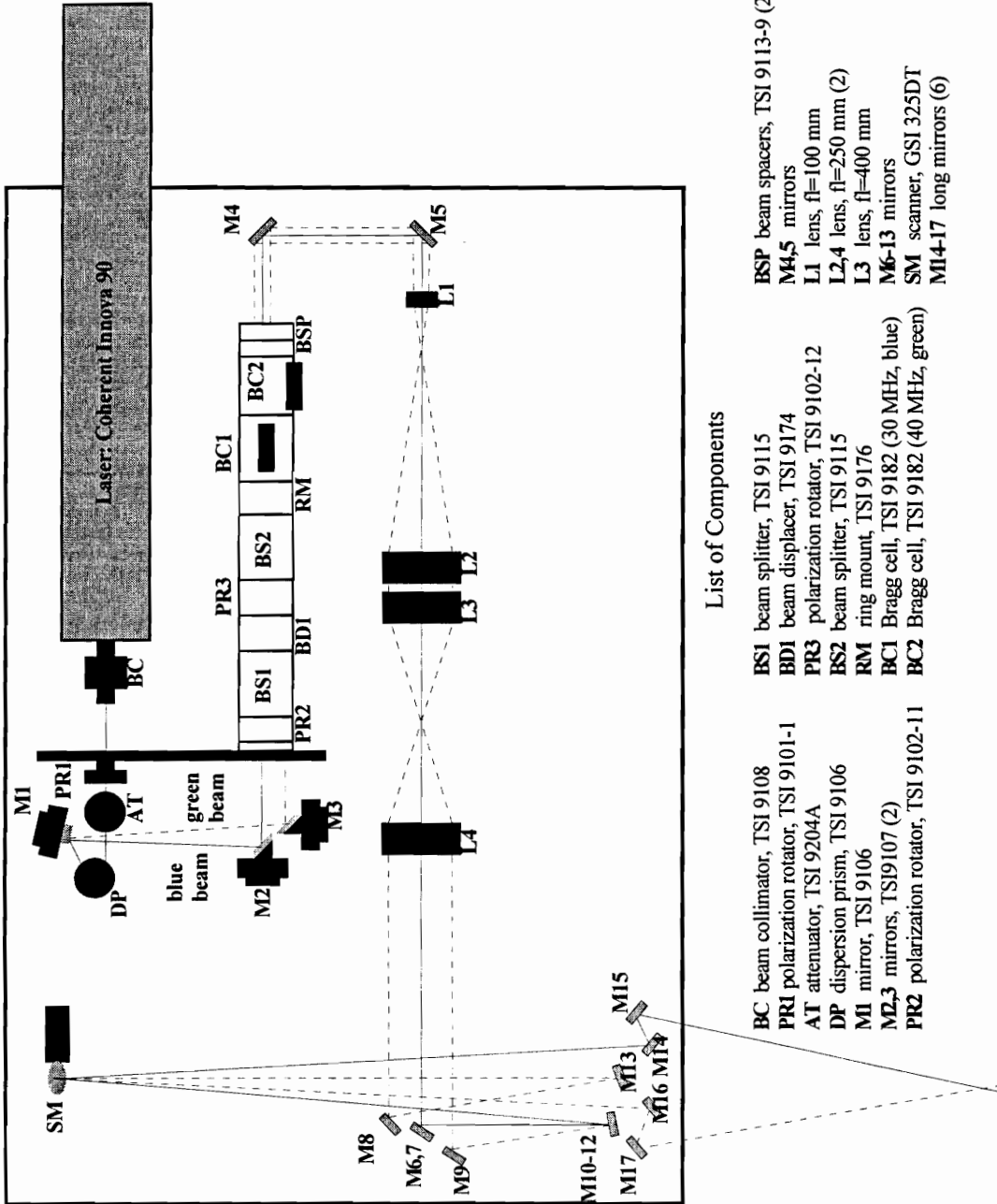
A rapidly-scanning two-velocity-component laser Doppler velocimeter has been designed. The system is capable of scanning up to 300 Hz, this is limited to less than 100 Hz by the Macrodyne processors. The proper use of this instrument was demonstrated by measurements in a wing-body junction flow. Space-time correlations can determine the sequence of events between the near wall and out region events. Space-time correlations show that the events preceding the ones near the wall are correlated for larger time lags

and further away from the wall than events following. This indicates that the fluctuations away from the wall drive those near the wall and that the u fluctuations in the outer region have the most influence on the near wall region.

References

- Chehroudi, B., and Simpson, R. L., "A Rapidly Scanning Laser Doppler Anemometer", *Journal of Physics E., Sci. Inst.*, vol 17, pp. 131-136, 1984; and *Selected Papers on Laser Doppler Velocimetry*, ed. R. J. Adrian, SPIE Milestone Series, MS 78, gen. ed. B. J. Thompson, pp. 319-324, 1993.
- Devenport, W. J., and Simpson, R. L., "Time Dependent and Time-Averaged Turbulence Structure near the Nose of a Wing-body Junction", *Journal of Fluid Mechanics*, vol 210, pp. 23-55, 1990.
- Durst, F., Lehmann, B., and Tropea, C., "Laser Doppler Systems for Rapid Scanning of Flow Fields", *Rev. Sci Instr.*, vol 52, pp. 1076-1681, 1981.
- Lehmann, B., and Mante, J., "Experimental Analysis of Turbulent Structures by Means of Rapid Two-Component Laser-Doppler Scanning", *ICIASF 93 Record, IEEE*, 1993.
- Simpson, R. L., "Scanning Laser Anemometry and Other Measurement Techniques for Separated Flows", *Advances in Fluid Mechanics Measurements Lecture Notes in Engineering*, Vol. 45, pp. 357-400, ed. M. Gad-el-Hak, Springer-Verlag, New York, 1989.
- Yariv, A., *Optical Electronics*, Holt, Rinehart and Winston, Inc., New York, 1985.

Figures



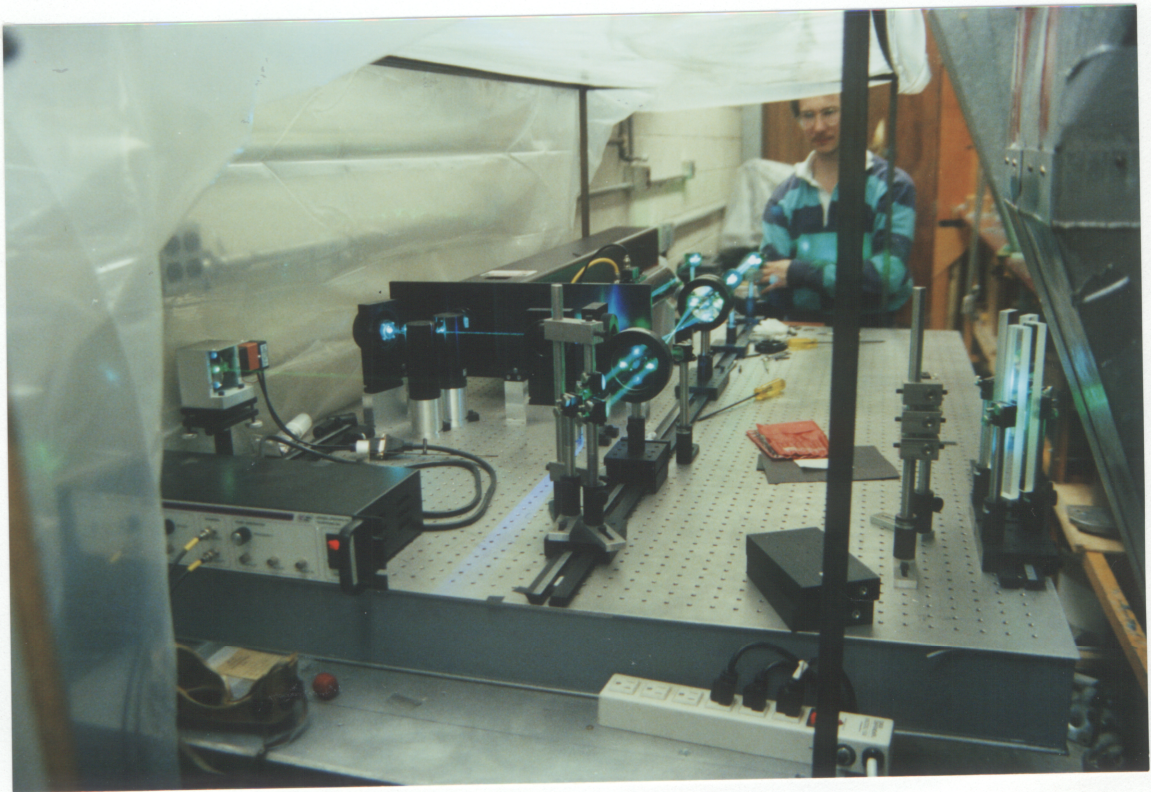


Figure 2. Photograph of transmitting optics.

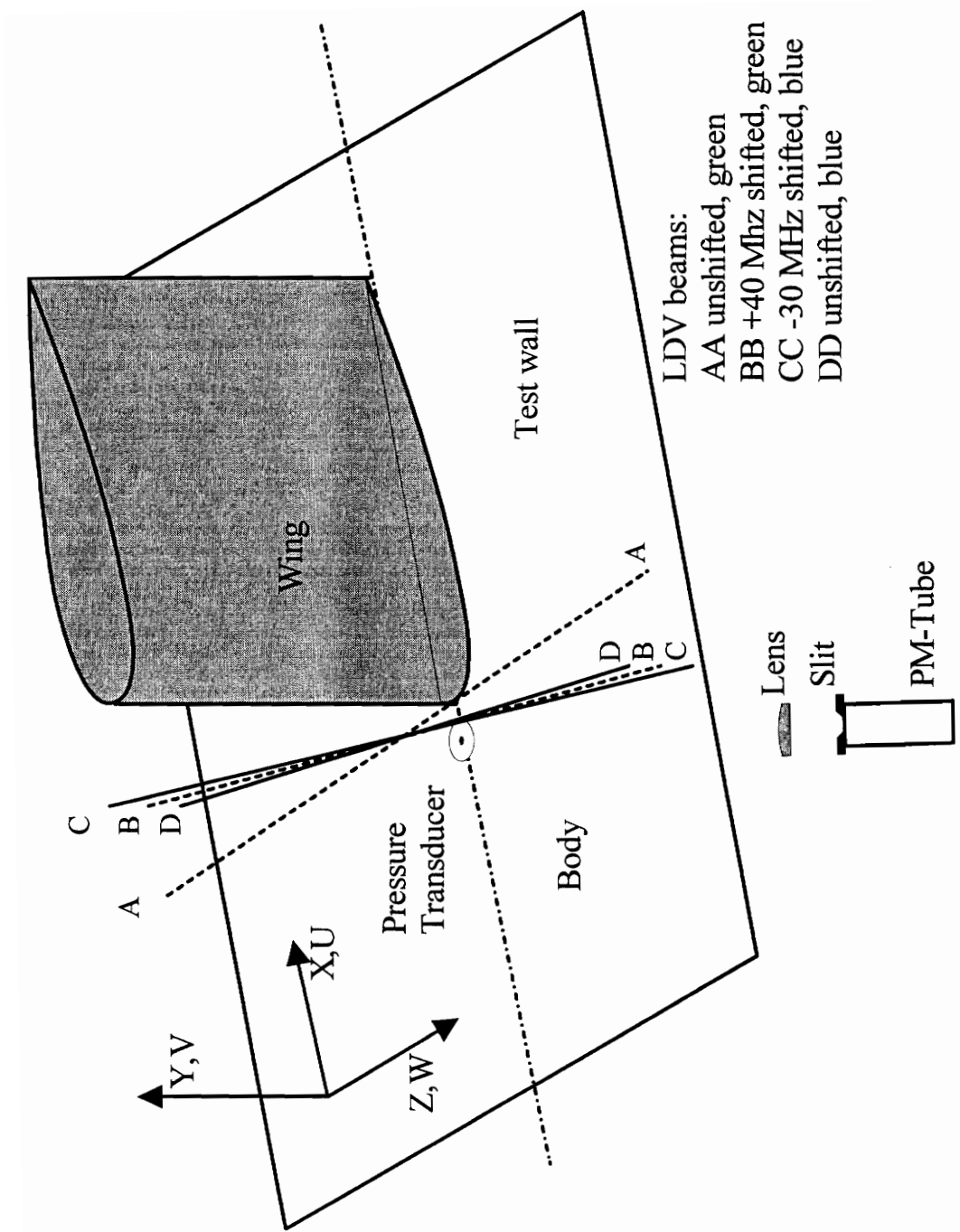


Figure 3. Schematic of wing-body junction and LDV beams.

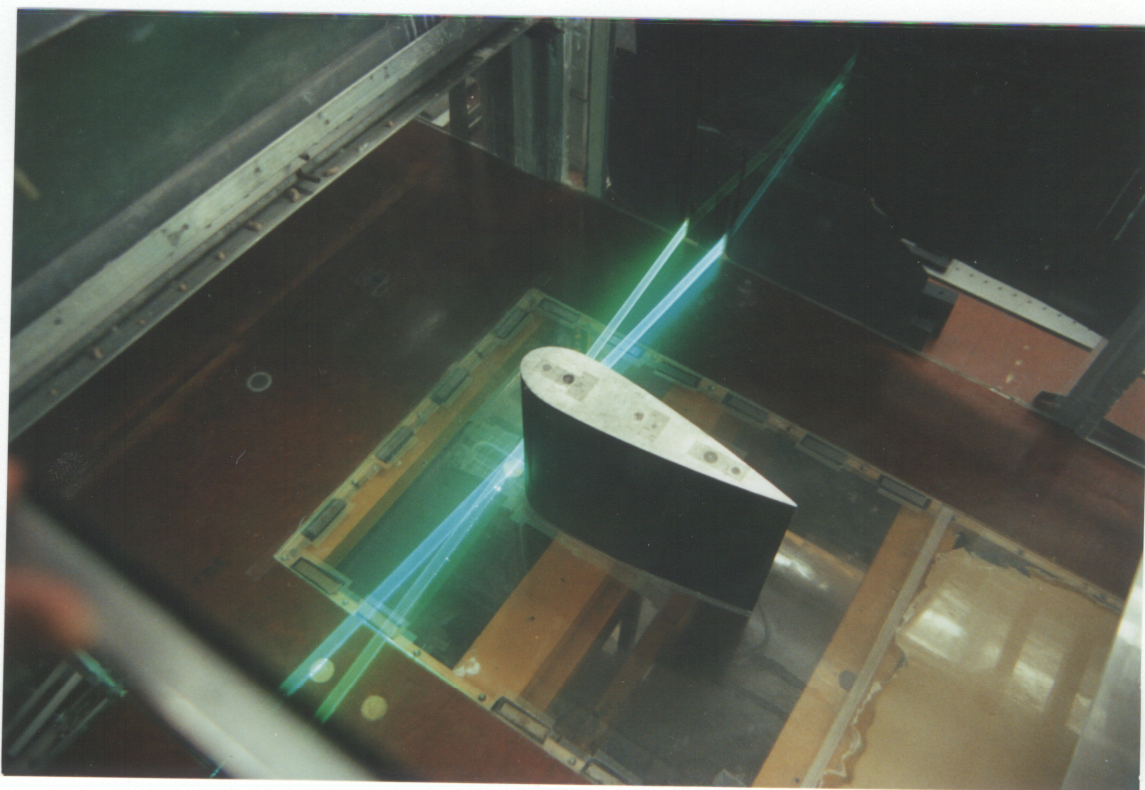


Figure 4. Photograph of scanning laser beams in front of wing-body junction.

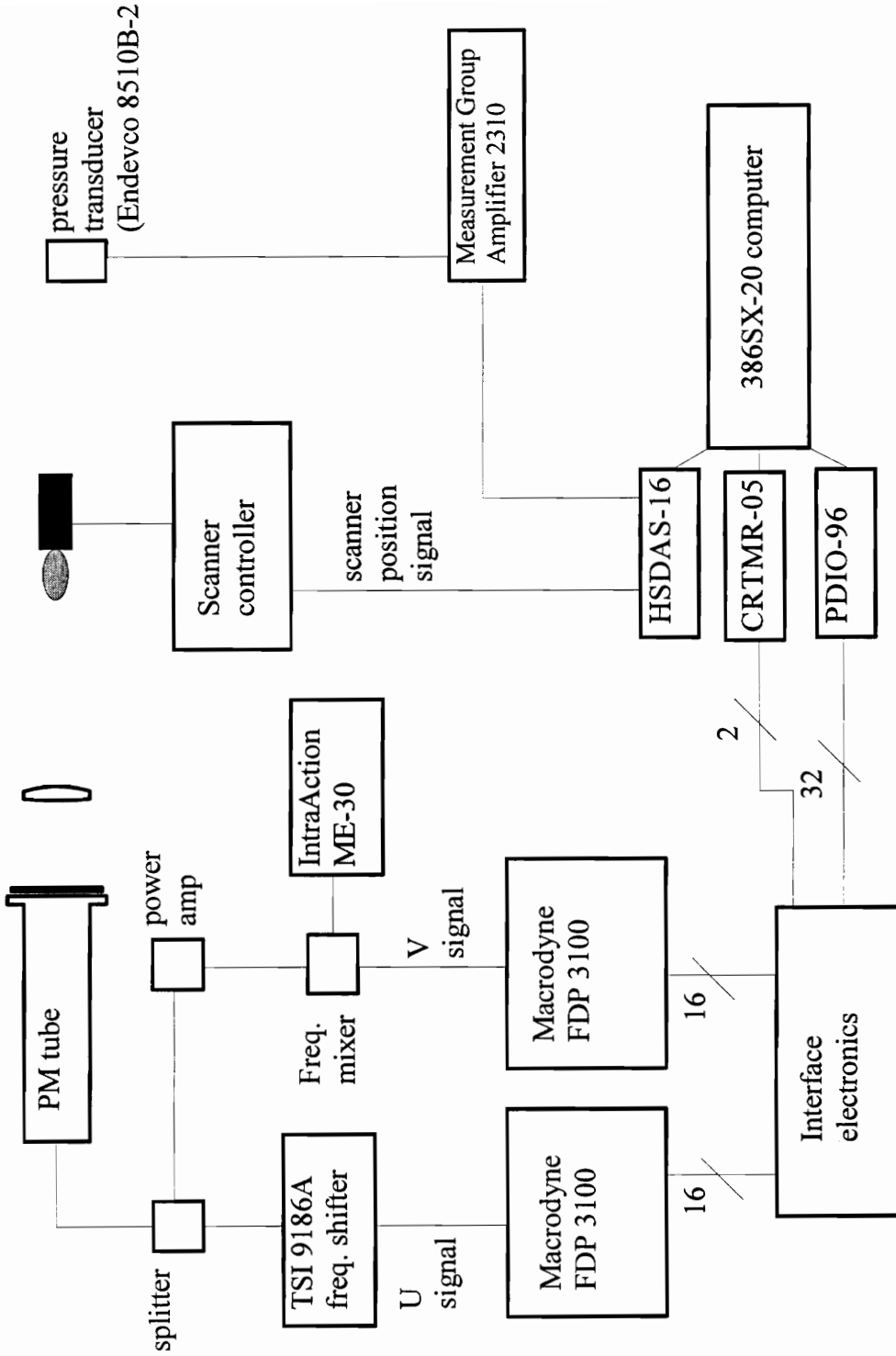


Figure 5. Schematic of data acquisition system.

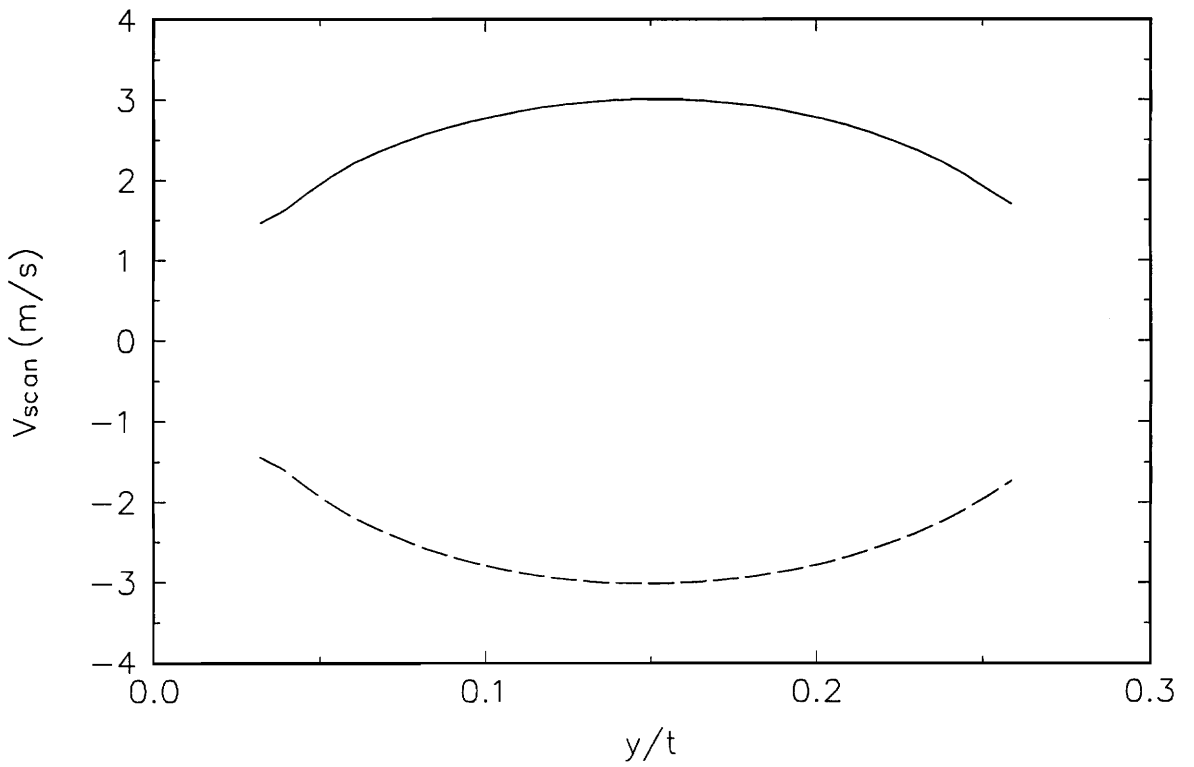


Figure 6. Typical scan velocity vs. y/t .

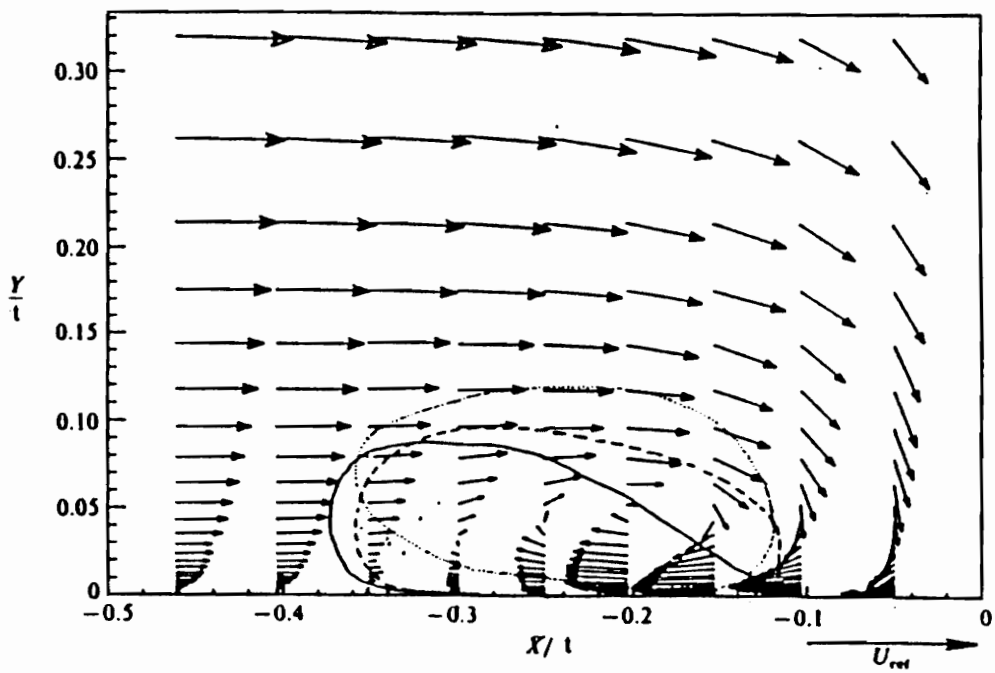


Figure 7. Mean velocity vectors in plane of symmetry of the wing-body junction flow from Devenport and Simpson (1990). Solid line shows the extent of the U bimodal flow, dashed line shows extent of V bimodal, and dotted line shows extent of U-V bimodal flow.

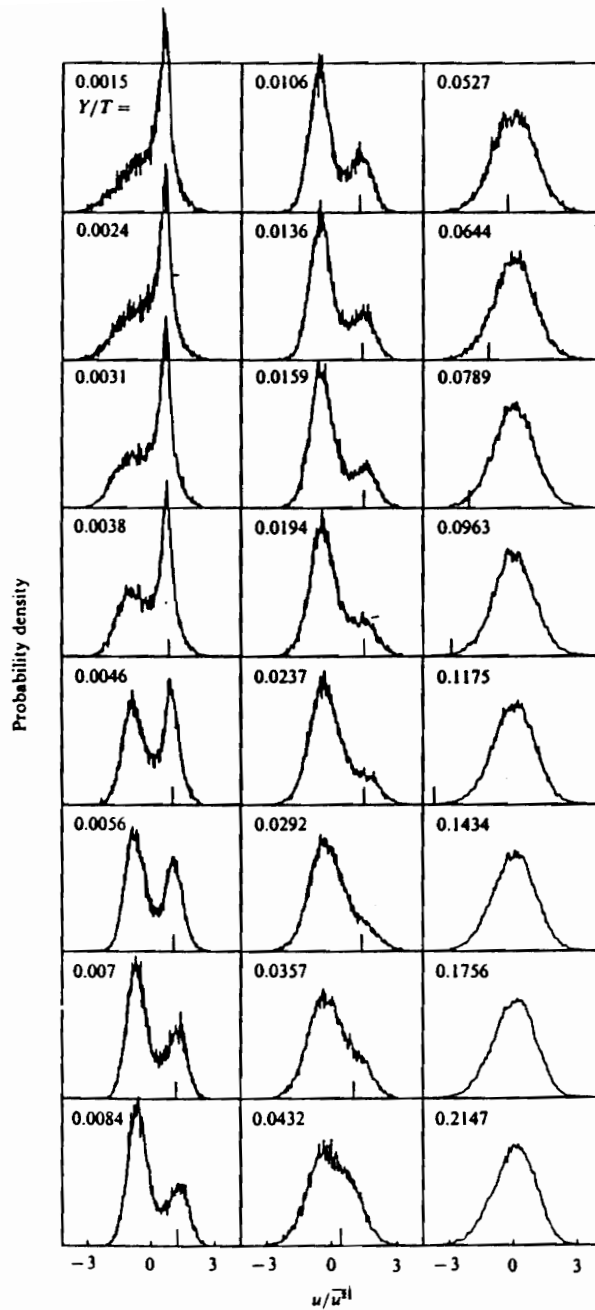


Figure 8. Example of a bimodal velocity histogram from Devenport and Simpson (1990).

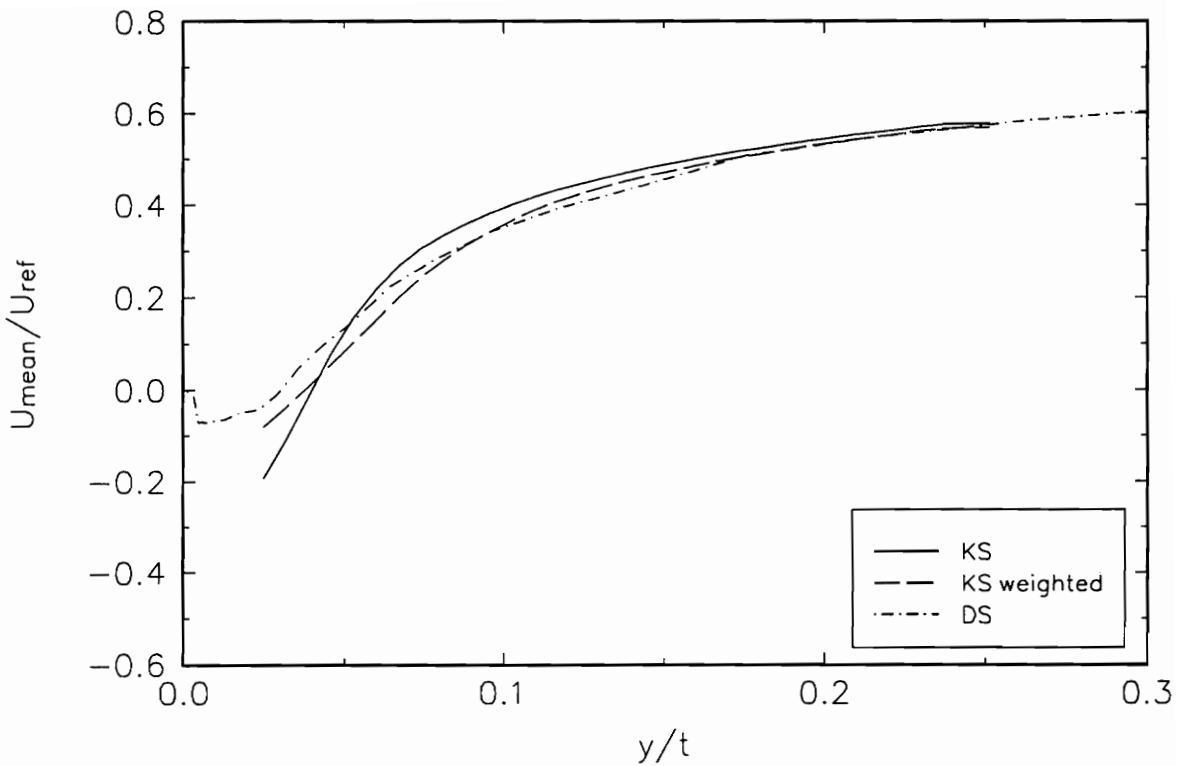


Figure 9. Mean U velocity at $x/t=-0.30$. Solid line is the present data, dashed line is present data with mean calculated from weighted histograms (equation 6), and dot-dash line is mean from Devenport and Simpson (1990).

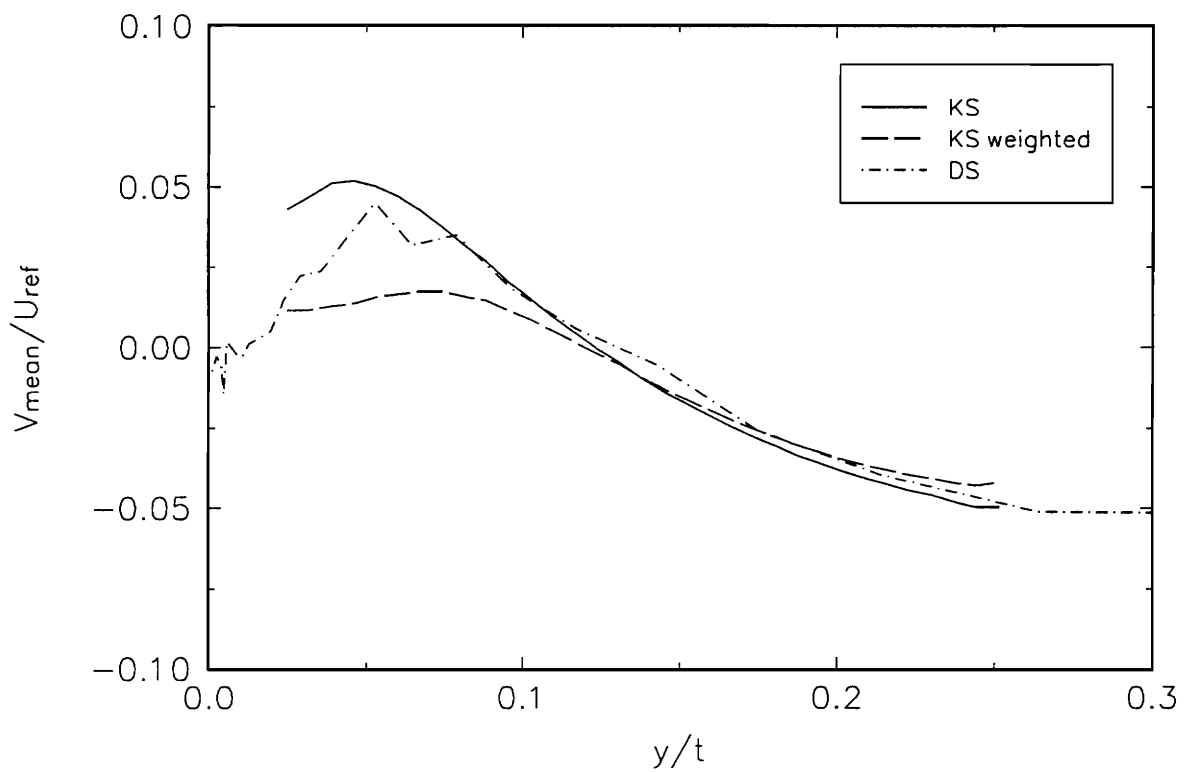


Figure 10. Mean V velocity at $x/t=-0.30$. Solid line is the present data, dashed line is present data with mean calculated from weighted histograms (equation 6), and dot-dash line is mean from Devenport and Simpson (1990).

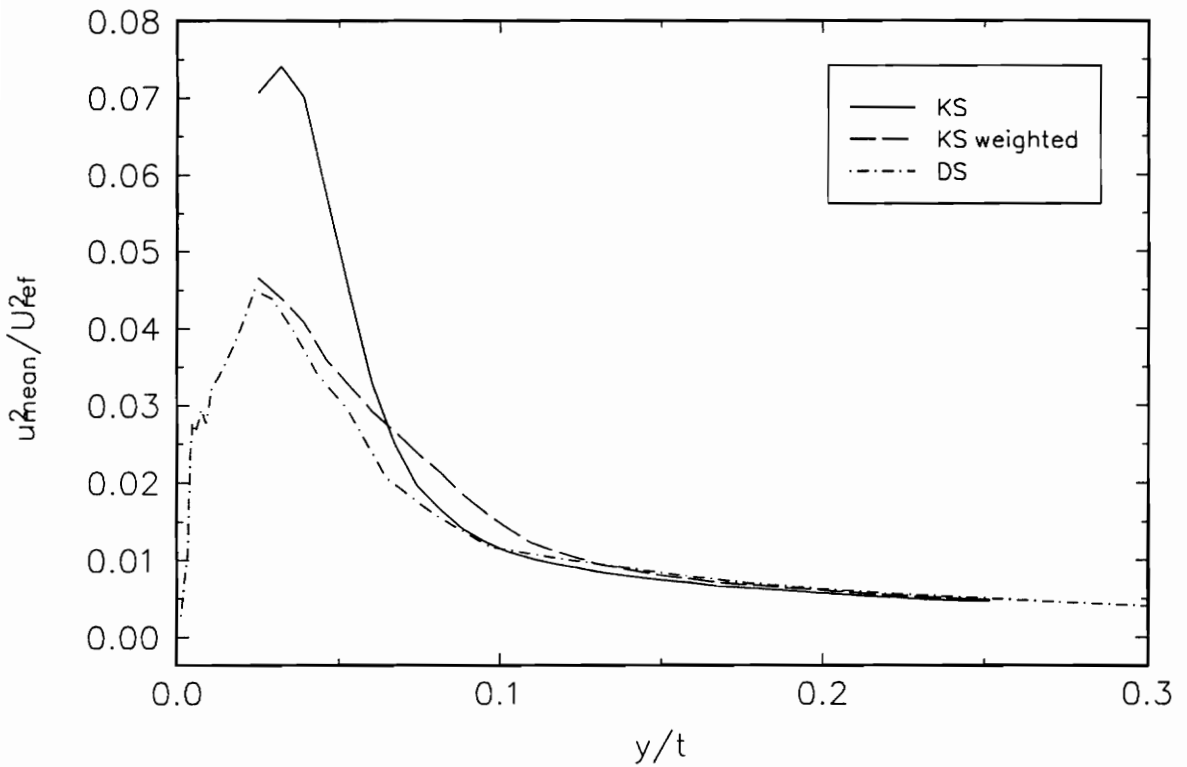


Figure 11. Mean u^2 velocity at $x/t=-0.30$. Solid line is the present data, dashed line is present data with mean calculated from weighted histograms (equation 6), and dot-dash line is mean from Devenport and Simpson (1990).

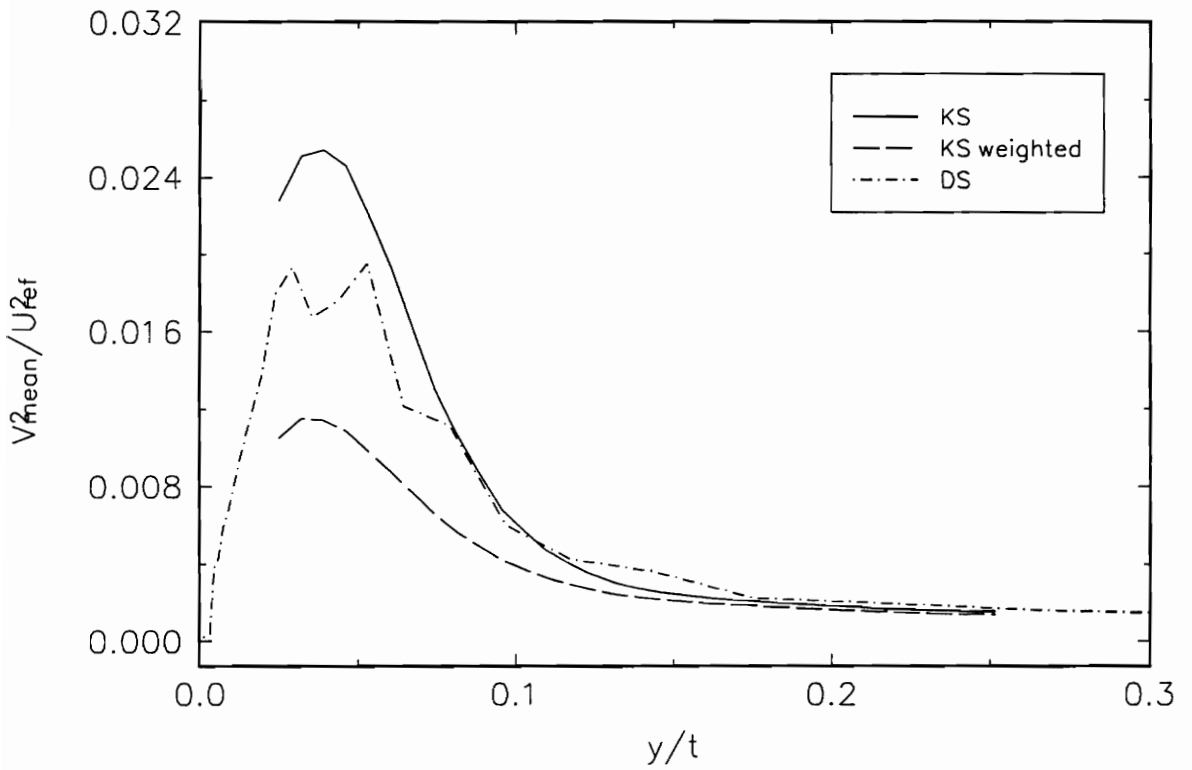


Figure 12. Mean v^2 velocity at $x/t=-0.30$. Solid line is the present data, dashed line is present data with mean calculated from weighted (equation 6), and dot-dash line is mean from Devenport and Simpson (1990).

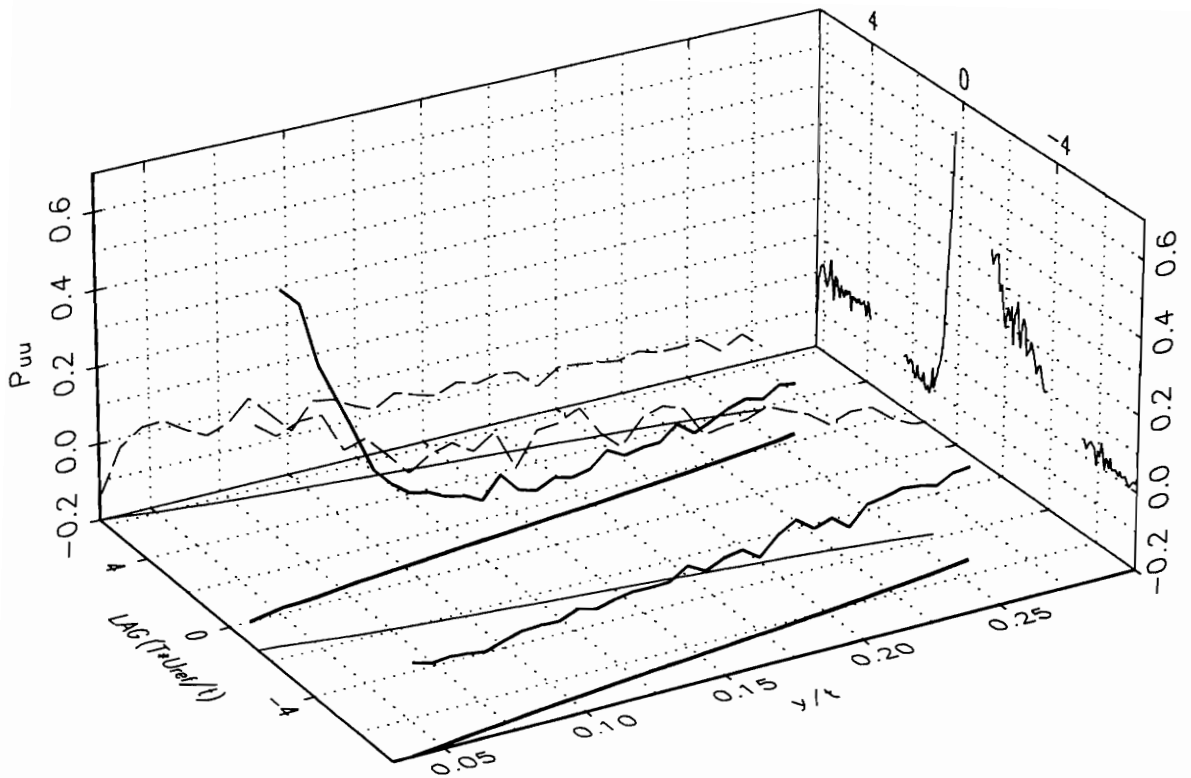


Figure 13. Space-time correlation function ρ_{uu} , correlation between u fluctuations at $y/t=0.039$ with u fluctuations through the scan (equation 11). Heavy solid line is ρ_{uu} for the up-scan, dashed line is ρ_{uu} for the down-scan, solid lines in time- y/t plane is the scan position, solid lines in ρ_{uu} -time plane are the projections of ρ_{uu} on to this plane.

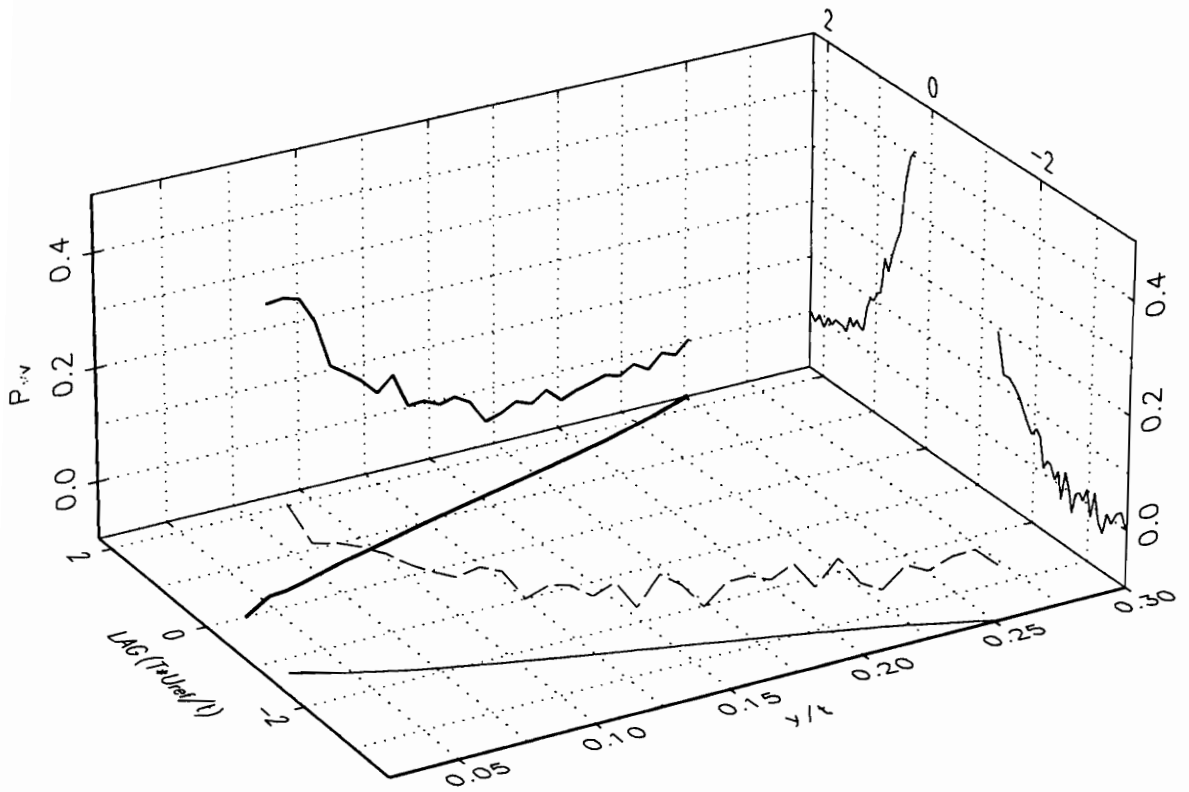


Figure 14. Space-time correlation function ρ_{vv} , correlation between v fluctuations at $y/t=0.039$ with v fluctuations through the scan (equation 12). Heavy solid line is ρ_{vv} for the up-scan, dashed line is ρ_{vv} for the down-scan, solid lines in time- y/t plane is the scan position, solid lines in ρ_{vv} -time plane are the projections of ρ_{vv} on to this plane.

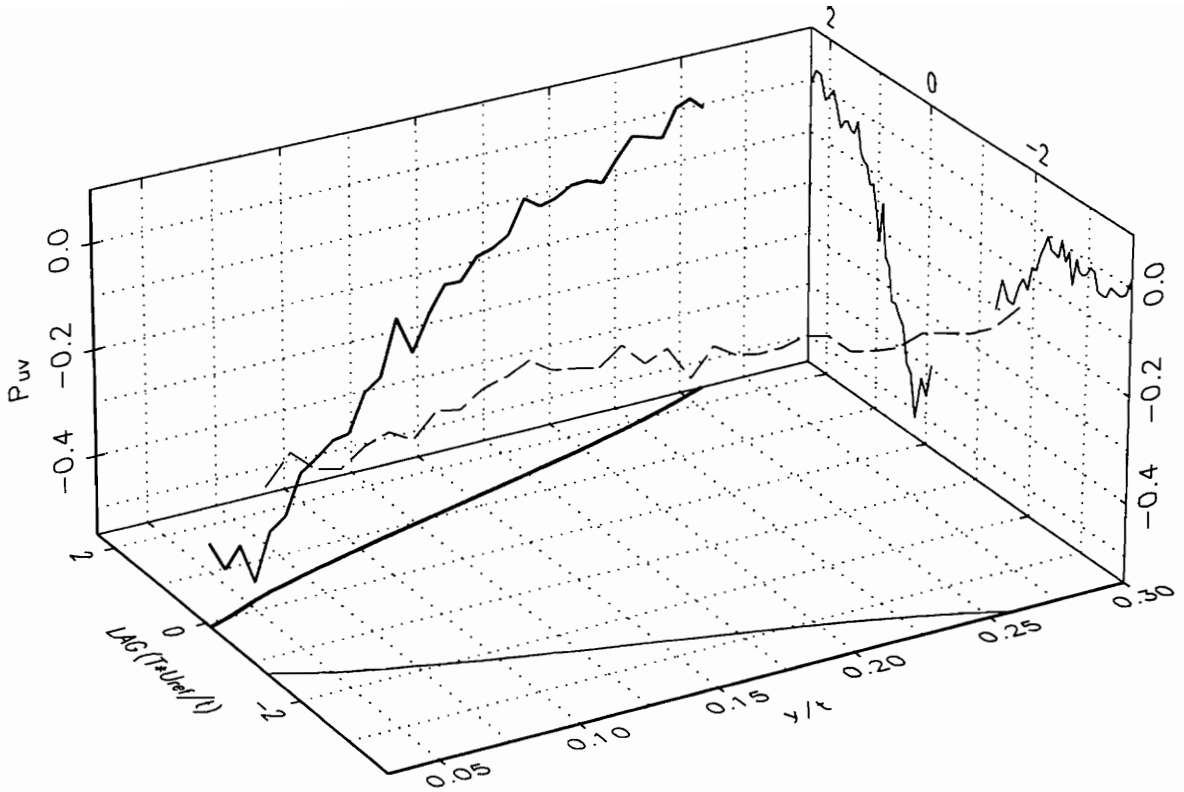


Figure 15. Space-time correlation function ρ_{uv} , correlation between u fluctuations at $y/t=0.039$ with v fluctuations through the scan (equation 13). Heavy solid line is ρ_{uv} for the up-scan, dashed line is ρ_{uv} for the down-scan, solid lines in time- y/t plane is the scan position, solid lines in ρ_{uv} -time plane are the projections of ρ_{uv} on to this plane.

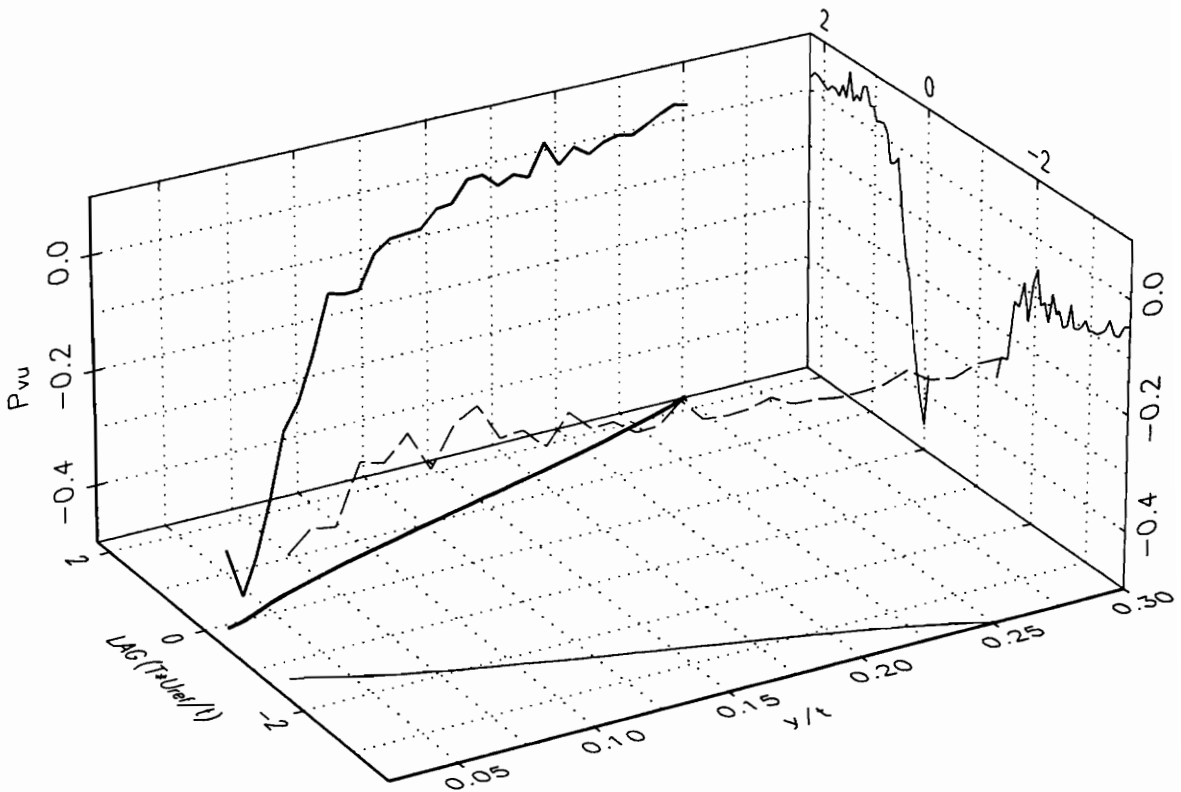


Figure 16. Space-time correlation function ρ_{vu} , correlation between v fluctuations at $y/t=0.039$ with u fluctuations through the scan (equation 14). Heavy solid line is ρ_{vu} for the up-scan, dashed line is ρ_{vu} for the down-scan, solid lines in time- y/t plane is the scan position, solid lines in ρ_{vu} -time plane are the projections of ρ_{vu} on to this plane.

Vita

The author was born on May 19, 1964 at Willis Air Force Base, Tripoli, Libya. He earned his B.S. degree in Aerospace Engineering from Virginia Polytechnic Institute and State University, Blacksburg, Virginia in June 1986.

Upon graduation, he joined the Aerospace and Ocean Engineering Department, VPI & SU. He completed a Master of Science in Aerospace engineering in 1989.

He has accepted a Post-Doctoral Fellowship at the Idaho National Engineering Laboratory in Idaho Falls, Idaho, with EG&G Inc.

A handwritten signature in black ink that reads "Ken A. Blum". The signature is written in a cursive style with a large, looping final letter.

PRELIMINARY ANNOUNCEMENT

NATIONAL CONFERENCE ON ENGINEERING LABORATORY AND INSTRUMENTATION EDUCATION

March 20-22 1995

PURPOSE: A conference to define, promote and enhance laboratory education in engineering

LOCATION: Hampton, Virginia

HIGHLIGHTS

- * Keynote speakers addressing the present state-of-the-art and the future computer platforms, ABET requirements, industrial needs, future directions of laboratory education, instrumentation, microtransducers, signal processing,
- * Two days of paper presentations on such important topics as computer interfacing, transducers, case studies, and software
- * Panel discussions addressing future directions of laboratory instrumentation, laboratory course content, and identification of industrial/government support of educational programs
- * Workshops focusing on laboratory software, teaching techniques, and typical courses
- * Industrial exhibits, poster sessions, tours of NASA facilities

For more information

Name _____ Title _____

Address _____

Phone _____ FAX _____

Interest: Participant _____ Poster _____ Industrial exhibitor _____

Mail to

Prof. A.L. Wicks Dept. of Mech. Eng. Virginia Tech Blacksburg, VA 24061-0238
Phone (703) 231-4323 FAX (703) 231-9100 Email: catawba@vtvm1.cc.vt.edu

CONFERENCE ORGANIZATION

DAY 1

8:30 AM Keynote Speaker #1 Role of laboratories in undergraduate education

9:15 -9:45 AM Open discussion

10:00 AM

Session 1

**Lab Topics
Mech.**

**Lab Topics
Chem.**

**Lab Topics
Elect.**

Possible topics in addition to the session topics

**Computerization of labs
Start-up problems
Lab Writing Skills
Faculty Training**

**Statistics
Design of Experiments
Case studies
Software**

Speaker requirements 12

12:00

L U N C H

1:15 PM Keynote Speaker #2 Computers /instrumentation in the engineering laboratory

2:00 -2:30 PM Open discussion

2:45 PM

Session 2

Session 3

Session Topics

**Basics of data acq.
Virtual Instruments
Basics of Signal Processing
Interfacing of Instruments**

**DSP's
VXI Instrumentation
Microtransducers
Digital/Analog conditioning**

Speaker requirements 8

Day 2

8:30 AM Keynote Speaker #3 Industrial Perspectives of Engineering Laboratory Education

9:15 -9:45 AM Open discussion

10:00 AM Vendors Exhibit and Poster display

12:00 LUNCH

1:15 PM Keynote Speaker #4 Future Directions in Engineering Laboratories

2:00 -2:30 PM Open discussion

Session 6

**Industrial Needs
Sources of Equipment support
ABET
NSF/NASA support**

**Speaker requirements 4
Day 3**

8:30 AM Panel Discussions

**Panel 1
5 Panelists/panel
Industrial needs**

**Panel 2
Laboratory content**

**Panel 3
Computers**

Coffee break 10:00-10:30

10:30 Panel 4

Future directions of labs and conference

12:00 LUNCH

1:00 -4:30 CONFERENCE WORKSHOPS